

Roadmap on Atomtronics

L. Amico,^{1,2,3,4,5} M. Boshier,⁶ G. Birkel,⁷ A. Minguzzi,⁸ C. Miniatura,^{5,3,9,10,11} L.-C. Kwek,^{3,5,12} D. Aghamalyan,³ V. Ahufinger,¹³ N. Andrei,¹⁴ A. S. Arnold,¹⁵ M. Baker,¹⁶ T.A. Bell,¹⁶ T. Bland,¹⁷ J.P. Brantut,¹⁸ D. Cassettari,¹⁹ F. Chevy,²⁰ R. Citro,²¹ S. De Palo,²² R. Dumke,^{3,10,5} M. Edwards,²³ R. Folman,²⁴ J. Fortagh,²⁵ S. A. Gardiner,²⁶ B.M. Garraway,²⁷ G. Gauthier,¹⁶ A. Günther,²⁵ T. Haug,³ C. Hufnagel,³ M. Keil,²⁴ W. von Klitzing,²⁸ P. Ireland,¹⁹ M. Lebrat,²⁹ W. Li,^{3,9} L. Longchambon,³⁰ J. Mompert,¹³ O. Morsch,³¹ P. Naldesi,^{8,4} T.W. Neely,¹⁶ M. Olshanii,³² E. Orignac,³³ S. Pandey,²⁸ A. Pérez-Obiol,³⁴ H. Perrin,³⁰ L. Piroli,³⁵ J. Polo,³⁶ A.L. Pritchard,¹⁶ N. P. Proukakis,¹⁷ C. Rylands,³⁷ H. Rubinsztein-Dunlop,¹⁶ F. Scazza,³⁸ S. Stringari,³⁹ F. Tosto,³ A. Trombettoni,^{40,41} N. Victorin,⁸ K. Khani,^{17,42} and A. Yakimenko⁴³

¹⁾ Dipartimento di Fisica e Astronomia 'Ettore Majorana', Via S. Sofia 64, 95127 Catania, Italy

²⁾ CNR-IMM & INFN-Sezione di Catania, Via S. Sofia 64, 95127 Catania, Italy

³⁾ Centre for Quantum Technologies, National University of Singapore, 3 Science Drive 2, 117543 Singapore

⁴⁾ LANEF 'Chaire d'excellence', Université Grenoble-Alpes & CNRS, F-38000 Grenoble, France

⁵⁾ MajuLab, CNRS-UCA-SU-NUS-NTU International Joint Research Unit, Singapore

⁶⁾ Physics Division, Los Alamos National Laboratory, Los Alamos, NM 87545, USA

⁷⁾ Institut für Angewandte Physik, Technische Universität Darmstadt, Schlossgartenstr. 7, 64289 Darmstadt, Germany

⁸⁾ Université Grenoble-Alpes, LPMCM & CNRS, LPMCM, F-38000 Grenoble, France

⁹⁾ Department of Physics, National University of Singapore, Singapore 117542

¹⁰⁾ Division of Physics and Applied Physics, Nanyang Technological University, 21 Nanyang Link, 637371 Singapore

¹¹⁾ Université Côte d'Azur, CNRS, INPHYNI, Nice, France

¹²⁾ Institute of Advanced Studies, Nanyang Technological University, 60 Nanyang View, 639673 Singapore

¹³⁾ Departament de Física, Universitat Autònoma de Barcelona, E-08193 Bellaterra, Spain

¹⁴⁾ Center for Materials Theory, Department of Physics and Astronomy, Rutgers University, Piscataway, NJ 08854

¹⁵⁾ Department of Physics, SUPA, University of Strathclyde, Glasgow G4 0NG, UK

¹⁶⁾ ARC Centre of Excellence for Engineered Quantum Systems, School of Mathematics and Physics, University of Queensland, Brisbane, QLD 4072, Australia

¹⁷⁾ Joint Quantum Centre (JQC) Durham-Newcastle, School of Mathematics, Statistics and Physics, Newcastle University, Newcastle upon Tyne, NE1 7RU, U.K.

¹⁸⁾ Institute of Physics, EPFL, 1015 Lausanne, Switzerland

¹⁹⁾ SUPA, School of Physics and Astronomy, University of St. Andrews, North Haugh, St. Andrews KY16 9SS, UK

²⁰⁾ Laboratoire Kastler Brossel, ENS-Université PSL, CNRS, Sorbonne Université, Collège de France, Paris, France

²¹⁾ Dipartimento di Fisica "E.R. Caianiello", Università degli Studi di Salerno, Via Giovanni Paolo II, I-84084 Fisciano (SA), Italy

²²⁾ CNR-IOM-Democritos National Simulation Centre, UDS Via Bonomea 265, I-34136, Trieste, Italy

²³⁾ Department of Physics, Georgia Southern University, Statesboro, GA 30460-8031 USA

²⁴⁾ Department of Physics, Ben-Gurion University of the Negev, Beer Sheva 84105, Israel.

²⁵⁾ CQ Center for Collective Quantum Phenomena and their Applications, Eberhard-Karls-Universität Tübingen, Germany.

²⁶⁾ Joint Quantum Centre (JQC) Durham-Newcastle, Department of Physics, Durham University, South Road, Durham DH1 3LE, UK

²⁷⁾ Department of Physics and Astronomy, University of Sussex, Falmer, Brighton, BN1 9QH, UK

²⁸⁾ Institute of Electronic Structure and Laser, Foundation for Research and Technology - Hellas, Heraklion, 70013, Greece

²⁹⁾ Institute for Quantum Electronics, ETH Zürich, 8093 Zürich, Switzerland and Department of Physics, Harvard University, Cambridge, MA 02138, USA

³⁰⁾ Laboratoire de physique des lasers, CNRS UMR 7538, Université Paris 13 Sorbonne Paris Cité, 99 avenue J.-B. Clément, F-93430 Villetaneuse

³¹⁾ CNR-INO and Dipartimento di Fisica 'Enrico Fermi', Largo Bruno Pontecorvo 3, 56127 Pisa, Italy

³²⁾ Department of Physics, University of Massachusetts Boston, Boston, MA 02125, USA

³³⁾ Univ Lyon, Ens de Lyon, Univ Claude Bernard, CNRS, Laboratoire de Physique, F-69342 Lyon, France

³⁴⁾ Laboratory of Physics, Kochi University of Technology, Tosa Yamada, Kochi 782-8502, Japan

³⁵⁾ Max-Planck-Institut für Quantenoptik, Hans-Kopfermann-Str. 1, 85748 Garching, Germany

³⁶⁾ Quantum Systems Unit, Okinawa Institute of Science and Technology Graduate University, Onna, Okinawa 904-0495, Japan

³⁷⁾ Joint Quantum Institute and Condensed Matter Theory Center, Department of Physics, University of Maryland, College Park, Maryland 20742-4111

³⁸⁾ CNR-INO and LENS, Università di Firenze, 50019 Sesto Fiorentino, Italy

³⁹⁾ CNR-INO BEC Center and Dipartimento di Fisica, Università di Trento, 38123 Povo, Italy

⁴⁰⁾ Department of Physics, University of Trieste, Strada Costiera 11, I-34151, Trieste, Italy

⁴¹⁾ CNR-IOM DEMOCRITOS Simulation Center and SISSA, Via Bonomea 265, I-34136 Trieste, Italy

⁴²⁾ European Laboratory for Non-Linear Spectroscopy (LENs), Università di Firenze, 50019 Sesto Fiorentino, Italy

⁴³⁾ Department of Physics, Taras Shevchenko National University of Kyiv, Ukraine

Abstract. Atomtronics is an emerging field of quantum technology dealing with matter-wave circuits of ultra-cold atoms manipulated in magnetic or laser-generated guides of different shapes and intensity. Atomtronic circuits promise the manipulation of coherent fluids whose operating conditions can be feasibly controlled with standards as provided by the atomic and molecular physics quantum technology. This way, atomtronics can provide the basis for new quantum devices with enhanced precision, control and flexibility. At the same time, the coherent currents in atomtronic circuits can be harnessed to define quantum simulators and emulators with a new logic. Here, we survey atomtronics-enabled quantum technology and we draw a roadmap for the field in the years to come. The latest progress achieved in matter-wave circuits design and atom-chips are reviewed. Atomtronic networks have been used as platforms to study many-body physics in a new way, both at equilibrium and at non-equilibrium. Relevant problems in mesoscopic physics, like persistent currents in closed architectures and quantum transport in circuits of fermionic or bosonic atoms, have been studied with a new twist. Rydberg atoms may provide a new platform for atomtronic circuits. Finally, we discuss the state of the art and the perspectives for quantum devices and sensors.

CONTENTS

I. INTRODUCTION	2	A. Mechanism for producing flow in a racetrack atom-circuit BEC by stirring	29
II. SCULPTED LIGHT	3	1. How stirring a racetrack atom circuit produces flow	29
A. Fast-scanning AODs	3	B. Creation of a single unit of flow: vortex swap	30
1. Feed-forward control	3	1. Final flow production: flow overtakes the barrier	30
2. Phase evolution in time-averaged potentials	3	C. Persistent Currents in Co-Planar Double-Ring Geometries	31
3. Atomtronics with time-averaged optical traps	3	1. Spontaneous Persistent Current Formation in a Ring Trap	31
B. Direct imaged DMD Optical potentials	4	2. Spontaneous Persistent Current Formation in Co-Planar Connected Ring Traps	31
1. Half-toning and time-averaging	4	D. Persistent Currents in Transversally coupled atomtronic circuits	33
2. Atomtronics with DMDs	4	E. Summary and future challenges	34
3. Turbulence with DMDs	5		
C. Hybrid atomic-superconducting quantum systems	5	VIII. PHASE SLIPS DYNAMICS IN RING SHAPED CONDENSATES	34
D. Optical potentials with liquid-crystal SLMs	5	A. Critical transport and vortex dynamics in a thin atomic Josephson junction	35
III. IMPLEMENTING RING CONDENSATES	6	B. Bose-Josephson junction among two one-dimensional atomic gases: a quantum impurity problem	37
A. Techniques based on magnetic traps	6	C. Bose-Einstein condensate confined in a 1D ring stirred with a rotating delta link	39
1. RF dressing and bubbles	7	1. Spectrum	39
2. Waveguides formed from Time-Averaged Adiabatic Potential (TAAP)	8	2. Adiabatic production of solitons and vortices	40
3. Dynamical ring in an rf-dressed adiabatic bubble potential	9	D. Thermal and quantum phase slips in a one-dimensional Bose gas on a ring	41
B. Trapping in rings with optical potentials	10	E. Conclusions	43
1. Pure optical potentials	11	F. Outlook	43
2. Bubble plus light sheet(s)	12		
C. Outlook	13	IX. ATOMTRONICS ENABLED QUANTUM DEVICES AND SENSORS	43
IV. ATOMTRONIC CHIPS AND HYBRID SYSTEMS	13	A. Diodes, transistors, and other discrete components	44
A. Precision Sensing	14	B. Atomtronic SQUIDs	45
B. Cryogenic Atom Chips and Hybrid Quantum Systems	15	C. Sagnac interferometry and rotation sensing	45
C. Outlook	17	D. Magnetometry	47
V. QUENCH DYNAMICS OF INTEGRABLE MANY-BODY SYSTEMS	18	E. Summary and outlook	48
A. Quench Dynamics	18	X. TWO LEVEL QUANTUM DYNAMICS IN RING-SHAPED CONDENSATES AND MACROSCOPIC QUANTUM COHERENCE	49
B. Evolution under integrable Hamiltonians	19	A. The Atomtronic quantum interference device:AQUID	49
1. The Lieb-Liniger model	19	B. Demonstration of the one qubit and two qubit unitary gates	51
2. The XXZ Heisenberg spin chain	23	1. Single qubit gates	52
C. Summary and Outlook	24	2. Two-qubit coupling and gates	52
VI. NON-EQUILIBRIUM PROTOCOLS FOR ONE DIMENSIONAL BOSE GASES IN ATOMTRONIC CIRCUITS	24	C. Readout of atomtronic qubits	52
A. Quench dynamics in the Lieb-Liniger model	25	1. Interferometric detection of the current states	53
1. The quench problem	25	D. Experimental realization of the ring-lattice potential with weak links	55
2. The Quench Action	26	E. Setup for adjustable ring-ring coupling	56
3. Quenches to the attractive regime	26		
B. Floquet Hamiltonian for the Periodically Tilted Lieb-Liniger Model	27		
C. Summary and Outlook	28		
VII. PERSISTENT CURRENTS AND VORTICES IN ATOMTRONIC CIRCUITS	29		

F. First experimental demonstration of the interference of atomtronic currents	57
G. Outlook	59
XI. TRANSPORT AND DISSIPATION IN ULTRACOLD FERMİ GASES	60
A. Superfluid transport with Fermi gases	61
1. Fermionic superfluidity and critical velocity	61
B. Josephson currents	61
C. Fermionic transport in mesoscopic channels	62
D. Fast spin drag in normal Fermi gases	63
E. Outlook	64
XII. TRANSPORT IN BOSONICS CIRCUITS	64
A. Matterwave guides	65
B. Ring-leads system	66
C. Y-junctions	68
D. Differences between fermions and hard-core boson	69
E. Entangled state generation with topological pumping in ring circuits	70
F. Outlook	70
XIII. ARTIFICIAL QUANTUM MATTER IN LADDER GEOMETRIES	71
A. The boson ladder at strong interaction	71
B. A ring ladder at weak interactions	72
C. Ultracold atoms carrying orbital angular momentum in a diamond chain	74
D. Conclusions and outlook	76
XIV. QUANTUM-ENHANCED ATOMTRONICS WITH SOLITONS	76
A. Creation and manipulation of Quantum Solitons	77
1. Quantum solitons in the Bose-Hubbard model	77
2. Soliton stability	77
3. Solitons in rotation	78
4. Entangling solitons with different L_z	79
B. Conclusions and outlook	79
XV. MANIPULATING RYDBERG ATOMS	79
A. Driven-dissipative Rydberg systems	80
B. Microwave-optical conversion using Rydberg atoms	80

I. INTRODUCTION

Quantum technologies can provide key innovations in the 21st century, with applications in many different areas like computation, simulation, sensing, and communication. At the core of this new technological development is the ability to control quantum systems from the macroscopic scale down to the single quantum level, which has been achieved in various physical systems ranging from atomic and spin systems to artificial atoms in the form of superconducting circuits^{1,2}.

In this article, we mostly focus on cold atoms systems. The existing atomic and molecular physics enabled quantum technology offers considerable degree of control over many systems. On top of that, significant progress has been achieved recently in the field for the coherent manipulation of atoms in trapping potentials characterized by wide ranges of intensities and shapes, in unprecedented precise manner^{3,4}. *Atomtronics* exploits the state-of-the-art of the field to realize matter-wave circuits in which ultra-cold atoms are manipulated in laser-generated or magnetic guides^{4,5}. Key aspects of this emerging field in quantum technology are the charge-neutrality and the coherence properties of the fluid flowing in the circuits, the bosonic/fermionic statistics that carriers may have, the tunable particle-particle interactions varying from short to long-range, and from attractive to repulsive, and the versatility of the operating conditions of the circuit elements. The terminology *Atomtronics* is inspired by the analogy between ultracold atoms confined in optical, magnetic, or photonic potentials and solid-state systems based on electrons in various forms of conductors, semiconductors or superconductors. As examples, a Bose-Einstein condensate (BEC) of neutral atoms in a double-well potential is analogous to a Josephson junction of coupled superconductors,⁶ while a BEC in an optical ring trap can exhibit quantized hysteresis⁷. It should be noted, however, that by virtue of the specific features of the atomtronic systems, quantum devices and simulators emerging from this novel idea are expected to be realized. For instance, the quantum properties of ultracold atoms as coherent matter waves enable systems that are equivalent to optical circuits, which are based on waveguides and beam-splitters for interferometric precision measurements in fundamental science and technological applications^{8,9}.

Atomtronic platforms can be conceived as extension to the scope of quantum simulators, revisiting textbook scenarios in many-body physics, like frustration effects, topological constraints, edge state formation etc., but with tunable boundary conditions and minimal finite size effects. Specific atomtronic circuits have been exploited to define a new diagnostic tool of the different many body quantum regimes, in terms of the current flowing through the cold atomic system. A clearly interesting domain in which atomtronics can play an important role is provided by mesoscopic physics^{10–12}. Important chapters of the field like persistent currents in ring-shape structures, problems of quantum coherent transport can be explored with a new twist.

Here, we summarise the recent activity and we draw a roadmap of the field of *Atomtronics*. In the first three chapters, we provide the fabrication principles for the atomtronic platforms, ranging from reconfigurable optical potentials employing acousto-optic deflectors, digital micromirror devices, and liquid-crystal spatial light modulators to micro-optical systems and hybrid solid state - cold atom systems circuits where the light pattern modifies the current density of the chip to create the desired trapping potential. These new capabilities allow us to probe the bulk of theoretical analysis on dynamics and quench in many-body systems in a new concept of experiments, chapters V and VI. Chapters VII and VIII deal with persistent currents in toroidal and ring shaped con-

densates. Such systems define the simplest atomtronic circuits with closed architecture. In particular, ring-shape bosonic circuits have been investigated as ideal platforms for matter-wave SQUID's (the Atomtronic QUantum Interference Device - AQUID) and flux qubits, chapter X; at the same time, a number of fundamental questions have been touched like the macroscopic quantum coherence, the nature of superfluidity in restricted sizes, vortex dynamics etc. Transport in specific fermionic and bosonic circuits are discussed in chapters XI and XII respectively. Chapter XIII and XIV discuss two specific configurations for atomtronics-enabled quantum technologies. Besides their interest in basic research of many-body physics, we envisage they can be instrumental for the fabrication of quantum sensors with enhanced performances. Atomtronic quantum sensors and devices are discussed in chapter IX. In Chapter XV, we discuss how Rydberg could provide the basis for a novel type of atomtronic circuits.

The present article was triggered by the Atomtronics@Benasque conference series. The Benasque staff is warmly acknowledged for invaluable help in the organization. Finally, we thank the Benasque director Jose-Ignacio Latorre for constant support of this line of research.

II. SCULPTED LIGHT

M. Baker, G. Gauthier, T.W. Neely, H. Rubinsztein-Dunlop, F. Tosto, R. Dumke, P. Ireland, D. Cassettari

In recent years, many experiments have been carried out with cold neutral atoms in arbitrary, reconfigurable optical potentials. Single atoms have been trapped in arbitrarily-shaped arrays,^{13–17} which have subsequently led to the demonstration of topological phases of interacting bosons in one-dimensional lattices.¹⁸ Various configurations of atomtronic circuits have been demonstrated, namely closed waveguides and Y-junctions,¹⁹ oscillator circuits,²⁰ atomtronic transistors,²¹ rings and atomtronic SQUIDs (AQUIDs)^{22–24}. Reconfigurable optical potentials have also been used to realise Josephson junctions in rubidium condensates²² and in fermionic lithium superfluids in the BCS-BEC crossover.²⁵ Finally, another area of interest is the realisation and study of quantum gases in uniform potentials.^{26,27} Some of these experiments are described in detail in the subsequent chapters of this review.

More generally, we note that sculpted light has many more applications beyond cold atom physics, e.g. to microscopy, optical tweezers and quantum information processing with photonic systems.³ In this chapter, we focus on the tools and techniques that underpin all these experiments: scanning acousto-optic deflectors (AODs), digital micromirror devices (DMDs), and liquid-crystal spatial light modulators (SLMs).

A. Fast-scanning AODs

By rapidly scanning a trapping laser beam much faster than the trapping frequencies for the atoms, the atoms experience

the time-average of the optical potential. Under these conditions, despite the modulated scanning action of the beam, the density of the atom cloud remains constant in time. The spatial location of the beam can be scanned in arbitrary 2D patterns, “painting” the potential landscape, simply by modulating the RF frequencies driving the crystal.^{28,29} Control over the RF power at each scan location allows local control over the potential depth. This feature can be used to error-correct, ensuring smooth homogeneous potentials, or can be deliberately engineered to implement barriers, wells, or gradients in the trap. The trapping geometry can be dynamically changed, with the use of deep-memory arbitrary waveform generators. Given the weak axial confinement provided by the scanned beam, this is best used in conjunction with an orthogonal light sheet, which provides tight confinement along the axis of the scanned beam, and ensuring excitation and phase fluctuations in the axial dimension are minimised.²⁹

1. Feed-forward control

The diffraction efficiency of AODs can change with the drive frequency. In order to correct for this, it is generally necessary to use feed-forward to compensate by adjusting the RF power of the AOD crystal, and hence beam intensity, for each (x,y) location. To correct for imperfections in other elements of the trapping potential, one can measure the atomic density distribution in the trap using absorption imaging and apply iterative correction to the RF power at each (x,y) location.²⁴

2. Phase evolution in time-averaged potentials

A full treatment time-averaged potentials needs to include the phase evolution of the condensate under the effect of the scanning beam. The time-varying potential $V(x,y,t)$ acts to imprint a phase ϕ , with the evolution $\hbar\partial\phi(x,y,t)/\partial t = V(x,y,t)$. For sufficiently fast scan rates, this effect is negligible, but at slower scan rates, this phase imprinting action can accumulate local phase, leading to residual micromotion in the condensate, the signatures of which have been observed.³⁰ This is an important consideration for atomtronic applications where the phase is an observable of interest, such as guided Sagnac interferometry.³¹

3. Atomtronics with time-averaged optical traps

The time-averaged optical dipole traps are extremely versatile, allowing a variety of geometries to be generated, and dynamically changed in structure by real-time adjustment of the scanning pattern. In the context of atomtronic geometries, BECs have been trapped into flat bottom line-traps, rings,^{24,32} lattices,³³ and dumbbell reservoirs (Fig. 1). Additionally, single mode matter-wave propagation and coherent phase splitting has been demonstrated in circuit elements such as waveguides and beamsplitters.¹⁹ The time-averaged optical beams

can be used to introduce multiple repulsive barriers and stirring elements to study persistent currents and superfluid transport in atomtronic circuits.²²

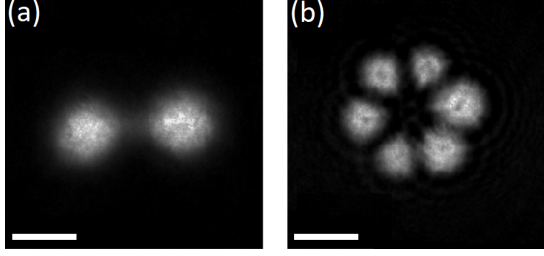


FIG. 1. Example geometries of time averaged optical dipole potentials - (a) BEC trapped in dumbbell potential, with two reservoirs connected through a channel of tunable length and width (b) Ring lattice of BECs. The scale bar on each image indicates $50 \mu\text{m}$.

B. Direct imaged DMD Optical potentials

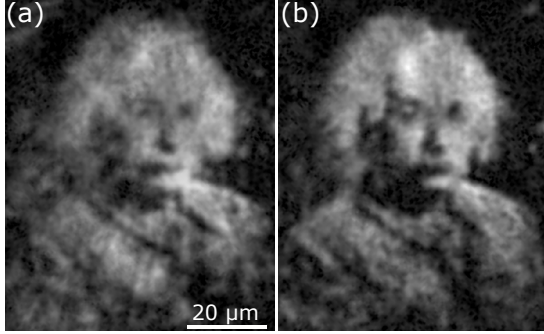


FIG. 2. Generating complex potentials using half-toning. (a) Initial in-situ image of the BEC density in a half-toned potential of Einstein, calculated using the optical system parameters. (b) Final converged BEC image after 11 feedback iterations where the atomic density is used to iteratively correct for imperfection in the density.^{34,35}

A recent addition to the spatial light modulator family is the digital micromirror device (DMD). Developed for digital light processing (DLP) applications, DMDs consist of millions of individually addressable, highly reflective mirrors. Each hinged mirror is mounted on a silicon substrate on top of control electrodes. The application of a control voltage tilts the mirrors between two ‘on’ or ‘off’ angles, typically $\pm 12^\circ$. The mirror array acts as a dynamical configurable amplitude mask for light reflected from their surface. The DMDs can be placed in the Fourier plane of the imaging/project system, similar to typical phase-based SLMs, where it can modulate both the phase and the amplitude of the light.³⁶ If phase modulation is not required, the DMD can be used as a binary amplitude mask in the object plane, similar to its DLP applications.^{37,38} In ‘DC’ mode, the mirrors are fixed to the ‘on’ angle and a static pattern can be projected. The true versatility of the device, however, lies in its dynamical (‘AC’) capability, with full frame refresh rates exceeding 20 kHz.

1. Half-toning and time-averaging

The projected image from the DMD is binary in nature. Although this would appear as a significant limitation in producing arbitrary optical potentials, a number of techniques exist to overcome this issue. The first of these is half-toning, or error-diffusion, which takes advantage of the finite optical resolution of the projection optical system to increase the amplitude control. With suitably high magnification, such that the projected mirror size is smaller than the resolution, multiple mirrors contribute to each resolution spot in the projected plane.³⁹ In this way, half-toning can be used to create intensity gradients in the light field, as shown in Fig. 2(a). Same as in the case of time-averaged AOD traps, feed-forward using the atomic density^{24,34,35} can be performed to correct for imperfections in the projection potential, as shown in Fig. 2(b).³⁵

One can also make use of the high-speed modulation of the mirrors to further improve the intensity control. The mirror array of the DMD is capable of switching speeds from DC to 20 kHz. By varying the on/off time of individual mirrors (pulse-width modulation), the time-average of the resulting light field can be utilised to improve the smoothness of the projected potentials.³⁵

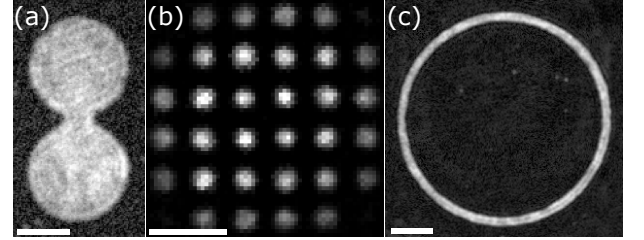


FIG. 3. Useful atomtronics geometries created with directly-imaged DMD trapping. (a) A dumbbell geometry of two reservoirs connected by a channel where the reservoir size, channel length and channel width can be varied to study superfluid transport.²⁰ (b) Square lattice of BECs with $10 \mu\text{m}$ period formed using the projection of a half-toned DMD pattern. The lattice period can be dynamically increased or decreased. (c) A ring-shaped BEC with a $110 \mu\text{m}$ diameter and $10 \mu\text{m}$ radial width useful for interferometry and transport experiments. The scale bar on each image indicates $20 \mu\text{m}$.

2. Atomtronics with DMDs

Atomtronics studies how to use neutral atom currents to create circuits that have properties similar to existing electrical devices. The advances in control and increased resolution of trapping potentials have been instrumental in the development of this field. The dynamic control over the potential given by DMDs have allowed time dependent implementations. Combined with other techniques such as the optical accordion lattice,³⁸ which allows smooth transitions between quasi-2D and 3D systems, they open up further avenues of control for future studies. The high resolution projection of DMD optical potentials enables the creation of complex masks. These have facilitated the study of superfluid transport in a variety

of traps, as shown in Fig. 3 where the three geometries relevant to superfluid transport experiments are shown.

3. Turbulence with DMDs

The dynamic properties of DMDs can be used for the creation of turbulence. As shown in Fig. 4, these techniques have been used to study Onsager vortices and their emergence in superfluids,^{40,41} the creation of tunable velocity solitons,⁴² and equilibration of chiral vortex clusters.⁴³

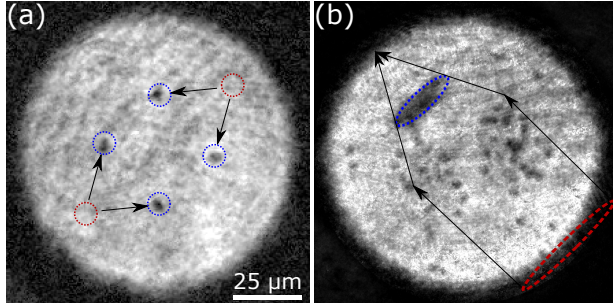


FIG. 4. Creating vortices using the dynamical capabilities of DMDs. (a) Deterministic creation of vortices using the 'chopstick' method.⁴⁴ The dashed red (blue) circle represent the initial (final) position of the optical barriers, with arrows indicating their trajectories. After a short 3 ms time-of-flight, the vortices are visible as density dips (black dots). (b) Creation of a vortex clusters⁴⁰ by sweeping a paddle-shaped optical barrier through a condensate. The red (blue) dashed ovals represent the paddle position at initial (picture) time with the arrows indicating the trajectory of the edges of the paddle.

C. Hybrid atomic-superconducting quantum systems

Superconducting (SC) atom chips have significant advantages in realizing trapping structures for ultracold atoms compared to conventional atom chips.^{4,45–50} We extend these advantages further by developing the ability to dynamically tailor the superconducting trap architecture. Heating chosen parts of a superconducting film by transferring optical images onto its surface, we are able to modify the current density distribution in a square SC film and create desired trapping potentials without having to change the chip or the applied field.

We use a high-power laser and a DMD to destroy the superconductivity and influence the shape and structure of a trap. We have been able to realize various trapping potentials and, in particular, to split a single trap (see Fig. 5) or to transform it into a crescent or a ring-like trap (see Fig. 6). Since the atomic cloud evolves with the trapping potential, cold atoms can be used as a sensitive probe to examine the real-time magnetic field and vortex distribution. We have also carried out simulations of the film heating, the corresponding redistribution of sheet current density, and the induced trapping potentials; the simulation results are in agreement with the experiments. Such simulations help to better understand the process and can be used to design a trap with the needed properties.

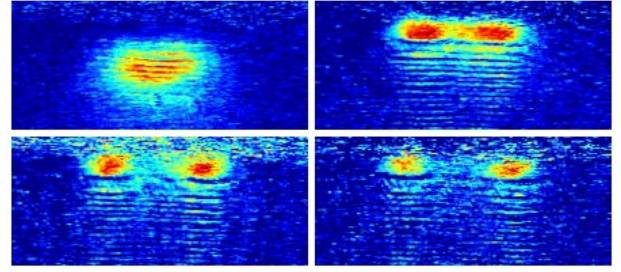


FIG. 5. Absorption images of the atomic cloud splitting taken after 0 (top-left), 20 (top-right), 30 (bottom-left) and 40 (bottom-right) ms of illumination time respectively.

More complex structures can be achieved by increasing the heating pattern resolution. This method can be used to create magnetic trap lattices for ultracold atoms in quantum computing applications and, in particular, optically manipulated SC chips open new possibilities for ultracold atoms trapping and design of compact on-chip devices for investigation of quantum processes and applications in atomtronics.^{51–57}

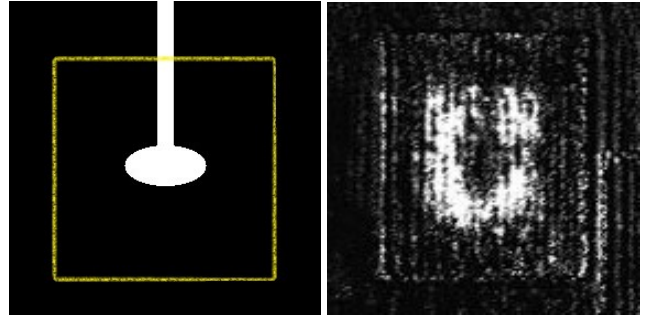


FIG. 6. DMD image on the left, where the real dimension of the SC film is highlighted in yellow and absorption image of the atomic cloud on the right.

D. Optical potentials with liquid-crystal SLMs

Differently from a DMD which spatially modulates the amplitude of the light, a liquid-crystal SLM spatially modulates the phase of the light. The phase pattern on the SLM acts as a generalised diffraction grating, so that in the far field an intensity pattern is formed, which is used to trap atoms. In practice, the far field is obtained by focusing the light with a lens, so that the intensity pattern that traps the atoms is created in a well-defined "output plane" coinciding with the lens focal plane. The SLM acts effectively as a computer-generated hologram, and the light field in the output plane is the Fourier transform of the light field in the SLM plane.

The first experiments with these holographic traps go back over ten years ago.^{58,59} A reason for the use of phase-only SLMs, rather than amplitude modulators, is that the former do not remove light from the incident beam. This is advantageous from the point of view of light-utilisation efficiency.

Moreover, as we show below, a phase-only SLM allows the control of both the amplitude and phase on the output plane.

The calculation of the appropriate phase modulation to give the required output field is a well-known inverse problem which, in general, requires numerical solution. Iterative Fourier Transform Algorithms (IFTAs) are commonly used, and variants which control both phase and amplitude have been recently demonstrated.^{60,61} In this work we use a different iterative method to create patterns with independent control over the phase and amplitude profiles. This is a conjugate gradient minimisation technique which efficiently minimises a specified cost function.^{62,63} The cost function can be defined to reflect the requirements of the chosen light pattern, such as removing optical vortices from the region of interest.

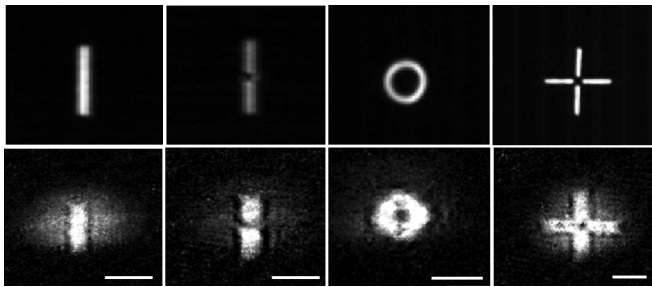


FIG. 7. ^{87}Rb condensates in SLM-generated optical potentials. The top row shows the intensity patterns used for trapping and the bottom row shows the condensates after a 2 ms time-of-flight. The ring trap contains $\sim 10^6$ atoms, while the other traps contain $\sim 5 \times 10^5$ atoms. The scale bar on the images indicates $100 \mu\text{m}$.

The intensity patterns obtained with this method are shown in the first row of Fig. 7. They are taken at a wavelength of 1064 nm , i.e. red-detuned relative to the rubidium transition, causing rubidium atoms to be trapped in the regions of high intensity. The SLM light is focused on the atoms by a $f=40 \text{ mm}$ lens, giving a diffraction limit of the optical system of $6 \mu\text{m}$ at 1064 nm . This is therefore the resolution that can be achieved in our light patterns.

Going from left to right in Fig. 7, we show a simple waveguide, a waveguide with a potential barrier halfway across, a ring trap, and a cross-like pattern. The latter has been proposed for the study of the topological Kondo effect.⁶⁴ In all these light patterns, the phase is constrained by the algorithm. For the simple waveguide, the ring and the cross, we program a flat phase across the whole pattern. We find that by controlling the phase this way, the shape of the intensity pattern is well maintained as the light propagates out of the focal plane for up to ~ 10 times the Rayleigh range. By comparison, a pattern with random phase loses its shape much sooner.

Differently from the other three patterns, for the waveguide with the barrier we program a sharp π phase change halfway across the line. In the resulting intensity profile, this phase discontinuity causes the intensity to vanish hence creating the potential barrier whose width is close to the diffraction limit.

The second row of Fig. 7 shows Rb BECs trapped in the potential created by the SLM light patterns, combined with an orthogonal light sheet that provides tight confinement along

the axis of propagation of the SLM light.^{65,66} The clouds are imaged after a 2 ms time-of-flight and undergo mean-field expansion during this time, leading to a final density distribution that is more spread out compared to the transverse size of the SLM traps.

In conclusion, controlling the phase of the light pattern opens new possibilities for the trapping and manipulation of ultracold atoms. Here we have shown that phase control gives an alternative way to create barriers close to the diffraction limit by using discrete phase jumps. In addition to this, phase control can also be useful for many more atomtronics applications, for instance phase imprint via a Raman transition,⁶⁷ and the realisation of artificial gauge fields.^{68,69} *Acknowledgments* The UQ group has been funded by the ARC Centre of Excellence for Engineered Quantum Systems (project number CE1101013), and ARC Discovery Projects grant DP160102085. The St Andrews group acknowledges funding from the Leverhulme Trust (RPG-2013-074) and from EPSRC (EP/G03673X/1; EP/L015110/1).

III. IMPLEMENTING RING CONDENSATES

M. Baker, T.A. Bell, T.W. Neely, A.L. Pritchard, G. Birkel, H. Perrin, L. Longchambon, M.G. Boshier, B.M. Garraway, S. Pandey, and W. von Klitzing

The many interesting properties of degenerate quantum gases, such as phase coherence, superfluidity, and vortices naturally make the geometry of these systems of great interest. Ring systems are of particular interest, as the simplest multiply connected geometry for coherent matter-wave guiding and as a potential building block for circuitual atomtronic devices. In addition, ring systems have interesting properties such as persistent flow, quantum hall states and the potential for Sagnac interferometry.

Advances in the control of quantum gases have seen the development of atom waveguides formed from both magnetic trapping and magnetic resonance, and optical dipole trapping, and more recent implementations using hybrids of both. These approaches satisfy the criteria needed for coherent quantum matter-wave flow: i.e. the waveguides are *smooth* and can form *loops* that are *dynamically* controllable. In this chapter we will discuss the experimental and theoretical developments in all three types of waveguide approaches.

In what follows, in Section III A we discuss approaches primarily involving magnetic and radio-frequency fields, and in Section III B we will discuss optical and hybrid approaches to implementing ultra-cold atoms and condensates in rings before concluding in Section III C.

A. Techniques based on magnetic traps

Experimental techniques for trapping atoms in magnetic fields are well developed since the first BECs, and it is natural to consider such an approach, and build on that approach, to make ring waveguides. Nevertheless, this brings particular

challenges because of the need to satisfy Maxwell's equations for fields trapping in a ring geometry, the need to avoid the loss of atoms from Majorana spin flips, occurring in the vicinity of field zeros, and the desire, for some experiments, to have trapping systems with high symmetry.

The earliest examples of waveguides for ultra-cold atoms were produced using static magnetic fields, where DC current carrying wires were used to create large area ring⁷⁰ and stadium⁷¹ geometries which initially trapped thermal atoms. With Ref. 72 we had the first demonstrations of a ring waveguide with a Bose-condensed gas. Subsequent experimental developments can be divided into systems which principally use macroscopic coils for generating the magnetic trap, and those systems which employ microfabricated structures in an *atom chip* to generate the spatially varying potentials. We will briefly discuss the latter next and the former in Sections III A 1–III A 3.

The appeal of atom-chip traps is their compact footprint, potential portability, and the ability to fabricate quite complex geometries, switches, and antenna components into a compact package^{73,74}. Additionally, the close proximity of the wires allows high trapping frequencies to be achieved, even for modest currents. However, trapping in close proximity to a surface brings with it its own challenges. Foremost of these are the corrugations in the magnetic guiding potential that arise from imperfectly directed currents in the conducting material. An additional challenge is the perturbing effect of the end connections, to supply current in and out of the conducting ring. Although these problems can be alleviated to some degree by the use of AC fields⁷⁵, which provides a smooth time-averaged current in the wire, as well as switching elements at the end connections to minimise the perturbative phase effects on the ring condensate⁷⁶, they cannot be removed completely. A comprehensive survey on the implementation of ring traps based on atom-chips, and their applications, is covered in detail in the recent review Ref. 77.

1. RF dressing and bubbles

It is not obvious that micron-scale trapping structures for ultra-cold atoms can be created using macroscopic scale magnetic coils. However, by means of the addition of radio-frequency coils, magnetic traps with a simple trapping geometry can be transformed into ring traps and other topologies. The theoretical basis is to treat the atom and radio-frequency field with adiabatic following and the dressed-atom theory⁷⁸. Originally introduced in the optical domain by Cohen-Tannoudji and Reynaud in 1977 we adapt it here in the radio-frequency domain where it has found several applications (see also sections III A 2, III A 3 and III B 2). The approach is suitable for ultra-cold atoms in magnetic traps where the trap potential is governed by the spatially varying Zeeman energy and the spatially varying energy difference between Zeeman levels can be in the radio-frequency range^{79,80}. The method relies on the adiabatic following of local eigenstates and it is notable that the superpositions of Zeeman states can provide some resilience to temporal noise and surface

roughness⁷⁵. The combination of static magnetic fields and radio-frequency fields with their different spatial and vector variation allows a flexibility in the resulting potentials for the creation of shell potentials, rings, tubes, and toroidal surfaces amongst others^{79,80}.

As a simple example we can consider a simple spatially varying static field and a uniform radio-frequency field. A simple spatially varying magnetic field (obeying Maxwell's equations) is the quadrupole field

$$\mathbf{B}_0(\mathbf{r}) = b'(x\hat{\mathbf{e}}_x + y\hat{\mathbf{e}}_y - 2z\hat{\mathbf{e}}_z), \quad (1)$$

where b' represents the gradient of the field in the x - y plane. This field is often generated by a pair of coils with current circulating in opposite directions. When an atom interacts with this static field via its magnetic dipole moment μ we obtain the ubiquitous interaction energy

$$U(\mathbf{r}) = -\mu \cdot \mathbf{B}_0(\mathbf{r}) \rightarrow m_F g_F \mu_B |\mathbf{B}_0(\mathbf{r})|, \quad (2)$$

responsible for magnetic potentials and the Zeeman energy splitting. The second form for $U(\mathbf{r})$ has the integer, or half integer $m_F = -F \dots F$ which arise from the quantisation of the energy, along with the Landé g -factor g_F and Bohr magneton μ_B . For our example static field (1) the resulting potential is $U(\mathbf{r}) = m_F \hbar \alpha \sqrt{x^2 + y^2 + 4z^2}$ where $\alpha = g_F \mu_B b' / \hbar$.

In the next step towards radio-frequency dressed potentials we add the RF field. The interaction is still given by Eq. (2), but with the replacement $\mathbf{B}_0(\mathbf{r}) \rightarrow \mathbf{B}_0(\mathbf{r}) + \mathbf{B}_{\text{rf}}(\mathbf{r}, t)$. The oscillating radio-frequency field $\mathbf{B}_{\text{rf}}(\mathbf{r}, t)$ is, in general, off-resonant to the local Larmor frequency, or local Zeeman energy spacing $|g_F \mu_B |\mathbf{B}_0(\mathbf{r})||$ and we define a spatially varying detuning of the RF field as

$$\delta(\mathbf{r}) = \omega_{\text{rf}} - \omega_L(\mathbf{r}). \quad (3)$$

Those locations defined by $\delta(\mathbf{r}) \rightarrow 0$ typically define a surface in space where RF resonance is found, and correspondingly there is a minimum in the interaction energy overall^{79,80}. In the linear Zeeman regime the local Larmor frequency is given by

$$\omega_L(\mathbf{r}) = \frac{|g_F \mu_B |\mathbf{B}_0(\mathbf{r})|}{\hbar}, \quad (4)$$

which is derived from the static potential $U(\mathbf{r})$. The oscillating field $\mathbf{B}_{\text{rf}}(\mathbf{r}, t)$ yields an interaction energy^{79,80} in terms of a Rabi frequency $\Omega_0(\mathbf{r})$

$$\hbar \Omega_0(\mathbf{r}) = \frac{g_F \mu_B}{2} |\mathbf{B}_{\text{rf}}^\perp(\mathbf{r})| \quad (5)$$

where the factor of two arises from the rotating wave approximation in the case of linear polarisation (more general polarisations are discussed in Ref. 80), and $\mathbf{B}_{\text{rf}}^\perp(\mathbf{r})$ is the component of $\mathbf{B}_{\text{rf}}(\mathbf{r}, t)$ perpendicular to the local static field $\mathbf{B}_0(\mathbf{r})$. Finally, by combining the energies (2) and (5) through diagonalisation of the Hamiltonian in a full treatment^{79,80}, we obtain the local

eigenenergies, or dressed potentials,

$$U(\mathbf{r}) = m'_F \hbar \sqrt{\delta^2(\mathbf{r}) + \Omega_0^2(\mathbf{r})} \\ = m'_F \sqrt{[\hbar\omega_{\text{rf}} - \hbar\omega_L(\mathbf{r})]^2 + [g_F \mu_B |\mathbf{B}_{\text{rf}}^\perp(\mathbf{r})|/2]^2}, \quad (6)$$

where the m'_F are a set of integers, or half-integers, similar to the m_F described above.

The result of this is that slow atoms are confined by the potential (6), which in a typical configuration, and to a first approximation, confines atoms to an iso- B surface defined by $\hbar\omega_{\text{rf}} - \hbar\omega_L(\mathbf{r}) = 0$, which approximately reduces the value of $U(\mathbf{r})$ in Eq. (6). The term $g_F \mu_B |\mathbf{B}_{\text{rf}}^\perp(\mathbf{r})|/2$ also plays a role, and in particular it can be zero at certain locations on the trapping surface allowing the escape of atoms. This latter effect prevents the trapping of atoms in a shell potential by using the static quadrupole field (1). However, shell potentials are possible with different field arrangements such as those arising from the Ioffe-Pritchard trap and variations^{79–84} which have become candidates for experiments on the International Space Station⁸⁵. The requirement is simply for a local extremum in the *magnitude* of the field $\mathbf{B}_0(\mathbf{r})$ together with a non-zero $\mathbf{B}_{\text{rf}}^\perp(\mathbf{r})$. The reason for the interest in shell potentials in earth orbit is that on the earth's surface a gravitational term mgz should be added to Eq. (6), which plays an important role for larger and interesting shells (e.g. see section III A 3).

Although the matter-wave *bubbles* produced by shell potentials have become an object of great interest, the shell potentials themselves are the building blocks for other potentials of interest such as ring traps: we will see an example in section III B 2. Another example is in the next section III A 2 where a modulated bias field is used to make a ring trap: then $\mathbf{B}_0(\mathbf{r}) \rightarrow \mathbf{B}_0(\mathbf{r}) + \mathbf{B}_m(\mathbf{r}, t)$ and $\mathbf{B}_m(\mathbf{r}, t)$ is a field varying in space, and time, but typically at a frequency rather lower than the radio-frequency case.

2. Waveguides formed from Time-Averaged Adiabatic Potential (TAAP)

Time averaged adiabatic potentials (TAAPs) allow the generation of extremely smooth matterwave guides⁸⁶ and are an excellent candidate for matterwave guiding and interferometry in an atomtronic circuit^{87,88}. They are formed by applying an oscillating homogeneous potential to the adiabatic bubble traps described in Sec. III A 1. If the modulation frequency ($\omega_m = 2\pi f_m$) is small compared to the Larmor frequency, but fast compared to the trapping frequency of the bubble trap, then the effective potential for the atoms is the bubble potential time-averaged over one oscillation period⁸⁹. Let us consider TAAP potentials formed from a quadrupole bubble trap and an oscillating homogeneous field of the form $\mathbf{B}_m = \{0, 0, B_m \sin \omega_m t\}$. The modulation field simply displaces the quadrupole (and thus the bubble trap) by $z_m = \alpha^{-1} B_m \sin \omega_m t$ at an instant in time. In order to find the *effective* potential that the atoms are subjected to by this method, one calculates the time-average. Time-averaging of a concave potential increases the energy of the bottom of the trap, as is readily illustrated by

taking the time average of a harmonic potential jumping between two positions: the curvature does not change since it is everywhere the same; however, the energy of the trap bottom increases since it is at exactly the crossing point between the two harmonic potentials. Returning to the modulated bubble trap, one notices that the modulation is orthogonal to the shell at the poles of the shell ($x = y = 0$), but tangential to the shell on the equator ($z = 0$). Therefore, the time averaging causes a larger increase in the trapping potential at the poles rather than the equator—and therefore creates a ring-like structure.

Assuming that ω_{RF} is modulated such as to stay resonant on the ring and to keep Ω_{RF} constant, the vertical and radial trapping frequencies can be controlled via the relative amplitude of the modulation $\beta = g_F \mu_B B_m / \hbar \omega_{\text{RF}}$ as

$$\omega_\rho = \omega_0 (1 + \beta^2)^{-1/4} \\ \omega_z = 2\omega_0 \sqrt{1 - (1 + \beta^2)^{-1/2}}, \quad (7)$$

where the radial trapping frequency of the bare bubble trap is $\omega_0 = m_F g_F \mu_B \alpha (m \hbar \Omega_{\text{RF}})^{-1/2}$ with the mass of the atom m , and the g_F is the Landé g -factor of the considered hyperfine manifold, μ_B is the Bohr magneton, and Ω_{RF} the Rabi frequency of the dressing RF. In order to achieve large RF field strengths (≈ 0.3 – 1 G) and Rabi Frequencies, (Ω_{RF}), one usually has to use RF-resonators, which make it very difficult to tune the RF frequency, and which results in a somewhat weaker confinement in the axial (i.e. vertical) direction. Trapping frequencies of the order of a hundred Hz are readily achieved.

In many cases it is also desirable to confine the atoms azimuthally. This is readily achieved either by tilting the ring away from being perfectly horizontal or by modifying the polarization of the rf-field. A gravito-magnetic trap results from tilting the direction of the B_m and thus tilting the ring against gravity⁸⁷. The gravito-magnetic potential forms a single minimum much like a tilted rigid pendulum. One can also create a trap by changing the polarization of the dressing RF: tilting a linear polarization from the z -axes will cause, due to its projection on the local B -field, a sinusoidal modulation of the Rabi frequency along the ring resulting in a two minima on opposite sides of the ring. Alternatively an elliptical RF polarization creates a single minimum. Combining these modulation techniques permits the creation of two arbitrarily placed traps along the ring, or more generally any longitudinal confinement of the form $a_1 \sin(\phi + \phi_1) + a_2 \sin(2\phi + \phi_2)$, where ϕ is the azimuthal angle and ϕ_1 and ϕ_2 are phase offsets. Note that there are no angular spatial Fourier components higher than 2ϕ present in the system.

Thermal atoms and BECs are readily loaded into the gravito-magnetic TAAPs from a trapping-frequency-matched dipole trap. This can be done fully adiabatically by ramping down the dipole confinement and at the same time ramping up the TAAP trap. With a sufficiently high level of control on the rf-fields, one can also load them from a TOP trap via a tilted dumbbell-shaped trap⁸⁷. Once in the ring, one can then manipulate the atoms with a simple manipulation of the time-averaging fields: The depth of the azimuthal trap can be

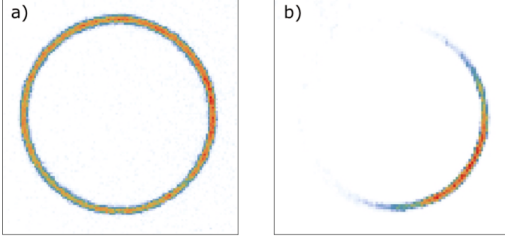


FIG. 8. a) BEC in a symmetric, ring-shaped TAAP ring with a diameter of $470\mu\text{m}$. b) BEC in a circular TAAP matterwave guide with superimposed gravito-magnetic modulation in the azimuthal direction.

changed by modifying the degree of tilt applied to the modulation field (\mathbf{B}_m). By changing the direction of the tilt (i.e. the phase between the modulation fields in the x and y directions) one can move the trap along the ring. This can be used, e.g. to accelerate the atoms along the ring, with angular momenta of $40000\hbar$ per atom being readily achieved⁸⁶. They can then travel in the waveguides over distances of tens of centimeters without any additional heating associated with the propagation. One can also remove the azimuthal confinement and allow the condensates to expand around the ring. Viewed in the co-rotating frame at high angular momenta, the atoms see an exceptionally flat potential with the largest resulting density fluctuations corresponding to an energy difference of a few hundred picokelvin: this is equivalent to a few nanometers in height⁸⁶. Current experiments have been performed with BECs in the Thomas-Fermi Regime with about 20 transverse vibration modes occupied. The 1D regime is readily accessible simply by reducing the atom number and increasing the radius of the ring.

The complete lack of any roughness combined with a picokelvin level control of the trapping parameters make the TAAP waveguides a very good candidate for guided matter-wave interferometry and the study of ultra-low energy phenomena such as long-distance quantum tunneling. A remaining challenge is to completely fill the ring with a phase coherent condensate. Current experiments allowed a condensate to expand along the ring, which converts the chemical potential of the BEC into kinetic energy. When the condensate touches itself at the opposite side of the ring, the two ends have a finite velocity in opposite directions, resulting in a spiral BEC, i.e. a BEC wrapped around itself. Using atom-optical manipulation of the expansion process kinetic energies in the pico-kelvin range (a few hundred micrometers per second) can readily be achieved. It will be interesting to study the very low energy collisions that will lead to a thermalisation of this system. A promising approach for a fully phase-coherent ring-shaped condensate is to first fill a small ring and then increase its radius. This should not induce any additional phase fluctuations, despite the fact that the lowest excitation has an energy of $E = \hbar^2/(2mr^2)$, which for a ring of 1 mm radius is 3 femtokelvin.

3. Dynamical ring in an rf-dressed adiabatic bubble potential

There is a formal analogy between the Hamiltonian of a neutral gas in rotation and the one of a quantum system of charged particles in a magnetic field. This makes rotating superfluids natural candidates to simulate condensed matter problems such as type II superconductors or the quantum Hall effect^{90,91}. For a quantum gas confined in a harmonic trap of radial frequency ω_r and rotating at angular frequency Ω approaching ω_r , the ground state of the system reaches the atomic analog of the lowest Landau level (LLL) relevant in the quantum Hall regime⁹²⁻⁹⁴. Reaching these fast rotation rates is experimentally challenging in a harmonic trap because the radial effective trapping potential in the rotating frame vanishes due to the centrifugal force. To circumvent this limit, higher-order confining potentials have been developed⁹⁵, which allow to access the regime where Ω even exceeds ω_r .

The adiabatic bubble trap has many features that make it a very good candidate to explore this regime. Indeed, it is very smooth and easy control of its anisotropy is possible through the dressing field polarization⁹⁶. This allows us to deform the bubble and rotate the deformation around the vertical axis in a very controlled way, allowing us to inject angular momentum into the cloud. The curved geometry of the bubble provides naturally the anharmonicity required to rotate the atoms faster than the trapping frequency ω_r at the bottom.

In the experiment at LPL⁹⁷, the atoms are placed in a quadrupole magnetic field of symmetry axis z dressed by a radio-frequency (rf) field of maximum coupling Ω_0 at the bottom of the shell. Here, the equilibrium properties in the absence of rotation ($\Omega = 0$) are well known⁹⁶: the minimum of the trapping potential is located at $r = 0$ and $z = z_0$ and around this equilibrium position the potential is locally harmonic with vertical and radial frequencies $\omega_z = 2\pi \times 356\text{Hz}$ and $\omega_r = 2\pi \times 34\text{Hz}$, without measurable in-plane anisotropy. This trap is loaded with a pure BEC of 2.5×10^5 ^{87}Rb atoms with no discernible thermal fraction. This atomic cloud has a chemical potential of $\mu/\hbar = 2\pi \times 1.8\text{kHz}$ which is much greater than ω_r and ω_z , and well in the three-dimensional Thomas-Fermi (TF) regime. In addition to the dressing field, a radio-frequency knife with frequency ω_{kn} is used to set the trap depth to approximately $\omega_{\text{kn}} - \Omega_0$ by outcoupling the most energetic atoms in the direction transverse to the ellipsoid^{98,99}. In a frame rotating at frequency Ω , the effective dressed trap potential is the usual trap described above with the addition of a $-\frac{1}{2}M\Omega^2 r^2$ term taking into account the centrifugal potential. In this frame, the atomic ground state consists of an array of vortices of quantized circulation, each vortex accounting for \hbar of angular momentum per atom. When only a few vortices are present, the velocity field differs strongly from the one of a classical fluid, but for a sufficiently large number of vortices the superfluid rotates as a solid body with a rotation rate Ω . When $\Omega < \omega_r$ the equilibrium position remains on the axis $r = 0$ at $z = z_0$, and the only difference is a renormalization of the radial trapping frequency: $\omega_r^{\text{eff}} = \sqrt{\omega_r^2 - \Omega^2}$. Of course, as this frequency decreases, the trap anharmonicity becomes more important in the determination of the cloud shape.

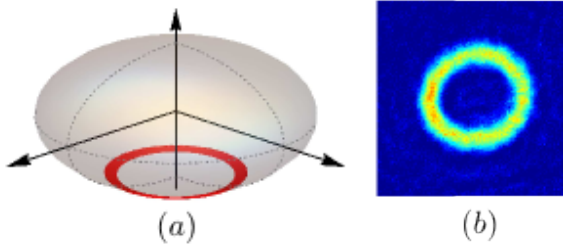


FIG. 9. (a): Density contour (red annulus) for a BEC rotating at $1.06\omega_r$ in the shell trap (gray ellipsoid). (b): *in situ* integrated 2D density of a dynamical ring⁹⁷. Picture size: $130 \times 130 \mu\text{m}^2$.

For $\Omega > \omega_r$ the trap minimum is located at a non-zero radius. In this situation, a hole grows at the trap center above a critical rotation frequency Ω_h ¹⁰⁰, leading to an annular two-dimensional density profile (Fig. 9(a)) which we will refer to as a “dynamical ring”⁹⁷. Moreover, the velocity of the atomic flow is expected to be supersonic¹⁰¹ *i.e.* exceeding by far the speed of sound. For increasing Ω , one expects the annular gas to sustain vortices in its bulk up to a point where the annulus width is too small to host them. The gas should then enter the so-called “giant vortex” regime^{101,102} where all the vorticity gathers close to the center of the annulus.

The experimental sequence is the following: angular momentum is injected into the cloud by rotating the trap with an ellipsoidal anisotropy at a frequency $\Omega = 31$ Hz. The trap rotation is then stopped and isotropy is restored. At this moment, which we take as $t = 0$, the cloud shape goes back to circular with an increased radius due to its higher angular momentum. An additional evaporation process, selective in angular momentum, continuously accelerates the superfluid and increases its radius⁹⁷. Due to this size increase, the chemical potential is reduced and the gas enters the quasi-2D regime $\mu \leq \hbar\omega_r$. After a few seconds a density depletion is established at the center of the cloud which is a signature of Ω now exceeding ω_r . After a boost in selective evaporation due to a lowering of the frequency of the rf knife, a macroscopic hole appears in the profile, indicating that Ω is now above Ω_h and that a fast rotating dynamical ring with a typical radius of $\sim 30 \mu\text{m}$ has formed as can be seen in Fig. 9(b). The rotation keeps increasing and a ring is still observable after $t = 80$ s. Rotational invariance is critical in that regard, and is ensured at the 10^{-3} level by a fine tuning of the dressing field polarization and of the static magnetic field gradients⁸⁰.

A Thomas-Fermi profile convoluted with the imaging resolution is much better at reproducing the experimental density profile than a semi-classical Hartree-Fock profile, demonstrating that the samples are well below the degeneracy temperature. Using the Thomas-Fermi model we can estimate the properties of the cloud. For example the ring obtained at $t = 35$ s has a chemical potential of $\mu/\hbar \simeq 2\pi \times 84$ Hz and an averaged angular momentum per particle $\langle \hat{L}_z \rangle / N \simeq \hbar \times 317$. Interestingly the estimated peak speed of sound $c = \sqrt{\mu/M} \simeq 0.62$ mm/s at the peak radius r_{peak} is much smaller than the local fluid velocity $v = \Omega r_{\text{peak}} \simeq 6.9$ mm/s: the superfluid is therefore rotating at a supersonic velocity corresponding to a

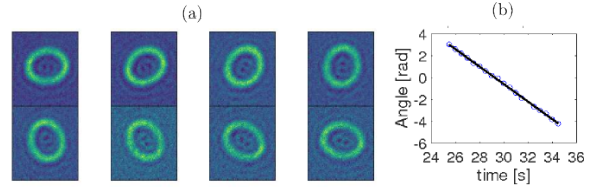


FIG. 10. (a): *in situ* evolution of a quadrupole deformation in the dynamical ring. The elliptical deformation is rotating against the supersonic flow. (b): Time evolution of the orientation of the ellipse major axis.

Mach number of 11. Moreover, due to the continuous acceleration of the rotation, the dynamical ring radius grows gradually with time which results in a decrease of the chemical potential and an increase of the Mach number. For $t > 45$ s the chemical potential is below $2\hbar\omega_r$ and the highest measured Mach number is above 18.

Superfluidity in the dynamical ring has also been evidenced by the observation of quadrupole-like collective modes. After the ring formation, the rotation rate, while accelerating, crosses a value where the quadrupole collective mode is at zero frequency, such that any elliptical static anisotropy can excite it resonantly. A very small bubble anisotropy is enough to excite this mode characterized by an elliptic ring shape rotating with a period of approximately 10 s in the direction opposite to the superfluid flow (Fig. 10). This counterpropagating effect is not predicted by a mean-field theory, and has been confirmed by resonant spectroscopy of the quadrupole mode during the ring acceleration⁹⁷.

The persistence of superfluidity at such hypersonic velocity raises fundamental questions about the decay of superfluidity in the presence of obstacles, and how superfluidity can be preserved at such speeds: nonlinear effects, the presence of vortices and the dependence on temperature would be particularly interesting to study experimentally and compare with theoretical predictions^{103–107}. This hypersonic superflow is not yet a giant vortex, but it is an important step towards this long-sought regime whose transition rotation frequency is not theoretically clearly identified. Moreover, the well-known elementary excitation spectrum for a connected rotating superfluid is strongly modified when the ring appears, and the important discrepancies observed between the experimental results and a mean-field theoretical approach for a quadrupole-like collective mode highlight the need to refine the description of fast rotating superfluids in anharmonic traps.

An alternative way of generating large angular momentum states in rf-dressed adiabatic bubble potentials is to first generate them in a TAAP ring and then reduce the vertical modulation, thus adiabatically transferring the atoms into the bubble.

B. Trapping in rings with optical potentials

Nearly conservative potentials for ultracold atoms can be formed through the use of focused far-detuned optical beams¹⁰⁸. Since the potential is directly proportional to the

intensity of the optical field, ring-shaped condensates may be created through the implementation of ring-shaped optical patterns. The most significant advantage in optical dipole ring traps is the insensitivity to the hyperfine state, allowing multi-component and spinor BECs to be trapped. The advent of spatial light modulator technologies means the optical ring trap has become highly configurable, allowing more complex geometries to be generated.

1. Pure optical potentials

We begin by looking at some of the pure optical beam techniques that are in use and have potential for atomtronic applications.

a. Laguerre-Gauss beams: One of the first proposed methods for a ring optical dipole trap was the use of Laguerre-Gaussian (LG) modes, circular symmetry¹⁰⁹. For far-off-resonance light, these provide the spatial structure for a toroidal trap. An additional advantage of such LG modes is that they also carry orbital angular momentum. With pulses of near-resonant light, the LG modes can be tailored to provide two-photon Raman transitions that transfer exact quanta of circulation to the condensate.

Ring traps and circulating currents using LG modes have been demonstrated in both single and spinor gases, and were early demonstrations of all-optical trapping of BEC in a ring geometry^{67,110,111}.

b. Painted optical traps: An alternative to projecting a ring shaped beam is to build a time-averaged potential with a moving, red-detuned, focused laser beam. By rapidly steering a Gaussian beam in a circular orbit, a ring trap can be generated. This is achieved through the use of two acousto-optical deflectors (AOM) controlling the two axes of the painting beam^{24,29}. This approach was used to create the first ring BEC²⁹, as shown in Fig. 11.

The advantages of this technique is that it allows to adapt the intensity locally to create desired features in the potential landscape and to flatten imperfections due to possible laser inhomogeneity¹⁹; the available laser power is used in an efficient way as only the relevant trapping locations are illuminated; the painting laser itself can be used as a stirrer to set the quantum fluid into rotation and demonstrate quantized superfluid flows¹¹²; and the technique enables for more complex geometries. As an example, the atomtronic analogue of a Josephson junction has been demonstrated²² and used to realize a DC atomtronic SQUID (AQUID). More recently, the dynamic potentials possible with painting were used to show that the AQUID exhibits quantum interference¹¹³.

The painting approach also comes with specific technical constraints that may need to be addressed. The phase of the time-averaged beam loop plays a role on the fine details of the potential and has to be compensated for³⁰. In addition, the transverse trap frequency which can be realized is limited by the finite response time of the AOMs to several kHz.

c. Conical refraction: A novel approach to generating ring traps has been demonstrated with the use of conical refraction occurring in biaxial crystals. A focused Gaussian

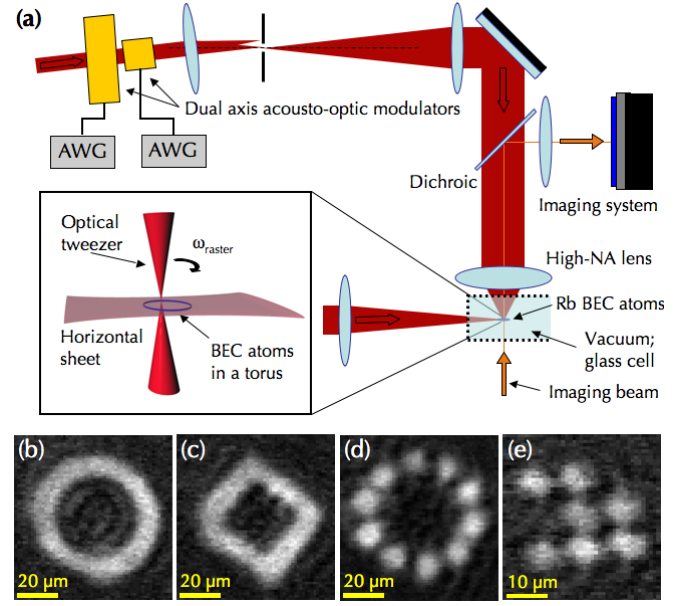


FIG. 11. Taken from²⁹. (a) A painted potential system in which a tightly-focused rapidly-moving red-detuned laser beam paints the desired potential on a horizontal light sheet providing vertical confinement. (b) In-trap absorption images of BECs formed in painted potentials. The technique can create a BEC in any shape that can be drawn on a sheet of paper.

beam passing along the optical axis of the crystal transforms, at the focal plane, into one or more concentric rings of light. In the case of a double-ring, the light field encloses a ring of null intensity, called the Poffendorff ring¹¹⁴. For a blue-detuned laser field the atoms are trapped between the bright rings. The advantage of this configuration is that it minimizes spontaneous scattering of photons responsible for heating when the laser beam is not very far detuned from resonance. Further advantages include the high conversion efficiency of the incoming Gaussian beam to the ring-trap light field and the access to different ring configurations. The ring diameter is defined by the refractive indices of the biaxial crystal and its length. The width of each ring is given by the focal waist of the focused Gaussian beam. A variation of the ratio of these numbers (e.g. by changing the focal waist) allows for a variation of the resulting light field topology from a single bright ring to a bright ring with a central bright spot and further to bright double rings of increasing diameter. First results on BECs transferred into a ring have been reported¹¹⁴. Ongoing work is directed towards implementing quantum sensors (e.g. Sagnac interferometers) for rings with large diameter and atomtronic SQUIDs for small rings.

d. Digital micromirror direct projection: Direct imaging of digital micromirror devices (DMDs) has recently emerged as a powerful tool for the all-optical configuration of BECs^{20,37,38,115}. Ring traps can be created by projecting the DMD-patterned light onto a vertically confining attractive potential^{37,115}, similarly to Fig. 12, or onto a vertically oriented accordion lattice³⁸. In Fig. 13, a ring trap is created, along with a central phase-uncorrelated reference BEC. After stirring the

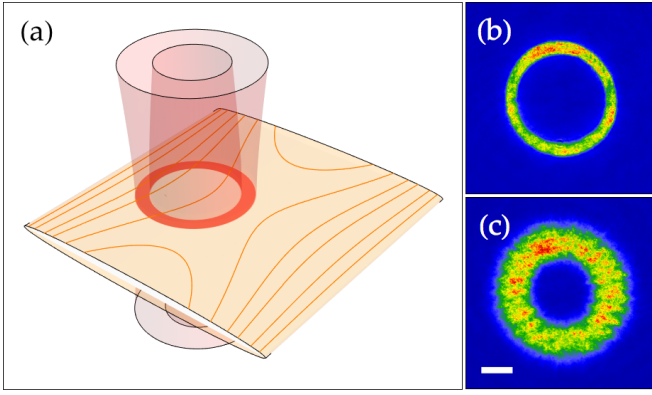


FIG. 12. (a) A typical optical ring trap configuration; the potential is formed at the intersection of the vertically focused ring pattern, and horizontal sheet beam. (b) In-trap absorption image of a ring BEC formed in a $164\ \mu\text{m}$ diameter time-averaged optical potential with $(\omega_r, \omega_z) = 2\pi(50, 140)$ Hz trapping frequencies. (c) Expanded ring after 20 ms time-of-flight. The scale bar is $50\ \mu\text{m}$.

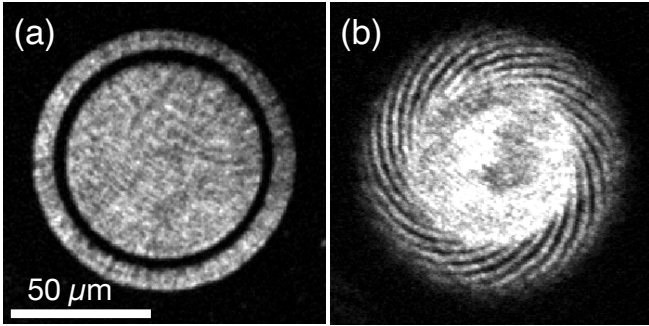


FIG. 13. (a) A ring trap with a diameter of $100\ \mu\text{m}$ is created using a repulsive DMD-patterned potential combined with an attractive horizontal sheet beam. By using the dynamic control of the DMD, a stirring barrier is introduced into the ring and then accelerated through 90° , before being removed from the ring. The resulting persistent current is imaged through interference with the central BEC in a short time-of-flight, determining a net circulation quanta of $N = 21$.

ring, the resulting 21-quanta persistent current, corresponding to an angular momentum of $\sim 132\hbar$ per atom, is visualised through interference with the reference central BEC after a short 5 ms time of flight¹¹⁶. The DMD technology can also be used to phase imprint an azimuthal light gradient such that angular momentum can be imparted to the atoms¹¹⁷ and a circulating current created¹¹⁸.

e. Micro-fabricated optical elements: An approach combining flexibility, integrability, and scalability can be based on the application of micro-fabricated optical elements for the generation of complex architectures of dipole traps and guides¹¹⁹. It draws its potential from the significant advancement in producing diffraction-limited optical elements with high quality on the micro- and nanometer scale. Lithographic manufacturing techniques can be used to produce many identical systems on one substrate for a scalable configuration¹²⁰. On the other hand, state-of-the art direct laser writing gives high flexibility in producing unique integrated systems and

allows for fast prototyping¹²¹. Applications range from integrated waveguides and interferometer-type structures¹²² to arrays of dipole-traps for quantum information processing¹²³ and single-atom atomtronics implementations¹²⁴. In combination with DMD-based control of the light field (see previous section), access to dynamic reconfiguration becomes possible. Integrability is not limited to the generation of light fields for dipole potentials but can be extended to the integration of light sources and detectors or even complex quantum-optical systems such as an entire magneto-optical trap¹¹⁹.

2. Bubble plus light sheet(s)

The bubble geometry is particularly suited to create a ring trap: by combining the rf-dressed bubble trap and an optical light sheet, one can create a toroidal trap. This is a hybrid trap with both the optical potentials of Section III B 1 and the static and rf magnetic fields of Section III A. The principle is the following: a horizontal light sheet is superimposed with a bubble trap which is rotationally invariant around the vertical direction^{125,126}. The light sheet is designed to achieve an optical dipole trap in the vertical direction, and the radial confinement is ensured by the bubble trap itself. Maximum radial trapping and maximum radius will be attained if the light sheet is located at the equator of the bubble, a situation which also ensures maximum decoupling between the vertical trapping frequency ω_z and the radial trapping frequency ω_r . Experimentally, the optical trap is formed between two horizontal light sheets which are made repulsive by their large blue detuning from the atomic transition. The bubble trap is made with the same rf-dressed quadrupole trap as depicted in Fig. 14(a). In order to load the atoms into the ring trap, one starts from an almost pure BEC of approximately 2×10^5 ^{87}Rb atoms. The relative positions of the magnetic bubble and optical trap are adjusted by vertically translating the bubble. This is achieved by adjusting a uniform magnetic bias field linearly polarized in the vertical direction. First, the center of the optical trap is aligned with the superfluid, at rest, at the bottom of the bubble. Then, the vertical bias field is used to translate the bubble downwards, until the light sheet reaches the equator. One has then created a trapped toroidal degenerate gas of approximately 10^5 atoms (Fig. 14(b)).

The gas can be set into rotation by different procedures. The first method, used in our experiment in Ref. 127, is to slightly deform the bubble trap with an ellipsoidal anisotropy, and then rotate this anisotropy at a given fixed frequency and restore the isotropy. In the second method, the rotation is induced by

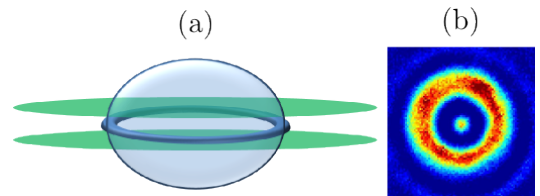


FIG. 14. (a): Principle of the ring trap. (b): *in situ* image of the ring.

a rotating optical defect^{127,128}. It could also be imparted by direct optical phase imprinting onto the ring trap¹¹⁷.

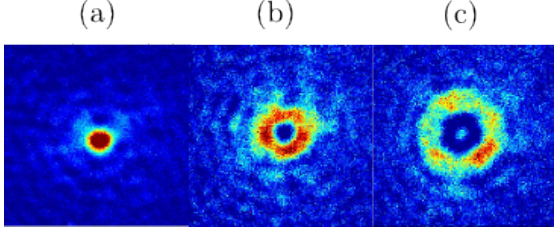


FIG. 15. Time-of-flight images of (a): a non-rotating ring, (b) and (c): rotating rings with different circulations. The rotation is imparted by a rotating $7\mu\text{m}$ -waist blue-detuned vertical Gaussian beam.

Above some critical rotation frequency depending on the excitation strength, one observes, after a time-of-flight imaging procedure, a hole in the atomic distribution. The hole is absent when the ring is non rotating, and is thus evidence for a non-zero circulation of the superfluid in the ring trap (Fig. 15). The hole area grows for increasing rotation rates, and shrinks with time when one lets the cloud rotate freely in the trap. In future experiments, optical barriers created by spatial light modulators could be imposed onto the ring and dynamically modulated in height and position. This would create the equivalent of Josephson junctions in superconductors and allow us to simulate models of non-equilibrium quantum systems and emulate new setups in mesoscopic superconductivity^{7,19}.

C. Outlook

The development of technology for controlling electronic systems and steering optical beams is giving ever greater control of ultra-cold atoms and condensates of atoms. We are at the point where optical potentials can be dialed-up and almost any network of guides created in a 2D plane over the scale of the steerable beam. The ring trap remains of particular interest because of the topology, the possibility for self-interference, circuitual currents, Sagnac interferometry and so on. In a way, it is its own primitive atomtronic circuit. The future challenges for the technology, after this development, will be to create particular atomtronic applications and test the limits of technology for creating large scale structures and structures which possibly have some 3D features. The systems based on magnetic trapping are also extremely flexible because of the level of electronic control. Accelerating and rotating atoms involves multiple frequencies which are changing in time. In the future we will undoubtedly see more control complexity and more hybrid approaches. Where surface interactions are less of a problem we can also envisage atomtronic circuits based on atom-chip technology, where rings, and complex guided circuits, may be enabled by the design of wire structures and the fields they produce from static and AC currents.

Acknowledgments. The UQ group acknowledges funding by the ARC Centre of Excellence for Engineered Quantum Systems (project number CE1101013), and ARC Discovery Projects grant DP160102085. WK would like to acknowledge

the contribution of the AtomQT COST Action CA16221 and of HELLAS-CH (MIS 5002735) implemented under “Action for Strengthening Research and Innovation Infrastructures,” funded by the Operational Programme “Competitiveness, Entrepreneurship and Innovation” (NSRF 2014-2020) and co-financed by Greece and the European Union (European Regional Development Fund). HP and LL acknowledge financial support from the ANR project SuperRing (Grant No. ANR-15-CE30-0012) and from the Région Île-de-France in the framework of DIM SIRTEQ (Science et Ingénierie en Région Île-de-France pour les Technologies Quantiques), project DyABoG. BMG would like to acknowledge support from the UK EPSRC grant EP/M013294/1. MGB acknowledges support from the US DOE through the LANL LDRD Program.

IV. ATOMTRONIC CHIPS AND HYBRID SYSTEMS

C. Hufnagel, M. Keil, A. Günther, R. Folman, J. Fortagh, R. Dumke

During the last decade atom chip approaches to quantum technology have become a powerful platform for scalable atomic quantum optical systems,^{73,74,129} with applications ranging from sensor and imaging technologies to quantum processing and memory. Atom chips coupled to solid state-based quantum devices, e.g. superconducting qubits or nitrogen vacancy centers, are thereby paving the way for promising quantum simulation and computation schemes.^{130–132} Along this research line, several groups around the world have developed versatile atom chip configurations, which allow trapping of ultracold atomic clouds and degenerate Bose-Einstein condensates (BECs) close to chip surfaces and well-defined manipulation of their internal and external degrees of freedom. Atom chips provide a very relevant technology for the emerging field of atomtronics,^{5,21,74,133–136} for which dynamic tunnelling barriers are required.^{137,138} Such barriers may be formed on atom chips with μm -scale widths, matching the length scale dictated by the atomic deBroglie wavelength. The atom chip offers the ability to realize guides and traps with virtually arbitrary architecture and a multitude of novel architectures,¹³⁹ with a high degree of control over atomic properties, like interactions and spin, enabling new quantum devices.^{5,74}

Here we review progress in our groups in Beer Sheva, Tübingen and Singapore on recent developments in atom chip technologies.

The Ben-Gurion University of the Negev (BGU) Atom Chip Group (<http://www.bgu.ac.il/atomchip>) is promoting the idea of atomtronics without light. This entails circuits for atoms based on electric and magnetic traps, guides and tunneling barriers. The vision is for a complete circuit, including particle sources and detection, that makes no use of gravity, e.g. no time-of-flight for the development of interference fringes. This requirement means that a future technological device could work at any angle relative to gravity.

As a basis for this effort we, of course, use the Atom Chip technology developed over the past 20 years.^{74,129} An exam-

ple of a circuit design we plan to implement is a continuous-wave, high-finesse Sagnac interferometer, where the multiple turns enabled by the guiding potential allow miniaturization of the loop while maintaining sensitivity to rotation.¹³⁷ In the following we briefly present some of the work that has been done to advance the atomtronics technology.

To begin with, a stable tunneling barrier (in terms of instabilities of tunneling rates) should be no wider than the de-Broglie wavelength, which is on the order of $1\ \mu\text{m}$. Since the resolution with which we can tailor fields is on the order of the distance from the field source, one must construct the atomic circuit at a distance of no more than a few micro-meters from the surface of the chip.¹³⁸ At these very small atom-surface distances, several problems must be avoided:

1. **Johnson noise.** This is a hindering process as it may cause spin-flips (reducing the trap/guide lifetime), as well as decoherence. In several papers we have shown ways to combat both effects either by the geometry or by the choice of material.^{49,138,140–142} We have also measured Johnson noise and calculated its interplay with phase diffusion caused by atom-atom interactions.¹³³
2. **Finite size effects.** As the atom-surface distance becomes smaller, so should the current-carrying wire width, or else the magnetic gradients will be severely undermined. Narrow wires require high-resolution fabrication¹³⁸ or thin self-assembled conductors such as carbon nanotubes.¹⁴²
3. **Casimir-Polder and van der Waals forces.** As the atom-surface distance becomes smaller, the magnetic barrier between the atoms and the surface should be strong enough to avoid tunneling of the atoms to the surface. This has been calculated for sub-micron distances.^{138,142}
4. **Fragmentation.** Due to electron scattering in the current-carrying wires (e.g. due to rough wire edges), the minimum of the trap or guide is not smooth and the atomic ensemble may split and exhibit a non-uniform density along the wire axis. This was studied by us both experimentally and theoretically.^{143–145}
5. **High aspect ratios.** As the atom-surface distance becomes smaller, the trap or guide exhibits much high transverse frequencies compared to the longitudinal frequency. This brings about low dimensionality and can cause different problems such as phase fluctuations in a 1D BEC. Alternative wire configurations allow more flexibility for adjusting the trap aspect ratio.

In a proof-of-principle experiment¹⁴⁶ we were able to avoid all the above hindering effects, and showed that spatial coherence could be maintained for at least half a second at an atom-surface distance of just $5\ \mu\text{m}$.

Another important problem that needs to be overcome is that of atom detection at very small atom-surface distances. At these distances of a few micro-meters, the stray light from

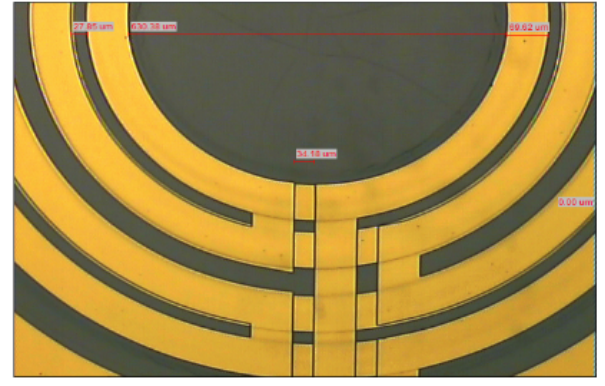


FIG. 16. A multi-layer current-carrying chip produced at BGU for a Sagnac experiment performed in Nottingham (Thomas Fernholz).

the nearby surface makes it very hard to achieve a reasonable signal-to-noise ratio for *in situ* detection with typical optical elements. As a solution, and also to avoid on-resonance spin-flips and decoherence, we studied the possibility of off-resonant atom detection with high-Q micro-discs.^{147–149}

With the above tools we are now preparing to go forward with our vision for a Sagnac circuit,¹³⁷ where as a first stage we have the goal of observing spatial coherence of atoms after one, and then several, turns in a guiding loop. The guiding potential is made in two alternative ways. The first method, using RF potentials, is being led by Thomas Fernholz of the University of Nottingham. It requires multi-layer chips (4 layers of currents), which are fabricated at BGU. Two such layers are shown in Fig. 16. The second effort also requires a unique chip. The guiding potential will be based on a repulsive permanent magnet potential in combination with an attractive electric field produced by a charged wire. The first experiments will be pulsed, whereby a BEC will be loaded onto the loop at the beginning of every cycle. Later on we will move towards realizing a continuous-wave version. We will first conduct the experiment in the pulsed mode by loading a thermal cloud, and later on use a 2D MOT as a continuous source.

Finally, let us note that quite a few groups around the world have realized free-space matter wave interferometry. It is now an important challenge to adapt these interferometers to the framework of atomtronics. Specifically, the BGU Atom Chip group has made significant steps in this direction by realizing, in the last 5 years, several types of novel interferometers which are not based on light. These interferometers are based on the magnetic splitting force (Stern-Gerlach) and they have already enabled the observation of spatial fringes,^{150,151} spin population fringes,¹⁵² unique T^3 phase accumulation,¹⁵³ clock interferometry,^{154,155} and the observation of geometric phase.¹⁵⁶

A. Precision Sensing

Precise sensors are one of the most important elements in applied and fundamental science. The use of quantum proper-

ties in sensing applications promises a new level of sensitivity and accuracy.¹⁵⁷ Using cold atoms on atom chips as probes will enable many interesting applications.

In the laboratories at the University of Tübingen we are working with atom chips that host one or two layers of lithographically implemented wire patterns. They allow the creation of spatially and temporally varying magnetic fields, as used for three-dimensional positioning and manipulation of cold atomic quantum matter.¹⁵⁸ We typically use wire patterns made of gold in room temperature environments¹⁵⁹ and superconducting patterns of niobium in 4K and mK surroundings.¹⁶⁰

With such a 'carrier chip' for cold atoms on hand, we established a dual-chip process, where a second chip hosting nanostructured solid state systems is attached on top of the carrier chip.¹⁵⁸ In this way, cold atoms can be efficiently coupled to other quantum systems and hybrid systems can be realized.

We have used this scheme to develop a novel cold-atom scanning probe microscope (CASPM), which uses ultracold atoms and BECs as sensitive probe tips for investigating and imaging nanoscale systems.¹⁶¹ Similar to an atomic force microscope (AFM), the probe tip is scanned across the surface of interest, while static and dynamical properties of the probe tip are monitored. Evaluating changes within the cold-atom tip density and motion then gives access to basic interactions and serves as a novel imaging and sensor technique. In contrast to conventional AFMs with their 'heavy and rigid' solid state tips, our CASPM uses a dilute gas of atoms, which not only allows for non-destructive measurements, but also for much higher sensitivity to external forces and fields. Inspired by conventional AFMs, we have been able to demonstrate several modes of operation.¹⁶² These include not only a contact mode, where we measure position-dependent losses of the probe tip, but also a dynamic mode, where we initiate a center-of-mass oscillation of the cold-atom tip and monitor the position-dependent changes of the probe tip oscillation frequency.¹⁶¹ Based on the latter, we have used cold-atom force spectroscopy to unveil anharmonic contributions in near-surface potentials. As in atomic force microscopy, this may be used to reconstruct the surface potentials. Moreover, we have developed a novel operation mode, not accessible to conventional AFMs, where we bring the dilute probe tip into direct overlap with the nano-object of interest. By measuring time-dependent probe tip losses, we have then been able to deduce the underlying van der Waals (Casimir-Polder) interactions.^{163,164} We have demonstrated and characterized all different operating modes of CASPM by measuring individual free-standing carbon nanotubes grown on a silicon chip surface. Here we have shown that CASPM extends the force sensitivity of conventional AFMs by several orders of magnitude down to the μN regime, and the working distance down to several micrometers.¹⁶² This makes CASPM a powerful tool for investigating fragile nano-objects with ultra-high force sensitivity.

While first measurements with CASPM suffered from long measurement times, we have just lately extended the microscope by a powerful single atom detection scheme.^{165,166} It is based on continuous sub-sampling of the probe tip via a multi-

photon ionization process in conjunction with temporally resolved ion detection and high quantum efficiency. This allows real-time monitoring of the probe tip dynamics and density while losing only few atoms from the probe tip.^{166,167} This not only speeds up probe tip oscillation frequency measurements by at least three orders of magnitude,¹⁶⁶ but also enables new applications for CASPM.

In one of these applications we proposed a quantum galvanometer to detect local currents and current noise in nanoscale mechanical quantum devices.^{168,169} Measuring the current noise would then give access to the quantum properties of the device. We successfully demonstrated the principal operating scheme of this galvanometer by coherently transferring artificially generated magnetic field fluctuations via a Bose-Einstein condensate onto an atom laser and investigating its single-atom statistics.^{170,171} Employing second-order correlation analysis, we could not only extract the microwave power spectral density (current noise spectrum) but also the noise correlations within the bandwidth of the BEC, which will give access to the quantum noise properties of the current source. This will extend CASPM to a promising quantum sensor, not only for detecting local forces and force gradients, but also for currents as well as electric and magnetic fields (AC and DC), including their specific noise spectra.

B. Cryogenic Atom Chips and Hybrid Quantum Systems

Atom chips made from superconducting circuits offer certain advantages over normal metal devices. The coherence properties of trapped atoms are improved by orders of magnitude due to reduction of magnetic noise, coming from the surface of the chip. Moreover, superconductors can be operated in the mixed state, where vortices can be used to generate self-sufficient atom traps. Also, working in cryogenic environments offers the possibility to interface atoms with solid state devices to form hybrid quantum systems.⁴⁹

Besides atom chip experiments in room-temperature environments, the group in Tübingen also operates superconducting atom chips with trapped BECs of rubidium atoms.^{160,172,173} As shown in Fig. 17, condensates are routinely transferred into coplanar cavity structures¹⁷⁴ and the measured coherence time between hyperfine ground state superpositions reaches several seconds. Microwave dressing is used to suppress the differential shift of state pairs with the "double-magic point" being the optimum working point for quantum memories¹⁷⁵. We have successfully demonstrated coherent coupling of a hyperfine state pair through a driven superconducting coplanar microwave cavity,¹⁷⁶ which paves the way for future cavity-based quantum gate operations.

In addition to manipulating ground-state atoms we have successfully implemented two-photon Rydberg excitation in a cryogenic environment near the superconducting chip.¹⁷⁷ We have developed techniques for optical detection of Rydberg populations and coherences¹⁷⁸ and measured the increased lifetime of Rydberg states in cryogenic environments.¹⁷⁷ In preparation for interfacing Rydberg atoms with superconducting circuits, we have obtained high-resolution spectra

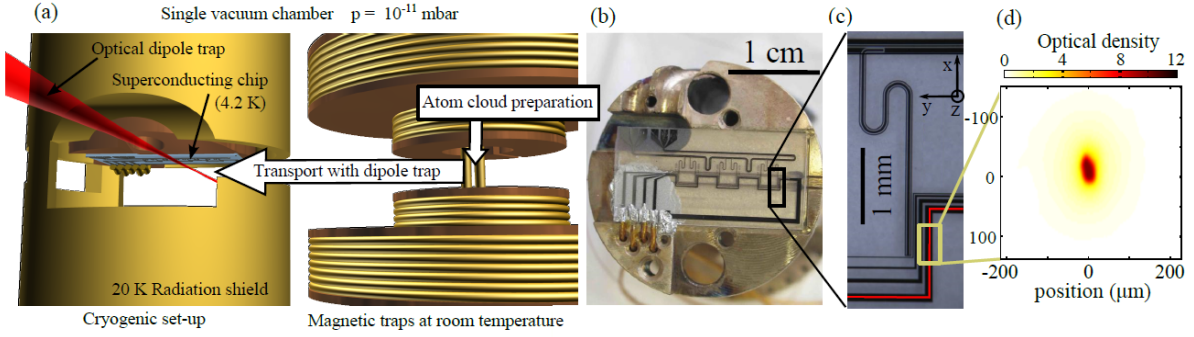


FIG. 17. Superconducting atom chip. a) In vacuo trap setup with electromagnets for cold atom preparation (right) and cryostat with a superconducting chip at 4.2 K (left). b) Photograph of the chip holder and the superconducting atom chip. c) The chip features superconducting wire components for magnetic trapping and positioning of atomic clouds and a coplanar microwave cavity. d) Bose-Einstein condensate of 3×10^5 ^{87}Rb atoms in a 15 ms time-of-flight image, released from the superconducting atom chip.

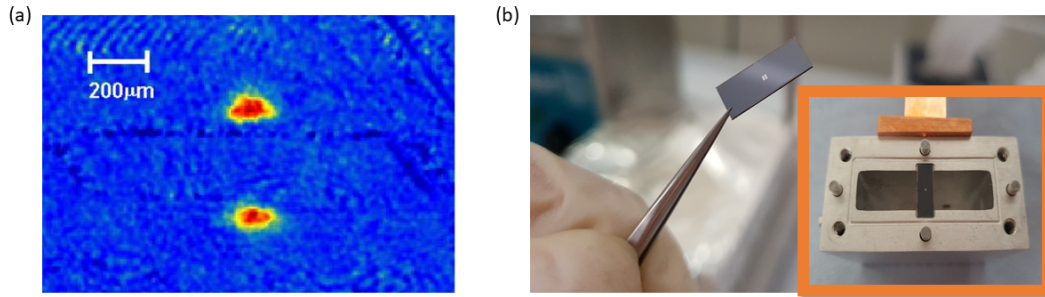


FIG. 18. (a) Image of an atomic cloud of ^{87}Rb trapped in a self-sufficient quadrupole magnetic trap generated by vortices on a 1mm x 1mm square of superconducting YBCO. The lower part of the image shows a mirror image of the cloud, caused by the reflection of the imaging beam from the chip surface. (b) Setup for a hybrid quantum system of atoms and superconductors. The image shows a transmon qubit fabricated on a silicon substrate. Inset: the transmon installed in a 3D microwave cavity. The cavity allows to read-out and manipulate the transmon with RF radiation. In the future we plan to bring atoms into the cavity to form a hybrid quantum system.

of rubidium Rydberg states in a field-free vapor cell as reference,¹⁷⁹ and in precisely controlled electrostatic fields¹⁸⁰ near surfaces at room and cryogenic temperatures. These studies add to our understanding of electrostatic fields of surface adsorbates that build up during experiments with cold atoms at chip surfaces.^{53,181,182} Based on the measured data, quasi-classical quantum defect theory,¹⁸³ Stark-map calculations,¹⁸⁰ suitable dressing techniques,^{175,184} and numerical methods developed for simulating quantum operations in the presence of thermal cavity photons,⁵⁴ we are currently focusing on the coherent manipulation of Rydberg atoms and quantum computation schemes in the presence of inhomogeneous fields at the surface of superconducting coplanar cavities.

The realization of hybrid quantum systems based on atoms and superconducting qubits requires truly cold temperatures in the 10 mK range, as dictated by the otherwise fast decoherence of the superconducting qubit. The great advantage is that at this temperature the number of microwave photons in the cavities that mediate the interaction between the solid state and the atomic system is near zero. The price to pay is a highly complex experimental system combining cold-atom technologies with a $^3\text{He}/^4\text{He}$ dilution refrigerator.^{185,186} Our dilution refrigerator consists of several temperature-shielded volumes

(stages), of which we use the 6K-stage and the 1K-stage for cold atom experiments. The 1K-stage includes a cold plate with a nominal base temperature of 25 mK.¹⁷² We routinely operate a magneto-optical trap at the 6K-stage, from which we transport magnetically trapped, ultra-cold rubidium clouds at 100 μK to the 1K-stage. The 1K-stage has a sufficiently large volume (several liters) to accommodate microwave cavities, such as coplanar waveguide cavities, and has convenient optical access for optical traps and laser beams for spectroscopic measurements. This experimental setup is currently being extended for studying the fully quantum regime of cold-atom superconductor hybrid systems.

In the Singapore group we are working in two directions. One is the exploration of superconducting atom chips using high-temperature superconductors and another is the development of coherent interfaces between superconducting circuits and ultracold atoms.

High temperature superconductors have various distinct properties when implemented as atom chips. First of all the technical demands are lower due to the higher working temperatures, which can be reached with liquid nitrogen, instead of liquid helium. Moreover, high temperature superconductors are type-II superconductors and allow the storage of mag-

netic fields in the remanent state. We have shown that these trapped fields can be used to generate novel traps for ultra-cold atoms.^{187,188} Ramping a magnetic field perpendicular to a planar structure of YBCO we were able to generate various magnetic traps for cold atoms (see Fig. 18(a)).¹⁸⁹ These traps can be generated either by using external magnetic fields together with vortices or in a completely self-sufficient way, where the trap is solely created by vortices. In the latter case, low noise potentials can be generated, as there is no technical noise coming from external power sources and the noise coming from the movement of vortices is expected to be an order of magnitude less than Johnson noise in normal conductors.⁴⁹

Another property of vortices in superconducting thin films is that their distribution can be manipulated with light. Heating parts of the superconductor will result in a force on the vortices, which shifts the position of the vortices and consequently changes the vortex distribution. We have used this effect to generate various trap patterns with a thin square of superconducting YBCO, using light patterns generated by a spatial light modulator.¹⁹⁰ The advantage of this technique is that multiple trap geometries can be generated with the same chip architecture in-situ, without the need of changing the chip and breaking the vacuum of the ultra-high vacuum chamber.

Aside from using superconducting chips exclusively to manipulate cold atoms, we are also working on interfaces between cold atoms and superconducting qubits fabricated on the superconducting chip. What we envision here is the coherent transfer of quantum states between cold atoms and qubits made of superconducting integrated circuits. These hybrid systems will have many application, like the transduction of quantum states between the microwave and optical regime or the creation of universal quantum computing devices.

As mentioned before in this article, the practical implementation of a hybrid atom-superconducting qubit system is technically challenging. In Singapore we decided to bring cold atoms inside the dilution refrigerator by magnetically transporting them from a room temperature vacuum chamber directly to the mK stage of the refrigerator. With this technique we are able to bring clouds of 5×10^8 ^{87}Rb atoms close to the mK stage, at a base temperature of 70 mK.¹⁸⁶ Trapped inside the mK stage, the atomic cloud exhibits an exceptional lifetime of 13 minutes, which is a promising starting point for future experiments.

In order to couple atoms and superconducting circuits a few scenarios are possible, which can be categorized in indirect and direct coupling. Also, the state of the atoms will i.e. ground state or highly excited (Rydberg), will have a significant influence on the experimental parameters. When indirectly coupled, the qubit and atom are individually coupled to a resonator, which mediates the interaction. In this case the coupling of the resonator to the qubit is easily implemented and can reach the strong coupling regime. Coupling ground state atoms to a planar resonator is an ambitious task. It was shown that the coupling strength of a single atom is only 40 Hz at a resonator-atom distance of $1 \mu\text{m}$.¹⁹¹ In order to reach strong coupling one consequently needs to collectively couple an ensemble of 10^6 atoms to the waveguide, which is experimentally challenging. Using Rydberg states can consid-

erably relax these requirements. We have shown that for Rydberg states strong coupling can be achieved with even a single atom.^{55,192} The strong coupling can even be reached with atom-resonator distances of tens of micro-meters, when using the fringe field of the capacitive part of the resonator to couple the atom.

When using Rydberg atoms, even directly coupling of atoms to charge qubits can be realized. A neutral atom placed inside the gate capacitor of a charge qubit acts as a dielectric medium and affects the gate capacitance, resulting in a modulation of the charge-qubit energy bands. Moreover, the local quasi-static electric field strongly depends on the charge-qubit state, leading to different DC Stark shifts of atomic-qubit states. We have shown that in such a setup quantum states can be transferred between the two qubits and CNOT and Hadamard gates can be realized.¹⁹³ Schemes for Rydberg atoms interacting with flux qubits have been theoretically proposed to realize quantum memories¹⁹⁴.

We think that we now have the tools at hand to interface cold atoms with superconducting circuits. In the near future we would like to first couple atoms to 3D transmons, see Fig. 18(b). For this we designed and tested superconducting 3D cavities that have free space access for the transport and optical manipulation of cold atoms. First experiments to transport atoms inside the cavity are currently under way. At the same time we are developing our own fabrication for superconducting qubits. First chips have already been fabricated and tested. With both systems at hand we can then go forward to build hybrid systems of cold atoms and superconducting circuits.

C. Outlook

In this review we have described applications of atom chips in atomtronics, precision sensing and quantum information. We illustrated the state of the art in these topics and touched upon future prospects and utilizations. In this zoomed-in view, we omitted many other excellent activities in the field, due only to unavoidable space limitations. Here, we would like to bring up other achievements that will shape the future of the atom chip platform.

Most of the experimental studies described above used bosonic rubidium atoms. In fact, many other species, like fermions, molecules and ions are used in atom chips.⁷⁴ Fermions are another one of the fundamental building blocks of matter and therefore highly interesting objects to study, including low dimensional physics, the interaction of fermions with different species, or spin physics.¹⁹⁵

Molecules, as the bridge between physics and chemistry, are an additional compelling candidate for many studies. Implementations range from fundamental science, like the measurement of the electric dipole moment and parity violation, to applied science in quantum processing. A 'Lab on a Chip' for molecules is thus a sought-after goal. Recently, the trapping of simple molecules on microchips was realized,^{196,197} opening the way for many interesting investigations.

Trapped ions are one of the most promising candidates for practical quantum computing. In order to control and measure

a large number of ions it will be necessary to fabricate surface-electrode traps on miniaturized microchips. The development and integration of these chips is currently ongoing and will be a major part in the future development of scalable quantum computer architectures with ions.¹⁹⁸

Using the wave nature of atoms, atom chips will in future be used as precise sensors for material research and fundamental science. So-called 'quantum gas microscopes' have been developed for room-¹⁴⁴ and cryogenic¹⁹⁹-temperature environments and are ready to be used in the nontrivial studies of unique materials. At the same time, matter waves are being employed for precision measurements in atomic interferometers. By analogy to the optical interferometer, the splitting and recombination of matter waves on atom chips are, for instance, being used to test theories in quantum thermodynamics²⁰⁰, quantum many-body physics²⁰¹, and find applications in gravitational sensing²⁰².

Intimately connected with precision sensing is the field of fundamental science. Many studies will be possible with atom chips, including tests of the Weak Equivalence Principle,²⁰³ interactions of antihydrogen with matter and gravity,²⁰⁴ non-Newtonian gravity, and the search for a fifth fundamental force.

All these examples show that atom chip technology has a bright future ahead. Combined with further integration and miniaturization, atom chips will play a role in many areas, both in fundamental research, as well as practical measurements.

Acknowledgments All groups are very thankful to their colleagues who have been working with them on the experiments and their interpretation.

The BGU work has been supported by the Israel Science Foundation, the Deutsche Forschungsgemeinschaft German-Israeli DIP program, the FP7 program of the European Commission, the Israeli Council for Higher Education, and the Ministry of Immigrant Absorption (Israel).

The Tübingen research team gratefully acknowledges financial support from the Deutsche Forschungsgemeinschaft through SPP 1929 (GiRyd) and through DFG Project No. 394243350 and 421077991.

The Singapore team is grateful for administrative assistance and financial support from the Centre for Quantum Technologies (CQT) in Singapore.

V. QUENCH DYNAMICS OF INTEGRABLE MANY-BODY SYSTEMS

N. Andrei and C. Rylands

The study of non-equilibrium quantum physics is currently at the intellectual forefront of condensed matter physics. One-dimensional systems in particular provide an exciting arena where over the last decade significant advances in experimental techniques have allowed very precise study of an array of nonequilibrium phenomena and where a number of powerful theoretical tools were developed to describe these phenomena. Here we give a brief account of a few systems

that are described by one dimensional integrable Hamiltonians, the Lieb-Liniger model and the Heisenberg chain and how integrability gives access to the study of some of their local and global nonequilibrium properties.

While the principles of equilibrium statistical mechanics are well understood and form the basis to describe a variety of phenomena, there is no corresponding framework for the non-equilibrium dynamics, although efforts to fully understand the underlying principles extend back to Boltzmann and beyond. The study of non-equilibrium quantum physics is currently at the intellectual forefront of condensed matter physics. Solving particular models numerically or analytically and comparing to experiments illuminate bits of the puzzle.

Here, is an extended version of talks given by the first author at Atomtronics 2019 at Benasque where some aspects of the questions were discussed. It is based on a review article²⁰⁵ written with Colin Rylands and builds on work carried out with several collaborators: Deepak Iyer, Garry Goldstein, Wenshuo Liu, Adrian Culver, Huijie Guan and Roshan Tourani to whom we are very grateful for many enlightening and useful discussions.

A. Quench Dynamics

A convenient protocol to observe a system out of equilibrium is to prepare it in some initial state $|\Psi_i\rangle$, typically an eigenstate of an initial Hamiltonian H_i , and then allow it to evolve in time using another Hamiltonian, H for which $|\Psi_i\rangle$ is not an eigenstate^{206–208}. One may then follow the correlations of local observables,

$$\langle \Psi_i | e^{iHt} \{ \mathcal{O}_1(x_1) \mathcal{O}_2(x_2) \dots \} e^{-iHt} | \Psi_i \rangle \quad (8)$$

as they evolve. One may be interested to know what new properties characterize the system, whether a dynamical phase transition occurs at some point in time²⁰⁹ or how its entanglements evolve. A particularly important question that arises in this context is whether the system thermalizes. Namely, can the system act as a bath to the small subsystem represented the local operators $\mathcal{O}_i(x_i)$, so that in the long time limit one has

$$\begin{aligned} \lim_{t \rightarrow \infty} \langle \Psi_i | e^{iHt} \{ \mathcal{O}_1(x_1) \mathcal{O}_2(x_2) \dots \} e^{-iHt} | \Psi_i \rangle \\ = \text{Tr } e^{-\beta H} \{ \mathcal{O}_1(x_1) \mathcal{O}_2(x_2) \dots \} \end{aligned} \quad (9)$$

with the final inverse temperature β determined by the initial energy, $E_0 = \langle \Psi_i | H | \Psi_i \rangle$.

Also global properties are of interest. These are commonly studied via the Loschmidt amplitude (LA), the overlap between the initial state with its time evolved self, conveniently expressed using a complete set of energy eigenstates, $|n\rangle$:

$$\mathcal{G}(t) = \langle \Psi_i | e^{-iHt} | \Psi_i \rangle = \sum_n |\langle n | \Psi_i \rangle|^2 e^{-iE_n t} \quad (10)$$

and its Fourier transform,

$$\begin{aligned}\mathcal{P}(W) &= \int_{-\infty}^{\infty} \frac{dt}{2\pi} e^{iWt} \mathcal{G}(t) \\ &= \sum_n \delta(W - (E_n - \varepsilon_i)) |\langle n | \Psi_i \rangle|^2\end{aligned}\quad (11)$$

which measures the work distribution done during the quench²¹⁰.

B. Evolution under integrable Hamiltonians

We shall consider evolutions effectuated by post-quench Hamiltonians that are integrable, namely Hamiltonians admitting a complete set of eigenstates $|n\rangle$ and eigen-energies E_n given by the Bethe Ansatz. The ability to obtain these follows from the existence of an infinite set of local charges, $\{Q_n, n = 1 \dots \infty\}$, that commute with the Hamiltonian and constrain the time evolution leading to a generalized Gibbs ensemble $e^{-\sum_n \beta_n Q_n}$ with the final inverse temperatures β_n determined by the initial values $q_n^0 = \langle \Psi_i | Q_n | \Psi_i \rangle$ ²¹¹.

Thus some features of integrable time evolution are non generic, but at the same time it turns out that many features observed in integrable models can also be observed when integrability is broken, such as "dynamical fermionization" of the bosons of the integrable Lieb-Liniger Hamiltonian to be discussed below, can be observed in the bose-Hubbard model, the lattice version of the Lieb-Liniger model, which is not integrable²¹². Further, many systems, in particular ultra-cold atom systems, are actually described by integrable Hamiltonians and can therefore be studied as such. Here we discuss two of them.

1. The Lieb-Liniger model

The model describes systems of ultracold gases of neutral bosonic atoms moving in one dimensional traps and interacting with each other via a local density interaction of strength c which can be repulsive $c > 0$ or attractive $c < 0$. Aside from being an excellent description of the experimental system, it is one of the simpler Hamiltonians for which there exists an exact solution via Bethe Ansatz. The Lieb-Liniger Hamiltonian reads

$$H = - \int dx \Psi^\dagger(x) \frac{\partial_x^2}{2m} \Psi(x) + c \int dx \Psi^\dagger(x) \Psi(x) \Psi^\dagger(x) \Psi(x) \quad (12)$$

(setting $\hbar = 1$). Here $\Psi^\dagger(x)$, $\Psi(x)$ create and annihilate bosons of mass m . The exact N -particle eigenstate is given by^{213,214},

$$\begin{aligned}|\{k_j\}\rangle &= \int d^N x \prod_{\substack{i,j=1 \\ i < j}}^N [\theta(x_i - x_j) + s(k_i, k_j) \theta(x_j - x_i)] \\ &\quad \times \prod_{l=1}^N e^{ik_l x_l} \Psi^\dagger(x_l) |0\rangle.\end{aligned}\quad (13)$$

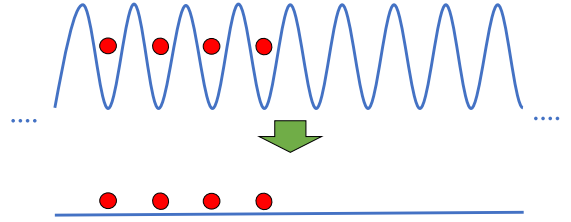


FIG. 19. The domain wall initial state : A cold atom gas is held in the left part of a deep optical lattice, extending from $j = -\infty$ to $j = 0$. This is then removed and the gas is allowed to expand.

Here $s(k_i, k_j) = \frac{k_i - k_j + ic}{k_i - k_j - ic} = e^{i\varphi(k_i - k_j)}$ is the two particle scattering matrix, $\varphi(k) = 2 \arctan(k/c)$ is the phase shift. The single particle momenta k_j are unrestricted in the infinite volume limit while with periodic boundary condition on a line segment L they must satisfy the Bethe Ansatz equations: $k_i L = \sum_{j=1}^N \varphi(k_i - k_j) + 2\pi n_i$, with the integers n_i being the quantum numbers of the state. The single particle momenta are related to the conserved charges by $q_n = \sum_{j=1}^N k_j^n$, in particular the energy is given by, $q_2 = E = \sum_{j=1}^N k_j^2$.

This set of eigenstates allows the study of time evolution through the partition of the unity, $\mathbb{1}_N = \sum_{k_1 \dots k_N} \frac{|\{k_j\}\rangle \langle \{k_j\}|}{\mathcal{N}(\{k_j\})}$. Here $\mathcal{N}(\{k_j\}) = \det [\delta_{jk} (L + \sum_{l=1}^N \varphi'(k_j - k_l)) - \varphi'(k_j - k_k)]$ is a normalization factor.

In terms of the partition identity, the time evolved wavefunction is given by,

$$\begin{aligned}|\Psi(t)\rangle &= e^{-iHt} |\Psi_i\rangle \\ &= \sum_{k_1 \dots k_N} e^{-it(\sum_{j=1}^N k_j^2)} |\{k_j\}\rangle \langle \{k_j\} | \Psi_i\rangle\end{aligned}\quad (14)$$

with the initial state encoded in the overlaps $\langle \{k_j\} | \Psi_i \rangle$. These overlaps have been studied by many groups, see e.g.²¹⁵ and are typically very difficult to calculate. Once these overlaps are known they can be put in exponential form and combined with matrix elements of a given operator to yield a quench action which is typically evaluated in the saddle point approximation²¹⁶.

Beyond overlaps: One may get around the difficulty of computing overlaps by choosing an alternate form of the partition identity obtained by exchanging the ordering in momentum space for ordering in coordinate space leading to the Yudson representation of the partition of the unity^{217,218}, or equivalently choosing appropriate trajectories for integrating over the momenta, see²¹²,

$$\mathbb{1}_N = \sum_{k_1, \dots, k_N} \frac{|\{k_j\}\rangle \langle \{k_j\}|}{\mathcal{N}(\{k_j\})}.\quad (15)$$

Here we have introduced the notation $|\{k_j\}\rangle$ (notice the parenthesis replacing the ket) to denote the Yudson state,

$$|\{k\}\rangle = \int d^N x \theta(\vec{x}) \prod_l^N e^{ik_l x_l} \Psi^\dagger(x_l) |0\rangle \quad (16)$$

with $\theta(\vec{x})$ denoting a Heaviside function which is non zero only for the ordering $x_1 > x_2 > \dots > x_N$. The Yudson state is simpler to work with than the full eigenstates of the model and its overlaps with the initial state can be readily calculated, particularly if the initial state is ordered in coordinate space.

The domain wall initial state: As an example we consider an initial state in the form of a domain wall and quench it with $c > 0$ Lieb-Liniger Hamiltonian. Its time evolution can be studied analytically and several interesting phenomena will be shown to emerge:

- *Nonequilibrium Steady state (NESS)*
- *RG flow in time*
- *Evolution along space-time rays*
- *Hanbury Brown-Twiss effect*
- *Dynamical fermionization*

The initial state, as depicted in Fig. 19, consists N cold atom bosons held in a very deep optical lattice of length L with $N, L \rightarrow \infty$ and $\delta = L/N$ held fixed. The lattice site $\bar{x}_j = j\delta$, $j = -\infty \dots -1, 0, 1 \dots +\infty$, are filled with one boson per site in the left half of the lattice: $j = -\infty$ to $j = 0$, and none in the half

to the right,

$$|\Psi_i\rangle = \int d^N x \prod_{j=-\infty}^0 \left[\frac{\omega}{2\pi} \right]^{\frac{1}{4}} e^{-\frac{\omega}{4}(x_j - \bar{x}_j)^2} \Psi^\dagger(x_j) |0\rangle. \quad (17)$$

The quench consists of suddenly releasing the trap and allowing the bosons to interact and evolve under the Lieb-Liniger Hamiltonian. Time evolving the system and using the Yudson representation we find,

$$|\Psi_i(t)\rangle = \left[\frac{8\pi}{\omega} \right]^{\frac{N}{4}} \sum_{k_1, \dots, k_N} \frac{e^{-\sum_{j=1}^N \left[\frac{1}{\omega} (1+i\omega t) k_j^2 + ik_j \bar{x}_j \right]}}{\mathcal{N}(\{k_j\})} |\{k_j\}\rangle. \quad (18)$$

When the lattice is removed the gas expands and the particle density will become nonzero between the lattice sites and also to the right of the domain wall. In the vicinity of the domain wall particles will begin to vacate the left hand side of the system and populate the right hand side, see Fig. 20. The effects of this quench can only be felt within a "light-cone" centered at the edge and determined by a finite effective velocity, v^{eff} which depends upon ω . On the right, $x \gg v^{\text{eff}} t$ the density will remain zero while to the left, $x \ll -v^{\text{eff}} t$, the average density will remain $1/\delta$ - the effects of the quench are still felt as the initially confined bosons will expand and begin to interact with each other.

We first examine the local portion of the quench around the domain wall. Since to the left there is an infinite particle reservoir and to the right an infinite particle drain the system will never equilibrate, however at long times a non-equilibrium steady state (NESS) consisting of a left to right particle current is established. This can be investigated by computing the expectation value of the density $\rho(x, t) = \langle \Psi_i(t) | \Psi^\dagger(x) \Psi(x) | \Psi_i(t) \rangle$. Utilizing the known formulae for the matrix elements of the density operator with Bethe eigenstates²¹⁹ this can be calculated exactly. To the right of the domain wall, at long times and to leading order in $1/c\delta$ three regions emerge²¹⁸

$$\rho(x, t) = \begin{cases} \rho_{\text{NESS}} = \frac{1}{2\delta} - \frac{4\pi}{c\delta^2} & \frac{1}{\sqrt{\omega}} \ll x \ll v^{\text{eff}} t \\ \rho_{\text{Cross}}(x) = \frac{1}{\delta} f + \frac{16}{\pi c \delta^2} \left[e^{-\frac{x^2}{\sigma}} \frac{x\sqrt{\pi}}{\sqrt{\sigma}} f - \frac{1}{2} e^{-2\frac{x^2}{\sigma}} + \frac{\pi}{2} f(1-f) \right] & x \sim v^{\text{eff}} t \\ \rho_0 = 0 & x \gg v^{\text{eff}} t \end{cases} \quad (19)$$

where $f = f(x, t) = \frac{1}{2} \text{erfc} \left(\frac{x}{\sqrt{\sigma(t)}} \right)$ and $\sigma(t) = \frac{t^2 \omega}{2} + \frac{2}{\omega}$. Far to the right $x \gg v^{\text{eff}} t$ we see that the density vanishes while closer to the light-cone some complicated crossover behavior occurs. Since the model is Galilean rather than Lorentz invariant the light-cone is not sharp giving instead this crossover regime. Most interesting is the region deep inside the light-cone in which the density is independent of x, t . This signifies the existence of the NESS with the particle density being reduced by the repulsive interactions. This nonequilibrium effect of an open system, corresponding to the order of limits with the size of the system L satisfying $L \gg t$ is to be contrasted with the behavior in a closed system, with the opposite order of limits, where the system will reach equilibrium with a density $\rho = 1/2\delta$. Within this region all local properties of the system can be calculated by taking the expectation value with respect to this NESS, $\langle \mathcal{O}(x, t) \rangle = \langle \Psi_{\text{NESS}} | \mathcal{O} | \Psi_{\text{NESS}} \rangle$ where $|\Psi_{\text{NESS}}\rangle$ can be determined by taking the appropriate limit of (18).

On the left portion of the lattice $x \ll -v^{\text{eff}} t$ we are outside the light-cone, the system is unaffected by the domain wall portion of the quench and the lattice translational invariance

is restored. At long times the density within this region is,

$$\rho(x, t) = \frac{1}{\delta} \left[1 + \sum_{s=1}^{\infty} e^{-\sigma(t) \frac{\pi^2 s^2}{\delta^2}} \cos \left(\frac{2\pi s x}{\delta} \right) \right] \quad (20)$$

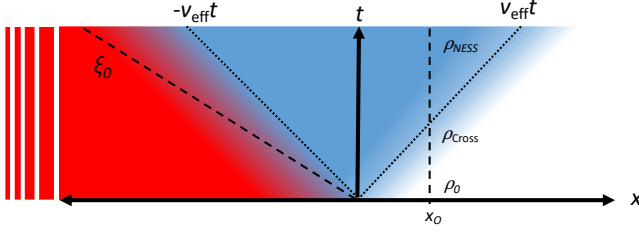


FIG. 20. At long times a non-equilibrium steady state (NESS) is established as depicted on the right. Measuring the density at $x = x_0$ one will see the initial density ρ_0 change to the crossover regime ρ_{Cross} at intermediate times ending up as time and space independent value ρ_{NESS} which encodes the interaction and the initial quench. Figure taken from²⁰⁵.

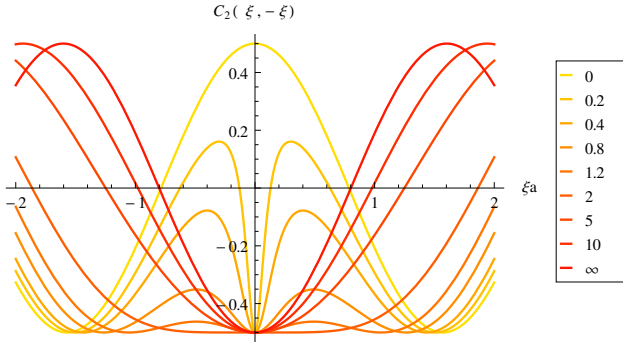


FIG. 21. The noise correlation function $C_2(\xi, -\xi)$, as a function of $\xi = x/\tau$ at long times for a quench from a lattice like initial state. For arbitrary values of $c > 0$, with δ fixed, the system develops a distinct fermionic dip at the origin. Figure taken from²¹².

which describes small oscillation about a uniform density of $1/\delta$.

This result coincides with what one would expect for a quench from a lattice initial state of the Tonks-Girardeau (TG) gas, the $c \rightarrow \infty$ limit of the LL model. To understand this one should go beyond the density and compute the normalised noise correlation function $C_2(x, x') = \frac{\rho_2(x, x', t)}{\rho(x, t)\rho(x', t)} - 1$ where

$$\rho_2(x, x', t) = \langle \Psi_i(t) | \Psi^\dagger(x) \Psi(x) \Psi^\dagger(x') \Psi(x') | \Psi_i(t) \rangle. \quad (21)$$

This correlation function is related to the Hanbury Brown-Twiss effect and will detect the nature of the interactions between particles, a peak indicating bosons while a dip indicates fermions^{220,221}. Computing the noise correlation function $\rho_2(x, -x, t)$ by inserting two copies of the identity and evaluating the integrals at long time by saddle point method²²² one finds it becomes a function only of the ray variables $\xi = x/t$ (measured with respect to $\xi_0 = x_0/t$ see Fig. 20). For sufficiently long times $\xi \sim 0$ a distinct fermionic dip is seen for arbitrary $c > 0$ while $c = 0$ shows a bosonic peak, the turn over to the dip occurring on the time scale, $t \sim c^{-2}$, see Fig. 21. This turn over results from an increase in time of

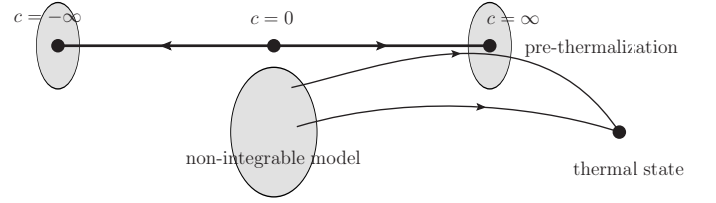


FIG. 22. Prethermalization in the Bose Hubbard model, Figure taken from²¹².

the effective coupling constant c - starting from any initial repulsive value it will flow to strong coupling in the long time limit^{223–225} doing so like \sqrt{t} ²²². Thus at long times the system will behave as if it consisted of non interacting fermions. This dynamical fermionization, the development of fermionic-like correlations, was subsequently observed in experiment²²⁶.

The flow of the coupling naturally leads to the concept of renormalisation group (RG) flow in time t . By analogy with conventional RG ideas, increasing time plays the role of reducing the cut off with $c = \infty$ being a strong coupling fixed point. For comparison we recall that in the usual RG picture c has scaling dimension 1 and so also flows to strong coupling. Subsequently, similar behavior was also seen in strongly coupled impurity models^{227,228}. Extending the dynamical RG analogy one can envisage that other Hamiltonians close to the Lieb-Linger will flow close the neighborhood of the same strong coupling fixed point, prethermalize in other words, only to end up thermalized on longer time scales if the model is not integrable, see Fig. 22. An example is provided by the lattice version of the Lieb-Liniger model, the non integrable Bose-Hubbard model which also exhibits dynamical fermionization²¹².

We turn now to study the global properties of the post quench system through the Loschmidt amplitude (10) and the work distribution function (11) focusing on the experimentally relevant case of a cold atom gas initially held in a deep optical lattice which is then removed entirely in the quench, see Fig. 23. The system is translationally invariant and described by the Lieb-Liniger model.

We consider N bosons on a circle of length L initially described by the state (17) with N consecutive sites filled, with $N\delta \ll L$ so that the unfilled part of the lattice is taken to be much larger than the filled portion to avoid complications arising from the boundary conditions. Employing the Yudson resolution of the identity, the Loschmidt amplitude can be determined to be²²⁹,

$$\mathcal{G}(t) = \left[\frac{8\pi}{\omega} \right]^{\frac{N}{2}} \sum_{n_1, \dots, n_N} e^{-\frac{2}{\omega} [1 + i\frac{\omega}{2}t] \sum_{j=1}^N \lambda_j^2} \frac{G(\{n\})}{\mathcal{N}(\{n\})} \quad (22)$$

where $G(\{n\}) = \det \left[e^{-i\lambda_j(\bar{x}_j - \bar{x}_k) - i\theta(j-k)\phi(\lambda_j - \lambda_k)} \right]$ and $\theta(j-k)$ is a Heaviside function. Using the same $1/c\delta$ expansion as before the Fourier transform of this can be explicitly found and analytic expressions for the work distribution, $\mathcal{P}(W)$ obtained. We plot this for both non interacting and strongly inter-

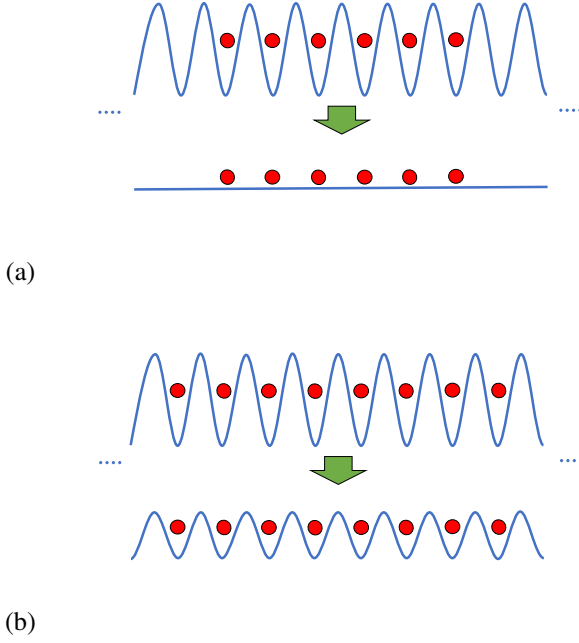


FIG. 23. The ultracold atom gas is initially held in a deep optical lattice which is (a) completely removed - post quench dynamics described by the Lieb-Liniger Hamiltonian or (b) merely lowered - the post quench dynamics given by Sine-Gordon Hamiltonian. Quench (b) is discussed in²³².

acting bosons $c\delta \gg 1$ in Fig. 24 for different particle number and see some commonalities as well as striking differences. Notice that the average work in both cases is the same, $\langle W \rangle = N\omega/4$ as is the large $W > \langle W \rangle$ behavior. The former statement can be understood from the fact that bosons are initially in non overlapping wavefunctions and $\langle W \rangle = \langle \Psi_0 | H | \Psi_0 \rangle$. In comparison, the small $W \ll \langle W \rangle$ behavior is strongly affected by the presence of interactions. Large resonant peaks are present in the interacting work distribution and can be attributed to the scattering of strongly repulsive excitations in the post quench system. Those peaks which are closest to $\langle W \rangle$ involve fewer scattering events while those $W = 0$ involve more. As the particle number is increased these fluctuations are suppressed like $1/\sqrt{N}$ ^{230,231}. For large systems of bosons the most interesting behavior therefore occurs in the region of $W \sim 0$ where the effects of the interaction are most keenly felt. In this region it can be shown that the distribution decays as a power law with the exponent drastically differing between the free and interacting cases. For the former we have $\mathcal{P}_{c=0}(W) \sim W^{\frac{N}{2}-1}$ whereas in the latter it is $\mathcal{P}_{c>0}(W) \sim W^{\frac{N^2}{2}-1}$, the presence of interactions in the system causing a dramatically faster decay of the work distribution. Behavior such as this will be seen in the next section also when the excitations are gapped as well as interacting.

We can use our knowledge of $\mathcal{P}(W)$ to investigate the global behavior of the post quench system. As a consequence of the large W agreement between the distributions for the in-

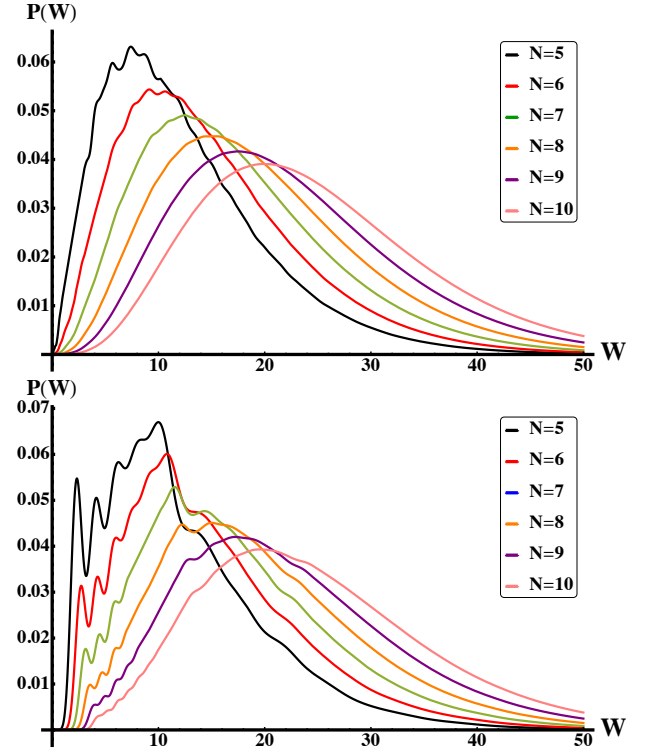


FIG. 24. The work distribution function, $\mathcal{P}(W)$, for different numbers of bosons released from an optical lattice with $\delta/m = 2$ and $\omega = 10$. We measure the work from ϵ_i the initial state energy. On the left we show the distribution for non interacting bosons while on the right we show the same quantity for interacting bosons, $c > 0$. Figure taken from²²⁹.

teracting and non-interacting systems we can determine that at short times $|\mathcal{G}(t)|^2$ is independent of the interactions. This corresponds to the initial period of expansion from the lattice in which the particles do not encounter one another. On the other hand, small W behavior provides insight to the long time dynamics, the power law decay of $\mathcal{P}(W)$ near the origin translating to the long time power law decay of the LE. Fourier transforming the distribution for free bosons we find that as $t \rightarrow \infty$, $|\mathcal{G}(t)|^2 \rightarrow 1/t^N$ while in the interacting case we have instead $|\mathcal{G}(t)|^2 \rightarrow 1/t^{N^2}$, a much faster decay. We attribute this dramatic difference in the decay away from the initial state to the fact that the large repulsive interactions acting on each other forcing them to spread out into the one dimensional trap, thereby decreasing their overlap with $|\Psi_i\rangle$. We should note that this is true regardless of the strength of the interactions and highlights the strongly coupled nature of even weakly interacting systems in low dimensions. As we saw earlier, in the long time limit any repulsive coupling flows in time strong coupling, therefore the exponent is independent of the initial strength of c , in the TG limit ($c = \infty$) one finds the same power law behavior at long times as for the finite c case. This is the dynamical fermionization discussed in the previous section.

The attractive regime is of significant interest. The proper-

ties of the attractive model both in and out of equilibrium are much less studied than its repulsive counterpart. This dearth of theoretical results stems from the increased complexity of the Bethe Ansatz solution in the attractive model. When $c < 0$ the model supports bound states and the ground state consists of a single bound state of all N particles²³³. While the eigenstates given by (13) remain valid, complex values of k which correspond to bound states are allowed. The resolutions of the identity (15) also remains formally valid provided these complex valued solutions are accounted for. A stumbling block however remains as the normalization of the Bethe states in the attractive regime is not known in closed form.

In the low density limit however it has been shown that for both repulsive and attractive interactions the spatially ordered identity (15) becomes^{212,217,222}

$$\mathbb{1}_N = \int_{\Gamma} \frac{d^N k}{(2\pi)^N} |\{k\}\rangle \langle \{k\}|. \quad (23)$$

The contours of integration, Γ , lie on the real line for repulsive interactions and are spread out in the imaginary direction for the attractive case with $\text{Im}(k_{j+1} - k_j) > |c|$.

Making use of this here in conjunction with the same $|c| \gg m\omega$ expansion we find that the work done in the attractive regime separates into two contributions,

$$\mathcal{P}_{c<0}(W) = \mathcal{P}_{\text{free}}(W) + \mathcal{P}_{\text{bound}}(W). \quad (24)$$

The first term $\mathcal{P}_{\text{free}}(W)$ is the contribution from particles which do not form bound states, it is identical to the expression in repulsive case only now $c < 0$. The major difference imposed by this is that the effective distance between the particles is smaller $\delta_{\text{eff}} < \delta$, the attractive interactions promoting the clustering of particles.

The simple analytic continuation to negative coupling of the first term is reminiscent of the the super Tonks-Girardeau gas. This highly correlated state of the LL model is created by preparing a repulsive LL gas in the Tonks-Girardeau limit, $c \rightarrow \infty$ and then abruptly changing the interaction strength from the being large and positive to large and negative. The result is a metastable nonequilibrium state which exhibits enhanced correlations. Many of the properties of this state can be shown to emerge from a simple analytic continuation of the coupling to large negative values. In effect the negligible overlap of each particle of our initial state mimics the density profile of the TG gas and so super-TG like behaviour is not unexpected. We should stress that the expression (23) is valid at arbitrary negative values c and so not limited to super-TG regime.

The second term $\mathcal{P}_{\text{bound}}(W)$ is entirely different. It is due to the bound states and is calculated by deforming the contours in (23) to the real line and picking up contributions due to the poles at $k_i - k_j = ic$ present in (13). An n -particle bound state can be shown to contribute $\mathcal{P}_{n\text{-bound}}(W) \propto |c|^{n-1} e^{-n|c|\delta}$ with factors from multiple bound states being multiplicative.

This exponential factor means that the probability that the initial state transitions to one containing bound states is highly suppressed and in the true super-TG limit vanish entirely. Despite this, for finite $|c|$ the bound states have a strong signature

in work distribution function. Since forming a bound state will lower the energy of the system²³³ the work distribution becomes non vanishing at negative values of W . There is a non zero probability that work can be extracted from the system. Importantly this does not violate the 2nd law of thermodynamics as the average work remains positive $\langle W \rangle$ ^{234,235}. In fact, it has been shown observed recently that the probability of extracting work from a single electron transistor can be as high as 65% whilst still satisfying the 2nd law²³⁶.

To see this we examine the leading term of $\mathcal{P}_{\text{bound}}(W)$ which arises due to the formation of a single two particle bound state

$$\mathcal{P}_{\text{bound}}(W) \approx N \sqrt{\frac{2\pi\omega}{m}} \frac{e^{-|c|\delta - \frac{2W}{\omega}}}{\Gamma(\frac{N}{2} - 1)} \left[\frac{2(W + \frac{|c|^2}{4m})}{\omega} \right]^{\frac{N}{2} - 2} \quad (25)$$

which is non vanishing for $-|c|^2/4m < W$. Determining the full bound state contribution is a straightforward yet involved calculation which we will not deal with here.

2. The XXZ Heisenberg spin chain

The XXZ Heisenberg chain provides another example of an experimentally relevant integrable model. The Hamiltonian

$$H = J \sum_{j=1}^N \{ \sigma_j^x \sigma_{j+1}^x + \sigma_j^y \sigma_{j+1}^y + \Delta \sigma_j^z \sigma_{j+1}^z \} \quad (26)$$

models a linear array of spin interacting via anisotropic spin exchange. The isotropic case $\Delta = 1$ is $SU(2)$ invariant and enjoys the distinction of being the first model solved by Bethe by means of the approach that bears his name²³⁷. The generalization to the anisotropic case was given by Orbach²³⁸. The eigenstates are again characterized by a set of Bethe momenta $\{k_j\}$ describing the motion of M down-spins in a background of $N - M$ up-spins, and are given by:

$$|\vec{k}\rangle = \sum_{\{m_j\}} \prod_{i < j} [\theta(m_i - m_j) + s(k_i, k_j) \theta(m_j - m_i)] \times \prod_j e^{ik_j m_j} \sigma_{m_j}^- | \uparrow \rangle \quad (27)$$

where m_j the position of the j th down spin is summed from 1 to N (the length of the chain), and the S-matrix is given by,

$$s(k_i, k_j) = -\frac{1 + e^{ik_i + ik_j} - 2\Delta e^{ik_i}}{1 + e^{ik_i + ik_j} - 2\Delta e^{ik_j}}. \quad (28)$$

The Heisenberg chain exhibits a complex spectrum which includes bound states in all parameter regimes. To carry out the quench dynamics for the model one needs to construct the appropriate Yudson representation and use it to time evolve any initial state²³⁹. Here we display in Fig. 25 the time evolving wavefunction of two adjacent flipped spins in the background of an infinite number of unflipped spins and compare it to the experimental results (no adjustable parameters are

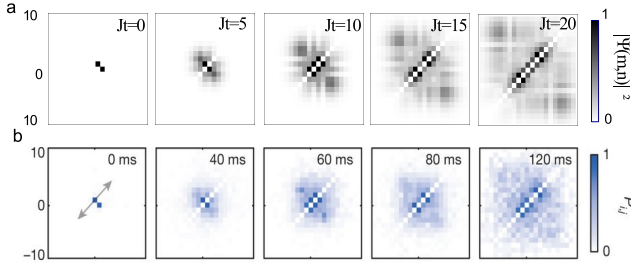


FIG. 25. (a) The norm of the wavefunction $|\Psi(m,n,t)|^2$ at different times for two flipped spins initially at $m = 1, n = 0$. (b) The joint probabilities at different times of two spins at sites i and j initially at $i = 1, j = 0$, measured experimentally in²⁴¹. Figure taken from²³⁹.

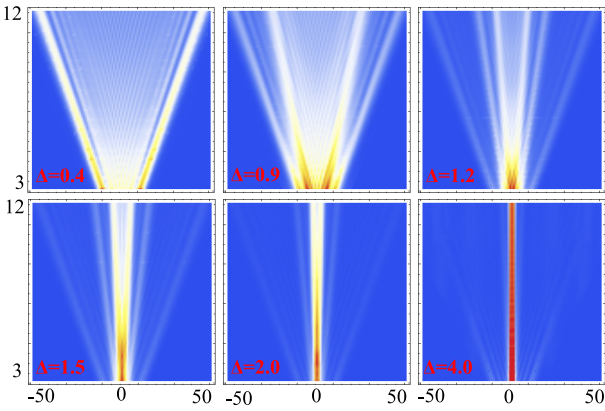


FIG. 26. The local magnetization after a quench from an initial state of 3 flipped spins at the origin for different values of the anisotropy Δ . Time, the vertical direction, is measured in units of the exchange coupling J . Figure taken from²³⁹.

involved.) The time evolution of the magnetization from an initial state of three flipped spins for different values of the anisotropy Δ is given in Fig. 26. We see that excitations propagate outward after the quench forming a sharp light-cone in contrast to the Lieb-Liniger model. The boundary of the light-cone arises from the propagation of free magnons which travel with the maximum velocity allowed by the lattice. Rays within the light-cone are the propagation of spinon bound states. As the anisotropy Δ is increased the bound states slow down and more spectral weight is shifted to them. Due to the integrability of (26) these excitations have infinite lifetime which prevents any dispersion of these features. The introduction of integrability breaking terms can therefore be expected to alter this picture, for example through spinon decay²⁴⁰.

C. Summary and Outlook

In this chapter we have explored some aspects of the far from equilibrium behavior of integrable models. After a broad overview of the current status of the field we investigated

some particular phenomena through a number of illustrative examples. We saw that the Bethe Ansatz solution of the Lieb-Liniger and Heisenberg models provided us with a powerful tool with which to study both the local and global, non-equilibrium behavior of these strongly coupled systems. The quench dynamics of more complex models such as the Gaudin-Yang model^{242,243} describing multi-component gases has also been accessed via the Yudson approach²⁴⁴ allowing the study of phenomena such as quantum Brownian motion or the dynamics of FFLO states^{245,246}. Similarly the quench dynamics of other models such as the Kondo and Anderson models are currently studied via the Yudson approach^{247,248}. They give access to such quantities as the time evolution of the Kondo resonance or of the charge or heat currents in voltage or temperature driven two lead quantum dot system.

These methods we discussed could be thought as being microscopic, starting from the exact eigenstates of the system. Recently these problems have been studied from a macroscopic perspective by combining integrability and ideas from hydrodynamics²⁴⁹. Generalized hydrodynamics (GHD) provides a simple description of the non-equilibrium integrable models on long length scales and times. It has been utilized in studies of domain wall initial states in the Lieb-Liniger and the emergence of light-cones in quenches of the XXZ model^{250,251}. This method allows the incorporation integrability breaking effects within the formalism, but is limited to “Euler scale” dynamics. It would be of great interest compare the results and expectations of GHD with the methods and results presented here to further understand the limitations of both the microscopic and macroscopic approaches.

VI. NON-EQUILIBRIUM PROTOCOLS FOR ONE DIMENSIONAL BOSE GASES IN ATOMTRONIC CIRCUITS

L. Pirolì and A. Trombettoni

The discussion of the properties of one-dimensional ultracold Bose gases was at center of several talks in the Benasque conference, with a special focus on their possible use for atomtronic circuits. Such systems are well described by the integrable Lieb-Liniger model, which was extensively studied since its introduction in the sixties, also in connection with other one-dimensional integrable systems. Therefore, on the one hand, the field of atomtronic circuits made of (possibly connected) one-dimensional ultracold systems is a natural arena to apply such a body of knowledge, while, on the other, it calls for new ideas and investigations. The following contribution summarizes and extends presentations done in Benasque and focuses on two topics in the theoretical study of the Lieb-Liniger model: *i*) integrable dynamics after a quench; *ii*) Floquet engineering.

One-dimensional systems provide an exciting arena where, over the past decade, significant experimental technical advances have allowed for very precise studies of a series of non-equilibrium phenomena. At the same time, a number of powerful theoretical tools were developed to describe them. The study of one-dimensional systems plays a role as well

in the field of atomtronics and in particular in atomtronics circuits, where matter-wave packets can be controlled and moved. When the transverse dimensions of the waveguides in which atoms move are small enough to create one-dimensional tightly confined traps and the energies involved are negligible with respect to the excitation energies of transverse degrees of freedom, then one enters the one-dimensional regime. Ultracold bosons are then effectively described by the Lieb-Liniger model^{252–254}, belonging to the family of integrable theories. In such one-dimensional regimes quantum fluctuations play a prominent role and a general issue is whether and for what applications such one-dimensional features hamper or at variance make it easier to realize atomtronics tasks.

Several talks and discussions in the Benasque conference revolved around the possible use of one-dimensional systems for atomtronics. Here we give an account of some interesting properties of the Lieb-Liniger model and how integrability gives access to the study of some of its local and global non-equilibrium properties. In the present contribution, L.P. wrote Section VI A, while the talk of A.T. is summarized in Section VI B.

A. Quench dynamics in the Lieb-Liniger model

In the early noughties, a series of cold-atomic experiments contributed to the emergence of a growing theoretical interest in the non-equilibrium dynamics of isolated quantum integrable systems^{94,255}. For instance, in the famous “quantum Newton’s cradle” experiment²⁵⁶, out-of-equilibrium arrays of trapped one-dimensional (1D) Bose gases were shown not to reach thermal equilibrium within the accessible time scales. This peculiar behavior was attributed to the approximate integrability of the system: indeed, in the idealized situation where longitudinal confining potentials are neglected, a 1D gas of N bosons with mass m and point-wise interactions can be described by the integrable Lieb-Liniger Hamiltonian²¹³. Denoting by L the length of the system, the Hamiltonian can be written as

$$H = \int_0^L dx \left(\frac{\hbar^2}{2m} \partial_x \Psi^\dagger \partial_x \Psi + c \Psi^\dagger \Psi^\dagger \Psi \Psi \right), \quad (29)$$

where Ψ , Ψ^\dagger are bosonic creation and annihilation operators satisfying canonical commutation relations. Here, the interaction strength is related to the one dimensional scattering length a_{1D} through $c = -\hbar^2/ma_{1D}$ ²⁵⁷ and can be varied via Feshbach resonances²⁵⁸ to take either positive or negative values.

Given its relative simplicity and experimental relevance, in the past decade a large number of studies have focused on the non-equilibrium dynamics in the Lieb-Liniger gas, especially within simplified protocols such as the one of a quantum quench^{259,260}: in this setting one considers the ground state of some Hamiltonian $H(c_0)$ (c_0 denotes an internal parameter), which is suddenly changed at time $t = 0$ by an abrupt variation $c_0 \rightarrow c$. These studies have played an important role for the development of a general theory of integrable systems out

of equilibrium²⁶¹. In this section, we provide a review of a selected number of them, focusing exclusively on the simplest case of homogeneous settings (see Section VI C for recent further developments in the presence of confinement potentials and inhomogeneities).

1. The quench problem

Physical intuition suggests that after a quench an extended system should act as an infinite bath with respect to its own finite subsystems, and that local properties should relax to stationary values described by a thermal Gibbs ensemble. While for generic models this picture turns out to be correct^{211,262,263}, a quite different scenario emerges in the presence of integrability, due to the existence of an extensive number of local conservation laws which strongly constrain the dynamics. In this case, it was proposed in Ref.²⁶⁴ that the correct post-quench stationary properties are captured by a generalized Gibbs ensemble (GGE), which is written in terms of all higher local conservation laws beyond the Hamiltonian^{264–266}. It was later discovered that quasi-local conservation laws must also be taken into account^{267–272} and the validity of the GGE is now widely accepted.

Despite the established conceptual picture, computations based on the GGE are hard, and more generally the characterization of the post-quench dynamics remains extremely challenging in practice. In order to explain the difficulties involved, it is useful to consider the time evolution of a physically relevant observable for the 1D Bose gas, namely so-called pair correlation function²⁷³

$$g_2 = \frac{\langle \Phi | \Psi^{\dagger 2}(x) \Psi^2(x) | \Phi \rangle}{D^2}, \quad (30)$$

where $D = N/L$ is the particle density, with L the system size, while $|\Phi\rangle$ is the state of the system. Physically, g_2 quantifies the probability that two particles occupy the same position. For a quantum quench, we have the formal expression (setting $\hbar = 1$)

$$\begin{aligned} \langle \Phi(t) | \Psi^{\dagger 2}(x) \Psi^2(x) | \Phi(t) \rangle &= \sum_{m,n} \langle \Phi(0) | n \rangle \langle m | \Phi(0) \rangle \\ &\times \langle n | \Psi^{\dagger 2}(x) \Psi^2(x) | m \rangle e^{-i(E_n - E_m)t}. \end{aligned} \quad (31)$$

Here we denoted by $|n\rangle$, E_n the energy eigenstates and eigenvalues respectively, while $|\Phi(t)\rangle$ is the state of the system evolved at time t after the quench. For the Lieb-Liniger model the Bethe Ansatz²¹⁹ is a very efficient tool to obtain most of the ingredients appearing in Eq. (31), including the matrix elements of the local operator $\Psi^{\dagger 2}(x) \Psi^2(x)$ ^{274,275}. However, due to the complicated form of the energy eigenfunctions, there appears to be no simple way to compute the overlaps $\langle \Phi(0) | n \rangle$ for general initial states. Furthermore, Eq. (31) involves the evaluation of a double sum over all the eigenstates of the Hamiltonian, which is currently out of reach in most of the physically interesting situations.

Due to the above difficulties, initial studies in the Lieb-Liniger model were restricted to the limit of either vanishing^{276,277} or infinitely repulsive post-quench interactions^{278–284}, where the Hamiltonian can be mapped onto free fermions through a Jordan-Wigner transformation. While these works already made it possible to explore in some detail interesting phenomena such as local relaxation²⁸¹ and “light-cone” spreading of correlation functions^{276,281}, it remained as an open problem to provide predictions in the case of finite values of the interactions.

2. The Quench Action

A conceptual and technical breakthrough came with the introduction, by Caux and Essler, of the so-called Quench Action method^{216,285}, which proved to be a powerful and versatile approach to the quench dynamics in integrable systems (other methods, that will not be discussed here, have also been developed, including a Yudson-representation approach, which is also suitable to study inhomogeneous initial states, see Refs.^{222,229} and the contribution of N. Andrei and C. Rylands).

It is well known that, in the thermodynamic limit, each eigenstate of an integrable system is associated with a distribution function $\rho(\lambda)$, where λ are the quasi-momenta of the (stable) quasi-particle excitations²¹⁹. Based on physical arguments, it was proposed in Ref.²¹⁶ that this description could be exploited to replace the double sum in Eq. (31) with a functional integral over all distribution functions $\rho(\lambda)$. This approach is particularly powerful to investigate the late-time limit, for which one can write (in the thermodynamic limit)^{216,285}

$$\begin{aligned} \lim_{t \rightarrow \infty} \langle \Phi(t) | \Psi^{\dagger 2}(x) \Psi^2(x) | \Phi(t) \rangle &= \\ &= \int \mathcal{D}\rho \, e^{S[\rho]} \langle \rho | \Psi^{\dagger 2}(x) \Psi^2(x) | \rho \rangle, \end{aligned} \quad (32)$$

where $|\rho\rangle$ denotes an eigenstate corresponding to the distribution function $\rho(\lambda)$. Here we introduced the “Quench Action” $S[\rho]$, which can be determined based on the knowledge of the overlaps $\langle \Phi(0) | n \rangle$. While, as we have already mentioned, it is not known how to obtain these in general, it turned out that they can be computed in several interesting cases^{286–304}.

Given $S[\rho]$, the functional integral can be treated exactly by saddle-point evaluation, so that the r.h.s. of Eq. (32) can be replaced by $\langle \rho_s | \Psi^{\dagger 2}(x) \Psi^2(x) | \rho_s \rangle$, where $\delta S[\rho_s] / \delta \rho = 0$. Crucially, the saddle-point distribution function $\rho_s(\lambda)$ determines all the post-quench local expectation values (which can be explicitly computed via exact Bethe Ansatz formulas^{274,305–308}), and thus represents an effective characterization of the late-times steady state.

The Quench Action approach was first applied in the Lieb-Liniger model for quenches from zero to positive values of the interactions, $c_0 = 0 \rightarrow c > 0$ ³⁰⁹. It was found that the steady state displays quantitative different features from a thermal

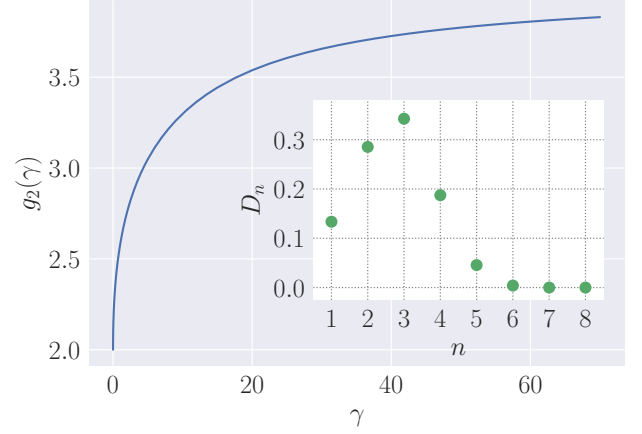


FIG. 27. Main panel: Pair correlation function, as defined in Eq. (30) in the steady state reached after a quench $c_0 = 0 \rightarrow c < 0$. The plot shows g_2 as a function of the rescaled interaction $\gamma = |c|/D$, and is computed using the results of Ref.³¹⁶. Inset: Densities D_n of the n -particle bound states for the same quench, and $\gamma = 2$.

state, unequivocally proving the absence of thermalization. The same approach also allowed for the computation of the full time evolution of g_2 ³¹⁰ (see also^{311,312}), unveiling a quite general power-law decay to stationary values for local observables, and for a detailed study of the statistics of the work performed by the quench^{313–315}.

3. Quenches to the attractive regime

In the case of quenches to repulsive interactions, the late-time steady state appears to display features that are only quantitatively different from those observed at thermal equilibrium³⁰⁹. In this respect, an even more interesting picture emerges for quenches to the attractive regime. These were investigated in Refs.^{316,317}, where the formalism of Refs.^{216,309} was employed to study interaction quenches of the form $c_0 = 0 \rightarrow c < 0$.

The main results of these works are arguably the prediction of the dynamical formation of n -boson bound states with finite densities D_n , and the characterization of the corresponding distribution of quasi-momenta $\rho_n(\lambda)$. Interestingly, it was shown that the value of n for which the density D_n is maximum decreases with the rescaled interaction $\gamma = |c|/D$. Although this result might appear counter-intuitive, there is in fact a simple physical interpretation: in the attractive regime, the bosons have a tendency to form multi-particle bound states. However, in the quench setup the total energy of the system is fixed by the initial state, while the energy of n -particle bound states increases, in absolute value, very rapidly with γ and n ³¹⁶. Therefore, n -particle bound states cannot be formed for large values of γ , while they become accessible as γ decreases.

We note that the structure of the stationary state predicted in Refs.^{316,317} is qualitatively very different from the super Tonks-Girardeau gas, which is obtained by quenching the one-

dimensional Bose gas from infinitely repulsive to infinitely attractive interactions^{279,318–323}. Indeed, the latter features no bound state, even though it is more strongly correlated than the traditional Tonks-Girardeau gas, as has been observed experimentally³²⁰. The findings of Refs.^{316,317} are thus also interesting because they show that the physics emerging at late times after a quench depends qualitatively on the initial state of the system.

Importantly, the formation of bound states after the quench have consequences on the local correlation functions. For instance, the value of g_2 at large times is always greater than 2, and increases with $\gamma = |c|/D$ ³¹⁷. This is displayed in Fig. 27, and is once again qualitatively different from the case of the super Tonks-Girardeau gas. We note that these results are consistent with subsequent numerical calculations reported in Ref.³²⁴ and based on the method developed in Ref.^{325,326}.

B. Floquet Hamiltonian for the Periodically Tilted Lieb-Liniger Model

When an integrable model is subjected to a periodic driving, then the resulting Floquet Hamiltonian is in general non-integrable. In the talk of the last author it was discussed the case of the Lieb-Liniger model subjected to a potential periodic in time and linear in space, which we refer to as a periodic tilting³²⁷. The Floquet Hamiltonian of the integrable Lieb-Liniger model for such linear potential with a periodic time-dependent strength is integrable and its quasi-energies can be determined using well known results for the undriven Lieb-Liniger model.

The Lagrangian density of the system is

$$\mathcal{L} = \frac{i}{2} (\Psi^\dagger \partial_t \Psi - h.c.) - \frac{1}{2m} \partial_x \Psi^\dagger \partial_x \Psi - \frac{c}{2} \Psi^\dagger \Psi^\dagger \Psi \Psi - V(x, t) \Psi^\dagger \Psi, \quad (33)$$

where $h.c.$ denotes the hermitian conjugate of the first term and $\Psi = \Psi(x, t)$. Moreover

$$V(x, t) = x f(t)$$

is the periodic tilting, with $f(t)$ a periodic function with period T .

Proceeding as one does for the single-particle and the two-particles cases^{327,328}, one can solve the Schrödinger equation of the many-body interacting model. To this aim, one introduces the following gauge transformation

$$\Psi(x, t) \equiv e^{i\theta(x, t)} \varphi(y(t), t), \quad (34)$$

where

$$y(t) = x - \xi(t),$$

with the functions $\xi(t)$ and $\theta(x, t)$ to be suitably determined in order to gauge away the potential term V from the Lagrangian density when rewritten in terms of the field φ .

The functions ξ and θ are determined as it follows. We start

by imposing

$$\partial_t \xi = \frac{1}{m} \partial_x \theta \quad (35)$$

and

$$-\partial_t \theta = \frac{1}{2m} (\partial_x \theta)^2 + x f(t). \quad (36)$$

We now make the Ansatz

$$\theta(x, t) = m x \partial_t \xi + \Gamma(t), \quad (37)$$

finding the conditions

$$m \partial_t^2 \xi = -f(t) \quad (38)$$

and

$$\partial_t \Gamma = -\frac{m}{2} (\partial_t \xi)^2, \quad (39)$$

determining $\xi(t)$ and $\Gamma(t)$ in terms of $f(t)$. From the differential equations (38)-(39) one gets³²⁷

$$\theta(x, t) = -x \int_0^t f(\tau) d\tau - \frac{1}{2m} \int_0^t \left[\int_0^\tau f(\tau') d\tau' \right]^2 d\tau. \quad (40)$$

Notice that, with our choices of the initial conditions [$\xi(0) = d\xi(0)/dt = 0$ and $\Gamma(0) = 0$], one has $\theta(x, 0) = 0$ and $y(0) = x$. Using (40), from (35), ξ can be readily determined.

For the sake of simplicity we will discuss the case

$$\int_0^T f(\tau) d\tau = 0 \quad (41)$$

(referring to³²⁷ for a discussion about the case $\int_0^T f(\tau) d\tau \neq 0$). The major simplification is that the gauge phase (40) does not depend anymore, at stroboscopic times, on the spatial variable, *i.e.* $\theta(x, T) \equiv \theta(T)$.

Provided the condition (41) holds, with the functions θ and ξ previously determined we can rewrite the Lagrangian density (33) in terms of $\varphi(y, t)$ which involves no longer the external potential:

$$\mathcal{L} = \frac{i}{2} (\varphi^\dagger \partial_t \varphi - h.c.) - \frac{1}{2m} \partial_y \varphi^\dagger \partial_y \varphi - \frac{c}{2} \varphi^\dagger \varphi^\dagger \varphi \varphi. \quad (42)$$

Notice that the outlined procedure also works for a more general potential of the form $V(x, t) = x f(t) + g(t)$.

To determine the Floquet Hamiltonian we need to determine the function θ at the stroboscopic times: $t \equiv nT$, with n integer. One has

$$\theta(nT) = -\frac{1}{2m} \int_0^{nT} dt \left[\int_0^t dt' f(t') \right]^2 \quad (43)$$

and

$$\xi(nT) = -\frac{1}{m} \int_0^{nT} dt \int_0^t dt' f(t'). \quad (44)$$

Now we want show that the ratios $\frac{\xi(nT)}{nT}$ and $\frac{\theta(nT)}{nT}$ do not depend on time, *i.e.* on n . Let be $\mathcal{F}(t)$ a function such that $\frac{d\mathcal{F}}{dt} = f(t)$. The constant of integration is chosen to be such that $\mathcal{F}(0) = 0$. From (41) one has

$$\int_0^T f(t)dt = \mathcal{F}(T) = 0, \quad (45)$$

so that one can see that $\mathcal{F}(t)$ is a periodic function of period T . Using the definition of the function \mathcal{F} , from (44) one gets

$$\xi(nT) = -\frac{1}{m} \int_0^{nT} \mathcal{F}(t)dt = -\frac{I}{m}n, \quad (46)$$

where $I \equiv \int_0^T \mathcal{F}(t)dt$. It follows that the ratio $\frac{\xi(nT)}{nT}$ is n -independent. The same reasoning applies for the gauge phase θ , since it is

$$\theta(nT) = -\frac{I'}{2m}n, \quad (47)$$

where $I' \equiv \int_0^T \mathcal{F}^2(t)dt$.

We are now able to write the Floquet Hamiltonian, which is found to be

$$H_F = \sum_{j=1}^N \left(\frac{\hat{p}_j^2}{2m} + \frac{\xi(T)}{T} \hat{p}_j - \frac{\theta(T)}{T} \right) + c \sum_{j<i} \delta(x_j - x_i). \quad (48)$$

The main point of this Section and of presentation at the talk in Benasque is that the Floquet Hamiltonian (48) is integrable, as it can be immediately seen. One can then apply the standard Bethe Ansatz techniques (see^{213,219}) to compute the quasi-energies and the eigenfunctions. More precisely, one has to compute the pseudo-momenta k_j obeying the Bethe equations. If the system is subjected to periodic boundary conditions (PBC), the pseudo-momenta k_j are determined in terms of the following Bethe equations

$$k_j L + 2 \sum_{i=1}^N \arctan \left(\frac{k_j - k_i}{mc} \right) = 2\pi \left(j - \frac{N+1}{2} \right), \quad (49)$$

for $j = 1, \dots, N$, where L is the circumference of the ring in which the system is confined. We refer to³²⁷ for a discussion on how to implement PBC in a realistic setup.

Using the previous results one can write the many-body states at the stroboscopic times. A multiparticle $|\psi\rangle$ state for the Lieb-Liniger model read (apart from the normalization factor)

$$|\psi\rangle = \int d^N x \chi(x_1, \dots, x_N, t) \times \Psi^\dagger(x_1, t) \dots \Psi^\dagger(x_N, t) |0\rangle \quad (50)$$

where $\chi(x_1, \dots, x_N, t)$ is the N -body wavefunction.

The wavefunction χ in (50) is a solution of the Schrödinger equation

$$i\partial_t \chi(x_1, \dots, x_N, t) = H \chi(x_1, \dots, x_N, t), \quad (51)$$

with H being the Lieb-Liniger Hamiltonian in first quantization

$$H = -\frac{1}{2m} \sum_{j=1}^N \partial_x^2 + c \sum_{j<i} \delta(x_j - x_i) + \sum_{j=1}^N V(x_j, t). \quad (52)$$

Using (34) one can write for the periodically driven model

$$|\psi\rangle = \int d^N y \eta(y_1, \dots, y_N, t) \times \varphi^\dagger(y_1, t) \dots \varphi^\dagger(y_N, t) |0\rangle. \quad (53)$$

The relation between the functions χ and η is given by

$$\chi(x_1, \dots, x_N, t) \equiv \prod_{i=1}^N e^{i\theta(x_i, t)} \eta(y_1, \dots, y_N, t), \quad (54)$$

where η is the solution of the same Schrödinger equation (51) but with *no* external potential ($V = 0$).

C. Summary and Outlook

The past few years have witnessed very rapid developments within the theory of integrable systems out of equilibrium. Arguably, the most important piece of progress pertains the introduction of the so-called generalized hydrodynamics (GHD)^{249,329}. This is a very powerful framework, which builds upon the techniques developed in the idealized case of homogeneous systems, and allows one to provide exact predictions also for inhomogeneous settings, although only at hydrodynamic scales.

While a review of these results is beyond the scope of the present article, we note that recent works have shown that GHD is more than adequate to tackle exactly experimentally relevant set-ups of repulsive *1D* Bose gases, including systems with confining potential^{330–333}, spatial inhomogeneities³³⁴ and dephasing noise³³⁵. In fact, quite remarkably, GHD predictions have now also been experimentally verified by monitoring clouds of bosonic cold atoms trapped on an atom chip³³⁶.

It would be extremely interesting to extend some of these recent results to inhomogeneous *1D* Bose gases with attractive interactions, where the study of homogeneous quantum quenches have already revealed unexpected new features. More generally, a promising route is to analyze the out-of-equilibrium dynamics of even more complicated inhomogeneous integrable quantum gases, such as multicomponent mixtures of fermions and bosons^{337,338}, for which the emergence of interesting phenomena at the hydrodynamic scale has been already pointed out in simple settings^{339,340}.

Going beyond quench protocols, the effect of a time-periodic tilting in the Lieb-Liniger model with repulsive interactions was discussed in the Benasque talk of the last author. It was shown that the corresponding Floquet Hamiltonian is integrable, by studying the spectrum of the quasi-energies and the dynamics of the system at stroboscopic times. Importantly, the analysis presented for the Lieb-Liniger model can

be extended to other 1D integrable systems in time-periodic linear potentials such as, for instance, the Yang-Gaudin model for fermions. In the future, motivated also by discussions in Benasque, it would be very interesting to study the effect of periodic tilting in more general configurations.

Acknowledgments: We are grateful to P. Calabrese, A. Colcelli, F. Essler, G. Mussardo and G. Sierra for several enlightening discussions on the subjects presented here and on related topics. Further acknowledgments go to the participants to the first week of the conference in Benasque, and in particular to V. Ahufinger, V. Bastidas, D. Cassettari, J. Mompart, N. Proukakis, F. Scazza and W. von Klitzing.

VII. PERSISTENT CURRENTS AND VORTICES IN ATOMTRONIC CIRCUITS

T. Bland, M. Edwards, N. P. Proukakis, A. Yakimenko

Atomtronics relies on the flow of coherent matter waves in the form of atomic Bose-Einstein Condensates (BECs) in closed circuits, such as in the form of closed toroidal traps, or more extended, race-track-like, potentials. Persistent currents in such geometries enable fundamental studies of superfluidity and may lead to applications in high-precision metrology and atomtronics^{5,114}. The question of the generation and stability of the atomic persistent currents – which in the absence of external driving should be topologically protected – is of fundamental importance; thus it has been the subject of numerous experimental and theoretical investigations^{7,22,67,109,110,128,341–357}.

The quantized circulation in a ring effectively corresponds to an m -charged vortex line pinned at the center of the ring-shaped condensate, where the vortex energy has a local minimum. Noting that there is no condensate density at that location, we can think of this as a ‘ghost’ vortex – in the sense that, at some radial distance from the centre of the closed loop where there is non-negligible superfluid density, the arising phase profile is identical to that corresponding to a vortex located at the centre, where the superfluid density is practically zero. Since such a vortex is bounded by the potential barrier, even multicharged ($m > 1$) metastable vortex states can be very robust. The generation and decay of a persistent current is governed by the dynamics of these quantum vortices, which can be deterministic, or random, depending on the particular setting considered.

Specifically, persistent currents can form in toroidal BECs by stirring the condensate with an optical paddle potential, imparting angular momentum in the ring through the generation of vortices and through the decay dynamics after an external perturbation^{7,22,67,128,342,343,347–349,351–353}. They can also be induced by transmitting angular momentum from a Laguerre-Gaussian beam^{109,110,350}. Moreover, persistent currents can also spontaneously form in toroidal BECs as phase defects appearing after a quench into the BEC state^{354–357}.

Coupled persistent currents of ultracold atomic gases provide a possibility to investigate the interaction of the superflows in a tunable and controllable environment, providing

the possibility for precision measurements and even potentially controllable quantum gate operations. Previous theoretical studies^{358–360} have drawn considerable interest to systems of coupled circular BECs. Using accessible experimental techniques, it is possible to consider a variety of physical phenomena in this setting: from Josephson effects in the regime of weak interactions (where the superflow decays by inducing phase slips reviewed in Section VIII) to quantum Kelvin-Helmholtz instability for merging rings.

In this contribution we review recent developments in the understanding of the formation and dynamics of persistent currents in such closed geometries. We start by considering the mechanism of formation of persistent currents in a race-track BEC, induced by a stirring potential (Section VII A) (which also encompasses ring-trap geometries as a special case). We then discuss more complicated atomtronic architectures, focusing on BECs trapped in two coupled toroidal potentials which are either embedded within a single plane, or are linked transversally. Specifically, we firstly review (Section VII C) recent work³⁵⁷ discussing the spontaneous formation of persistent currents in co-planar double ring geometries. We then present a brief overview (Section VII D) of recent investigations^{361–363} of the dynamics of quantum vortices in a pair of vertically stacked atomtronic circuits. We end with some concluding statements.

A. Mechanism for producing flow in a racetrack atom-circuit BEC by stirring

1. How stirring a racetrack atom circuit produces flow

We start by presenting a picture of how macroscopic flow is produced in a BEC confined in a racetrack atom-circuit by stirring with a wide rectangular barrier within the Gross-Pitaevskii model. The atom-circuit BEC is strongly confined to a horizontal plane and the 2D racetrack channel potential (see Fig. 28) consists of two half-circles separated by straightaways of length L ; we note that in the limit $L = 0$, this reduces to a ring potential, so the present discussion fully encompasses that setting.

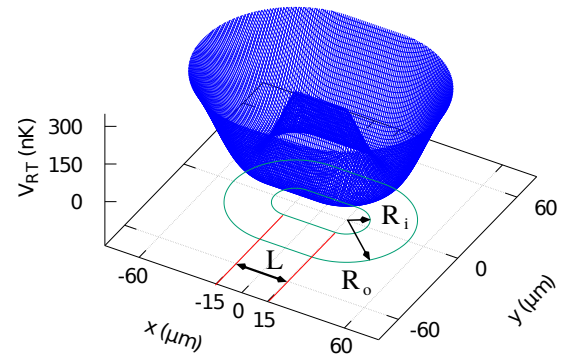


FIG. 28. The atom-circuit racetrack potential consists of two semi-circular endcaps (inner radius $R_i = 12 \mu\text{m}$, outer radius $R_o = 36 \mu\text{m}$) separated by straightaways of length L .

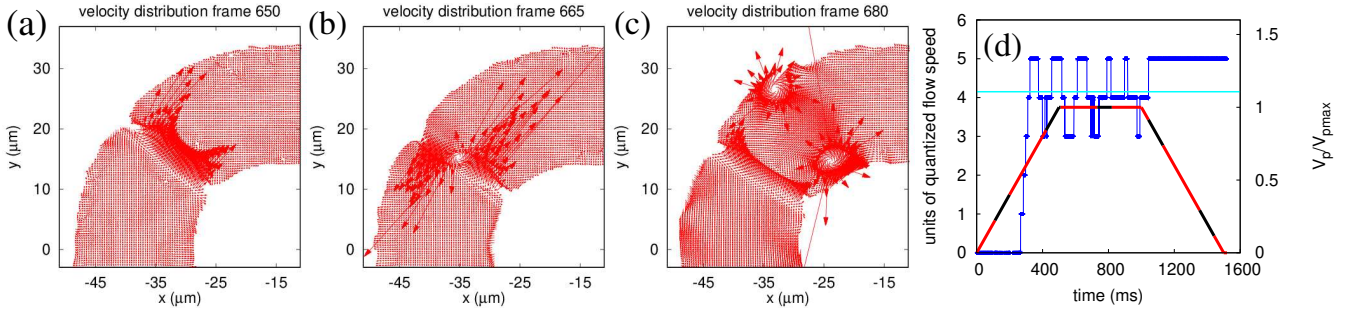


FIG. 29. Velocity distributions of the racetrack condensate during the ramp-up of the stirring. (a) A backflow plus vortex/antivortex pair develops in the barrier region, (b) the vortex/antivortex pair swap, (c) the the vortex/antivortex pair move away form the barrier in the anti-stir direction while a compression wave moves off in the stir direction. (d) Circulation around the midline track versus time for this case. Parameters: $L = 30 \mu\text{m}$, $v_{\text{stir}} = 339 \mu\text{m/s}$. Results based on Gross-Pitaevskii mean-field, so corresponding to $T = 0$ nK.

It is well-established that flow is accompanied by production and motion of vortices^{67,128,342,343} or dark solitons³⁶⁴ in the condensate. Here we describe how and where vortices form, how they move thereafter, how circulation localized to a vortex is converted into macroscopic flow around the entire racetrack, and what conditions lead to the final amount of flow.

B. Creation of a single unit of flow: vortex swap

Flow can be induced in a racetrack BEC atom circuit by stirring with a weak-link potential barrier. As the stirring barrier moves and strengthens it produces a region of lowered density. This region of depressed density causes a backflow (flow opposite the stir direction) to develop in this region. This backflow spawns a vortex (circulation same as the stir) located on the outside of the channel and an antivortex (anti-stir circulation) on the inside. At a critical value of the barrier height the two vortices swap positions. This event generates two disturbances that move away from the barrier in opposite directions at the average speed of sound. The first is the vortex/antivortex pair that moves off in the anti-stir direction and the second is a compression wave moving in the stir direction.

This backflow is illustrated in Fig. 29(a). In the full figure we have plotted a series of snapshots of the velocity distribution from shortly before until shortly after the creation of the first unit of flow. It is easy to see that the backflow speed is greatest at the inner and outer edges of the channel where the racetrack plus barrier potential is largest. As the barrier moves the condensate in front of the barrier must migrate to the back of the barrier. The atoms at the inner and outer channel edges must move faster to avoid the regions of high potential. In this way vortices are formed by stirring with a barrier that is much wider than the stirred condensate.

When the height of the barrier reaches a critical value, the vortex migrates from the outside to the inside of the channel as can be seen in Fig. 29(b). Shortly after this vortex swap two disturbances are generated. The first is the vortex/antivortex pair, located on the inside and outside of the channel respectively, move away from the barrier in the anti-stir direction.

This vortex pair causes atoms on the anti-stir side of the barrier to flow in the stir direction between the vortices. The second disturbance is a compression wave that propagates away from barrier region in the stir direction. This compression wave also moves atoms in the stir direction. Both disturbances move at a speed that is approximately the local speed of sound ($c(\mathbf{r}) = \sqrt{gn_c(\mathbf{r})/m}$) averaged over the cross section of the condensate. These disturbances are the mechanism by which the localized circulation in the form of a vortex is converted into macroscopic flow around the entire racetrack.

1. Final flow production: flow overtakes the barrier

The final circulation produced can be roughly predicted as the number of units of quantized flow that lies closest to the speed of the stirring barrier. The exact number depends on the details of the stirring and the geometry of the racetrack as we describe below. When vortices inside the racetrack potential are generated the circulation they provide is localized near their cores. As stirring proceeds this circulation is converted into a nearly constant tangential velocity component around the midline track by the pair of disturbances generated each time a vortex swap occurs.

The circulation as a function of time is shown in Fig. 29(d) for the case where $L = 30 \mu\text{m}$, $v_{\text{stir}} = 339 \mu\text{m/s}$ and, $T = 0$ nK). This graph shows that the circulation (shown as the blue curve) is zero until a succession of vortex-swap events produces enough flow so that the flow generated is greater than the speed of the stirring barrier (shown as the cyan horizontal line in the figure in quantized flow speed units).

In this case, five units of flow exceeds the barrier speed by almost a full flow speed unit. When the disturbance pair generated by the first vortex swap travels around the racetrack and comes back to sweep through the barrier region again they cause a *forward flow* to develop in the barrier region. At this moment an inverse vortex swap event can occur causing the total circulation to decrease by one unit. In this way the circulation can oscillate around the number of units that makes the flow closest to the stir speed of the barrier.

Another circulation-changing mechanism that is only

present in the non-ring racetrack case occurs when the barrier transitions from straight parts of the racetrack to curved parts or vice-versa. The times when the barrier is on straight or curved parts are indicated in Fig. 29(d) by the red- and black-colored curve that depicts the barrier height. This graph is colored red for times when the barrier is on the curved parts of the racetrack and black-colored when it is on the straightaways. Careful examination of the circulation graph shows that, when the barrier transitions from curved to straight (red to black) racetrack parts, the circulation increases by one unit. When the barrier transitions from straight to curved parts the circulation decreases by one unit. We also note that this only happens when the barrier strength is above a critical value.

The general mechanism for flow production in the racetrack by stirring with a rectangular barrier in the context of the Gross-Pitaevskii equation can thus be summarized as follows. The stirring barrier both moves and increases in strength. This generates a backflow in the region of depressed density. This backflow is fastest at the inner and outer channel edges in this region. This flow spawns a vortex/anti-vortex pair at the outer and inner edges, respectively. Eventually these two vortices swap locations generating a moving vortex (now on the inner channel edge)/anti-vortex (now at the outer edge) pair that moves away from the barrier in the anti-stir and also generating a compression wave that moves away from the barrier in the stir direction. These disturbances both move at the average speed of sound. The total amount of flow produced is roughly the number of flow-speed units closest to the speed of sound.

C. Persistent Currents in Co-Planar Double-Ring Geometries

Having identified the key mechanism for flow production in the context of a pure $T = 0$ BEC, it is natural to also consider the role of phase fluctuations and dissipation on the (spontaneous) emergence of supercurrents, and what happens when multiple ring-trap geometries are coupled.

1. Spontaneous Persistent Current Formation in a Ring Trap

The formation of persistent currents in a ring trap can also proceed spontaneously; it is well-known that the generation of a superfluid in such a geometry can carry with it a randomly-generated winding number, which is expected to be statistically distributed about the most probable ‘zero’ (0) value [which corresponds to the absence of a persistent current]^{354,356}. This is because phase coherence forms locally in a ring, and the size and width of the toroidal geometry, along with the rate of the actual quench leading to the formation of the ring-trap condensate, control the maximum winding number that can spontaneously emerge^{347,357}.

This is already well-known in the context of the Kibble-Zurek mechanism^{365,366}, which relates the generated winding number to the quenching rate of the driven phase transition, an effect already discussed and observed across different physi-

cal systems. Among those, this effect has also been confirmed in ultracold atoms in ring-trap geometries through a controlled gradual cooling rate quench, producing an experimentally observed distribution of winding numbers³⁵⁴, in agreement with numerical and theoretical expectations³⁵⁷. In fact, the local nature of such coherence evolution implies that this effect of spontaneous persistent current generation already manifests itself even in the limit of very rapid (or instantaneous) quenches towards a coherent superfluid regime. The existence of phase fluctuations and non-zero winding numbers can, for example, affect the dynamics of otherwise deterministically-generated dark solitons in ring-trap geometries³⁶⁷.

2. Spontaneous Persistent Current Formation in Co-Planar Connected Ring Traps

Next, we turn our attention to the dynamics of winding numbers in connected geometries, focusing here on the simplest possible such co-planar example, based on the 2D geometry shown in Fig. 30(a). Utilizing state-of-the-art numerical simulations based on the stochastic (projected) Gross-Pitaevskii equation^{356,357,368–375}, we find that – as in the case of a single ring trap – coherence within the double-ring trap forms locally during condensate growth, as shown in Fig. 30(b).

After a quench, the phase develops locally along and across the ring circumference³⁵⁶, with an early such example of typical evolution shown by the phase profile of Fig. 30(b)(iv). Although at the common interface around $x \sim 0$ (where the trap depth has the same depth and width as the outer double-ring edges) the phase of the superfluid is constrained to be the same in both connected rings, this does not nonetheless dictate the behaviour of the emerging phase in the remaining ‘unconnected’ regions forming the bulk of the ring’s spatial extent. Specifically, the ‘unconnected’ regions in the double-ring geometry are free to randomly establish their own phase dynamics (constrained by the size and width of the unconnected regions), thus often leading to non-zero winding numbers with varying (nonlinear) phase gradients across the ring circumference.

An example of such long-term behaviour with winding numbers -1 and $+2$ across the left and right rings respectively, is shown in Fig. 30(b)(vi), with a positive winding number referring arbitrarily, by convention^{348,357}, to clockwise rotation. In the double-ring case, we also find a distribution of winding numbers about the most probable value of zero net winding number, as shown in Fig. 30(c). In fact, when integrating over the winding numbers of the other ring, we find that (in our chosen, experimentally-relevant, geometry), the distribution of winding numbers in each ring actually exactly matches that of the single ring trap with the same radius, width and depth³⁵⁷. We expect this to be true for the majority of experimentally-relevant potentials, for which the ring radius typically largely exceeds any transversal width (and motion is frozen out in the third, transverse, direction).

Remarkably, our previous work³⁵⁷ has shown such features to be largely independent of the exact details of the

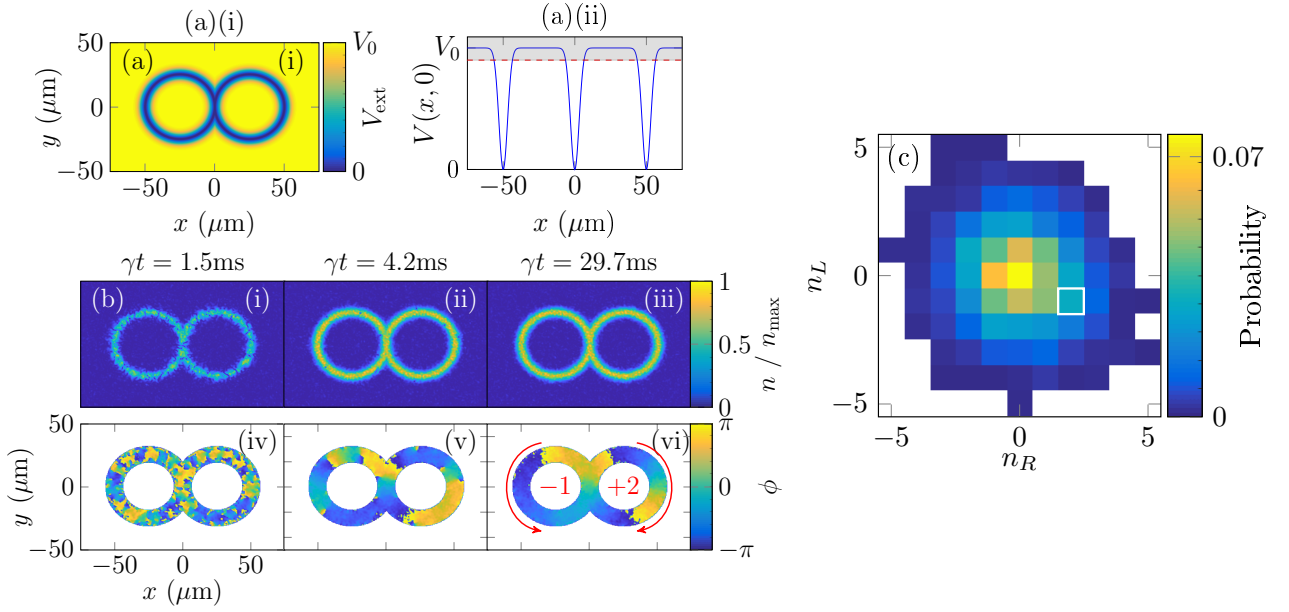


FIG. 30. (a) Simplest co-planar connected double-ring geometry: Shown are (i) the 2D potential, and (ii) the cut through $y = 0$. Note that the interfacial potential considered here is identical to that of the outer unconnected regions of the rings. (b) Formation dynamics of characteristic numerical realization with different winding numbers across the two rings: shown are growing density (from a noisy initial configuration; top row (i)-(iii)) and corresponding phase evolution (bottom row, (iv)-(vi)), for a characteristic example with distinct winding numbers $n_{\text{left}} = -1$ and $n_{\text{right}} = +2$ across the left and right rings respectively. (c) Histogram of all possible steady-state winding number contributions, when performing numerical quenches from an initial noisy configuration. The indicated white box highlights the case $(n_{\text{left}}, n_{\text{right}}) = (-1, +2)$ considered in (b). We have explicitly verified that once such an unequal winding number contribution forms after sufficient system relaxation/equilibration, it does remain stable for all subsequent evolution (with this feature also found to be insensitive to the precise choice of the ‘growth’ parameter γ in the stochastic simulations). Parameters: $N \sim 2 \times 10^5$ ^{87}Rb atoms, $T = 10\text{nK}$, effective 2D interaction strength $\tilde{g} = 0.077$; Tight harmonic transverse confinement with $\omega_z = 2\pi \times 1000\text{Hz}$, with the 2D potential defined by $V(x, y) = V_0 \min \left(1 - \exp \left[-2(\rho(x - R, y) - R)^2 / w^2 \right], 1 - \exp \left[-2(\rho(x + R, y) - R)^2 / w^2 \right] \right)$, where $\rho(x, y) = \sqrt{x^2 + y^2}$, $V_0 = 1.1\mu$, the ring radius is $R = 25\mu\text{m}$ and its width is $w = 6\mu\text{m}$.

connected geometry, provided it does consist of two (2D) planar-connected closed geometries with a unique single (extended) connected region. For example, we have verified all above conclusions to be also valid in a figure-of-eight (‘lemniscate’) potential, where there is a real crossing in the path of propagating ultracold atoms³⁵⁷. By extension, we would therefore expect similar features to hold in extended or ‘flattened’ geometries, such as connected race-track geometries, as the underlying physics is that of how much winding can be supported by the combination of loop radius R and width w , which are found to obey the winding number relation $\langle |n_w| \rangle \sim \sqrt{2\pi R/w}$ ^{356,357,366}.

Given the potential independence of winding numbers supported across two identical connected ring traps, it is interesting to enquire about the stability of such features. Essentially, one can think of a winding number of, say, $\pm n$ (where $n = 0, 1, 2, \dots$) around a closed loop (whether exactly ring-shaped, or not), as being due to the existence of a ‘ghost’ vortex trapped in the middle of the closed loop. Using such an intuitive interpretation, the winding number of a ring trap can only change by an integer unit if such a ‘ghost’ vortex is allowed to leave its enclosure, mapped out by the underlying trap potential. As the winding number is topologically protected, such an effect can only be achieved by deforming the

system topology through a change in the trap potential: in the single ring-trap case, this would amount to opening a small hole in the potential, such that the enclosed ‘ghost’ vortex can escape to the region outside of the ring.

In the double-ring geometry, we have explicitly verified that the transfer of the winding number from one side of the double-ring geometry, to the other can be facilitated by allowing for a zero-potential region to connect the two sides. Such a transfer can be reasonably controlled by the specific details of the potential deformation, even potentially leading to the annihilation of oppositely-oriented superflows (corresponding to ‘ghost’ vortices of opposite circulation, which can hence annihilate), a topic of active ongoing research investigations to harness potential atomtronic applications. Our present work for interacting superfluids adds to that of tunnelling angular momentum states considered at the single-particle level in single-component condensates^{376–378} and also for two-component condensates³⁷⁹.

Although work discussed here has been restricted to a coupled geometry with a single extended interface, once such transfer process becomes reasonably controlled for multi-particle systems, one may envisage possible extensions to multiple connected closed-loop geometries (whether ring-shaped, race-track, or related), with the aim of determinis-

tic transfer of winding numbers across a multiple-loop atomtronic architecture. Research into this promising direction is currently very active by the present authors.

Next, we discuss coupled persistent current dynamics in an alternative geometry of two transversally stacked ring-trap potentials connected by tunneling.

D. Persistent Currents in Transversally coupled atomtronic circuits

Here we briefly overview our recent findings^{361–363} on dynamics of quantum vortices in two coupled vertically stacked toroidal condensates with persistent currents (see Fig. 31 (a)).

In the experiment, the double-ring system with different angular momenta in its top and bottom parts may appear spontaneously as a result of cooling, with different momenta, m_1 and m_2 , being frozen into the two rings after the transition into the BEC state, similar to spontaneous persistent current formation in co-planar coupled rings, described in Sec. VII C. The asymmetry of the density distribution in the top and bottom rings makes it possible to excite the vorticity also by applying a stirring laser beam, similar to the mechanism described in Sec. VII A. Generating a vortex in the lower-populated ring only, keeping the higher-populated one in the zero-vorticity state is illustrated in Fig. 31 (b).

In our recent work³⁶¹ it was demonstrated that the azimuthal structure of the tunneling flows in double-ring system with topological charges m_1, m_2 implies formation of $|m_1 - m_2|$ Josephson vortices, also known as rotational fluxons. The azimuthal structure of the tunneling flow (see the inset in Fig. 32 (a)) implies zero net (integral) current through the junction for hybrid states ($m_1 \neq m_2$), built of persistent currents with different topological charges in coupled rings. In particular, these include the case of opposite topological charges ($m_1 = -m_2$) – hybrid states³⁸⁰. It turns out that the fluxons' cores rotate and bend, following the action of the quench, i.e. formation of tunnel junction with chemical potential difference. It was found in Ref.^{361–363}, as the barrier decreases, and the effective coupling between the rings respectively increases, the Josephson vortices accumulate more and more energy. When the persistent currents merge the relaxation process to new equilibrium state is driven by 3D dynamics of interacting Josephson vortices and vortex lines of the persistent currents (see for example Fig. 32 (b)).

In our simulation of the merging rings we have used the dissipative Gross-Pitaevskii equation in the form:

$$(i - \gamma)\hbar \frac{\partial \psi}{\partial t} = -\frac{\hbar^2}{2M} \nabla^2 \psi + V_{\text{ext}}(\mathbf{r}, t) \psi + g|\psi|^2 \psi - \mu \psi, \quad (55)$$

where $g = 4\pi a_s \hbar^2 / M$ is the coupling strength, M is the atomic mass ($M = 3.819 \times 10^{-26}$ kg for ^{23}Na atoms), a_s is the s -wave scattering length (positive $a_s = 2.75$ nm, corresponding to the self-repulsion in the same atomic species, is used below), μ is the chemical potential of the equilibrium state, and $\gamma \ll 1$ is a phenomenological dissipative parameter. This form of the dissipative GPE has been used extensively in previous stud-

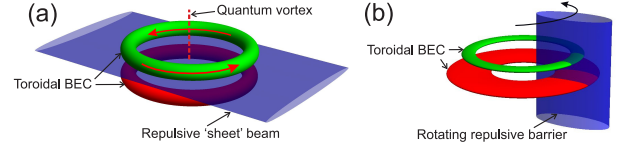


FIG. 31. (a) Schematics of the coupled ring-shaped condensates. Coaxial rings separated by repulsive potential, allowing investigation regime of tunneling coupling (long Josephson junction) and regime of merging rings (when the barrier is eliminated). (b) Schematics of preparation of the state with different angular momenta in double-ring system. Coaxial rings with different number of atoms are stirred by a rotating potential barrier. A persistent current is generated in a less populated ring (shown by green) while more populated toroidal condensate (shown by red) remains in non-rotating state.

ies of vortex dynamics (see, e.g.,^{342,344,346,371,381}). Note that main results of our work, concerning the role of the symmetry breaking in the interacting superfluids rings are not sensitive to the weak dissipative effects. We demonstrated in our works^{362,363} that the symmetry of the system is the key feature explaining remarkable properties of the interacting quantized superflows. Certainly, the symmetry is in no way related to details of the dissipative terms. We have found that the subsequent relaxation process is determined by the initial stage of the evolution of the merging ring, in the course of several first microseconds after the barrier was switched off. Obviously, an effect of the weak dissipation on these fast processes is practically negligible. The dissipation plays a significant role in the course of subsequent temporal evolution of the condensate. In fact, in most experiments in-situ observation of the vortices is not possible, and only the final state can be analyzed after the completion of the relaxation. We include the dissipative effects in our model to investigate the final states of the merging superflows, which can be directly compared with expected experimental observations.

The relaxation of the merging rings is driven by substantially 3D nonlinear dynamics of the vortex lines corresponding to persistent currents and Josephson vortices, as illustrated in Fig. 32 (b). It turns out that the final state of the condensate crucially depends on an initial population imbalance in the double-ring set, as well as on the shape of the 3D trapping potential, oblate or prolate³⁶³. In the oblate (axially squeezed) configuration, a ring with non-zero angular momentum can impose its quantum state onto the originally non-rotating ring only above a well-defined critical value of the population imbalance.

Surprisingly, merging counter-rotating flows in the axially-symmetric trap *never evolve towards the non-rotating ground state*, with $L_z = 0$, even for small imbalances, $P \ll 1$ (see Fig. 32). The vorticity of the final state is imposed by the *less populated component* if $P < P_{cr} \approx 0.1755$, and by the stronger component if $P > P_{cr}$. These counter intuitive results are explained in Ref.³⁶² by the symmetry of the system.

Instead of the development of the classical Kelvin-Helmholtz instability at the interface of the merging persistent currents in a prolate potential trap, sufficiently elongated

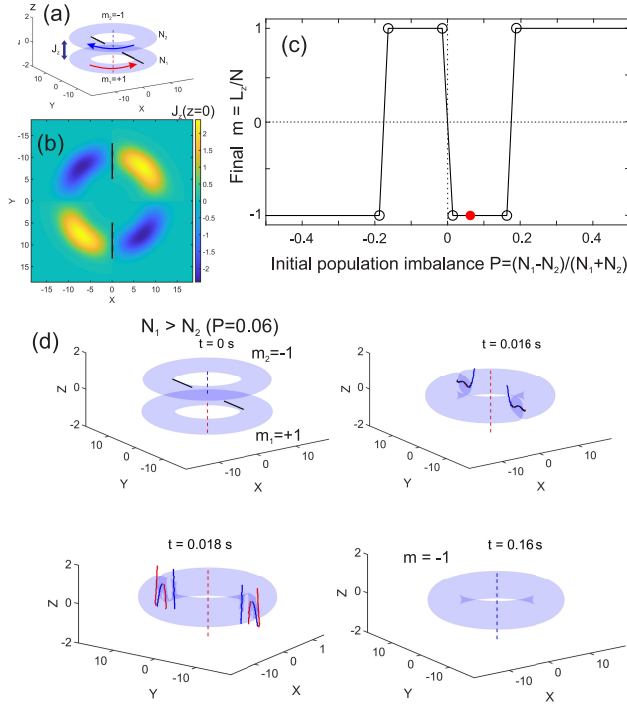


FIG. 32. Coupled coaxial superfluid atomic circuits with counter-propagating persistent currents. Hybrid vortex stationary states with hidden vorticity. (b) Density isosurfaces and (c) z -component of the corresponding tunnel-flow density distribution through the barrier, $J_z(x, y, z = 0)$. The cores of the Josephson vortices are indicated by solid black lines. (c) The final value of the total angular momentum per particle L_z/N for the merging rings with initial vorticities $(+1, -1)$ as a function of initial population imbalance $P = (N_1 - N_2)/(N_1 + N_2)$. Vertical red and blue dashed lines designate cores of the counter-propagating persistent currents in the two rings³⁶¹. (d) The evolution of the merging rings in oblate trapping potential. The barrier separating two rings is switched off at $t > t_d = 0.015$ s, dissipative parameter $\gamma = 0.03$. Red (blue) lines indicate positions of the vortex (antivortex) core. The population of the bottom ring, with vortex $m_1 = +1$, is slightly larger than in the top one, with antivortex $m_2 = -1$ [initial imbalance parameter, $P = 0.06$, is indicated by filled red circle in (a)]. The final state has $m = -1$. The symmetric drift of two diametrically opposite antivortices towards the central hole leads to subsequent annihilation of the central vortex and relaxation of the toroidal condensate into a final *antivortex* $m = -1$ state³⁶².

in the axial direction, we observe the formation of nonlinear robust hybrid vortex structures (as illustrated in Fig. 33 and explained in Ref.³⁶³).

Thus, the ring-merging process and topological charge of the final state can be controlled by the perturbation of the trapping potential, specially adapted for the initiation of symmetry-breaking of the system, and by tuning of the initial population imbalance^{362,363}.

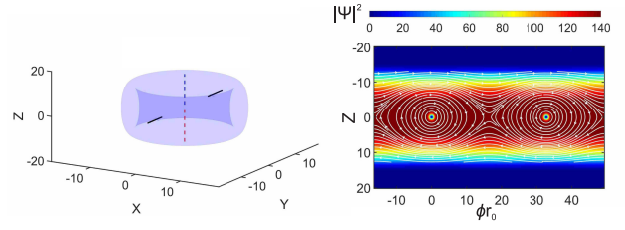


FIG. 33. A long-lived hybrid complex is produced by the evolution of merging strongly elongated toroidal condensates found in Ref.³⁶³. Shown are 3D isosurface with constant condensate density (left) and maps of the distribution of the density (right) on the cylindrical surface at the radius corresponding peak density of the condensate, ϕ being the angular coordinate.

E. Summary and future challenges

We have reviewed our current understanding of the spontaneous and controlled formation and stability of persistent currents in basic atomtronic circuits consisting of single or coupled ring-trap potentials and extended racetrack potentials. The control over quantum topological excitations in such geometries offers an outstanding route to emerging quantum technologies with applications ranging from novel types of quantum sensors for acceleration and rotation to topologically protected fault-tolerant quantum computation. However, more theoretical and experimental work is needed for reaching a reliable method for engineered generation, transport, and gate-like manipulation of the quantum topological excitations in atomtronic circuits.

Acknowledgments. ME acknowledges substantial contributions from Ben Eller and Olatunde Oladehin. This work was supported in part by the US National Science Foundation grant no. PHY-1707776. TB and NP acknowledge contributions by Paolo Comaron, Quentin Marolleau, and Boris Malomed, and discussions with Veronica Ahufinger, Jordi Mompart, Jerome Beugnon, Jean Dalibard, Muntsa Guilleumas and Fabrizio Larcher. TB would like to thank support from the EPSRC Doctoral Prize Fellowship Grant No. EP/R51309X/1, while TB and NP acknowledge financial support from the Quanterra ERA-NET cofund project NAQUAS through the EPSRC, Grant No. EP/R043434/1. AY acknowledges contributions from Boris Malomed, Artem Oliinyk, and Igor Yatsuta.

VIII. PHASE SLIPS DYNAMICS IN RING SHAPED CONDENSATES

A. Minguzzi, A. Perez-Obiol, J. Polo, N. P. Proukakis, K. Xhani

The phenomenon of superfluidity and its consequences can reveal itself in different ways in a quantum gas. One of the most remarkable manifestations of superfluidity is the frictionless motion of particles within the fluid, which is in direct relation with the macroscopic quantum phase coherence of the fluid. However, in certain circumstances this frictionless motion can be broken, with dissipation taking over. Phase

slips represent one of the fundamental mechanisms leading to dissipation in superfluid systems^{128,352,382–386}. Therefore, understanding phase slip processes can prove crucial for the development of quantum technologies and, in particular, Atomtronic devices. Currents in ring geometries are ideal candidates for the study of superfluidity in interacting quantum gases. In particular, these currents are metastable states that can maintain the flow of particles even when no external field or force is applied. However, these metastable states can decay in different scenarios. Examples of dissipative motion have been observed in hysteresis dynamics^{7,128,343,387,388} where thermal activation plays an important role³⁸⁹. In addition, phase slips can also be triggered by an external mechanism, for instance a weak link can catalyze the production of vortices at zero temperature³⁹⁰. It has been shown that thermally activated phase slips can become dominant in the damping dynamics of some observables, at relatively low temperatures^{349,391}.

Recent studies have demonstrated the connection between the dissipative motion observed in Josephson systems and phase slips^{386,392–394}. In this case, vortex nucleation can be triggered through the weak link producing the Josephson-like junction³⁹⁵ or through thermal activation, depending on the range of parameters. In a similar case, the connection between low-energy excitations and dissipative motion was proven to be the main mechanism³⁹⁶ leading to the damping of Josephson oscillations³⁹⁷.

In this chapter, we present recent developments in the topic of phase slips and their role in the dissipative dynamics of observables such as population imbalance of Josephson systems and current dynamics in ring potentials. Special attention is given to the nonlinear excitations of the different systems, such as vortex rings and dark solitons. In the following sections we summarize different studies that illustrate how phase slips can emerge in Atomtronic devices and isolated quantum systems.

Section VIII A is devoted to the study of nucleation of vortex rings in a weakly linked three-dimensional elongated superfluid. In Sec. VIII B we consider the damping of Josephson oscillations in a one-dimensional (1D) strongly interacting Bose gas. Section VIII C is dedicated to the excitation spectrum of a 1D stirred Bose gas. Section VIII D focuses on the dynamical phase slips occurring in a phase imprinted Bose gas trapped in a ring potential. Finally, in Sec. VIII E–VIII F we present the conclusions and outlook, summarizing and discussing how phase slips play a crucial role on Atomtronic-based devices.

A. Critical transport and vortex dynamics in a thin atomic Josephson junction

We start our analysis by giving an intuitive picture of the emergence of phase-slips in a full three-dimensional (3D) atomtronic geometry, consisting of a single Josephson junction in a harmonically-trapped superfluid. This has been analysed in great detail in the context of an elongated superfluid, where a carefully characterised experiment^{386,392} has enabled

us to not only make connections between microscopic and macroscopic observables and manifestations, but also to link those directly to experimental observables, thus fully clarifying the emerging physical picture via *ab initio* simulations³⁹³, in a regime beyond the validity of the simple 2-mode model³⁹⁸ of Josephson junctions.

The relevant experiment was conducted in Florence^{386,392}, in the context of an elongated ${}^6\text{Li}$ fermionic superfluid, separated by a thin Gaussian barrier induced by a focussed laser beam located at $x = 0$ and of $1/e^2$ width $w \sim 4\xi \sim 2\mu\text{m} \ll R_x \sim 110\mu\text{m}$, where ξ (R_x) denotes the superfluid healing length (axial system size). The experiment probed all regimes of values of $(k_F a)^{-1}$, where k_F denotes the Fermi wavevector and a the s-wave scattering length. Although relevant and subtle differences were observed when transitioning from the BEC to the BCS superfluid regimes – mainly associated with different critical velocities and spatial extents due to the changing interaction dependence and the increasing importance of the fermionic degrees of freedom –, the key underlying physical process leading to dissipation of superflow was found to be the same in all regimes: The initial population imbalance across the two wells separated by the barrier (initiated by moving the superfluid relative to the barrier at $t = 0$) induced a neutral current flow in the negative x -direction. As a result of this flow, the magnitude of the population imbalance decreases in time as the particles are transferred from the right to the left well. At sufficiently long evolution times, small values of population imbalance were found to lead, as expected, to symmetric Josephson ‘plasma’ oscillations about a zero population imbalance, and associated oscillations in the relative phase^{398,399}. Nonetheless, when the fractional population imbalance exceeded a critical value, the system population dynamics transitioned to a different regime. Based on earlier experiments with ultracold Josephson junctions^{384,400,401}, one may have expected a transition to a so-called macroscopic quantum self-trapping regime, in which the population transferring oscillations proceed around a non-zero value of the population imbalance (i.e. one side of the junction always has a higher population than the other), and with a running phase^{398,399}; the existence of such a regime has been argued to be related to the presence of a vortex ring in the barrier region^{402,403}. Specifically in our case – and in particular during the first part of the dynamical evolution when particle flow is still in a single direction – and for sufficiently large population imbalances, the very narrow nature of the barrier⁴⁰⁴ was found to induce a local superfluid flow which accelerates in time and exceeds the local critical velocity for vortex excitation which, in this geometry, takes the form of a vortex ring excitation. As a result, the presence of a Josephson current flow led to the generation of a vortex ring, associated with a phase jump of 2π across the axial direction. Such a phase slippage process is well documented in related contexts of Josephson junctions in superfluids and superconductors^{382,383}, where it can be described in terms of *phenomenological* models.

Here we shed more light to this process in a highly controlled environment of an ultracold atomic gas, performing detailed numerical simulations of the full 3D Gross-Pitaevskii equation describing the low-temperature regime of

a weakly-interacting condensate. Our key findings are clearly highlighted in Fig. 34, based on experimental parameters of Refs.^{386,392} in the molecular BEC regime. More details about this phase-slip process and the associated acoustic emission – which can actually amount to a significant fraction of the total flow energy – can be found in³⁹³.

The fractional population imbalance z_{BEC} across the junction starts at a positive value (i.e. right well has higher population than left well), and initially decreases due to the induced Josephson dynamics which induces (initial) superflow towards the left side of the junction (Fig. 34(a)). However, as the fractional population imbalance decreases at an increasing rate, implying an increase in the superfluid velocity (and corresponding superfluid current), there comes a point when the magnitude of the superfluid velocity exceeds some threshold value (loosely set by the mean speed of sound shown by the horizontal dashed line in Fig. 34(b)), acquires a temporally local maximum value, as a result of which it becomes energetically favourable for a vortex ring excitation to be generated at the barrier at $x = 0$. Such a process is associated with an abrupt jump of $\sim 2\pi$ in the condensate relative phase, as shown in Fig. 34(c). The vortex ring generation instantaneously opposes the population transfer (leading to the flattening of $z_{\text{BEC}}(t)$ visible in Fig. 34(a)), and can even lead to a reversal of the background superflow (i.e. $-\langle v_x \rangle$ changing sign in Fig. 34(b)) due to the additional ‘swirling’ velocity of the induced vortex ring. The vortex ring, initially generated (as a ‘ghost’ vortex) in the low density region outside the local transversal spatial extent of the BEC, remains initially within the axial barrier region $x_{\text{VR}} \sim 0$ (Fig. 34(d)), shrinking transversally (Fig. 34(e)) and entering the Thomas-Fermi radius. After a short time, the accelerating vortex ring reaches the axial edge of the barrier (the superfluid density maximum is located at $x_{\text{VR}} \sim 2w$) and starts travelling at a constant speed (linear part of decreasing $x_{\text{VR}}(t)$), while maintaining its radius. A detailed instructive visualization of the overall superfluid geometry and the narrow nature of the barrier region can be found in Fig. 34(f)-(i), which also displays the vortex ring generation and initial dynamics.

The long-term dynamics after the generation of a vortex ring from the decay of the superflow depends critically on the system parameters. If the initial population imbalance is relatively weak (but still above the required threshold for defect-inducing decay of superflow), a single (small, short-lived) vortex ring may be generated. However, in cases of larger initial population imbalance, after the first vortex ring has been generated and left the central region, the background superflow due to the remaining population imbalance, i.e. chemical potential difference, picks up its pace (around $t \sim 13\text{ms}$ in Fig. 34(b)), until at some time later, when the previously generated vortex ring has already travelled a (potentially significant) axial distance from the barrier region, it once again exceeds the local critical speed and a second vortex ring is generated (around $t \sim 16.3\text{ms}$). This process can repeat itself, leading to even more vortex ring generation, until (due to the decreasing population imbalance) the background flow weakens to the point that it can no longer exceed the critical velocity. A generated vortex ring eventually decays either by

shrinking into a rarefaction pulse during its axial propagation (as relevant for the case considered here), or by interacting with the transversal condensate boundaries as the transversal spatial extent decreases during its propagation towards the axial condensate edge³⁹³. In cases of high initial population imbalance, the time window between successive vortex ring generation events (depending on $\hbar/\Delta\mu$ with $\Delta\mu$ being the chemical potential difference between the two wells) can be shorter than the vortex ring lifetimes, allowing the co-existence of multiple sequentially-generated vortex rings, and their interaction, which significantly complicates the long-term dynamics of the population imbalance.

The experimental observations^{386,392} are consistent with the picture described here. More concretely, the experiments led to the observation of one, or more, individual vortices, seen after removing the barrier (an added experimental complication required for imaging purposes), allowing the system to evolve and expand. This is consistent with the underlying picture described above, upon detailed consideration of the transversally asymmetric nature of the potential (which leads to excited, non-circular, vortex rings exhibiting Kelvin wave excitations), inherent fluctuations (which lead to asymmetric generation, propagation and decay of the vortex rings, and can thus explain the presence of single/odd-number-of defects in experimental expansion images) and dynamical barrier removal (which is found to significantly extend the lifetime of generated vortex rings)³⁹³.

We have also considered the role of temperature and thermal fluctuations by means of a self-consistent (‘ZNG’) kinetic theory^{371,374,375,405}, in which the condensate is described by a dissipative Gross-Pitaevskii equation which explicitly includes friction and collisional population transfer with the thermal cloud, the latter being treated by a quantum Boltzmann equation. We found that the presence of small thermal fluctuations does not significantly influence the above vortex generation process, although we have observed that a high enough temperature can in fact induce *additional* thermally-activated vortex rings; examples of the latter behaviour in the one-dimensional context are discussed by means of a different finite-temperature model in Sec. VIID below. Beyond the initial generation process, thermal effects were found³⁹³ to have a significant role on the long-term vortex dynamics, where they act both to destabilize the otherwise symmetric motion of the vortex ring through the introduction of fluctuations, and to damp the motion through a mutual friction damping mechanism^{406,407}.

The process we have discussed here is generic, and applies to any geometry and dimensionality, even though specific details will vary. For example, in the case of one-dimensional systems (see Sec. VIIB and Sec. VIID), the underlying defects generated are dark solitons, with the corresponding dynamics in ring traps of direct relevance to atomtronics discussed in Sec. VIIC. Similar findings have also been discussed in the context of an atomtronic ‘dumbbell’ circuit consisting of two reservoirs connected by a configurable linear channel of variable length and width³⁹⁵.

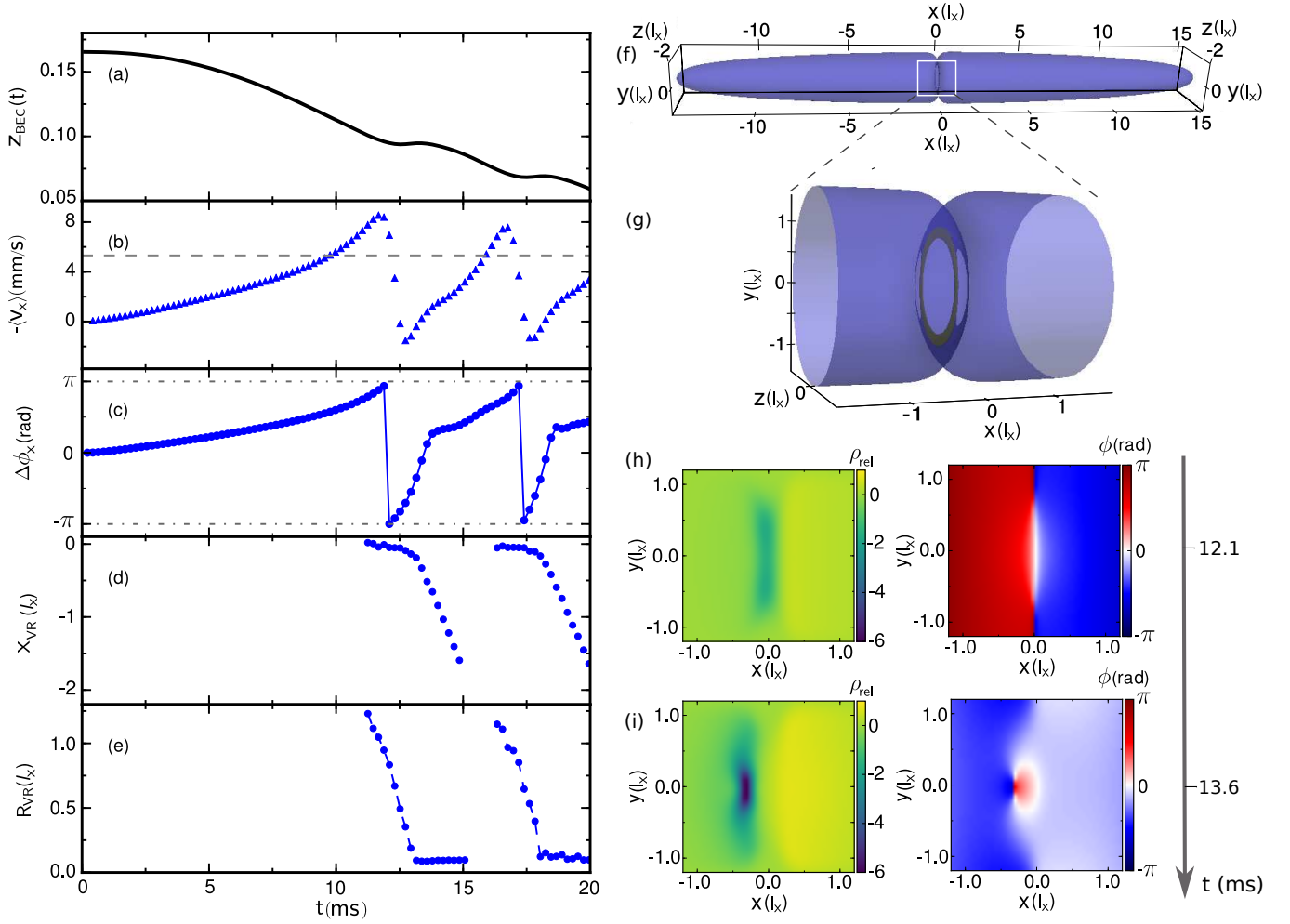


FIG. 34. Characterization of phase slip process and subsequent vortex ring dynamics in a weakly-interacting elongated 3D condensate: (a) Fractional population imbalance $z_{\text{BEC}} = (N_R - N_L)/(N_R + N_L)$ across a thin Josephson junction against time. (b) Induced superfluid velocity along x , weighted over the transverse density in the $x = 0$ plane. (c) Induced superfluid relative phase along x , evaluated at $z = 0$, $y = 0.8l_x$, corresponding to the vortex ring semi-axis along the y direction at $t = 12.1$ ms (see subplots (g)-(h)). (d)-(e) Corresponding position x_{VR} and mean radius R_{VR} of the generated vortex rings as a function of time. (f)-(g) 3D density profile (density isosurface taken at 0.002 of maximum density) at $t = 12.1$ ms, revealing the superfluid geometry and narrow barrier, along with a zoom-in to the highlighted central region (enclosed within the white rectangle in (f)) where the generated vortex ring (green near-circular structure) becomes clearly visible. (h)-(i) Corresponding planar ($z = 0$) 2D snapshots of the condensate density (left) after subtracting the background density and scaled to its maximum value, and phase profiles (right) revealing the emergence and early dynamics of the first generated vortex ring at the indicated times. Spatial axes are plotted in terms of the harmonic oscillator length along the x -axis, $l_x \simeq 7.5 \mu\text{m}$. Parameters for this figure³⁹³: $N_{\text{BEC}} = 60,000$ bosonic ^6Li molecules, $1/(k_F a) \simeq 4.6$, $z_{\text{BEC}}(t = 0) = 0.17$, $\omega_x \simeq 2\pi \times 15$ Hz, $\omega_y \simeq 2\pi \times 187$ Hz, $\omega_z \simeq 2\pi \times 148$ Hz (cigar-shaped trap), based on a double-well potential defined by $V_{\text{trap}}(x, y, z) = (M/2)(\omega_x^2 x^2 + \omega_y^2 y^2 + \omega_z^2 z^2) + V_0 e^{-2x^2/w^2}$, where $M = 2m$ is the molecular mass, $V_0 = 0.8\mu$ is the height of the Gaussian barrier and $w \approx 2.0 \mu\text{m}$ is the barrier $1/e^2$ width.

B. Bose-Josephson junction among two one-dimensional atomic gases: a quantum impurity problem

The one-dimensional (1D) geometry in ultracold Bose gases provides an ideal physical platform for the study of the quantum dynamical behavior of Bose-Josephson junctions, as the low dimensionality of these systems leads to the enhancement of quantum fluctuations and correlations. Recent experiments have realized and studied the 1D strongly interacting

regime by using quasi-one-dimensional cigars-shaped potentials in which the transverse motion of the particles is effectively frozen^{320,397,408–412}. One-dimensional systems present features that clearly separate them from the higher dimensional ones, especially in the strongly interacting limit where the motion of the particles is defined principally by its collective behavior. This collective motion is tightly connected to the low-energy excitation spectrum of the gas and to the origin of phase slips in these systems. In this section, we will present our study of the microscopic origin of phase slips

in 1D Josephson junctions, consisting of two weakly-coupled strongly correlated Bose gases.

Model: The intermediate and large interaction regimes of a 1D Bose gas are difficult to treat, both numerically and analytically, due to the many-body character of the system. Using the Luttinger liquid (LL) theory⁴¹³ we can calculate the low-energy dynamical response of two strongly interacting one-dimensional bosonic fluids confined within an effective 1D waveguide of length L , tunnel-coupled through a weak link created by a barrier. In particular, we will study the system's response to a quench in the particle number difference between the two subsystems. By using a mode expansion of the density fluctuation and phase field operators from the LL theory (see³⁹⁶), and by defining the relative coordinates for the field operators, we identify the zero modes \hat{N} and $\hat{\phi}_0$ as the relative population and phase differences between the two coupled wires, and \hat{Q}_μ and \hat{P}_μ as the relative coordinates for the excited modes. The resulting Hamiltonian reads:

$$\hat{H}_T^{\text{rel}} = \frac{\hbar^2}{2ML^2}(\hat{N} - N_{\text{ex}})^2 - E_J \cos(\hat{\phi}_0) \quad (56)$$

$$+ \sum_{\mu \geq 1} \left[\frac{1}{2M} \left(\hat{P}_\mu + \frac{\sqrt{2}\hbar}{L}(\hat{N} - N_{\text{ex}}) \right)^2 + \frac{1}{2} M \Omega_\mu^2 \hat{Q}_\mu^2 \right]$$

with effective mass $M = \hbar K / 2\pi v L = K^2 m / 2\pi^2 N_0$, N_0 being the average particle number in each tube and $N_{\text{ex}} \ll N_0$ the excitation imbalance, which may be tuned by a suitable choice of the initial conditions. We point out that the center-of-mass coordinates are completely decoupled from the relative ones and they simply take the form of a harmonic oscillator, which can be readily diagonalized, not playing any role in the observable of interest.

Discussion: We identify in Eq. (56) three terms: (i) a *quantum impurity particle* term corresponding to the two collective variables \hat{N} and $\hat{\phi}_0$, (ii) a bath of harmonic oscillators formed by the excited modes, and (iii) a coupling term $\propto \hat{P}_\mu \hat{N}$, obtained by expanding the second line of Eq.(56). Hamiltonian Eq. (56) has the same structure as that of the Caldeira-Leggett model⁴¹⁴⁻⁴¹⁶. However, it is important to remark that in our model the bath of harmonic oscillators is intrinsic to the microscopic model, while in the Caldeira-Leggett model it is phenomenologically introduced. The energy scales E_Q and E_J depend on interactions, the latter being renormalized by quantum fluctuations³⁶⁴. Concomitantly, the sound velocity and the Luttinger parameter vary with the interaction strength as described in⁴¹³. The first two terms of Eq. (56) correspond to the familiar Josephson Hamiltonian, where two regimes can be identified depending on the ratio of the Josephson energy, E_J , and kinetic energy, $E_Q = \hbar^2 / ML^2 = 2\Delta E / K$, with $\Delta E = \hbar\pi v / L$ being the level spacing among the phonon modes of the bath.

Case 1: We first consider $E_J \gg E_Q$, i.e. the Josephson potential term $-E_J \cos(\hat{\phi}_0)$ dominates upon the kinetic energy term in Eq. (56). In particular, starting from an initial particle imbalance among the two wires, its dynamical evolution is readily obtained from the Heisenberg equations of motion³⁹⁶, leading to the quantum Langevin equation of mo-

tion with three dominant parameters: the Josephson frequency $\omega_J = \sqrt{\omega_0^2 - \gamma^2}$ where $\omega_0 = \sqrt{E_J E_Q} / \hbar$, the memory-friction kernel $\xi_N(t)$ whose large temperature properties are given by $\langle \xi_N(t) \rangle = 0$ and $\langle \xi_N(t) \xi_N(t') \rangle = 2E_J^2 k_B T / \hbar^2 M L v \delta(t - t')$ and a damping rate given by $\gamma = \pi E_J / \hbar K$ (assuming a large frequency cut-off for the LL theory):

$$\ddot{\hat{N}} + \omega_0^2 \cos(\hat{\phi}_0) \hat{N} + \int_0^t dt' \gamma_N(t, t') \dot{\hat{N}}(t') = \xi_N(t) \quad (57)$$

Within this Josephson regime, we have two different behaviors depending on interactions. In the weakly interacting limit, where $K \sim 1/\sqrt{g_{1D}}$ and $v_s \sim \sqrt{g_{1D}}$ with g_{1D} being the 1D interaction strength, we recover the predictions of the two-mode model in its small-oscillation limit, i.e. we find $E_Q \propto g_{1D}$ and γ/E_Q vanishing for $g_{1D} \rightarrow 0$, yielding undamped Josephson oscillations. However, for strong interactions E_Q increases, as it is related to the compressibility of the system, and E_J decreases, since it is renormalized by increasingly larger phase fluctuations. Thus, if we look at the dimensionless damping rate $\gamma_Q \equiv \gamma/\omega_0 = \pi\sqrt{E_J}/\sqrt{E_Q}K$, we predict that the Josephson oscillations will be more and more damped at increasing interactions.

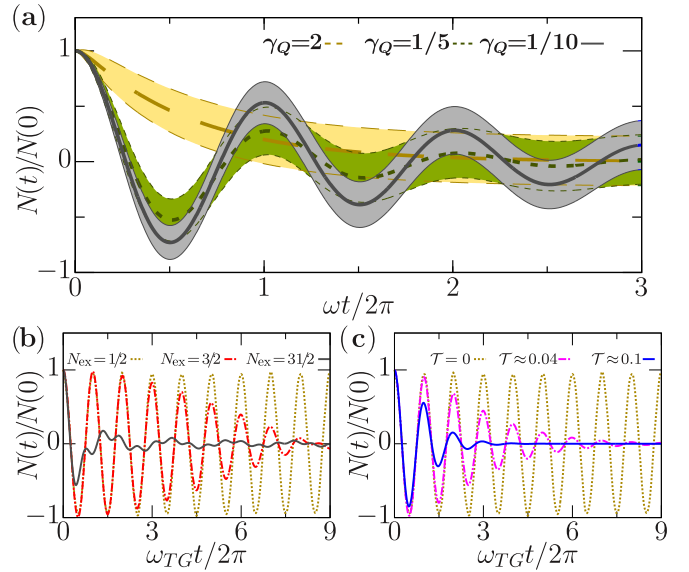


FIG. 35. (a) Relative number dynamics $N(t)/N(0)$ (dimensionless) in two tunnel-coupled wires (LL approach) for various values of $\gamma_Q = \gamma/\omega_0$. Stochastic noise uncertainties are indicated in shaded areas. (b-c) Relative-number oscillations (TG regime) following a quench of the step potential δV_0 creating the initial imbalance: (b) at zero temperature for $\delta V_0/E_F = 0.07$ (yellow-dotted line), 0.14 (magenta dashed line) and 0.72 (blue solid line), with E_F the Fermi energy; (c) at finite temperature for $\delta V_0/E_F = 0.07$ ³⁹⁶.

Case 2: In the $E_J \ll E_Q$ limit, the phase is only weakly pinned and therefore it will display large fluctuations. In this regime, it is more convenient to use the Fock basis for the relative number. Here, we can see that the energy levels of the quantum particle in Eq. (56) can be described as a function of the number of excitations N_{ex} , which now plays the role

of quasi-momentum in the effective crystal, taking the form of parabolas $\varepsilon_n(N_{\text{ex}}) = E_Q(n - N_{\text{ex}})^2/2$, with $\hat{N}|n\rangle = n|n\rangle$. These parabolas will present gaps of amplitude E_J opening at semi-integer values of N_{ex} . If we focus on the anticrossing points $N_{\text{ex}} = \pm 1/2, \pm 3/2, \dots$ the system effectively behaves as a two-level model and the Josephson dynamics correspond to the Rabi oscillations of the quantum particle, with frequency E_J/\hbar . Note that the large value of E_Q fixes the scale of bath-modes level-spacing. This, creates a large gap between the level-spacing of the bath and that of the quantum particle, $\hbar\omega$. In the strongly interacting limit there exists an exact solution for infinitely repulsive interactions, corresponding to $K = 1$ in the LL theory, known as the Tonks-Girardeau (TG) regime^{417–419}. In particular, in Fig. 35 (b) we observe that for a small initial imbalance, i.e. $N_{\text{ex}} = 1/2$, undamped oscillations occur with a frequency $\omega_{TG} = \varepsilon_{N+1} - \varepsilon_N$. This is where the correspondence between the LL and TG regime can be made as $E_J = \hbar\omega_{TG}$ and $E_Q = \hbar^2\pi^2N/mL^2$. Hence, the oscillations observed in the exact solutions at small δV_0 are the undamped Rabi oscillations of the quantum particle predicted by the LL model. For a larger imbalance, and thus beyond the low-energy description given by the LL theory, an effective damping appears due to the high energy excitations produced by the quench. The finite temperature regime is also addressed within the exact TG regime, as shown in Fig. 35 (c) for small-imbalances. Unlike in the LL predictions, in the TG exact solution we find damped oscillations. In order to pinpoint the origin of this damping, we compute the spectral function of the system at finite temperature³⁹⁶. We find that the exact spectral function contains multiple particle-hole excitations while the LL model assumes a linear excitation spectrum. In fact, the exact spectral function also contains several low-energy excitations with frequencies of the order of E_J , which are associated with the presence of a finite barrier and give rise to the observed damping.

In summary, the LL model for two tunnel-coupled atomic gases can be mapped on a quantum impurity problem in the presence of a bath. The exact TG solution validates the frequency of the Josephson oscillations predicted in the LL model, and that the oscillations may in fact be damped by an intrinsic bath made out of low-energy excitations, but points out the existence of other modes that are beyond the LL model and that also provide damping of the excitations.

C. Bose-Einstein condensate confined in a 1D ring stirred with a rotating delta link

Analyzing the spectrum of BECs trapped in ring settings is an important step towards understanding the generation and decay of supercurrents. The spectrum of a BEC in a 1D ring stirred by a rotating link can be first illustrated in the mean field limit, at zero temperature, and with a Dirac delta potential rotating at constant speed^{420,421}. This approach has the advantage that the stationary solutions in the delta comoving frame are the ones of the free 1D GPE, and the effect of the moving potential is relegated to fixing specific boundary conditions. This is in contrast to models with finite width

potentials^{422–424}, and a generalization of a static point like impurity^{425,426}.

Our goal is to analyze the possible stationary solutions, given by the condensate wave function, $\phi(\theta)$, $\theta \in [0, 2\pi)$, and the corresponding chemical potential, μ , in the delta comoving frame. Using natural units, $\hbar = M = R = 1$, with M the mass of the atoms and R the radius of the ring, the GPE, boundary conditions and normalization read,

$$-\frac{1}{2}\phi''(\theta) + g|\phi(\theta)|^2\phi(\theta) = \mu\phi(\theta), \quad (58)$$

$$\phi(0) - e^{i2\pi\Omega}\phi(2\pi) = 0, \quad (59)$$

$$\phi'(0) - e^{i2\pi\Omega}\phi'(2\pi) = \alpha\phi(0), \quad (60)$$

$$\int_0^{2\pi} d\theta |\phi(\theta)|^2 = 1, \quad (61)$$

where $g > 0$ is the reduced 1D coupling, assumed to be repulsive, and $\frac{\alpha}{2} > 0$ and Ω the strength and velocity of the Dirac delta. The spectrum is thus determined by three parameters, g , α , and Ω . A general solution, $\phi(\theta) = r(\theta)e^{i\beta(\theta)}$, can be written in closed form in terms of one of the twelve Jacobi functions⁴²⁵. These functions contain two free parameters, the elliptic modulus, m , which generalizes the trigonometric functions into the Jacobi ones, and a frequency k . Any set of values for k and m entails a solution that satisfies Eqs. (58)-(61) for a specific strength α , velocity Ω , and chemical potential μ .

1. Spectrum

The free and stationary solutions, $\Omega = \alpha = 0$, consist in plane waves, real symmetry breaking solutions, and complex symmetry breaking solutions⁴²⁷. They correspond to vortex states, dark solitonic trains with an even number of zeros, and gray solitonic trains. The latter is a generalization of the former two, plane waves representing the limit in which gray solitons become infinitely shallow, and dark solitons the limit in which the minima of gray solitons become zero. All these solutions are found by imposing a phase jump $\beta(2\pi) - \beta(0) = 2\pi n$, with n an integer. If instead one constrains an arbitrary phase difference of $2\pi\Omega$, the obtained solitonic trains move at velocity Ω —and are stationary in the frame of reference rotating at Ω . The spectrum of stationary solutions from the point of view of an observer moving at Ω is plotted in the left panel of Fig. 36. These solutions also include plane waves under a boost of Ω .

Dark solitonic trains with an even number of zeros comove with the condensate at $\Omega = l$, while trains with an odd number of zeros travel at $\Omega = l + \frac{1}{2}$, where l is an integer. Waves moving at velocities departing from $\Omega = \frac{l}{2}$ consist in gray solitonic trains, with shallower solitons the larger $|\Omega - \frac{l}{2}|$. At $\Omega = \frac{l}{2} \pm |\Omega_n - \frac{n}{2}|$, with $\Omega_n = \sqrt{\frac{g}{2\pi} + \frac{n^2}{4}}$ and n indicating the number of dark solitons in the original train, the amplitudes become constant, and the gray soliton solutions merge into plane waves, see Fig. 36.

Once a barrier is created, the rotational symmetry is broken, and gray and dark solitonic train solutions are split into

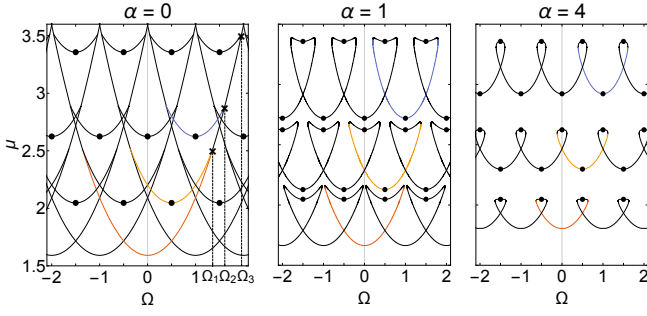


FIG. 36. Lower part of the spectrum $\mu(\Omega)$, in the reference frame of a Dirac delta of strengths $\alpha = 0, 1$, and 4 , moving at constant velocities $\Omega \in (-2, 2)$, and where $g = 10$. Dots mark the velocities and energies of dark solitonic trains. Crosses in the left panel mark the velocities Ω_n at which gray solitonic trains merge into the ground state for $\Omega > 0$.

two. In one solution the delta creates a downward kink at the valley, while in the other in the peak. The energy spectrum, as observed in the Dirac delta comoving frame, is split into a set of swallowtail (ST) diagrams, see middle and right panels of Fig. 36. We organize the spectrum according to the position n , from bottom to top, each set of swallowtails occupies. The n th set of swallowtails consists in solitonic trains with n depressions, including both the valleys and the downward kink at the position of the delta. Dark solitonic trains move together with the condensate at the same velocities as in the free case, $\Omega = \frac{1}{2}$. They too gradually transform to shallower gray solitons as their velocities depart from $\Omega = \frac{1}{2}$. However, in contrast to the symmetric case, there are now a pair of critical velocities, one $\Omega < \frac{1}{2}$ and another $\Omega > \frac{1}{2}$, beyond which stationary solutions do not exist for the particular ST centered at $\Omega = \frac{1}{2}$. These pair of velocities are marked by the tips in each swallowtail, and depend on the magnitude of the delta. In the limit $\alpha \rightarrow 0$, the upper and lower critical velocities of the n th ST become $\Omega \rightarrow \frac{1}{2} \pm |\Omega_n - \frac{n-1}{2}|$, and correspond to the point at which gray solitonic trains and plane waves merge. In general, the upper (lower) critical velocity decreases (increases) with α , converging to $\Omega = \frac{1}{2} + \frac{1}{2}$ ($\Omega = \frac{1}{2} - \frac{1}{2}$) in the limit $\alpha \rightarrow \infty$.

By plotting this critical velocity in terms of α , one can map the regions in parameter space where stationary solutions exist. A sample of these regions, corresponding to the bottom of the first three ST, are plotted in Fig. 37. They define the set of stationary solutions which are adiabatically connected through paths $(\alpha(t), \Omega(t))$. In order to know if these paths are stable, a Bogoliubov analysis is performed for the first three ST diagrams. The bottom parts of the first two ST and all the top parts are found completely stable and unstable, respectively. The bottom part of the third ST is found stable except for a stripe of metastability near the critical line delimiting the region. This metastable part is marked in yellow in the right panel of Fig. 37.

So far, the spectrum has been analyzed in terms of the delta rotation and velocity, and only illustrated for a specific value of the nonlinear coupling g . The maximum width of the STs is

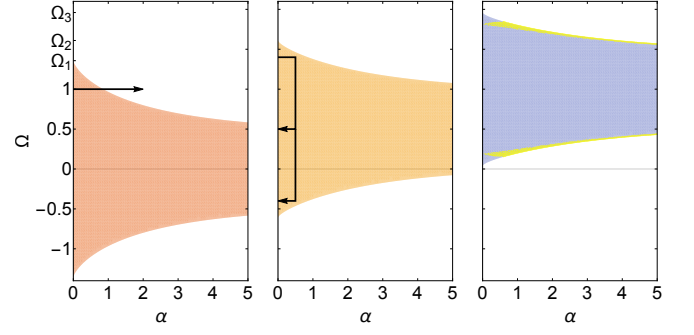


FIG. 37. Regions where stationary solutions exist corresponding to the bottom of the first three ST centered at $\Omega = 0, \frac{1}{2}, 1$ and for $g = 10$. They are colored as the corresponding sections in Fig. 36. A path which explicitly leaves the stationary region is drawn on the left panel. The paths in the middle panel represent cycles to obtain a dark soliton and a vortex with one quantum of angular momentum.

at $\alpha = 0$ and given by $\Delta\Omega_{\max} = 2\Omega_n - \frac{n}{2}$, which grows with g , while the minimum, at $\alpha \rightarrow \infty$, is always fixed to $\Delta\Omega_{\min} = 1$. As g grows, therefore, the regions plotted in Fig. 37 become wider, implying a larger overlap of STs. In the linear limit, $g \rightarrow 0$, the critical velocities become constant, the tails in the ST diagrams and their overlap vanish, and the Jacobi elliptic functions can be replaced by trigonometric ones. The metastability analysis does not qualitatively change for all the nonlinearities tested ($g = 1$ to $g = 50$): all regions found completely unstable or stable remain the same, while the metastability stripe in the bottom of the third ST grows thicker (thinner) with increasing (decreasing) g .

The spectrum is mainly characterized by the values of the velocities Ω_n , which have been presented in natural units, where $\Omega_{\text{nat}} = \frac{\hbar}{MR^2} = 1$ and $\alpha_{\text{nat}} = g_{\text{nat}} = \frac{\hbar^2}{MR} = 1$. In terms of \hbar , M , and R , these velocities read $\Omega_n = \sqrt{\frac{1}{2\pi} \frac{g}{g_{\text{nat}}} + \frac{n^2}{4}} \Omega_{\text{nat}}$. For ^{87}Rb atoms, and radii between $R_1 = 20 \mu\text{m}$ and $R_2 = 100 \mu\text{m}$, the natural velocities range from $\Omega_{\text{nat}}^{(1)} = 1.83 \text{ rad/s}$ to $\Omega_{\text{nat}}^{(2)} = 0.0731 \text{ rad/s}$.

2. Adiabatic production of solitons and vortices

With the general features of the spectrum and its metastability laid out, one can devise adiabatic paths that avoid both, the critical lines delimiting the tips of the ST, and the metastable regions. A possible first step of such a path is to set a Dirac delta while rotating at $\Omega_i \in (\Omega_n, \Omega_{n+1})$, $n \geq 1$. Assuming the condensate is initially in the ground state, the rotating delta creates a gray solitonic train with $n + 1$ small depressions moving at Ω_i . A small current moving in the same direction is also created. In the comoving frame, the bottom part of the $1 + n$ th ST is accessed. By gradually decreasing the velocity, the depressions become deeper, and at $\Omega = \frac{n}{2}$ a black solitonic train comoving with the condensate at $\Omega = \frac{n}{2}$ is formed. Decreasing further the velocity, the dark solitons become gray again, while the current keeps increasing. At any velocity

$\Omega \in (-\Omega_n + n, \Omega_n)$, the rotating delta can gradually be turned off, and one is left with a gray or dark solitonic train. If the delta magnitude is lowered to $\alpha = 0$ while rotating at velocities $\Omega < -\Omega_n + n$, but larger than the corresponding critical velocity, the depressions become flat again, and a vortex of n quanta of angular momentum is obtained. As an example, cycles to obtain one dark soliton and a vortex are drawn in the middle panel of Fig. 37. The densities and phases corresponding to the vertices of this rectangular path are plotted in Fig. 38.

One can also devise paths which explicitly cross the critical line separating the stable and unstable regions. In this case, one can expect the condensate to enter an unstable state and decay. One such path is schematically plotted in the left panel of Fig. 37.

All these paths are constrained by the critical velocity lines and the stability of the solutions along the path. The latter has only been analyzed for the lower part of the spectrum, and therefore one should also perform a Bogoliubov analysis for any proposed cycle involving higher ST levels. Alternatively, these processes can be simulated by numerically solving the time dependent GPE, with the Dirac delta replaced by a peaked Gaussian potential. We solve this equation using the method of lines, and defining a Gaussian with a height and a velocity varying in time such that the paths described above are qualitatively reproduced. Dark solitonic trains with various zeros and vortices with up to a few quanta of angular momenta are obtained. Similarly, simulations show that the condensate is able to sustain stable solutions when stirred by a Gaussian link, up to a certain velocity. This critical velocity decreases with the Gaussian height, as expected from the regions of stationary solutions in Fig. 37. Note that, in contrast to 2D and 3D rings, a decay to vortex antivortex is not possible, and the instabilities found consist in waves becoming turbulent.

D. Thermal and quantum phase slips in a one-dimensional Bose gas on a ring

In this section we study the phase slip processes between different angular momentum states occurring in a one-dimensional Bose gas trapped in a ring potential. Particularly, we focus on the case where the current is induced through phase imprinting^{117,428,429}. Note that the one-dimensional geometry does not allow for vortex nucleation within the ring, contrary to what has been discussed in previous sections for larger dimensionality. Therefore, phase slips require the existence of a different microscopic mechanism, which we investigate using several theoretical approaches and considering different regimes of inter-atomic interactions as well as the effects of finite temperatures on the system.

Model and methods: We consider N bosons of mass m with repulsive contact interactions on a ring of circumference L with periodic boundary conditions. The coupling between different angular momentum states is triggered by the presence of a barrier, a procedure analogous to the experimental implementations of phase imprinting^{117,428,429}.

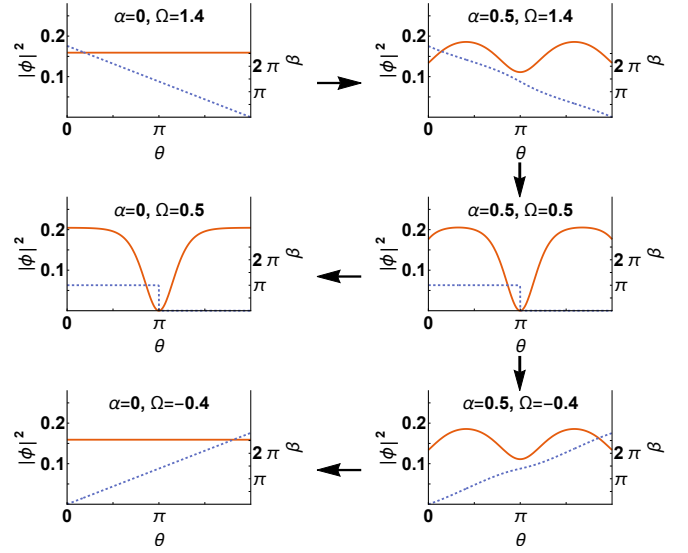


FIG. 38. Densities (solid lines) and phases (dashed lines) in the Dirac delta comoving frame corresponding to the key points of the dark solitons and vortex cycles in Fig. 37 (where $g = 10$). The first steps in both of them consist in setting a delta on the ground state (top left plot) while rotating at $\Omega = 1.4$, and then lowering its velocity to $\Omega = \frac{1}{2}$ (top and middle right plots). At this point, one can unset the delta and obtain a dark soliton, or further decrease the velocity down to $\Omega = -0.4$, and then unset the delta, in which case the state of one vortex is reached.

In order to investigate phase-slips in the system, we start from the equilibrium state Ψ_0 in which a static barrier is present, and then induce a quench in the many-body wavefunction such that $\Psi_0(x_1, \dots, x_N) \rightarrow \Psi_1(x_1, \dots, x_N) = \Psi_0 \times e^{i2\pi\ell \sum_j x_j/L}$. The current dynamics is then obtained from:

$$J(t) = -i \frac{\hbar}{2m} \frac{1}{N} \int_0^L \frac{dx}{L} \langle \hat{\Psi}^\dagger \partial_x \hat{\Psi} - (\partial_x \hat{\Psi}^\dagger) \hat{\Psi} \rangle. \quad (62)$$

The dynamical response is found using different methods depending on the interaction strength, $\gamma = mg/\hbar^2 n$, and temperature regimes: (i) the Gross-Pitaevskii equation (GPE) and analytical two-mode model adapted from³⁹⁸ at $T = 0$ for a weakly interacting gas ($\gamma \ll 1$); (ii) the projected Gross-Pitaevskii equation (PGPE) at $T > 0$ and $\gamma \ll 1$ ^{372,375,430} and (iii) the time-dependent Bose-Fermi mapping at $\gamma \gg 1$, describing the infinitely strong interaction Tonks-Girardeau (TG) limit for the entire temperature range⁴¹⁷⁻⁴¹⁹. We focus on a quench inducing a circulation $\ell = 1$. Depending on the model, we consider two types of barriers: a delta potential $V(x) = \alpha\delta(x)$, for which analytical results can be obtained, and a Gaussian potential $V(x) = V_0 \exp(-x^2/2w^2)$, which is more realistic from the experimental point of view. Both cases are compared using a dimensionless parameter for the barrier strength: $\lambda_{GP} = V_0/\mu_0$ for weak interactions, with $\mu_0 = gn$ being the chemical potential of the homogeneous annular gas, and $\lambda_{TG} = V_b/E_F$ for strong interactions, with $V_b = \alpha n$ being the energy associated to the barrier and $E_F = \hbar^2 n^2 \pi^2 / 2m$ the Fermi energy.

Discussion: We find that the current dynamics depends on interaction and temperature regimes. Figure 39(a-c) shows the results in the weakly interacting regime. At zero temperature we observe that the current remains very close to the initial quenched circulating state for weak to moderate barriers, up to $\lambda_{GP} \sim 1$. Above this critical value, we observe a fast decay of the current, followed by oscillations around the 0 value. This behavior is found to correspond to the transition of the currents from self-trapping to Josephson oscillations, in analogy to the well known Josephson effect for particle imbalance predicted in³⁹⁸.

For temperature $T = \mu_0/k_B$ ⁴³¹, the dynamics of the current are quite different. At low barriers, i.e. $\lambda_{GP} \leq 0.5$, we observe an exponential decay of the current, while for larger barriers we observe damped oscillations. In this regime, thermal phase slips occur deterministically at the position of the barrier where the density vanishes. In order to elucidate the mechanisms behind the current decay, Fig. 39(c) shows a *single* classical field trajectory, showing many spontaneous thermal gray solitons⁴³². While most of the solitons present a small density dip, thus being fast and transmitted through the barrier⁴³³, we notice that the current undergoes discrete jumps each time a soliton reflects on the barrier. In this case, the density profile vanishes when the soliton reaches zero velocity, allowing for a phase slip to occur. This corresponds to the adiabatic process indicated by the dashed red line in Fig. 39(c). The observed exponential decay of the average current can be understood as an intrinsically stochastic process occurring when the barrier couples the soliton dynamics to the long wavelength sound excitations⁴³³.

The strongly interacting regime $\gamma \gg 1$, where the classical picture does not apply, is described using the exact Tonks-Girardeau solution. We show that the dynamics of the current microscopically corresponds to quantum coherent oscillations between different angular momentum states. At zero temperature, in contrast to the weakly interacting regime, we observe that for weak barriers ($\lambda_{TG} \ll 1$) there is no self-trapping (see Fig. 39(d)). Rather, the current undergoes Rabi-like oscillations. These oscillations correspond to coherent quantum phase slips due to backscattering induced by the barrier, which breaks the rotation symmetry thus coupling different angular momentum states^{364,434}. Microscopically, it corresponds to dynamical processes involving the whole Fermi sphere, i.e. multiple-particle hole excitations where each particle coherently undergoes oscillations of angular momentum from $L_z = \hbar$ to $L_z = -\hbar$. At increasing barrier strength, an envelope appears on top of the current oscillations, degrading the Rabi oscillations. This envelope originates from the population of higher-energy modes, each transition being characterized by a different frequency (see³⁹⁴), leading to a mode-mode coupling and dephasing, and more complex current oscillations. At finite temperatures the quench dynamics of the current involves high-energy excitations with an amplitude weighted by the Fermi distribution³⁹⁴. The resulting dynamics corresponds to an effective damping of the current oscillations with an exponential decay (see Fig. 39(e)), due to the effect of incoherent phase slips. The revivals observed for large barriers at zero temperature are highly suppressed due to the thermal excita-

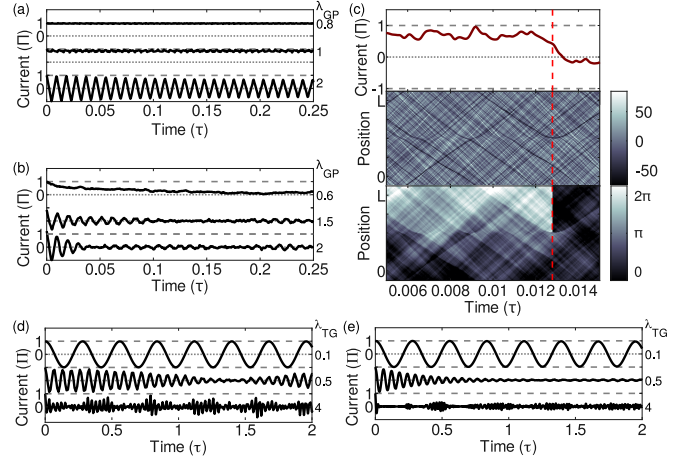


FIG. 39. (a-c) Classical field simulations of the quench dynamics in the mean-field regime for $\gamma = 0.02$ ³⁹⁴. (a) Average current per particle (solid lines, unit: $\Pi = \hbar/(Nm)$) as a function of time (unit: $\tau = mL^2/\hbar$) at $T = 0$. Top to bottom: $\lambda_{GP} = \{0.8, 1, 1.05, 2\}$. (b) Current at $T = \mu_0/k_B$ for barrier strengths $\lambda_{GP} = \{0.6, 0.9, 1.5, 2\}$. (c) Zoom on a single classical field trajectory at $T = \mu_0/k_B$ and $\lambda_{GP} = 0.6$, illustrating a phase slip. This consists in a jump in the current (top panel), corresponding to the reflection of a slow soliton on the barrier, also visible in the density deviation map (middle panel) and appearing as a singularity in the phase profile (bottom panel). (d-e) Exact solutions in the Tonks-Girardeau regime³⁹⁴. (d) Average current per particle vs. time after the quench for $N = 23$, at $T = 0$, for barrier strength $\lambda_{TG} = \{0.1, 0.5, 1, 4\}$. (e) Current at $T = E_F/k_B$ (solid lines) for $\lambda_{TG} = \{0.1, 0.5, 1, 4\}$ from top to bottom. (a-e) Horizontal dotted (dashed) lines indicate the values for $J = 0 (\pm 1)$.

tions. We identify the oscillation frequency as Josephson oscillations, in which at increasing barrier strength the frequency crosses over from a Rabi-like regime with $\omega = \pi^2 N \lambda_{TG}$ to a Josephson-like regime with $\omega \propto \sqrt{\lambda_{TG}}$. This is in agreement with the predictions of the low-energy Luttinger liquid theory (see³⁹⁶ and Sec. VIII B above).

In summary, in this section, we have studied the dynamics of a one-dimensional ring pierced by a localized barrier, following a phase imprinting. From a static point of view, a localized barrier can lead to solitonic excitations as seen in Sec. VIII C. However, these can also be thermally activated or created dynamically by quenching a current in the system. Within the mean field regime, the self-trapping behavior of the current prevents coherent phase slips, but at finite temperatures incoherent phase slips are observed. Their microscopic origin is related to the coupling between the soliton dynamics and the long wavelength sound excitations which are intrinsically stochastic, leading to an exponential decay of the average current. A similar microscopic behavior is found in higher dimensions, however the excitations take other specific forms such as vortex rings as seen in Sec. VIII A. When considering the strongly interacting regime, coherent phase slips dominate the dynamics. Finally, at finite temperatures, incoherent dynamics appears due to thermally occupied high-energy excitations that lead to an average decay of the current.

E. Conclusions

We have discussed different regimes of ultracold atomic gases in which phase slips play a crucial role on the dissipative motion of certain macroscopic observables, and discussed their connection to low-lying and macroscopic excitations in such systems. Understanding these processes in detail is crucial to harnessing future atomtronic applications.

To understand the microscopic origin of such mechanisms we have considered the diverse settings of 3D harmonic traps, and 1D systems in harmonic and ring traps with weak and strong interactions. We have also considered the effect of thermal fluctuations on such dynamics.

In the context of a weakly-interacting harmonically-confined 3D ultracold quantum gas, with a weak link creating a Josephson-like junction, the phase slips are related to the generation of vortex rings and associated sound emission, with increasing population imbalances leading to sequential ring generation, even potentially opening up an avenue for a turbulent-like regime. Our analysis was performed for a bosonic system, but the relevant experiment is actually performed across different superfluid regimes of an ultracold fermionic gas. As such, our results only strictly apply to the BEC side, and numerous interesting open questions remain on how the explicit nature of the fermionic statistics affects this picture as one moves towards the unitary and BCS superfluid regimes^{386,392,435}

In a 1D strongly correlated Bose gas, it is low-energy excitations within the bulk that provide the underlying mechanism leading to the dissipative motion across the junction. Although in this regime we also observe that damping of large particle imbalances proceeds through higher-energy modes. On the other hand, in 1D ring potentials the relevant excitations leading to the decay of the current at weak interactions are dark solitons, although low-energy excitations are also involved in the decay mechanism. In our studied regime, dark solitons were thermally activated, however they can also have other origins, e.g. being triggered by the presence of an impurity. In that case, the specific soliton or solitonic train generated depends on the size of the impurity and its velocity relative to the current. The microscopic origin of the phase slippage is then related to the coupling between the soliton dynamics and the long wavelength sound excitations (which are intrinsically stochastic). We note that, while the 1D systems considered in Secs. VIII B-VIII D allow to identify the microscopic origin of excitations, the barriers and topologies considered in these microscopic theories are significantly simplified ones, and extending this work to more realistic scenarios could bring new insight regarding the energy scales at which the damping of oscillations occurs. Indeed, present-day experiments use finite width barriers and external confinements to trap strongly correlated atoms, which could influence the damping. Moreover, the results shown in Sec VIII B rely on the low-energy theory given by the Luttinger liquid model. Beyond the low-energy model, one should approach the problem numerically. However, numerical simulations of strongly correlated systems are highly complex. Therefore, developments in this field could prove of great importance in corroborating and extending the

dynamics of strongly correlated Josephson coupled systems for strong quenches. Finally, we note that the spectrum and role of impurities presented in Sec. VIII C and the microscopic mechanism leading to damping can notably depend on the dimensionality.

F. Outlook

One of the main challenges for quantum technologies is to control the system's quantum state while maintaining its quantum coherence for longer times². Thus, reducing dissipative motion becomes crucial for the development of atomtronic devices. Moreover, controlling and understanding the mechanisms involving coupling to low-energy excitations can also lead to a reduction of this dissipation. In addition, the initial quantum state can also be of consequence to the system's final stability, as the projection to high energy excitations can lead to complex damped dynamics. From these results we can draw some insight regarding future directions for improving and reducing dissipative behavior. Integrable or quasi-integrable systems, in which many conserved quantities exist compared to the system's degrees of freedom, have been shown to present a long-lived coherence and dissipation-free dynamics^{211,256,264}. Also, several recent studies have focused on topologically protected states^{436,437} as the main building blocks for future atomtronic devices, as these states prove very robust against perturbations.

Acknowledgements

Juan Polo and Anna Minguzzi would like to especially thank: Verónica Ahufinger - for her contribution to the work on the 1D Josephson junction; the late Frank Hekking - who greatly helped us in understanding Josephson junctions; Romain Dubessy and Paolo Pedri - for their contributions to the theoretical development and numerical simulations as well as for fruitful discussions regarding dynamical phase slips in rings. In addition, we thank Maxim Olshanii and Jook Walraven for stimulating discussions. We also acknowledge financial support from the ANR project SuperRing (Grant No. ANR-15-CE30-0012). LPL is a member DIM SIRTEQ (Science et Ingénierie en Région Île-de-France pour les Technologies Quantiques). Axel Pérez-Obiol thanks Taksu Cheon for his contribution on the topic of stirred BECs on 1D rings. Klejdja Xhani and Nick Proukakis acknowledge contributions to the theoretical modelling and understanding by Carlo Barenghi, Luca Galantucci, Kean Loon Lee, Andrea Trombettoni and to the experimentalists Alessia Burchianti, Elettra Neri, Giacomo Roati, Francesco Scazza and Matteo Zaccanti. Nick Proukakis acknowledges financial support from the Quanterra ERA-NET cofund project NAQUAS through the Engineering and Physical Science Research Council, Grant No. EP/R043434/1.

IX. ATOMTRONICS ENABLED QUANTUM DEVICES AND SENSORS

D. Anderson, V. Ahufinger, A. S. Arnold, G. Birkel, M. Boshier, S.

In this section we will discuss some example cases where the atomtronics approach is leading to novel components (which may be part of a larger device) and applications such as rotation sensing and magnetic sensing.

A. Diodes, transistors, and other discrete components

The terminology *Atomtronics* suggests, correctly, but not exclusively, an analogy between circuits for atomic matter and those based on standard *electronics*. The flow of electrons in an electric circuit can be considered in a way analogous to the flow of cold neutral atoms in an atomtronic circuit (At present, there is some flexibility in this interpretation.). Important questions concern how to confine the atoms to a circuit, how to control them, and what devices and applications can arise.

It would be a gross over-simplification to suggest that an atomtronic circuit should merely mimic an electronic circuit. Whilst this *might* be the case, it is by no means essential, and indeed, it is very much intended that future atomtronic systems go beyond analogs of standard electronic circuits. To be specific: Although we may start with these basic analogs, the future hope is for devices that use the properties of matter-wave coherence and other quantum properties of matter to go beyond these direct analogs, and to even create devices with no electronic counterpart because of the unique properties of the quantum physics of matter. Meanwhile, however, in this first part of Section IX we will explore the progress made in formulating and implementing discrete atomtronic components that are similar to electronic ones.

The basic electronic elements are often regarded to be batteries, resistors, capacitors, diodes, transistors, and the like. If we start with the battery, in the atomtronic world it can be regarded as a reservoir of atoms. Clearly, that is too simplistic and not enough on its own. So first steps are to involve atoms contained in a reservoir and allowed to flow out of that reservoir into a more complex circuit, or at least into another reservoir as in cases of two-terminal flow⁴³⁸. The current of neutral atoms is driven by the difference in the chemical potential between two reservoirs, typically implemented by the two sides of a barrier, in a way that is analogous to Ohm's law in conventional circuit theory. The battery is later intended to supply power to an atomtronic circuit via the transport of cold atoms.

Such a battery was demonstrated in Ref. 439 which was complemented by the respective theoretical description in Ref. 440. In this 'battery' experiment a relatively large confining potential for ultra-cold atoms is divided into two parts by introducing a spatially narrow beam of blue-detuned light acting as a barrier (see Fig. 40a). Atoms can be confined on one side of the combined potential, the other side, or both. During the experiment discussed here, atoms are initially loaded on one side (the left side in Fig. 40a) and then allowed to flow to the right side as controlled by the sharp barrier which essentially controls the 'resistance'. To prevent the reflection of atoms

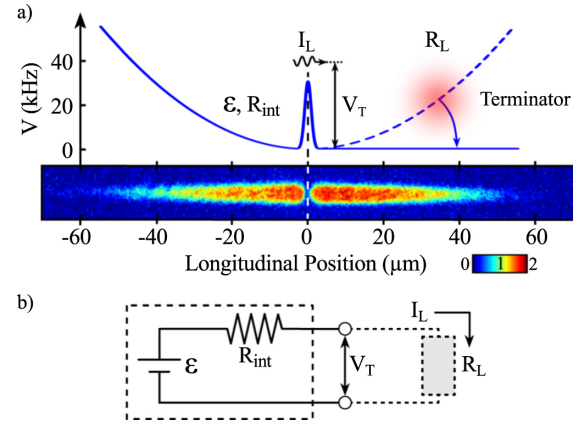


FIG. 40. An atomtronic battery. (a) The confining fields for the atoms are formed using magnetic and optical potentials. The image of atoms demonstrates the situation when they fully occupy the system with the terminator off. (b) An equivalent circuit for the atomtronic battery. Taken from Ref. 439.

from the second well, a 'terminator' is added to the system by means of an optical beam that pumps atoms in the second well into untrapped states, such that they are lost from the system. This terminator also represents a load-matched impedance (see Fig. 40b) in the analogous electric circuit.

A similar system has been used to demonstrate the dynamics of an *RLC* circuit⁴⁴¹. In this case, a light sheet trap is modified with additional dipole beams to create 2D confinement of the atoms: two reservoirs are generated that are joined by a narrow link. This 'capacitor'-like systems is charged by loading atoms into one of the reservoirs. Subsequently the flow of atoms through the narrow channel discharges the capacitor. The channel possesses a finite resistance and appears to have inductance as well⁴⁴¹.

In analogy to solid state materials modifying the electronic wave function, optical lattices offer band-gap structures for cold atoms (In this context, see e.g. Ref. 442.). These allow the creation of diodes and transistors by changing the baseline potential of the lattice across a discontinuity or junction in just the same way as for semi-conductors across a NP- or PN-type junction^{443,444}. However, it is interesting to note that the atomtronic diode can display its functionality with just a few lattice sites (i.e. with just a few potential minima) and the atomtronic transistor is proposed to be functional with just three potential wells²¹. It can be constructed in the same way as the battery experiment discussed above⁴³⁹, but with an additional blue-detuned dipole beam adding one additional barrier to the passage of the atoms. The transmission of atoms through the double-barrier system is now dependent on the chemical potential between the two barriers^{135,445}, giving a transistor-like behaviour with 'source', 'gate', and 'drain' assigned to the three regions around the barriers. Furthermore, by cascading transistor junctions, i.e. by adjusting the sets of lattice potentials, a logic gate (AND gate) has been proposed consisting of just five lattice sites⁴⁴⁴.

One direction for future extensions is the development of more exotic circuit elements. For example, asymmetric double

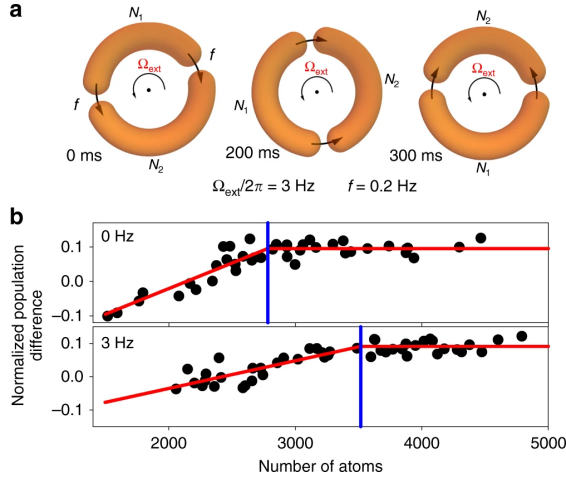


FIG. 41. (a) We show how the ‘Josephson junction’ barriers move in the atomtronic SQUID in order to observe a synthetic external rotation. The two barriers move at different rates $\Omega_{\text{ext}} \pm 2\pi f$. The number of atoms on either side of the barriers is N_1 and N_2 . (b) The normalised population difference $(N_2 - N_1)/(N_2 + N_1)$ is plotted as a function of the number of atoms in each experimental run. The blue line indicates the point at which a critical atom number is reached, where the system switches from AC to DC Josephson regimes. The critical atom number varies with the ‘rotation’ rate, being larger in the lower panel of (b). Taken from Ref. 113.

well potentials made by optical dipole beams have been used to create a Josephson junction for an atomtronic system^{446,447}. In the direction of increasing the complexity of circuits, for example, the proposal for an AND gate starts to open the way for a very unusual type of quantum logic which is based on the flow of neutral atoms. Here, we can imagine going from AND gates to NAND gates, which are universal gates, and then by further increasing the complexity, a universal matter-wave quantum computer is accessed—at least in principle.

B. Atomtronic SQUIDS

Quantum interference has a high importance in atomtronics which is particularly true in the case of *atomtronic SQUIDS*. Atomtronic SQUIDS are *not* superconducting devices, but are named for their analogy with SQUIDS. They are sometimes denoted AQUIDS for Atomtronic QUantum Interference Devices⁵.

A conventional SQUID can be built from a superconducting ring with one or two ‘weak links’ which form Josephson junctions. At each junction the current and the junction phase are closely related in such a way that magnetic field strengths can be determined from the oscillatory behaviour of the voltage drop across the junction. The resulting device makes an excellent magnetic field sensor⁴⁴⁸.

A basic atomtronic SQUID consists of a ring waveguide for ultra-cold neutral atoms with two barriers inserted^{22,113} (see Fig. 41a). In the analogy, the ring waveguide replaces the superconducting ring, and the barriers replace the Josephson junctions. The current-phase relation for atomtronic tun-

nel junctions and weak links was explored in refs^{7,22}. Each barrier clearly affects the phase of the wavefunction and, just like the super-conducting analogs, there is a critical current: in the atomtronic case, when the flow is too fast it breaks up into vortex - antivortex pairs^{67,128}. In a conventional SQUID, current flow in the superconducting loop is established by changing the magnetic flux through the loop. In the atomtronic SQUID, current flow in the waveguide loop is created by rotation of the system. It follows that the device’s behavior is sensitive to rotation of the SQUID (or equivalently rotation of the barriers). This principle, including quantum interference effects, has been recently demonstrated in Ref. 113. Figure 41b shows the transition from the AC Josephson regime (AC current through the junctions with non-zero chemical potential difference across them) to the DC Josephson regime (DC tunnelling current flowing through the junctions with no chemical potential) marked with the vertical blue line as a function of the number of atoms for two different rotation rates. This transition point becomes oscillatory as a function of the rotation rate (for a fixed number of atoms) or as a function of the number of atoms (at different rotation rates as shown here). These oscillations can be used to determine the rotation rate (Ω_{ext} in Fig. 41). Another recent work has shown that the atomtronic SQUID also exhibits hysteresis behaviour analogous to the conventional SQUID⁷.

The recent experiments with ring traps and barriers^{7,22,67,113,128,352} are based on optical dipole potentials. The ring trap and weak link can be created with a Laguerre-Gauss beam (with a hole) and a focussed Gaussian beam⁶⁷. For the ring part, potentials created by conical refraction are possible as well¹¹⁴. Alternatively, a very flexible approach is to use ‘painted’ potentials^{19,29}, where an optical dipole beam is rapidly scanned around the region of interest. As the beam is scanned, the intensity of the light is modulated so that a two-dimensional image is formed which produces a rather flexible 2D potential. Confinement in the third dimension is provided by a light sheet and the dipole potential from that. The painted potential can include a ring, and the ‘weak link’ barriers which can be moved around the ring at will.

The atomtronic SQUID has the clear potential of being a central building block for atomtronic devices: e.g., for rotation or magnetic field sensors. However, it may also play other important roles in atomtronic circuits. It could be a component in a more complex circuit where matter wave interference is essential, or allow for the storage of quantum information in the quantum states of the atomtronic SQUID.

C. Sagnac interferometry and rotation sensing

Rotation detection devices come in many forms, including micro-electromechanical systems (MEMS), hemispherical resonator gyros (HRGs), ring laser gyros (RLGs), and fiber-optic gyroscopes (FOGs). They are ubiquitous in the sense that mobile phones contain low-sensitivity gyroscopes that users can access via apps such as Phyphox. These more ‘traditional’ sensors have been reviewed with viewpoints that

are mainly academic⁴⁴⁹ and industrial⁴⁵⁰.

Atoms can also be used as gyroscopes, for example via nuclear spins in co-magnetometers⁴⁵¹. Alternatively, demonstration of atom-optical manifestations of the Sagnac effect date back to 1991⁴⁵², and already in 1997 short-term sensitivities of 2×10^{-8} (rad/s)/ $\sqrt{\text{Hz}}$ were demonstrated in an atom-based Sagnac interferometer^{31,453}; since then there have been many technical advances in such “free space” interferometers,⁴⁵⁴ commonly based on a Mach–Zehnder-type configuration.

From an atomtronic standpoint we wish to consider “closed-path” guided configurations, which have been used for cold molecules⁴⁵⁵, cold atoms^{70,122}, and Bose-Einstein condensates^{72,456} (BECs) since the early 2000s, and have been recently considered for chip-scale development^{77,136}. Theoretical and experimental guiding geometries include optical dipole, magnetic and Stark confinement using constant, time-averaged, inductive or dressed potentials^{19,24,29,37,71,76,88,110,111,125,126,351,364,457–474}. Highly supersonic superfluid flow is also possible^{72,86,97}, however whilst the concept of closed-path cold atom configurations has long held traction, the sensitivity has yet to reach the high levels of free-space cold atom gyros⁴⁷⁵. There has been some important recent experimental progress on this front^{476,477}, i.e., all the necessary experimental tools appear in principle to be present.

This means we consider Bose-condensed atoms held within an appropriate (e.g., toroidal, as used in atomtronic SQUIDS) trapping potential V . This is necessarily assumed to be in a rotating frame defined by the angular velocity vector Ω , manifesting as an additional term $i\hbar\Omega \cdot (\mathbf{x} \times \nabla)$ in either the single-particle Schrödinger equation, or the Gross–Pitaevskii equation (GPE) when describing mean-field dynamics of Bose-condensed atoms. A coordinate system where Ω points along the z axis (dynamics viewed from within a frame rotating anti-clockwise around the z axis with angular frequency Ω) simplifies this term to $i\hbar\Omega(x\partial_y - y\partial_x)$. A good general starting point for describing the dynamics within a variety of such systems is the following system of GPEs:

$$i\hbar \frac{\partial}{\partial t} \Psi_j = -\frac{\hbar^2}{2m} \nabla^2 \Psi_j + i\hbar\Omega \left(x \frac{\partial}{\partial y} \Psi_j - y \frac{\partial}{\partial x} \Psi_j \right) + V_j \Psi_j + \sum_{j'} g_{jj'} |\Psi_{j'}|^2 \Psi_j. \quad (63)$$

The j index labels different internal atomic states, the V_j incorporate energy differences between the internal states and any internal state dependences of the trapping potential, and the $g_{jj'}$ quantify the strengths of s -wave scattering terms (ignoring the possibility of internal-state-changing collisions).

We first consider a tight toroidal trapping potential, reducing our treatment to a radius R one-dimensional ring geometry, leaving only the polar angle ϕ free, reduce to a single internal state, and neglect all interactions. The GPE then becomes

$$i\hbar \frac{\partial}{\partial t} \psi(\phi) = \left(-\frac{\hbar^2}{2mR^2} \frac{\partial^2}{\partial \phi^2} + i\hbar\Omega \frac{\partial}{\partial \phi} \right) \psi(\phi). \quad (64)$$

Note the interactions are genuinely insignificant if the gas is very dilute, or if interactions are tuned away using an appropriate Feshbach resonance. The evolution of an initial, localized matter wave split into an equal superposition with opposite velocity splitting products can, at the simplest level, be considered without explicit mention of the initial wave packet. At this level, an initial state $\psi(0) = (e^{i\ell\phi} + e^{-i\ell\phi})/\sqrt{4\pi} = \cos(\ell\phi)/\sqrt{\pi}$ evolves as $\psi(t) = e^{-i\hbar\ell^2 t/2mR^2} \cos(\ell[\phi + \Omega t])/\sqrt{\pi}$, yielding intensity fringes proportional to $(2/\pi) \{ \cos(2\ell[\phi + \Omega t]) + 1 \}$ multiplied by the number of atoms whenever the matter wave splitting products overlap in space. For a matter wave initially centred at $\phi = 0$, this occurs at: $\phi = \pi$, when $t = A m / \hbar \ell$ ($A = \pi R^2$ is the enclosed area of the ring), yielding a phase shift of $\Delta\phi = \Omega t = 2A\Omega m / \hbar$; and at $\phi = 0$ when $t = A m / \hbar \ell \Rightarrow \Delta\phi = 4A\Omega m / \hbar$.

Using the speed $v = \hbar\ell/Rm$ and wavelength $\lambda = 2\pi R/\ell$ of the propagating atoms we express the latter phase shift as $\Delta\phi = 8\pi A\Omega/\lambda v$, the same form as the phase shift accumulated by an optical Sagnac interferometer, with λ and v replaced by the wavelength and speed of light, respectively. This highlights the promise of atom interferometry, in that λv can be made much smaller than its optical equivalent. Note also that if the initial state is literally $\psi(0) = \cos(\ell\phi)/\sqrt{\pi}$, i.e., there is no localizing “envelope” to the wave packet, the accrued fringe shift can be observed at any time, effectively increasing the enclosed area of the interferometer. This highlights an important feature, in that as the speed of light is a constant, it is necessary to increase A in order to increase the interrogation time; with cold atoms this is not the case.

With typical repulsive interactions (positive g), such standing wave fringes will rapidly disperse, however in a two-component system with very similar scattering lengths ($\Rightarrow g_{11} \approx g_{12} \approx g_{22}$, as can be achieved in ⁸⁷Rb),⁴⁷⁸ producing an equal superposition initial state such that $\psi_1(0) = \cos(\ell\phi)/\sqrt{2\pi}$, $\psi_2(0) = \sin(\ell\phi)/\sqrt{2\pi}$, the two components stabilise each other by making the total mean field potential $g(|\psi_1|^2 + |\psi_2|^2)$ essentially flat (hence, no gradients and no dispersive forces). Alternatively, initializing the system such that $\psi_1(0) = e^{i\ell\phi}/\sqrt{4\pi}$, $\psi_2(0) = e^{-i\ell\phi}/\sqrt{4\pi}$, followed by an evolution time $T/2$, a π pulse swapping the internal states, and a second evolution time $T/2$, produces $\psi_1(T) = e^{-i\varphi T} e^{-i\ell(\phi + \Omega T)}/\sqrt{4\pi}$, $\psi_2(T) = e^{-i\varphi T} e^{i\ell(\phi + \Omega T)}/\sqrt{4\pi}$ (φ is a global phase depending on ℓ^2 and the values of g_{11} , g_{12} , and g_{22}). Repeating the initializing process produces $\psi_1(T) = -ie^{-i\varphi T} \sin(\ell[\phi + \Omega T])/\sqrt{2\pi}$, $\psi_2(T) = e^{-i\varphi T} \cos(\ell[\phi + \Omega T])/\sqrt{2\pi}$. The value of Ω can then be inferred from population measurements: $N_1 = N[1 + \cos(2\ell\Omega T)]/2$, $N_2 = N[1 - \cos(2\ell\Omega T)]/2$, where N is the total particle number. The π swap pulse at $T/2$ is carried out to counteract accumulation of relative phase due to differences in internal state energy and values of g_{11} and g_{22} ; if $g_{11} \approx g_{22}$ and the energy gap between the internal states is well known, this can be neglected, and a detailed experimental proposal based around ⁸⁷Rb and magnetic vortex pumping has been determined by Helm *et al.*⁴⁷⁹ This alternative has the advantage of there being no mean field gradients even when the scatter-

ing lengths are quite different, and turns a measurement of interference fringes into a measurement of relative population. Note, however, that optimum sensitivity of such a measurement is when the slope of the response curve is maximal, e.g., when $2\ell\Omega T \approx \pi/2$ ^{479,480}; it may therefore be advisable to add a controlled relative phase in an experimental realisation.

A quite different approach, again in near 1D, is to have a single component condensate with attractive interactions, using, e.g., ⁸⁵Rb or ⁷Li, again ideally in a ring geometry, as illustrated in Fig. 42.⁴⁸¹ In this case, the GPE exhibits soliton solutions: stable, non-dispersive, localized wave packets which are robust to collisions, behaving something like classical particles. Given a sufficiently sharp barrier — ideally a δ -function, more realistically a Gaussian barrier with width significantly smaller than the soliton's characteristic length^{482,483} formed e.g. by a focused off-resonant sheet of light⁴⁸⁴ — an initial soliton can be split into two halves propagating with equal and opposite velocity if its incoming velocity is correctly calibrated to the barrier size. In an essentially similar way, the splitting products can accumulate a relative Sagnac phase, which could in principle be visualised through spatial interference fringes.⁴⁸⁵ The solitons' small size can make this a less suitable approach, however, than recombining them again on a barrier, where the relative phase manifests through the relative sizes of the wave packets emerging on either side of the barrier as the result of this second collision, i.e., again as relative population measurement, with an essentially similar (ideal) dependency on Ω as that outlined above. This second barrier interaction can take place either at a second barrier exactly opposite to the first,⁴⁸⁶ or, due to the fact that solitons are robust to collisions and therefore in some sense should “pass through” one another, back at the same barrier at which the initial splitting took place, following both splitting products having completely circumnavigated the ring.⁴⁸¹

The roles of quantum noise and interaction for rotation sensing with bright solitons in the quantum regime were studied in⁴⁸⁷. It was found that interaction and noise should be carefully considered in order the performances of the system are not spoiled. In addition, the GPE analysis is of limited accuracy for the quantitative analysis of the sensitivity of atom interferometry in the presence of interaction. For other features of bright soliton interferometers, please see Chap. XIV.

Finally, we note that everything we have described is in a sense “classical,” in the sense of a classical field description of the BEC being completely adequate, and that more explicitly quantum elaborations have been proposed, exploiting spin squeezing⁴⁸⁸ or ideas from quantum information⁴⁸⁹.

D. Magnetometry

The development of compact highly sensitive magnetometers with high spatial resolution is one of the current challenges of Atomtronics. The capability of measuring with high precision and accuracy very weak magnetic fields is at the basis of numerous applications including bio-magnetism, geology, data storage and archaeology⁴⁹⁰. Different approaches have been followed in the previous years to reach this goal,

mainly using superconducting quantum interference devices (SQUIDS), nitrogen-vacancy diamonds magnetometers, and atomic magnetometers.

Atomic magnetometers can be classified depending on whether the magnetic field drives the internal or the external degrees of freedom of the atoms. The former are typically based on the measurement of the Larmor spin precession of optically pumped atoms either using thermal clouds or BECs. In the case of thermal clouds double-resonance optically pumped magnetometers are an attractive instrument for unshielded magnetic-field measurements due to their wide dynamic range and high sensitivity⁴⁹¹. In the BEC case, the use of stimulated Raman transitions has been reported⁴⁹² as well as the separate probe of the different internal states of a spinor BEC after free fall⁴⁹³, or the measure of the Larmor precession in a spinor BEC^{494–499}. Note also that a two-component BEC has been also investigated for magnetometry⁵⁰⁰.

An alternative approach to atomic magnetometry is based on encoding the magnetic field information in the spatial density profile of matter waves. Some examples of this approach are those based on detecting density fluctuations in a BEC due to the magnetic induced deformation of the trapping potential^{199,501,502}. Recently, a different scenario has been explored and a quantum device for measuring two-body interactions, scalar magnetic fields and rotations based on a BEC in a ring trap has been proposed⁵⁰³. To this aim, the BEC is prepared in an imbalanced superposition of the two counter-propagating Orbital Angular Momentum (OAM) $l = 1$ modes and due to quantum interference, a line of minimal atomic density appears. In the presence of non-linear interactions, this nodal line shows a soliton-like rotating motion. An analytical expression relating the angular frequency of the rotation of the minimal density line, Ω_m , to the strength of the non-linear

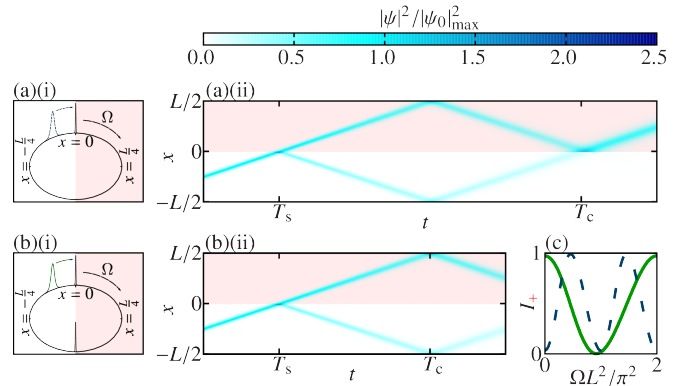


FIG. 42. (Taken from Ref.⁴⁸¹). An incoming soliton splits at time T_s on a barrier into two solitons of equal amplitude and opposite velocity. At a time T_c the solitons recombine either at the same barrier (a), or a second barrier (b) antipodal to the first (the example value of Ω is the same in both cases). The resulting phase difference is read out via the population difference in the final output products within the positive (shaded) and negative domains. (c) Final population in the positive domain I_+ as a function of Ω . The sensitivity of the single barrier case (dashed line) is twice that of the double barrier case (solid line) because the interrogation time $T_c - T_s$ is doubled.

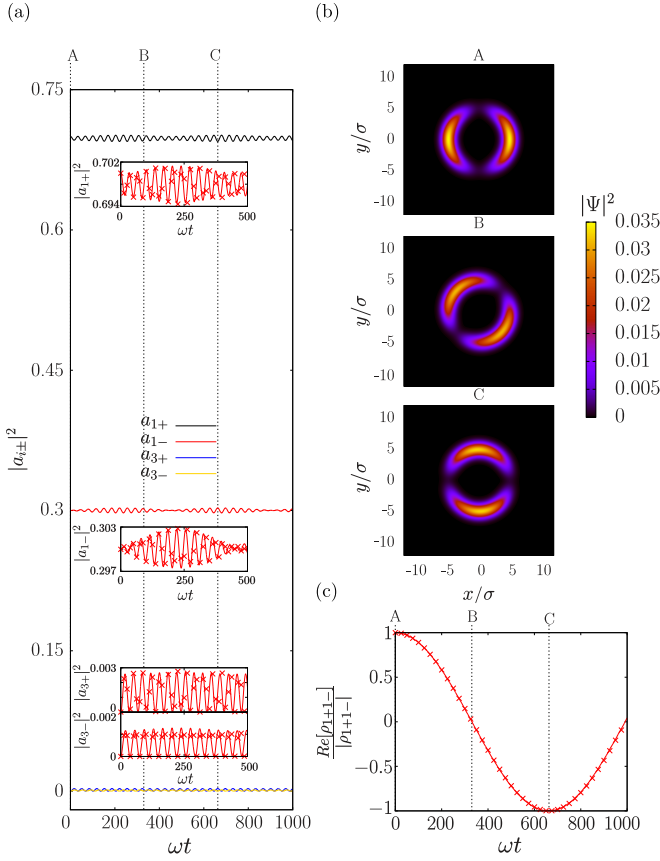


FIG. 43. (a) Time evolution of the population of the states involved in the dynamics. (b) Snapshots of the density profile for different instants of the dynamical evolution. (c) Time evolution of the real part of the coherence between the $|1, +\rangle$ and $|1, -\rangle$ states. The points correspond to the numerical simulation of the GPE, while the continuous lines are obtained by solving the FSM equations. The considered parameter values are $R = 5$, $g_{2d} = 1$, for which $U = 0.0128$, $\mu_1 = 0.529$ and $\mu_3 = 0.699$, $a_{1+}(0) = \sqrt{p_{1+}(0)} = \sqrt{0.7}$ and $a_{1-}(0) = \sqrt{p_{1-}(0)} = \sqrt{0.3}$. Taken from Ref. 503.

atom-atom interactions and the difference between the populations of the counter-propagating modes is derived:

$$\Omega_m = \frac{U n_{1\pm}}{2(1 + \frac{U}{\Delta})}. \quad (65)$$

where $n_{1\pm}$ is the population imbalance between the $l = \pm 1$ modes, U is a non-linear parameter proportional to the scattering length, and Δ is the chemical potential difference between the $l = 3$ and $l = 1$ modes, see⁵⁰³. This expression constitutes the basis to use the physical system under consideration as a quantum sensing device by measuring the rotation frequency of the minimum density line by direct imaging, in real time, the spatial density distribution of the BEC. In fact, a full experimental protocol based on direct fluorescence imaging of the BEC that allows to measure all the quantities involved in the analytical model is proposed.

Let us assume that the lifetime of the BEC is τ . Then, the condition $\Omega_m \omega \gtrsim 1/\tau$ being ω the ring trapping frequency

must be fulfilled to be able to observe the rotation of the minimum density line for the time the experiment lasts. The upper limit of observable values of Ω is imposed by the regime of validity of the model, i.e., $\Omega_m < 0.025$ to avoid the excitation of states with OAM higher than 1. A magnetic field produces, in general, a variation of the scattering length, which does not depend on the magnetic field orientation. Therefore, the presence of an external magnetic field will induce a variation of Ω_m and the system could be used as a scalar magnetometer by relating changes on the frequency of rotation of the minimal line to variations of the modulus of the magnetic field. The sensitivity in the measurement of magnetic field variations increases with the number of condensed particles but keeping the scattering length small and having a strong dependence of the scattering length on the magnetic field modulus. Thus, close to a Feshbach resonance, these requirements could be met. However, close to a Feshbach resonance the three-body losses may limit the lifetime of the BEC making difficult the measurement. Nevertheless, some atomic species such as ^{85}Rb , ^{133}Cs , ^{39}K or ^7Li have been reported to form BECs that are stable across Feshbach resonances with lifetimes on the order of a few seconds, so they could be potential candidates for using the system as a magnetometer. Taking into account that the trapping frequency ω , is typically of the order of a few hundreds of Hz for ring-shaped traps, and considering typical values of $\Omega_m \omega \sim 1\text{Hz}$ compatibles with typical times for the experiment of around $\tau \sim 1\text{s}$, the minimum density line would perform some complete round trips. Assuming that one could resolve angular differences on the order of ~ 0.1 rad, variations in the rotation frequency on the order of 10^{-2}Hz could be measured. Thus, for the parameter values reported in⁵⁰⁴, in principle, this magnetometer would allow to measure changes in the magnetic field on the order of a few pT at a bandwidth of 1 Hz.

E. Summary and outlook

In this section we have presented some examples for engineering of atomtronic devices. We have discussed recent advances in the development of basic components for atomtronics such as batteries, diodes, and transistors. However, atomtronics applications are expected to go beyond analogs of electronic circuits with atoms by making use of the specific quantum properties of ultra-cold atomic matter. In this context, we have shown that by taking advantage of quantum coherence and interactions between ultra-cold atoms, it is possible to design atomtronic SQUIDS, matter-wave interferometers, as well as rotation and magnetic sensors with extremely high accuracy and resolution. All these applications open the door to the future development of completely new types of quantum devices, which might be integrated into complex and large-scale atomtronic circuits.

Acknowledgements V.A. and J.M. would like to thank Gerard Pelegrí for fruitful discussions and acknowledge financial support from the Ministerio de Economía y Competitividad, MINECO, (FIS2017-86530-P), from the Generalitat de Catalunya (SGR2017-1646), and from the European Union

Regional Development Fund within the ERDF Operational Program of Catalunya (project QUASICAT/QuantumCat). V.A., G.B., and J.M. thank the DAAD for financial support through contracts DAAD 50024895 and DAAD 57059126. B.M.G. and A.S.A. would like to acknowledge support from the UK EPSRC grant EP/M013294/1.

X. TWO LEVEL QUANTUM DYNAMICS IN RING-SHAPED CONDENSATES AND MACROSCOPIC QUANTUM COHERENCE

D. Aghamalyan, M. Boshier, R. Dumke, T. Haug, A. Minguzzi, L.-C. Kwek, L. Amico

A qubit is a two state quantum system that can be coherently manipulated, coupled to its neighbours, and measured. Several qubit physical implementations have been proposed in the last decade, all of them presenting specific virtues and bottlenecks at different levels^{505–510}. In neutral cold atoms proposals the qubit is encoded into well isolated internal atomic states. This allows long coherence times, precise state read-out and, in principle, scalable quantum registers. However, individual qubit (atom) addressing is a delicate point^{511,512}. Qubits based on Josephson junctions allow fast gate operations and make use of the precision reached by lithography techniques⁵¹³. The decoherence, however, is fast in these systems and it is experimentally challenging to reduce it. For charge qubits the main problem arises from dephasing due to background charges in the substrate; flux qubits are insensitive to the latter decoherence source, but are influenced by magnetic flux fluctuations due to impaired spins proximal to the device⁵⁰⁵.

Here we aim at combining the advantages of cold atom and Josephson junction based implementations. The basic idea is to use the persistent currents flowing through ring shaped optical lattices^{360,514–520} to realize a cold atom analogue of the superconducting flux qubit (see^{514,521–523} for the different schemes that can be applied to induce persistent currents). A barrier potential painted along the ring gives rise to a weak link, acting as a source of back-scattering for the propagating condensate, thus creating an interference state with the forward scattered current. This gives rise to an atomic condensate counterpart of the celebrated rf-SQUID—a superconducting ring interrupted by a Josephson junction^{6,505}, namely an Atomtronics Quantum Interference Device (AQUID). Due to the promising combination of advantages characterizing Josephson junctions and cold atoms, the AQUID is now object of intense investigation^{7,352}. The first experimental realizations have been done by means of a Bose-Einstein condensate free to move along a toroidal potential, except through a small spatial region, where a very focused blue-detuned laser creates weak links, namely an effective potential constriction^{22,67,128}. By adapting the logic applied in the context of solid state Josephson junctions^{505,524} to a specific cold atoms setup, a cold atom version of the SQUID can be created. On the theoretical side, it has been demonstrated that the two currents flowing in the AQUID can, indeed, define an ef-

fective two-level system, that is, the cold-atom analog of flux qubits^{514–517,525}. The system is assumed to be driven by an effective flux piercing the ring lattice. The potential constriction breaks the Galilean invariance and splits the qubit levels, that otherwise would be perfectly degenerate at half-flux quantum. By a combination of analytic and numerical techniques, one can demonstrate that the system can sustain a two-level effective dynamics^{514–517}. We also review a physical system consisting of a Bose-Einstein condensate confined to a ring shaped lattice potential interrupted by three weak links⁵¹⁶. By employing path integral techniques, we explore the effective quantum dynamics of the system in a pure quantum phase dynamics regime. By a combination of analytic and numerical techniques, it was demonstrated that the system can sustain a two-level effective dynamics giving other realization of atomtronic qubit.

The current and type of state inside these atomic qubits can be read out via time-of-flight measurements⁵²⁶. When the ring is interfered with a reference condensate, a spiral pattern appears in the time-of-flight, which indicates the magnitude and direction of the current. For low resolution images, these spirals can be read out from the density-density correlation images. Furthermore, the type of superposition state can be measured from the noise in the time-of-flight images.

Progress towards an experimental realization has been made recently. Here, the interference of currents has been demonstrated experimentally in AQUIDs¹¹³. By inducing a bias current in a rotating atomic ring interrupted by two weak links, the interference between the Josephson current with the current from the rotation creates a oscillation in the critical current with applied flux. This oscillation is measured experimentally in the transition from the DC to the AC Josephson effect.

A. The Atomtronic quantum interference device: AQUID

We start by considering analytical models for the confined one-dimensional many-body systems and use them to demonstrate an emerging effective two level dynamics of the system. Let us start by considering N interacting bosons at zero temperature, loaded into a 1D ring-shaped optical lattice of M sites. The discrete rotational symmetry of the lattice ring is broken by the presence of a localized potential in one lattice site (later we also consider case of three weak links), which gives rise to a weak link. The relevant physics of the system is captured by the Bose-Hubbard Model. The Hamiltonian reads

$$\mathcal{H}_{\text{BH}} = \sum_{i=1}^M \left[\frac{U}{2} n_i(n_i - 1) + \Lambda_i n_i - J_i \left(e^{-i2\pi\Omega/M} a_{i+1}^\dagger a_i + \text{h.c.} \right) \right] \quad (66)$$

where a_i (a_i^\dagger) are bosonic annihilation (creation) operators on the i th site of a ring with length M and $n_i = a_i^\dagger a_i$ is the corresponding number operator. Periodic boundaries are imposed, meaning that $a_M \equiv a_0$. The parameter U takes into account the finite scattering length for the atomic two-body collisions on the same site: $U = 4\pi\hbar^2 a_0 \int dx |w(x)|^4 / m$, $w(x)$ being the Wannier functions of the lattice, m the mass of atoms and

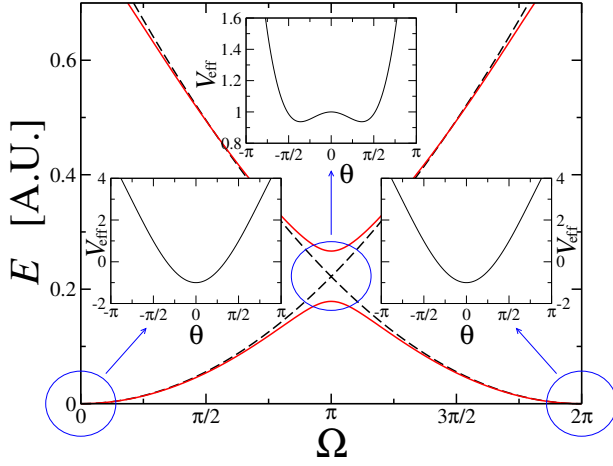


FIG. 44. Main panel: sketch of the qubit energy splitting, due to the barrier Λ , for the two lowest-lying energy states in the many-body spectrum of model (66). Black dashed lines denote the ground-state energy in absence of the barrier, as a function of the flux Ω . Switching on the barrier opens a gap at the frustration point $\Omega = \pi$ (continuous red lines). The three insets show the qualitative form of the effective potential at $\Omega = 0, \pi, 2\pi$. Note the characteristic double-well shape forming at $\Omega = \pi$. The qubit, or effective two-level system, corresponds to the two lowest energy levels of this potential. In this figure the energies are plotted in arbitrary units.

a_0 the scattering length. To break the translational symmetry, there are two possible ways: Either, the hopping parameters are all equal $J_i = J$ except in one weak-link hopping i_0 where $J_{i_0} = J'$. The other alternative, which we choose in this review, is to place a potential barrier at a single site $\Lambda_i = \Lambda$ and at all other sites the potential is set to zero, with $J_i = J, \forall i$. The two options show qualitatively the same physics⁵¹⁶. The ring is pierced by an artificial (dimensionless) magnetic flux Ω , which can be experimentally induced for neutral atoms as a Coriolis flux by rotating the lattice at constant velocity^{22,67,128}, or as a synthetic gauge flux by imparting a geometric phase directly to the atoms via suitably designed laser fields^{523,527}. The presence of the flux Ω in Eq.(66) has been taken into account through the Peierls substitution: $J_i \rightarrow e^{-i2\pi\Omega/M} J_i$. The Hamiltonian (Eq.71) is manifestly periodic in Ω with period 1. In the absence of the weak-link, the system is also rotationally invariant and therefore the particle-particle interaction energy does not depend on Ω . The many-body ground-state energy, as a function of Ω , is therefore given by a set of parabolas intersecting at the frustration points $\Omega_n = (n + \frac{1}{2})$ ^{414,528}. The presence of the weak-link breaks the axial rotational symmetry and couples different angular momenta states, thus lifting the degeneracy at Ω_n . This feature sets the qubit operating point^{515,516}.

It is worth noting that the interaction U and the weak-link strength induce competing physical effects: the weak-link sets an healing length in the density as a further spatial scale; the interaction tends to smooth out the healing length effect. As a result, strong interactions tends to renormalize the weak link energy scale^{364,516,518}.

In the limit of a large number of bosons in each well $\bar{n} =$

$N/M, a_i \sim \sqrt{\bar{n}} e^{i\phi_i}$, and the Bose-Hubbard hamiltonian (BHH) (66) can be mapped to the Quantum-Phase model employed to describe Josephson junction arrays^{529,530}:

$$\mathcal{H} = \sum_{i=1}^M \left[\frac{U}{2} n_i^2 - J_i \cos(\phi_{i+1} - \phi_i - \Omega) \right] \quad (67)$$

where $[n_i, \phi_i] = i\hbar \delta_{il}$ are canonically conjugate number-phase variables and $J_i \sim \bar{n} t_i$ are the Josephson tunneling amplitudes.

a. The rf-AQUID qubit. In this case, a single weak link occurs along the ring lattice $t'' = t$. The presence of the weak link induces a slow/fast separation of the effective (imaginary time) dynamics: the dynamical variables relative to the weak link are slow compared to the 'bulk' ones, playing the role of an effective bath (nonetheless, we assume that the ring system is perfectly isolated from the environment). Applying the harmonic approximation to the fast dynamics and integrating it out, the effective dynamics of the AQUID is governed by (See for detailed derivation appendix material of⁵¹⁵)

$$\mathcal{H}_{\text{eff}} = \mathcal{H}_{\text{syst}} + \mathcal{H}_{\text{bath}} + \mathcal{H}_{\text{syst-bath}} \quad (68)$$

The slow dynamics is controlled by

$$\mathcal{H}_{\text{syst}} = U n^2 + E_L \varphi^2 - E_J \cos(\varphi - \Omega) \quad (69)$$

where φ is the phase slip across the weak link, with $E_L = J/M$, and $E_J = J'$. For $\delta \doteq E_J/E_L \geq 1$, $\mathcal{H}_{\text{syst}}$ describes a particle in a double well potential with the two-minima-well (See Fig. (44)) separated from the other features of the potential. The two parameters, U and t'/t , allow control of the two level system. The two local minima of the double well are degenerate for $\Omega = \pi$. The minima correspond to the clock-wise and anti-clockwise currents in the AQUID. The presence of a finite barrier, $\Lambda > 0$, breaks the axial rotational symmetry and couples different angular momenta, thus lifting the degeneracy at the frustration points by an amount ΔE , see Fig. 44. Provided other excitations are energetically far enough from the two competing ground-states, this will identify the two-level system defining the desired qubit and its working point. Because of the quantum tunneling between the two minima of the double well, the two states of the system (qubit) are formed by symmetric and antisymmetric combinations of the two circulating current states.

The WKB level splitting is (see for detailed derivation Appendix C.3⁵³¹)

$$\Delta \simeq \frac{2\sqrt{UE_J}}{\pi} \sqrt{1 - \frac{1}{\delta}} e^{-12\sqrt{E_J/U}(1-1/\delta)^{3/2}}. \quad (70)$$

From this formula we can see that the limit of a weak barrier and intermediate to strong interactions form the most favourable regime to obtain a finite gap between the two energy levels of the double level potential as depicted on Fig. (44). Incidentally, we comment that the bath Hamiltonian in Eqs.(68), (69), is similar to the one describing the dissipative dynamics of a single Josephson junction in the framework of the Caldeira-Leggett model⁴¹⁴. As long as the ring has fi-

nite size, however, there are a finite number of discrete modes and no real dissipation occurs⁵³². In the limit $N \rightarrow \infty$, a proper Caldeira-Leggett model is recovered. In agreement to the arguments reported above, the qubit dynamics encoded in the AQUID is less and less addressable by increasing the size of the ring^{515,516}.

b. Atomtronic flux-qubit: Ring lattice interrupted with three weak links. Here we consider N Bosons in an M site ring described by the Bose-Hubbard Model. The Hamiltonian reads

$$\mathcal{H}_{\text{BHH}} = \sum_{i=1}^M \left[\frac{U}{2} n_i(n_i - 1) - t_i \left(e^{i\Omega} a_{i+1}^\dagger a_i + \text{h.c.} \right) \right]. \quad (71)$$

where a_i (a_i^\dagger) are bosonic annihilation (creation) operators on the i th site and $n_i = a_i^\dagger a_i$ is the corresponding number operator. Periodic boundaries are imposed, meaning that $a_M \equiv a_0$. The parameter U takes into account the finite scattering length

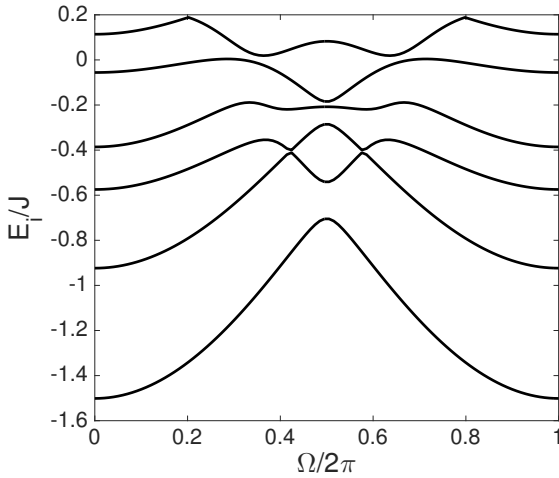


FIG. 45. Six first energy levels of the reduced system given by the effective potential Eq. (75) as a function of the dimensionless external flux Ω . Here $J' = 0.7J$, $J'' = 0.8J$, $U = 0.5J$, and $\theta_1 = -\theta_2$.

for the atomic two-body collisions on the same site. The hopping parameters are constant $t_j = t$ except in the three weak-links lattice sites i_0, i_1, i_2 where they are $t_{i_0} = t'$, $t_{i_1} = t_2 = t''$. The ring is pierced by an artificial (dimensionless) magnetic flux Ω , which can be experimentally induced for neutral atoms as a Coriolis flux by rotating the lattice at constant velocity^{128,533}, or as a synthetic gauge flux by imparting a geometric phase directly to the atoms via suitably designed laser fields^{527,534,535}. The presence of the flux Ω in (Eq.71) has been taken into account through the Peierls substitution: $t_i \rightarrow e^{-i\Omega} t_i$. The Hamiltonian (Eq.71) is manifestly periodic in Ω with period 2π ; in addition it enjoys the symmetry $\Omega \leftrightarrow -\Omega$. The presence of the weak-link breaks the axial rotational symmetry and couples different angular momenta states, thus lifting the degeneracy at Ω_n . This feature sets the qubit operating point^{515,516}.

Here again in the limit of a large number of bosons in each well $\bar{n} = N/M$, $a_i \sim \sqrt{\bar{n}} e^{i\phi_i}$, and the Bose-Hubbard hamiltonian

(BHH) (Eq.71) can be mapped to the Quantum-Phase model and equivalent Hamiltonian is given by Eq. (67).

The effective action for the quantum phase model reads (See for details⁵¹⁷)

$$S_{\text{eff}} = \sum_{\alpha=0,1,2} \int_0^\beta d\tau \left[\frac{1}{U} \dot{\theta}_\alpha^2 + V(\theta_\alpha) \right] \quad (72)$$

$$- \frac{J}{U} \int d\tau d\tau' \theta_\alpha(\tau) G_\alpha(\tau - \tau') \theta_\alpha(\tau') \quad (73)$$

where

$$V(\theta_\alpha) \doteq J c_\alpha \theta_\alpha^2 - \frac{J'}{3} \cos(\theta_1 - \theta_2 - \Omega) - \frac{J''}{3} (\cos \theta_1 + \cos \theta_2) \quad (74)$$

with $c_\alpha = \frac{1}{2} \left(\frac{1}{2} - UJ \sum_{k=1}^{M-4} \frac{\zeta_{\alpha k}^2}{\omega_k^2} \right)$. The interaction between the fast and the slow modes is described by the kernel

$$G_\alpha(\tau) = \sum_{l=0}^{\infty} \sum_{k=1}^{M-4} \frac{\omega_l^2 \zeta_{\alpha k}^2}{\omega_k^2 + \omega_l^2} e^{i\omega_l \tau}. \quad (75)$$

We observe that $V(\theta_\alpha)$ defines the effective dynamics of the superconducting Josephson junctions flux qubits^{524,536}, but perturbed by the θ^2 terms; by numerical inspection, we see that the corresponding coefficients are small in units of J , and decreases by increasing M . Moreover, on Fig.45 we introduce the numerical result for the spectrum of the quantum particle which moves in the potential given by Eq. (75) under the additional assumption that θ^2 terms do not contribute. From this figure we clearly see that near the frustration point $\Omega = \pi$ two lowest energy levels are well separated from each other and from higher excitations, which means that effective dynamics of the system defines a qubit. It is important to point out that quantum phase model is applicable in the limit of the high filling, however the results for the effective-two level description were demonstrated to hold in the limit of low filling by applying an exact diagonalization method for the Boese-Hubbard model as it has been demonstrated in Refs.^{516,517}.

B. Demonstration of the one qubit and two qubit unitary gates

The aim of this section is to show how the effective phase dynamics of optical ring-lattices with impurities serves to the construction of one- and two-qubit gates - a necessity for a universal quantum computation. Here, we adapt results which were obtained by Solenov and Mozyrsky⁵³⁷ for the case of homogeneous rings with impurities. It results, that a single ring optical lattice with an impurity is described by the following effective Lagrangian (see the Eq. (69)):

$$L = \frac{1}{2U} \dot{\theta}^2 + \frac{J}{N-1} (\theta - \Phi)^2 - J' \cos \theta \quad (76)$$

Then we introduce the canonical momentum P in a usual way:

$$P = \frac{\partial L}{\partial \dot{\theta}} = \frac{1}{U} \dot{\theta} \quad (77)$$

After performing a Legendre transformation we get the following Hamiltonian:

$$H = J' \left[\frac{P^2}{2\mu} - \frac{J}{J'(N-1)} (\theta - \Phi)^2 + \cos \theta \right], \quad (78)$$

where $\mu = J'/U$ is an effective mass of the collective particle. The quantization is performed by the usual transformation $P \rightarrow -d/d\theta$. For $\delta = \frac{J'(N-1)}{2J} > 1$ the effective potential in Eq. (78) can be reduced to a double well; for $\Phi = \pi$, the two lowest levels of such double well are symmetric and antisymmetric superpositions of the states in the left and right wells respectively. The effective Hamiltonian can be written as:

$$H \simeq \varepsilon \sigma_z \quad (79)$$

and the lowest two states are $|\psi_g\rangle = (0, 1)^T$ and $|\psi_e\rangle = (1, 0)^T$. WKB estimate for the energy splitting ε of the qubit is given by the Eq.(70).

1. Single qubit gates

For the realization of single-qubit rotations, we consider the system close to the symmetric double well configuration $\Phi \simeq \pi$. In the basis of the two-level system discussed before, the Hamiltonian takes the form:

$$H \simeq \varepsilon \sigma_z + \frac{\Phi - \pi}{\delta} \langle \theta \rangle_{01} \sigma_x, \quad (80)$$

where $\langle \theta \rangle_{01}$ is the off-diagonal element of the phase-slip in the two-level system basis. It is easy to show that spin flip, Hadamard and phase gates can be realized by this Hamiltonian. For example, a phase gate can be realized by evolving the state through the unitary transformation $U_z(\beta)$ (tuning the second term of Eq.(80) to zero by adjusting the imprinted flux)

$$U_z(\beta) = \exp(i\varepsilon\tau\sigma_z) = \begin{pmatrix} e^{i\varepsilon\tau} & 0 \\ 0 & e^{-i\varepsilon\tau} \end{pmatrix}. \quad (81)$$

After tuning the gap energy close to zero (adjusting the barrier height of the impurity), we can realize the following rotation

$$U_x(\beta) = \exp(i\alpha\tau\sigma_x) = \begin{pmatrix} \cos \alpha & i \sin \alpha \\ i \sin \alpha & \cos \alpha \end{pmatrix} \quad (82)$$

where $\alpha = \frac{\Phi - \pi}{\delta} \langle \theta \rangle_{01} \tau$. When $\alpha = \pi/2$ and $\alpha = \pi/4$ the NOT and Hadamard gates are respectively realized.

2. Two-qubit coupling and gates

The effective dynamics for two coupled qubits, each realized as single ring with localized impurity (as in Fig.50), is governed by the Lagrangian

$$L = \sum_{\alpha=a,b} \frac{1}{2U} \dot{\theta}_\alpha^2 + \left[\frac{J}{2(N-1)} (\theta_\alpha - \Phi_\alpha)^2 - J' \cos(\theta_\alpha) \right] - \tilde{J}'' \cos[\theta_a - \theta_b - \frac{N-2}{N} (\Phi_a - \Phi_b)] \quad (83)$$

Where J'' is the Josephson tunnelling energy between the two rings. When $\Phi_a = \Phi_b = \Phi$ and $J'' \ll J'$ the last term reduces to $-J'' \frac{(\theta_a - \theta_b)^2}{2}$ and the Lagrangian takes the form

$$L = J' \left[\sum_{\alpha=a,b} \frac{1}{2J'U} \dot{\theta}_\alpha^2 + \left[\frac{J}{2J'(N-1)} (\theta_\alpha - \Phi_\alpha)^2 - \cos(\theta_\alpha) \right] + \frac{J''}{J'} \frac{(\theta_a - \theta_b)^2}{2} \right]. \quad (84)$$

By applying the same procedure as in the previous section, we obtain the following Hamiltonian in the eigen-basis of the two-level systems of rings a and b

$$H = H_a + H_b + \frac{J''}{J'} \sigma_x^1 \sigma_x^2 \langle \theta \rangle_{01}^2, \quad (85)$$

$$H_\alpha = \varepsilon \sigma_z^\alpha + \left(\frac{\Phi - \pi}{\delta} + \frac{J'' \pi}{J'} \right) \langle \theta \rangle_{01} \sigma_x^\alpha. \quad (86)$$

From this equations it follows that qubit-qubit interactions can be realized using our set-up. If we choose the tuning $\varepsilon \rightarrow 0$ and $\Phi \rightarrow \pi - \frac{\delta J'' \pi}{J'}$ the natural representation of a $(\text{SWAP})^\alpha$ gate⁵³⁸ can be obtained:

$$U(\tau) = \exp[-i \frac{J''}{J'} \sigma_x^1 \sigma_x^2 \tau], \quad (87)$$

where $\alpha = \frac{\tau J''}{J'}$. A CNOT gate can be realized by using two $\sqrt{\text{SWAP}}$ gates⁵³⁸. It is well known that one qubit rotations and a CNOT gate are sufficient to implement a set of universal quantum gates⁵³⁹.

C. Readout of atomtronic qubits

After preparing the atomtronic qubit, to verify the properties of the qubit, a readout of the current has to be performed. The existence of the atomic current flowing in AQUID can be detected by standard time-of-flight measurement of the ring condensate⁵¹⁶. A more in-depth analysis can be performed by interfering the ring condensate with a second condensate confined in the center of a ring. This condensate sets a phase reference for the phase winding of the ring condensate. By *in-situ* measurement of the two interfering condensates the self-heterodyne detection of the phase of the wave function is realized. For weakly interacting continuous ring systems, where no entanglement is present, both the orientation and the intensity of the current states have been detected^{116,354,355,540,541}.

For atomtronic qubits, this detection scheme has to be applied to the case of ring lattices with stronger interactions. This has been studied in⁵²⁶ and the key results are shown below.

1. Interferometric detection of the current states

To read-out the direction and the intensity of the current in the ring lattice, an approach originally carried out by the Maryland and Paris groups to map-out the circulating states in continuous ring-shaped condensates can be applied^{7,110,128,354,540}. Accordingly, the ring condensate is made to interfere with another condensate at rest, located at the center, fixing the reference for the phase of the wavefunction. The combined wavefunction evolves in time, interferes with itself and finally is measured. The number of spirals gives the total number of rotation quanta.

In the actual experiment, the condensate is imaged through in-situ measurements. In this way, the current direction and magnitude is well visible as a spiral pattern. The position of the spirals depends on the relative phase between ring and the central condensate. In a single experimental run, the spirals will be visible for a condensate with high number of particles. However, if the number of particles is low or the atom imaging is inefficient, one has to average over multiple shots and take expectation values, which experimentally corresponds to take averaged results over many experimental runs. However, every realization of the experiment has a random phase in the phase of the spirals, which is averaged out over many repetitions. As the relative phase between ring and central condensate is determined randomly upon measurement, the expectation value of the density operator will average over different realizations of the spiral interference pattern, washing out the information on the current configuration structure. However, as we show below, the information about the spirals can be recovered using density-density correlations.

The expansion dynamics is modeled with the Bose-Hubbard model. The ring wavefunction is calculated by solving the ground state of the Bose-Hubbard Hamiltonian, while the central condensate is simply a single decoupled site with N_c particles. The dynamics of the density $\hat{n}(\mathbf{r}, t) = \hat{\psi}^\dagger(\mathbf{r}, t)\hat{\psi}(\mathbf{r}, t)$ is initialized assuming that the bosonic field operator of the system is $\hat{\psi}(\mathbf{r}) = \sum_n w_n(\mathbf{r})\hat{a}_n$, where $w_n(\mathbf{r})$ are a set of Wannier functions forming a complete basis^{542,543}. In our calculation, we approximate the full basis for wave functions living in the ambient space on which the condensate expands with the set of Wannier functions composed of Gaussians peaked at the ring lattice sites and at its centre (the Gaussian approximation for the Wannier functions is a well verified approximation for single site wavefunctions – see f.i.^{544,545}). For the free evolution (we are indeed in a dilute limit) we assume that each particle at site n expands in two dimensions as

$$w_n(\mathbf{r}, t) = \frac{1}{\sqrt{\pi}} \frac{\sigma_n}{\sigma_n^2 + \frac{i\hbar t}{m}} e^{-\frac{(\mathbf{r}-\mathbf{r}_n)^2}{2(\sigma_n^2 + \frac{i\hbar t}{m})}}, \quad (88)$$

where σ_n is the width of the condensate located at the n -th site. The dynamics of the condensates is then approximated as $\hat{\psi}(\mathbf{r}, t) = \sum_n w_n(\mathbf{r}, t)\hat{a}_n$. We observe that such approximation works well in the situations in which the optical lattice is assumed to be sufficiently dense in the space in which the condensate is released (as in the release from large three dimensional optical lattices).

To observe the interference, and thus the qubit properties, using averaging over multiple shots, the interference pattern is measured with higher order density-density correlations. We calculate the density-density covariance^{546–549}

$$\text{cov}(\mathbf{r}, \mathbf{r}', t) = \langle \hat{n}(\mathbf{r}, t)\hat{n}(\mathbf{r}', t) \rangle - \langle \hat{n}(\mathbf{r}, t) \rangle \langle \hat{n}(\mathbf{r}', t) \rangle. \quad (89)$$

We also define the root of the density covariance which has the same unit as the density to improve the contrast of the measured interference pattern

$$\sigma(\mathbf{r}, \mathbf{r}', t) = \text{sgn}(\text{cov}(\mathbf{r}, \mathbf{r}', t)) \sqrt{|\text{cov}(\mathbf{r}, \mathbf{r}', t)|}. \quad (90)$$

First, we plot the expectation value of the density of expanded atoms for different values of interaction at the degeneracy point $\Omega = 1/2$ in Fig.46. The density of expanded atoms at longer times has some characteristic features depending on the interaction. For interaction energy smaller than the potential barrier, the center shows a characteristic bright and dark spot. For stronger interaction, it becomes a single, blurred spot. At the degeneracy point we observe a superposition of counter-flowing current states. Interaction modifies the many-body entanglement, which changes the characteristic time-of-flight pattern. After a long enough free expansion, the atom density assumes the initial momentum distribution. However, it is difficult to read out the exact state of the current as the characteristic spirals are not visible in the expectation values of the density.

Next, we show the density-density covariance $\sigma(\mathbf{r}, \mathbf{r}')$ in Fig.47. A clear spiral pattern emerges here. In this case, a step in the spirals at the weak link site (here at the center bottom) is clearly visible for intermediate times. This indicates the appearance of a superposition of two winding numbers. Although the interferometric pictures can look similar, different interactions lead to current states that may be very different in nature. For $U = 0$, the current is in a non-entangled superposition state, whereas for interaction $U = J$ in a highly entangled NOON state.

Below, we shall see how additional information on the states can be grasped analysing the noise in the momentum distribution of the ring condensate. Indeed, the noise for zero momentum depends strongly on the specific entanglement between the clockwise and anti-clockwise flows. In the case of an entangled cat state all atoms have together either zero or one momentum quanta. A projective measurement will collapse the wavefunction to either all atoms in the zero or one momentum state. Averaging over many repeated measurements will result in erratic statics of the measurements. In contrast, in non-entangled single-particle superpositions, each particle has independently either zero or one momenta quanta. A single projective measurement will result in on average half

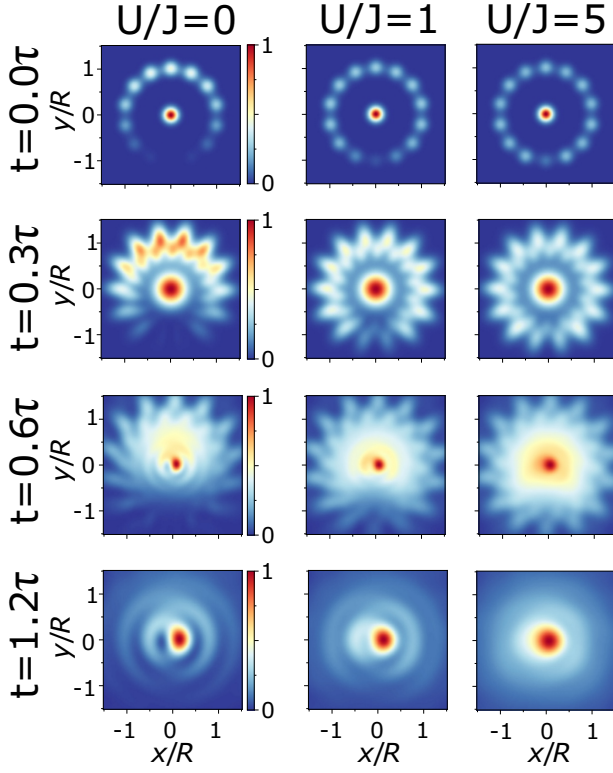


FIG. 46. Density of expanding atoms at times $t = 0, 0.3\tau, 0.6\tau, 1.2\tau$, with $\tau = mR\sigma_r/\hbar$. From left to right: $U = 0, U/J = 1, U/J = 5$. Flux $\Omega = \frac{1}{2}$ at the degeneracy point. At intermediate time, we observe some spiral-like structure at the edges. This is not the interference with the central condensate, but a residue of the ring lattice interfering with itself. Calculated using Bose-Hubbard model, no interaction during expansion. Data in color and normalized to one. Ring has 7 particles, $M = 14$ ring sites, ring radius R . Width of central and ring cloud is $\sigma_r = 2R/L$ and potential barrier $\Lambda = J$, 25% of atoms in central condensate. Barrier at $x = 0, y = -R$.

the atoms having zero and half the atoms having one rotation quantum. Therefore, fluctuations averaged over many measurements will be low. We define the noise of the momentum distribution

$$\sigma_k(\mathbf{k}) = \sqrt{\langle \hat{n}(\mathbf{k}) \hat{n}(\mathbf{k}) \rangle - \langle \hat{n}(\mathbf{k}) \rangle \langle \hat{n}(\mathbf{k}) \rangle}. \quad (91)$$

Having in mind a time-of-flight experiment, the optimal point to measure the noise is at $\mathbf{k} = 0$, as at this point the density is maximal for zero rotation quanta, and zero for one or more rotation quanta. We plot the noise of the time-of-flight image at $\mathbf{k} = 0$ without a central condensate in Fig.48. First, the interaction U and weak link Λ is plotted in Fig.48a. We see that the momentum noise is minimal in the parameter regime $U/J \ll 1$ and $\Lambda/J > cU/J$, where c is some constant, which corresponds to the mean-field limit. As soon the interaction becomes larger than the energy gap induced by the potential barrier, the noise increases. Here, entangled phase winding states of zero and one winding quantum appear. For large interaction, the noise decreases again, however remains higher than in the mean-field regime. With increasing interac-

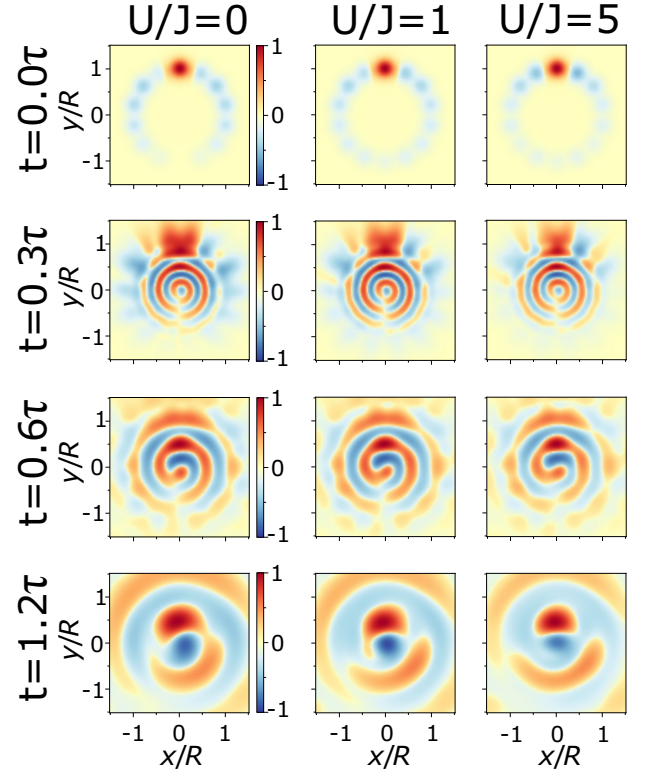


FIG. 47. Root of density-density covariance $\sigma(\mathbf{r}, \mathbf{r}') = \{0, R/2\}$ of expanding atoms with flux $\Omega = \frac{1}{2}$ at the degeneracy point. The discontinuity in the bottom of the spirals at intermediate times $t = 0.3\tau$ and $t = 0.6\tau$ shows that the ring condensate is in a superposition of zero and one rotation quantum. Same parameters as Fig. 46.

tion, we can define three regimes of entanglement⁵⁵⁰. At the degeneracy point $\Omega = \frac{1}{2}$, for interaction smaller than the energy gap created by the weak link, we observe one-particle superposition states $|\Psi\rangle \propto (|l=0\rangle + |l=1\rangle)^N$, where N is the number of particles and l is the angular momentum of the atom. This regime is well described by the Gross-Pitaevskii equation. Here, the noise at $\mathbf{k} = 0$ is minimal and is given by $\sigma_k^{\text{GP}}(\mathbf{k} = 0) \propto \sqrt{N}/4$. When the interaction and the weak-link energy gap is on the same order, the near-degenerate many body states mix and entangled NOON states are formed $|\Psi\rangle \propto |l=0\rangle^N + |l=1\rangle^N$. The noise is maximal and given by $\sigma_k^{\text{NOON}}(\mathbf{k} = 0) \propto N/4$. The ratio of the minimal and maximal noise is \sqrt{N} . Thus, with increasing particle number the superposition and entangled states are clearer to distinguish. Increasing interaction further will fermionize the system. With interaction, angular momentum of each atom individually is not conserved, however the center of mass angular momentum K of the whole condensate is. Then, the ground state is a superposition of $|\Psi\rangle \propto |K=0\rangle + |K=N\rangle$.

Next, the momentum noise is plotted against applied flux Ω in Fig.48b. Due to the two level system effective physics, the noise in the time-of-flight of the ring condensate is particularly pronounced at the degeneracy points. This phenomenon allows to detect the degeneracy point in the ring condensate, without resorting the heterodyne detection protocol. The noise

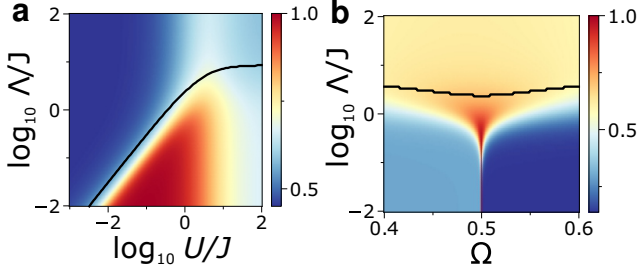


FIG. 48. Momentum noise $\sigma_k(\mathbf{k}=0)$ (in color, normalized to one) plotted for potential barrier Λ against **a)** on-site interaction U ($\Omega = \frac{1}{2}$) and **b)** flux Ω ($U/J = 1$). Momentum noise is extracted from time-of-flight image after long expansion. Only ring is expanded, without central condensate. Black line shows the critical point where depletion at the potential barrier is 1% of the average particle number per site. Above the line the potential barrier site is depleted. Other parameters are $M = 11$ ring sites and 5 particles.

is maximal at the degeneracy point and when barrier and interaction are on the same order. Changing the flux away from the degeneracy point decreases the noise.

Further information can be identified by looking at the density at the site of the weak link. For zero on-site interaction, the site at the potential barrier is always depleted at the degeneracy point for any value of potential barrier strength. However, when the interaction exceeds a critical value, particles start occupying the site⁵¹⁶. This is plotted as black line in Fig.48. For small interaction the critical value has a linear relationship between U and Λ ⁵¹⁶. The filling of the potential barrier site indicates the onset of entanglement between different flux quanta. The depletion factor can be measured by a lattice-site resolved absorption measurements.

D. Experimental realization of the ring-lattice potential with weak links

In this section, we provide the experimental details for the realization of ring-lattice potentials with weak-links. Among the different architectures, the focus is on the structure that can be relevant for the construction of two level quantum systems.

a. A ring lattice with single weak link The optical potential was created with a liquid crystal on silicon spatial light modulator (PLUTO phase only SLM, Holoeye Photonics AG) which imprints a controlled phase onto a collimated laser beam from a 532 nm wavelength diode pumped solid state (DPSS) laser. The SLM acts as a programmable phase array and modifies locally the phase of an incoming beam. Diffracted light from the computer generated phase hologram then forms the desired intensity pattern in the focal plane of an optical system (doublet lens, $f=150$ mm). The resulting intensity distribution is related to the phase distribution of the beam exiting the SLM by Fourier transform. Calculation of the required SLM phase pattern (kinoform) has been carried out using an improved version of the Mixed-Region-Amplitude-Freedom (MRAF) algorithm^{551,552} with angular spectrum propagator. This allows to simulate numerically the

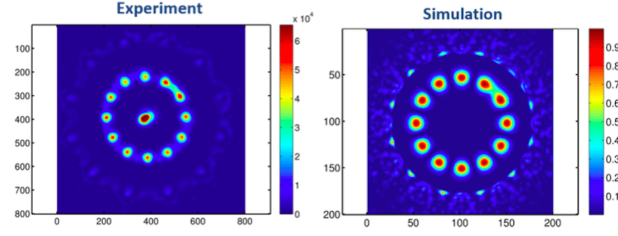


FIG. 49. Simulation(left) and experimentally realized(right) intensity distribution of a ring- lattice with a weak link between two lattice sites.

wavefront propagation in the optical system without resorting to paraxial approximation. A region outside the desired ring lattice pattern (noise region) is dedicated to collect unwanted light contributions resulting from the MRAF algorithm's iterative optimization process. This can be seen in the measured intensity pattern in Fig. 49 as concentric, periodic structures surrounding the ring-lattice and can be filtered out by an aperture.

The ring-lattice potential shown in Fig. 49 and Fig. 50 can be readily scaled down from a radius of $\sim 90 \mu\text{m}$ to $5-10 \mu\text{m}$ by using a 50x microscope objective with $\text{NA}=0.42$ numerical aperture (Mitutoyo 50x NIR M-Plan APO) as the focusing optics for the SLM beam and with $\lambda_2 = 830 \text{ nm}$ light, suitable for trapping Rubidium atoms. Accounting for the limited reflectivity and diffraction efficiency of the SLM, scattering into the noise region and losses in the optical system only about 5% of the laser light contributes to the optical trapping potential. However this is not a limiting factor for small ring-lattice sizes in the tenth of micrometer range as discussed here where $\sim 50 \text{ mW}$ laser power is sufficient to produce well depths of several E_{rec} . The generated structures are sufficiently smooth, with a measured intensity variation of 4.5% rms, to sustain persistent flow-states⁶⁷. The barrier height can be dynamically modified at a rate up to 50 ms per step, with an upper limit imposed by the frame update rate of the SLM LCD panel (60 Hz).

b. Experimental realization of the ring-lattice potential with three weak links We produce the optical potential using a spatial light modulator (Holey Photonics AG, PLUTO-NIR II), SLM. A collimated Gaussian beam, of 8 mm diameter, is reflected from the SLM's surface forming an image through a $f = 200$ mm lens. The light is then split into the two sides of our system, with 10% of the light in the "monitoring" arm, and 90% into the "trapping" arm used to create a red-detuned dipole trapping potential for a gas of Rb ⁸⁷ atoms. A Ti:Saph laser (Coherent MBR-110) produces a 1W, 828 nm beam, which is spacially filtered and collimated, before reflection on the SLM. To produce the trapping potential the SLM's kinoform is imaged through a $4f$ lens system reducing the beam size to 3 mm diameter and focused through a 50X microscope objective with a 4 mm focal distance and a numerical aperture of $\text{NA} = 0.42$ (Mitutoyo 50X NIR M-Plan APO). The monitoring arm of the system creates an image of the potential through a 10X infinity-corrected microscope objective focused on a CCD camera (PointGrey FL3-GE-13S2M-

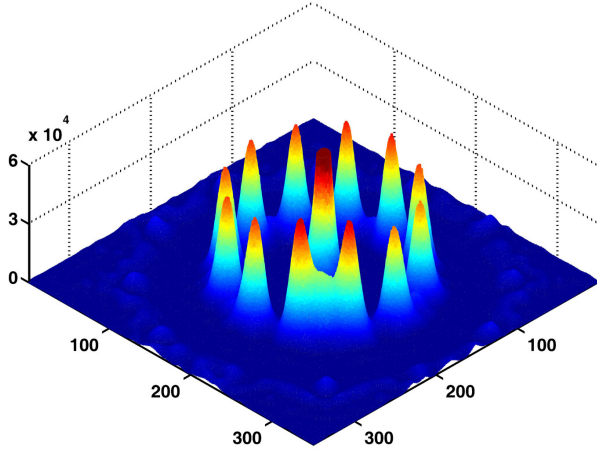


FIG. 50. Experimental realization of a ring-lattice potential with an adjustable weak link (red arrow). Measured intensity distribution with an azimuthal lattice spacing of $28 \mu\text{m}$ and a ring radius of $88 \mu\text{m}$. The central peak is the residual zero-order diffraction. The size of the structure is scalable and a lower limit is imposed by the diffraction limit of the focusing optics.

C). The CCD camera views, therefore, an enlarged image of the optical potential.

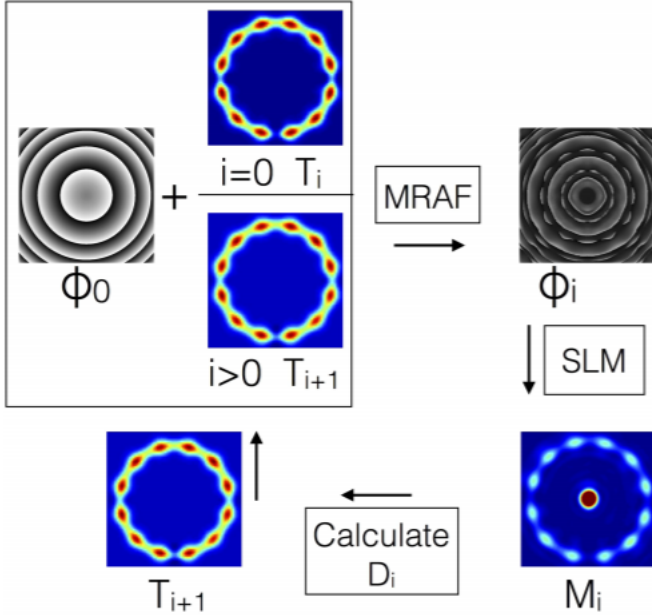


FIG. 51. Our feedback algorithm. Starting at the top left the initial phase and target are used in the MRAF code. This generates the phase guess, ϕ_i , which is uploaded to the SLM and an image captured by the CCD camera, M_i . This is used to calculate the discrepancy between the image and the original target, and a new target T_{i+1} is created. The loop then repeats.

To increase the accuracy of the output potential we use the computationally generated kinoform and produce an image of the optical potential in the monitoring arm of our system, and use this as a further source of feedback to the MRAF al-

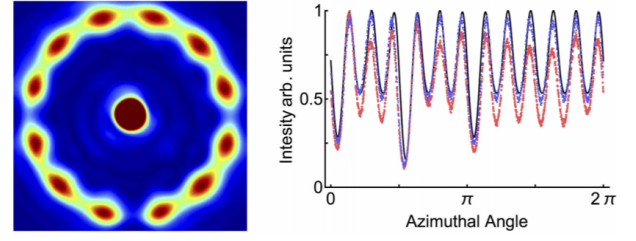


FIG. 52. Left: Final image of the ring lattice after completion of the feedback algorithm. Right: Azimuthal Profile. The solid line plots the target profile. This is compared to the result after the 1st and 5th iteration of the feedback algorithm (red and blue lines respectively).

gorithm. Our method is broadly similar to Bruce *et al*⁵⁵³, however it is specialised for producing ring-lattices. Fig. 51 shows a flow chart of our improved algorithm. In the first step, the target image, T_i , and the initial phase, ϕ_0 , is loaded as an input to the MRAF code. This runs for 20 iterations (this was found to be sufficient to get good convergence in most cases) and outputs a phase kinoform, ϕ_i . The kinoform is now applied to the SLM and an image recorded on the camera in the monitoring arm of our system, M_i . The discrepancy, D_i , between the original target and the measurement is calculated and used to form an updated target T_{i+1} . Here our algorithm differs from⁵⁵³ as we take the discrepancy to be $D_i = -(M_i^2 + T_0^2)/2T_0$. Also, we do not take into account the whole image, the discrepancy is calculated by comparing the maxima and minima around the azimuthal, 1D, profile of the lattice to the target profile. The targets maxima and minima are then adjusted with $T_{i+1} = T_i + \alpha D_i$, where α is a problem specific feedback gain and i the iteration number. The process now repeats with, ϕ_0 and T_{i+1} , as the inputs to the MRAF code. The feedback gain, α , is set to be 0.3 to ensure a quick convergence and this process iterates 30 times. At this point the algorithm is complete and the best image from the set M is selected that minimises the discrepancy below 2%. With this method we produce the ring-lattice potential shown in Fig. 52 (left), that on the trapping side of our apparatus creates a scaled-down lattice with radius of $5\text{-}10 \mu\text{m}$ with more than sufficient power to trap ultra-cold atoms. On the right of Fig. 52, the azimuthal profile around the ring lattice is shown. The red curve indicates the profile on the first iteration of the feedback loop. After 5 iterations (blue curve), the algorithm has converged significantly towards the original target (solid line).

E. Setup for adjustable ring-ring coupling

In this section proposal for experimental realization of ring lattices with tunable distance between the rings is suggested by utilizing SLM technic^{551,552}. With a SLM arbitrary optical potentials can be produced in a controlled way only in a $2d$ -plane – the focal plane of the Fourier transform lens – making it challenging to extend and up-scale this scheme to 3d trap arrangements. The experiment, however, showed (see Fig.54) that axially the ring structure potential remains almost

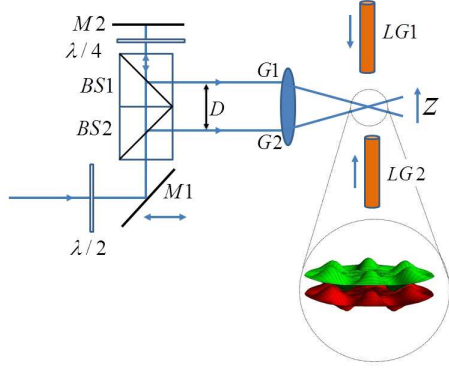


FIG. 53. Proposed setup for the ring-ring coupling. Two gaussian laser beams of wavelength λ and distance D , pass through a lens and interfere in the focal plane (f is the focal length). The distance D can be easily controlled by moving the mirrors. The distance between the fringes is a function of $1/D$ ⁵⁵⁴. The resulting Gaussian laser beam with wave vector $k_G = 2\pi D/(\lambda f)$, then, interferes with two counter propagating Laguerre-Gauss laser beams of amplitude E_0 . The inset shows the ring lattice potentials separated by $d = \lambda f/D$. Here $l = 6$ and $p = 0$.

undisturbed by a translation along the beam propagation axis of $\Delta z = \pm 2.2 \cdot R$, where R denotes the ring-lattice radius. The ring-lattice radius is only weakly affected by an axial shift along z and scales with $\Delta R/R = 0.0097 \cdot z$, where z is normalized to the ring-lattice radius. For larger axial shifts from the focal plane the quality of the optical potential diminishes gradually. Based on our measurements this would allow implementation of ring-lattice stacks with more than 10 rings in a vertical arrangement, assuming a stack separation comparable to the spacing between two adjacent lattice sites. Propagation invariant beams may allow a potentially large number of rings to be vertically arranged⁴⁷³.

Besides making the inter-ring dynamics strictly one dimensional, the lattice confinement provides the route to the inter-rings coupling.

To allow controlled tunnelling between neighbouring lattice along the stack, the distance between the ring potentials needs to be adjustable in the optical wavelength regime (the schematics in Fig.53 can be employed). A trade-off between high tunnelling rates (a necessity for fast gate operations) and an efficient read out and addressability of individual stack sites, needs to be analysed. Increasing the lattice stack separation after the tunnelling interaction has occurred well above the diffraction limit while keeping the atoms confined, optical detection and addressing of individual rings becomes possible.

This arrangement produces equal, adjustable ring-ring spacing between individual vertical lattice sites and can therefore not readily be used to couple two two-ring qubits to perform two-qubit quantum-gates. The SLM method, however, can be extended to produce two ring-lattices in the same horizontal plane, separated by a distance larger than the ring diameter. The separation between these two adjacent rings can then

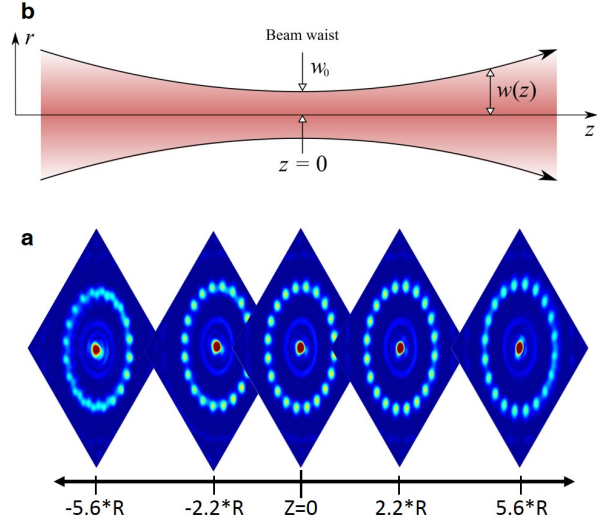


FIG. 54. Effect of an axial translation on the ring lattice potential. a) Ring lattice intensity distribution measured at various positions along the beam propagation axis around the focal plane ($Z=0$). Note that the initial beam, phase modified by the SLM, is not Gaussian any more. The optical potential remains undisturbed by a translation of 2.2 times the ring-lattice radius centred around the focal plane ($Z=0$). Here R designates the ring-lattice radius of $87.5 \mu\text{m}$. b) This is in contrast to a Gaussian laser beam which exhibits a marked dependence on the axial shift from the focal plane where the beam waist $w(z)$ scales with $\sqrt{1 + (z/z_0)^2}$ and Rayleigh range z_0 .

be programmatically adjusted by updating the kinoform to allow tunnelling by mode overlap⁵⁵⁵. Combined with the adjustable vertical lattice (shown in Fig.53) this would allow, in principle, two-ring qubit stacks to be circumferential tunnel-coupled to form two-qubit gates

F. First experimental demonstration of the interference of atomtronic currents

A key ingredient to realize the atomtronic qubit is the interference of currents that make up the qubit dynamics. Recently, quantum interference of currents in an AQUID has been realized for the first time. The interference can be revealed by a periodic modulation of the critical current with applied flux in an atomtronic ring, interrupted by two weak links.

The periodic modulation of the critical current can be understood by calculating the total current within a model of the atomtronic SQUID based on quantum phase-controlled Josephson junction currents and a toroidal trap geometry (Fig.55a). The total current is the result of quantum interference of the two Josephson junction currents, given by

$$I_1 = \frac{1}{2}(I_t + I_j) = I_c \sin(\phi_1) \quad (92)$$

$$I_2 = \frac{1}{2}(I_t - I_j) = I_c \sin(\phi_2) \quad (93)$$

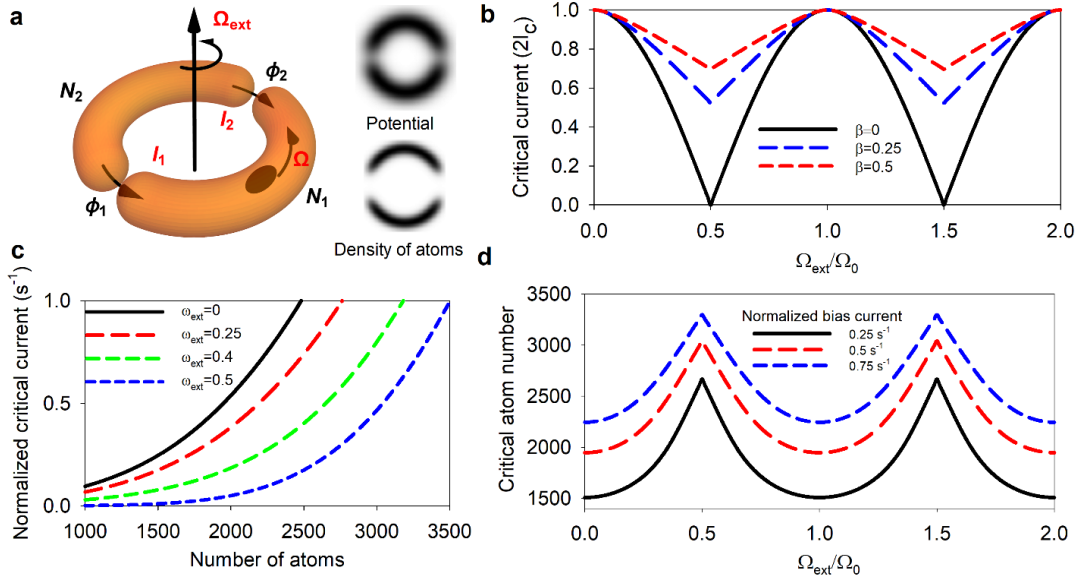


FIG. 55. Calculation of the periodic modulation of the critical current. **a)** Schematic of a double junction atomtronic SQUID. The atomtronic SQUID was created by scanning a single 834 nm laser beam with 1.7 μm waist and the barrier full width at half maximum (FWHM) was 2.1 μm . Ω_{ext} is the rotation rate of the atomtronic SQUID and Ω is the rotation rate of atoms. ϕ_1 and ϕ_2 are the phase differences across the Josephson junctions, I_1 and I_2 are Josephson junction currents, and N_1 and N_2 are numbers of atoms in each half. Arrows represent the movement of the junctions. The calculated potential of the atomtronic SQUID and the density of atoms are shown for the radius of 3.85 μm . **b)** Critical current as a function of $\Omega_{\text{ext}}/\Omega_0$ calculated for different values of β_{atom} . **c)** Normalized critical currents ($2I_c/N$) where I_c is the critical current and N is the total number of atoms as a function of the number of atoms with different ω_{ext} for the atomtronic SQUID with 3.85 μm radius. β_{atom} varies with the number of atoms and the critical current. For each number of atoms, β_{atom} was calculated to find the variation of the normalized critical current. **d)** Modulation of the critical atom number as a function of $\Omega_{\text{ext}}/\Omega_0$ for three different normalized bias currents with the 3.85 μm radius atomtronic SQUID.

where I_c is the critical current of atoms, I_t is the total current, and I_j is the circulating current around the atomtronic SQUID. Because of the toroidal geometry and single valuedness of the wavefunction describing the atoms, the phases should satisfy $\phi_1 - \phi_2 + 2\pi\omega = 2\pi n$ where $\omega = \Omega/\Omega_0$, with Ω being the rotation rate of atoms, and n is an integer. The rotation rate of the atoms can be shown to be

$$\omega = \omega_{\text{ext}} + \beta_{\text{atom}} \frac{I_j}{I_c} \quad (94)$$

where $\omega_{\text{ext}} = \Omega_{\text{ext}}/\Omega_0$, Ω_{ext} is the external rotation rate of the atomtronic SQUID, $\beta_{\text{atom}} = \frac{2\pi I_c}{N\Omega_0}$, and N is the total number of atoms. This equation for the rotation rate of atoms can be derived from the relation between the circulating current and the movement of atoms relative to the Josephson junctions. The parameter β_{atom} is analogous to the screening parameter in the conventional SQUID and can be thought as proportional to the “inductance” which induces the deviation of the rotation rate of atoms from the imposed external rotation rate of the atomtronic SQUID. Equations (1-4) are equivalent to those of a DC SQUID⁵⁵⁶, reflecting the fact that the fundamental underlying physics of a double junction atomtronic SQUID and a DC SQUID is the same. In the limit of $\beta_{\text{atom}} = 0$ (for example, when $I_c \approx 0$ with much higher barrier height), we can analytically calculate the total currents:

$I_t = 2I_c \cos(\pi\omega_{\text{ext}}) \sin(\phi_1 - \pi\omega_{\text{ext}})$ Thus, the critical current is $|2I_c \cos(\pi\omega_{\text{ext}})|$, which establishes a clear modulation of the critical currents with a period of Ω_0 . With finite β_{atom} , we can numerically calculate the critical current, and the periodic modulation amplitude decreases with the increasing β_{atom} , as can be seen in Fig.55b. By using the calculated modulation in Fig.55b, the expected periodic modulation of the critical current in an atomtronic SQUID can be calculated with the Gross-Pitaevskii equation (GPE) in 2D. Fig.55c shows the normalized critical current (see Methods for the details on the Josephson effects in an atomtronic SQUID), which is the critical current of atoms normalized to the number of atoms $\frac{2I_c}{N}$, as a function of the number of atoms for the different rotation rates of the atomtronic SQUID. For a fixed number of atoms, the normalized critical current shown in Fig.55c modulates with rotation rate. However, it is very difficult to experimentally observe this modulation because of the strong dependence of the normalized critical current on the number of atoms and the difficulty in producing a BEC with the same number of atoms consistently. Instead of a fixed number of atoms, we therefore used a fixed normalized bias current, generated by moving Josephson junctions with a fixed speed. When the rotation rate changes, the critical atom number—which is the number of atoms at the transition from DC to AC Josephson effect with the chosen normalized bias current—modulates periodically, as shown in the GPE calculation of

Fig.55d. We chose this modulation of the critical atom number as a way to observe the quantum interference of currents.

The theoretic prediction of the modulation of the critical current (measured using the critical atom number) and the theoretical predictions are plotted in Fig.56. The experimental values clearly show the characteristic modulations of the critical current with flux, revealing the interference of currents in the AQUID.

G. Outlook

In this roadmap review, we have introduced atomtronic qubits constructed with neutral atomic currents flowing in ring-shaped optical lattice potentials interrupted by few weak links, which give rise to the Atomtronics Quantum Interference Device (AQUID). The effective quantum dynamics of the system is proved to be that one of a two-level system. The spatial scale of the rings radii would be in the range of 5 to 20 microns. The ring-ring interaction can be realized with the physical system of two Bose-Einstein condensates, flowing in ring-shaped optical potentials, and mutually interacting through tunnel coupling. Clearly, such systems may be relevant for quantum computation purposes, which was demonstrated further by showing how single and two qubit gates can be obtained in our setup.

The initialization of our qubit can be accomplished, for example, by imparting rotation through light-induced torque from Laguerre-Gauss (LG) beams carrying an optical angular momentum. Stacks of $n \sim 10$ homogeneous ring lattices with tunable distance and stacks of AQUIDs have been realized experimentally (in the lab coordinated by R. Dumke) with Spatial Light Modulators (SLM). Such configurations are realized by making use of the cylindrical symmetry of Laguerre-Gaussian beams and exploiting the flexibility (in terms of generating light fields of different spatial shapes) provided by the SLM devices. Stack of qubits can be realized following very similar protocols. Indeed, similar goals were carried out by realizing the AQUID with homogeneous condensates (i.e. without lattice modulation)^{7,22,67,113,128,540}. We remark that the lattice confinement brings important added values with respect to that realization. First of all, the gap between the two levels of the qubit displays a more feasible dependence with the number of atoms in the system compared with the case of homogeneous rings with a delta barrier. This is ultimately due to the fact that the barrier can be localized on a lattice spacing spatial scale⁵⁵⁰; thereby the k-mixing—that is the key feature to have a well defined two level system—is not suppressed (as, in contrast, happens for homogeneous condensates with a realistic barrier. As a second positive feature, the lattice provides a platform for qubit-qubit interaction. These two features, we believe, could ultimately facilitate the exploitation of the device in future atomtronic integrated circuits.

We also reviewed the construction of a flux qubit employing a ring condensate trapped in a regular lattice potential except for three specific lattice points with a reduced tunneling amplitude. The three weak links solution was originally suggested in quantum electronics to facilitate the function of the

system as a qubit⁵²⁴. We apply a similar logic leading to fluxonium from the rf-SQUID: the continuous quantum fluid, in our system, is replaced by a chain of junctions connecting the different weak links. We believe that the additional lattice helps in adjusting the persistent current flowing through the system. The three weak links architecture, indeed, realizes a two-level effective dynamics in a considerably enlarged parameter space. The qubit dynamics can be read-out via time-of-flight measurements. A spiral pattern emerges when the expanding atomic ring with a specific current is interfered with a reference condensate. The noise in the time-of-flight images is a hallmark of the entanglement present in the current, allowing to characterize the atomic qubit. With these methods, the type of current (entangled vs non-entangled), the magnitude and direction can be read out. The depletion at the weak-link can be used to determine the state of the qubit as well. This opens up a way to experimentally characterize atomic qubits in the lab.

Recent experiments have demonstrated the interference of currents in atomic SQUIDs for the first time. Oscillations in the critical current with applied flux are a clear hallmark of interference of atomic currents. These advances open up the path to create atomic qubits via superposition of currents and observe their macroscopic entanglement.

Decoherence, of course, is an important issue for our proposal that remains to be studied. We comment, however, that measurements of the decay dynamics of a rotating condensate in an optical ring trap show that the quantized flow states have remarkably long lifetimes, of the order of tens of seconds even for high angular momentum ($l = 10$)¹¹⁰. Phase slips (the dominant mechanism of decoherence), condensate fragmentation and collective excitations which would ultimately destroy the topologically protected quantum state are found to be strongly suppressed below a critical flow velocity. Although atom loss in the rotating condensate does not destroy the state, it can lead to a slow decrease in the robustness of the superfluid where the occurrence of phase slips becomes more likely. We believe that the decoherence rates could be controlled within the current experimental know-how of the field. The Atomtronics' positive trend crucially relies on the recent progress achieved in the optics microfabrication field. Thereby, central issues, of the cold atoms system, like scalability, reconfigurability, and stability can be feasibly addressed. In many current and envisaged investigations, there is a need to push for further miniaturization of the circuits. The current lower limit is generically imposed by the diffraction limit of the employed optics. Going to the sub-micron, although challenging, might be accessible in the near future. At this spatial scales, mesoscopic quantum effects could be traced out. The scalability of multiple-ring structures will be certainly fostered by tailoring optical potentials beyond the Laguerre-Gauss type (f.i. employing Bessel-Gauss laser beams). A central issue for Atomtronics integrated circuits, is the minimization of the operating time on the circuit and the communication among different circuitual parts (i.e. AQUID-AQUID communication). Currently, typical time rates are in the millisecond range, but a thorough analysis of the parameters controlling time rates is still missing.

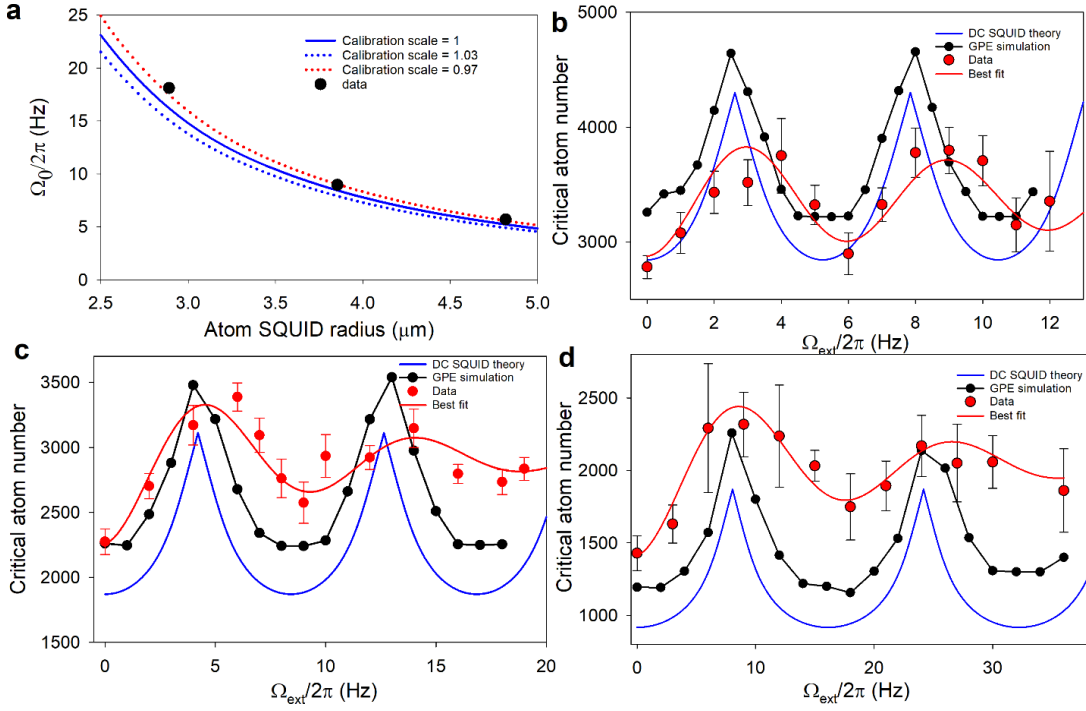


FIG. 56. Comparison between experiment and theory. **a)** Comparison of the measured and calculated values of $\Omega_0/(2\pi)$ (calculation done using GPE). The three curves correspond to calibration scales of the atomtronic SQUID radius. **b,c,d)** Critical atom number as a function of the rotation rates obtained with GPE simulation and DC SQUID theory, along with the measured data and the best fit. For **b)** the radius is 4.82 μm , for **c)** the radius is 3.85 μm and for **d)** the radius is 2.891 μm .

XI. TRANSPORT AND DISSIPATION IN ULTRACOLD FERMION GASES

J.P. Brantut, F. Chevy, M. Lebrat, F. Scazza, S. Stringari

Atomtronics is based on the flow of quantum gases in circuits or devices. It therefore provides a natural framework in which transport and dissipation, two fundamental dynamical processes, can be observed, studied and controlled. These processes are of fundamental interest in the entire field of many-body physics: first, because they involve not only equilibrium or ground state properties but chiefly that of excitations, they are intrinsically difficult to calculate from first principles. Second, for the same reason, they are very sensitive investigation tools for experimentalists. Third, they underly most of the functionalities of solid-state based quantum devices.

Fermionic quantum gases provide the most direct connection between atomtronics and solid-state electronics. The obvious analogy between the transport of Fermionic atoms in light-imprinted structures and that of electrons in condensed matter systems suggests that atomtronics systems could be used as quantum simulators for their electronic counterparts, for which ab-initio modeling is very challenging⁵⁵⁷. The vastly different scales of cold atoms, presented in Table I, as well as the specific control tools make them especially promising in this perspective.

While electronic systems benefit from their ability to reach low relative temperatures, and from more than a century of development of methods and control protocols for currents and voltages, cold atomic systems reach for previously uncharted parameter regimes, comprising for example very high temperatures, large spin imbalance, or multi-component gases and mixtures of quantum gases. Of particular interest is the possibility of cold Fermi gases to operate in the strongly interacting regime, close to a Feshbach resonance. In this regime, the system is described by the so-called BEC-BCS crossover which interpolates between weakly attractive fermions described by BCS (Bardeen-Cooper-Schrieffer) theory, and a Bose-Einstein Condensate (BEC) of strongly bound molecules^{558,559}. The equilibrium properties of gases in this regime have been extensively investigated in the last decade, and several key thermodynamic properties such as the ground state energy, critical temperature or pairing gap are now known with high precision^{560,561}.

The recent years have seen a growing number of experiments exploring the dynamics of fermionic gases in this strongly interacting regime. New systems mixing Bosonic and Fermionic superfluids provides renewed opportunities to study superfluid flow^{562–564}. The development of two-terminal systems for cold atoms in particular provides the simplest device-like geometry⁴³⁸. For a long, low dimensional channel, this has allowed for the measurement of particle⁵⁶⁵, spin⁵⁶⁶ and heat conductances⁵⁶⁷ as well as off-diagonal transport coefficients such as spin-drag or thermopower. For short, planar junctions it realizes a tunnel connection, for which su-

TABLE I. Comparison between cold Fermi gases and electrons in solids

	Cold Fermi gases	Electrons in solids
Interactions	Contact, tunable	Coulomb, with density-dependent screening
Internal states	Hyperfine states	Spin
Structure shaping	Light-induced	Gating, crystal growth
Energy scales	$E_F \sim 1 \mu\text{K}$	$10 \text{ K} < E_F < 10^4 \text{ K}$

perfluidity yields the celebrated Josephson effect^{25,386,392,393}.

This contribution presents some of the most recent development of ultracold Fermi gases in the atomtronics context. In section XI A, transport phenomena in superfluid Fermi gases are discussed, first in the perspective of the Landau criteria, then in the case of Josephson junctions. In section XI C, we describe transport of Fermi gases in mesoscopic channels. In section XI D, the physics of the fast spin drag in normal Fermi gases is presented.

A. Superfluid transport with Fermi gases

1. Fermionic superfluidity and critical velocity

The first microscopic theory of dissipation in superfluids was proposed by Landau who predicted the existence of critical velocity below which an object in motion in a superfluid feels no drag⁵⁶⁸. Landau's original argument was based on constraints imposed by energy and momentum conservation when elementary excitations are shed in the superfluid. In this limit, the critical velocity is simply given by the minimum value of $\omega(k)/k$, where $\omega(k)$ is the dispersion relation of low-energy modes of the system. For a concave dispersion relation, this is the slope of $\omega(k)$ at the origin and the critical velocity is therefore simply the sound velocity.

In fermionic systems the excitation spectrum is composed of both bosonic collective modes (the so-called Anderson-Bogoliubov modes) corresponding to phonons and fermionic quasi-particles associated with broken Cooper pairs⁵⁶⁹. These two sectors lead to different predictions for the critical velocity when interactions are varied across the BEC-BCS crossover. In the BEC regime, where pairs are tightly bound, phonons set the critical velocity, as in a traditional atomic Bose-Einstein condensate. On the contrary, on the BCS side of the resonance, the Cooper pairs are loosely bound and are easily broken by a moving object. In this regime the critical velocity is $v_c \simeq \Delta/p_F$, where Δ is the excitation gap and p_F is the Fermi momentum. The existence of these two excitation branches leads to a maximum of Landau's critical velocity close to the unitary limit that was observed experimentally by stirring an optical potential in the cloud^{570,571}.

Recent experiments on atomic mixtures have raised the question of the onset of dissipation in two counterflowing superfluids^{562,564,572}. Experiments on dual Bose/Fermi superfluids revealed the existence of a critical velocity which was later on interpreted as an extension of Landau's seminal argument similar to parametric down-conversion in quantum op-

tics. In this scenario, the relative motion of the two superfluids can excite *pairs* of excitations in the superfluids^{563,573–575}. This modifies the expression of the critical velocity which is equal to the sum of the sound velocities of the two superfluids when phonons limit superfluidity, a prediction that agrees with experimental measurements⁵⁶⁴ performed on mixtures of ⁶Li and ⁷Li.

Let's conclude this subsection by stressing some of the hypotheses underlying Landau's scenario. Firstly, as mentioned earlier, the identification of Landau's critical velocity in the phonon sector with sound velocity assumes that the dispersion relation is convex. Although this is true for bosons in free space, this is no longer the case for fermions, for which the coupling with the broken-pair particle-hole continuum bends the dispersion relation downwards⁵⁷⁶. Likewise, the presence of a transverse trapping in experiments leads to a reduction of the critical velocity due to an inversion of the concavity of the dispersion relation at large momenta, a feature first pointed out in weakly interacting Bose-Einstein condensates^{577,578} and recently generalized to arbitrary hydrodynamic superfluids⁵⁷⁹. Second, Landau's argument assumes that the velocity of the moving disturbance is constant while in experiments the motion of the disturbing potential is usually oscillatory to account for the finite size of the system. By analogy with an accelerated electric charge that radiates electromagnetic wave at an arbitrarily small velocity, Landau's critical velocity is suppressed for accelerated disturbances⁵⁸⁰. Finally, as initially proposed by Feynman and Onsager^{581,582} topological defects, such as quantized vortices, are responsible for the onset of dissipation for stronger disturbances⁴³⁵.

B. Josephson currents

The Josephson effect represents a quintessential manifestation of macroscopic quantum phase coherence, stemming from spontaneous gauge symmetry breaking in superfluid states. A so-called Josephson junction is typically created by weakly coupling two superfluid order parameters through a thin insulating barrier. In the solid state, this is achieved by separating two superconductors with a nanometer-sized insulating layer. Josephson first predicted that a dissipationless supercurrent $I_s = I_c \sin(\varphi)$ should flow across a tunnel junction in the absence of an applied voltage, associated with the coherent tunnelling of Cooper pairs and sustained only by the relative phase φ between the two order parameters. The maximum value I_c of the supercurrent is coined the Josephson critical current, and it is directly related to the strength of the

tunnel coupling between the two order parameters within the insulating barrier. The measurement of I_c provides a powerful probing tool offering fundamental insights into the microscopic properties of the involved superfluid states, and their robustness against dissipation. For example, for BCS superconductors I_c is directly related to the order-parameter amplitude, i.e. the gap $|\Delta|$, by the Ambegaokar-Baratoff relation. For applied currents above I_c , the junction enters a resistive regime, where a non-zero stationary conductance arises from dissipative excitation processes and a finite electro-chemical potential response is generated across the junction.

Experimental studies with atomic superfluids have so far mainly targeted coherent transport in BECs

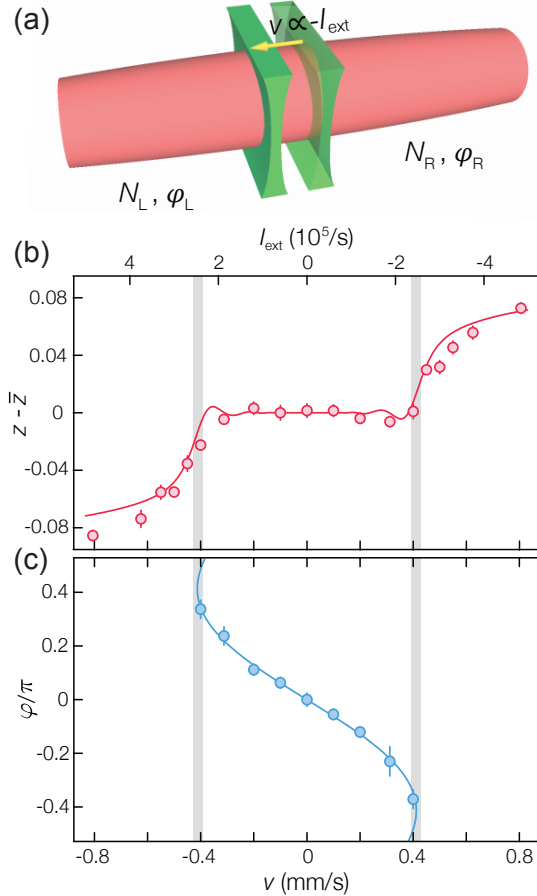


FIG. 57. Realization of a current-biased Josephson junction between ultracold fermionic superfluids. (a) Two superfluid reservoirs (L, left; R, right) of ^6Li fermion pairs are weakly coupled through a thin optical repulsive barrier created using a DMD. An external current I_{ext} is imposed by translating the tunnelling barrier at a constant velocity v . Pair transport is tracked by recording the relative imbalance $z = (N_R - N_L)/(N_R + N_L)$ through *in-situ* absorption imaging, while the order-parameter relative phase ϕ is revealed through matter-wave interference. (b) Experimental current-imbalance characteristic, and (c) current-phase relation $I(\phi)$ for a crossover Fermi gas on the BEC side of the Feshbach resonance. The solid line denotes the fit to a resistively-shunted Josephson junction circuit model, while the shaded vertical lines indicate the extracted I_c . Figure adapted from Ref. 25.

with various geometries and optically engineered weak links^{7,22,67,352,384,400,540,585}. On the other hand, the study of supercurrents between weakly coupled superfluid Fermi gases is of high relevance both from the fundamental and the practical point of view^{386,586,587}, since transport therein is crucially influenced and complicated by strong inter-particle interactions and their interplay with fermionic statistics. Only recently, dc Josephson supercurrents have been observed in strongly interacting Fermi gases close to a Feshbach resonance²⁵. Reminiscent of the behavior of the Landau critical velocity across the BCS-BEC crossover⁵⁵⁸, the Josephson critical current was found to exhibit a pronounced maximum around unitarity, resulting from the opposite variations of the chemical potential and the pair condensate fraction, the latter playing the role of the order-parameter amplitude throughout the crossover²⁵. Recent experiments also showed the breakdown of coherent Josephson transport to be accompanied by the nucleation of topological defects, generated above critical flows by the barrier constriction and subsequently emitted into the superfluid bulk^{392,393}. More efforts will be necessary to shed light on the precise mechanisms underlying dissipation in Josephson junctions between crossover Fermi superfluids, and on the interplay of bosonic and fermionic excitation mechanisms, corresponding to the Bogoliubov-Anderson and pair-breaking excitation branches observed for an obstacle moving through the superfluid^{435,569-571}. Such explorations will be essential for our understanding of dissipative transport in highly correlated fermionic systems, and for extending the applications of the Josephson effect to emerging atomtronic devices.

C. Fermionic transport in mesoscopic channels

Mesoscopic devices refer to small-size systems whose transport properties are influenced by the quantum nature of matter. For example, the conductance of a narrow constriction becomes quantized when its width is comparable to the de Broglie wavelength of the particles traversing it. Initially demonstrated with electrons in semiconducting nanostructures⁵⁸⁸, mesoscopic transport can be naturally extended to fermionic atoms.

As quantum gases have to be particularly shielded from environmental perturbations they are intrinsically closed systems, which is both a blessing and a complication to study mesoscopic transport phenomena. On the one hand, the relaxation of thermodynamical quantities involved in transport such as momentum or spin mostly depend on interparticle interactions, which can be tuned for instance via Feshbach resonances. On the other hand, real-life transport measurements with electrons imply connecting macroscopic leads acting as particle and heat baths to a smaller system of interest, usually treated as a grand canonical ensemble. With quantum gases, such a paradigm for transport requires partitioning the isolated system into a mesoscopic conductor and two or more macroscopic reservoirs that thermalize fast enough compared to the transport timescales to be considered in thermodynamical equilibrium. Cold-atom realizations

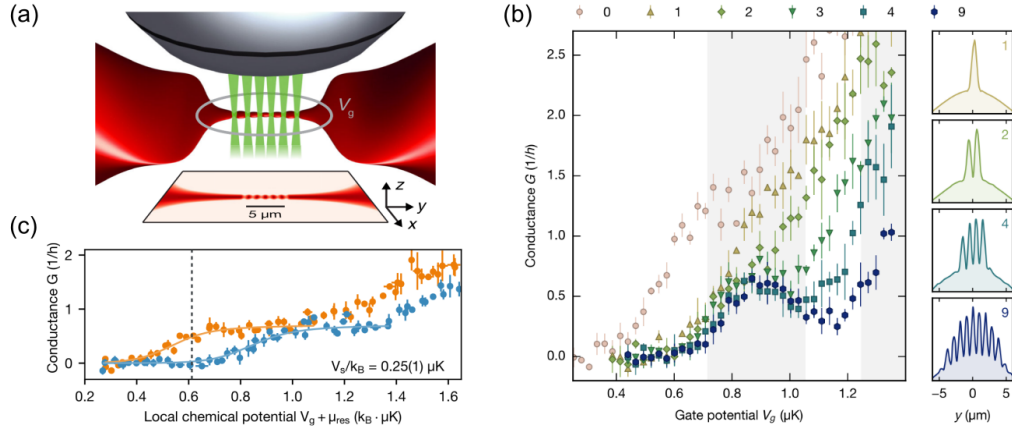


FIG. 58. Studying mesoscopic transport with ultracold Fermions. (a) A degenerate Fermi gas of lithium-6 atoms is shaped using repulsive light potentials into a one-dimensional channel smoothly connected to two macroscopic reservoirs. Spatial light modulation techniques combined with high-resolution optics allow to imprint additional structures to the 1D channel, such as a lattice of variable length. (b) For weak interactions, the current through the lattice is proportional to applied bias and particle transport is captured by a linear conductance coefficient. Conductance shows a local minimum as a function of the overall chemical potential, indicating the emergence of a band gap when approaching the infinite lattice limit. (c) Spin-dependent quantized conductance in the presence of a near-resonant obstacle focused on the 1D channel, realizing the cold-atom equivalent of a spin filter. Adapted from Refs. 583,584.

close to such multi-terminal setups include single and multiple Josephson junction arrays of trapped BECs^{400,589}, weak links in ring traps^{7,128} and planar junctions between two fermionic superfluids^{25,386,392}.

By reducing the dimensionality of the mesoscopic region, the atomic equivalent of quantum point contacts has been realized, displaying quantized conductance⁵⁹⁰. Starting from this two-terminal configuration, more complex structures can be engineered by projecting arbitrary light potentials via holographic techniques⁵⁹¹. Recently, this technique allowed to investigate the insulating properties of a mesoscopic lattice imprinted site by site within a quantum wire⁵⁸³, visible as a suppression of conductance at Fermi energies located in the lattice band gap. Strikingly, this insulating behavior persists as attractive interactions are increased to the point where reservoirs become superfluid. The robustness of the fermionic character of transport can be attributed to the existence a Luther-Emery liquid⁵⁹², a strongly correlated phase of matter distinctive of the 1D character of the channel. In a more recent set of experiments, optical control in atomic point contacts was extended to spin by using light tuned close to atomic resonance to create local effective Zeeman shifts. This lead to the realization of an ideal spin filter with cold atoms, one of the most fundamental spintronic devices⁵⁸⁴. In the presence of weak interactions, near-resonant light scattering can be entirely accounted for by including losses in a Landauer-Büttiker model⁵⁹³. Such progress spin-dependent transport opens avenues for exploring the transport dynamics of strongly correlated heterostructures, where novel nonequilibrium spin and heat transport^{594,595} and exotic phases of matter⁵⁹⁶ could be observed.

D. Fast spin drag in normal Fermi gases

Spin drag is an ubiquitous concept in many branches of physics. It is usually associated with spin interactions which affect the Euler equation for the spin current. Spin drag can be of collisional nature, giving rise to spin diffusion, since collisions do not conserve the spin current, or of collisionless nature, being at the origin of non dissipative dynamics^{597–601}. An intriguing example of spin drag, which is the object of the present contribution, concerns the role of spin current interactions, which modify the equation of continuity in the spin channel and result in the violation of the usually model independent f-sum rule. An important example of this non conventional spin drag (hereafter referred to as fast spin drag) takes place in the so-called Andreev-Bashkin effect, caused by quantum fluctuations in a mixture of two interacting superfluids^{602,603}. This effect is very tiny and difficult to observe in dilute quantum gases, unless one considers one dimensional configurations⁶⁰⁴. Here, we will discuss the fast spin drag in the case of a normal (non superfluid) mixture of two interacting Fermi gases, where the effect can be sizable and hopefully measurable.

To investigate fast spin drag, it is convenient to consider a perturbation of the form $H_{pert} = \lambda f(\mathbf{r})\Theta(t)$ coupled to the many-body system, where $\Theta(t)$ is the usual Heaviside step function (equal to 0 for $t < 0$ and 1 for $t > 0$) and the function $f(\mathbf{r})$ characterizes the nature of the perturbation, while λ is its strength. For example, in an ultracold atomic gas a static perturbation caused by two counter-propagating lasers yields $f(\mathbf{r}) \propto \cos qx$, while a suitable gradient of the external magnetic field can give rise to a dipole perturbation of the form $f(\mathbf{r}) \propto x$. The perturbation, switched on at $t = 0$, causes a dynamic excitation of the system. The basic question that we raise in this work is: let us suppose that the perturbation applies only to one component (hereafter called 1) of a quantum

mixture. How will the other component (hereafter called 2) react? For long times the perturbation will generate a dynamic motion of the whole system with modification of both the total density ($n = n_1 + n_2$) and the spin density ($s = n_1 - n_2$) of the gas. For very short times the perturbation will instead provide a kick to the component 1, the component 2 reacting only in the presence of spin current interactions. In this case the wave function of the system will take the form of a typical phase imprinting $\Psi(t) = \exp[-i\lambda t f(\mathbf{r}_1)]\Psi_0$, with $f(\mathbf{r}_1) = \sum_{k1} f(\mathbf{r}_{k1})$ the one-body excitation operator relative to the component (1) of the mixture (for simplicity we have set $\hbar = 1$). The perturbation will then cause a time evolution of the signal $\langle f(\mathbf{r}_2) \rangle$ of the component 2, according to the law

$$d\langle f(\mathbf{r}_2) \rangle / dt = i\langle \Psi(t) | [H, f(\mathbf{r}_2)] | \Psi(t) \rangle \quad (95)$$

$$= -\lambda t \langle \Psi_0 | [f(\mathbf{r}_1), [H, f(\mathbf{r}_2)]] | \Psi_0 \rangle, \quad (96)$$

fixed by the crossed double commutator $\langle \Psi_0 | [f(\mathbf{r}_1), [H, f(\mathbf{r}_2)]] | \Psi_0 \rangle$, involving the Hamiltonian of the system.

In the absence of current dependent interactions the double commutator identically vanishes, since in this case the commutator $[H, f(\mathbf{r}_2)]$ is uniquely fixed by the kinetic energy term in the Hamiltonian and hence commutes with $f(\mathbf{r}_1)$. As a consequence the motion of the component (2) is not affected at short times (no fast spin drag) and will evolve only at longer times. A non-vanishing crossed double commutator in Eq. (96) results in the violation of the model-independent value $(1/m) \int d\mathbf{r} n(\mathbf{r}) |\nabla f(\mathbf{r})|^2$ of the f-sum rule $\langle \Psi_0 | [f(\mathbf{r}_1) - f(\mathbf{r}_2), [H, f(\mathbf{r}_1) - f(\mathbf{r}_2)]] | \Psi_0 \rangle$, caused by the presence of spin current interaction terms in the Hamiltonian.

A nice example of fast spin drag, where the crossed double commutator does not vanish, is provided by Landau theory of normal Fermi liquids, yielding the result

$$\langle [f(\mathbf{r}_1), [H, f(\mathbf{r}_2)]] \rangle = \int d\mathbf{r} n(\mathbf{r}) |\nabla f(\mathbf{r})|^2 \frac{1}{4m} \frac{(F_1 - G_1)/3}{1 + F_1/3}, \quad (97)$$

where F_1 and G_1 are, respectively, the so called in phase (density) and out of phase (spin density) Landau parameters entering the Landau's theory of Fermi liquids. The in-phase Landau parameter F_1 is directly related to the effective mass of quasi-particles and fixes the value of the specific heat of the system⁶⁰⁵. In a dilute Fermi gas the values of the Landau's parameters are available in both three^{606,607} and two dimensions⁶⁰⁸ using second-order perturbation theory. For example in 3D one has:

$$F_1 = \frac{8}{5\pi^2} (7 \ln 2 - 1) (k_F a)^2; \quad G_1 = -\frac{8}{5\pi^2} (2 + \ln 2) (k_F a)^2, \quad (98)$$

showing explicitly that fast spin drag is quadratic in the dimensionless parameter $k_F a$, where a is the s -wave scattering length and k_F is the Fermi wave vector. It consequently corresponds to a typical beyond mean field effect. The possibility of measuring the Landau's parameters F_1 and G_1 in available experimental configurations of interacting Fermi gases, employing the proposed fast spin drag effect, will be the object of future investigation.

E. Outlook

The investigation of transport and dissipation in Fermi gases has only started recently, and many new directions are already emerging. The available light-shaping techniques allow in principle for complex geometries to be investigated^{29,552}. A particularly appealing situation is the ring trap, which has been successfully explored for weakly interacting Bosons³⁵¹. Complex geometries are accessible using the concept of synthetic dimensions⁶⁰⁹, where multi-terminal geometries are naturally arising from two physical terminals⁶¹⁰. Transport of correlated Fermions in optical lattices has started recently in bulk lattice systems with promising results on the quantum simulation of the Hubbard model^{601,611,612}.

The intrinsically low energy scales also implies that currents are weak, calling for new methods of detection. Single atom sensitive methods have been demonstrated, such as fluorescence based counting⁶¹³⁻⁶¹⁵ or quantum-gas microscopy⁶¹⁶. For transport processes where it is desirable to follow the flow of atoms within a cloud over a single realization, a cavity-assisted detection scheme has been proposed⁶¹⁷.

The physics of complex atomtronics devices featuring Fermi gases with strong interactions opens many possibilities, also of interest in the condensed matter community at large. An overarching goal is the manipulation of topological superfluids⁶¹⁸, such as p -wave superfluids or Kitaev chains⁶¹⁹, which would provide an avenue to study topologically protection of quantum information, thus guiding the development of topological quantum computers.

XII. TRANSPORT IN BOSONICS CIRCUITS

L. Amico, R. Dumke, T. Haug, L.-C. Kwek, W. von Klitzing

Atomtronics opens up a new approach to study fundamental problems of transport of quantum matter in various settings with widely different light-controlled atomic circuits⁴. Of particular interest is transport generated by attaching a circuit to reservoirs, that induce a directed current through the system. Transport between atomic reservoirs has been studied to realize fundamental condensed matter systems^{438,565,587,590}. Furthermore, extreme precise control of the light potentials allow to transport bosonic fluids at hypersonic speeds in ring circuits^{86,97} and in a coherence preserving manner⁶²⁰. Often these basic atomic circuits can be understood by using a simplified lumped element model, that relies only on a few elements³⁹⁵. From there, larger circuits composed of many basic circuits could be constructed to realize large scale atomtronic networks. To this end, there is a considerable interest in understanding the transport through basic circuit elements.

Recent studies investigated the transport and dynamics in other circuits like rings and Y-junctions^{87,621-624}. These systems have been well studied in electronic setups. Surprising differences arise with bosonic atoms instead of fermionic electrons: Andreev reflections, known from superconductor-metal interfaces, can also occur at the interface of two bosonic con-

densates: If the density wave excitation in a one-dimensional condensate is transmitted from the first to second condensate, a hole (an excitation with negative amplitude) is reflected back into the first condensate^{622,625–628}. For ring circuits, Aharonov-Bohm oscillations occur in the current for electronic systems when an a magnetic field is applied to the ring⁶²⁹; For bosonic rings, no Aharonov-Bohm effect occurs^{621,625}. Transport can also be achieved by topological pumping: Driving the circuit parameters such that a directed transport arises, which is protected by topological features of the system^{623,630–632}. For ring systems with applied flux, the transmission becomes fractional in atom number, and highly entangled states can be generated⁶²³.

Recent advances in matter-waveguides allow to transport cold atoms over long distances (see Sec.XII A). Then, we review the dynamics of the two elemental Atomtronic circuits that can be constructed: A ring attached to leads (see Fig.61, Fig.62 and Fig.66, and a Y-junction (see Fig.63, Fig.64 and Fig.65). A sketch of the systems is shown in Fig.59b,c). We investigate different limits: Atoms prepared in a non-equilibrium initial state, with all atoms on one side of the system. Secondly, density wave excitations that propagate through a system filled with atoms. Finally, we also review features of topological pumping of atoms in atomic circuits (see Fig.67).

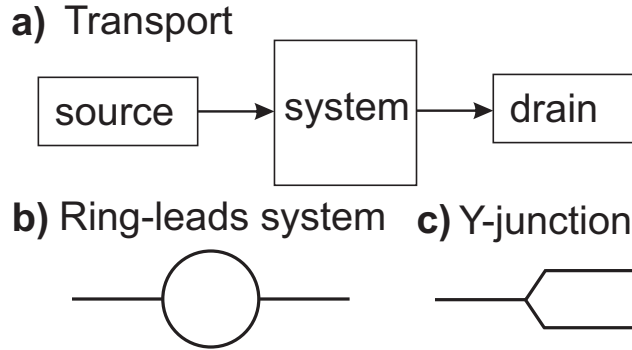


FIG. 59. **a)** General transport setup, composed of a source, system and drain. Atoms flow from source, via the system to drain. The current flowing through the system is the fundamental quantity of interest, that reveals fundamental features of the system. Specific examples of this kind of setup studied here are **a b)** ring-leads system or **a c)** Y-junction.

A. Matterwave guides

A perfect waveguide allows the guided wave to travel undisturbed over any distance. In practice, there are always imperfections such as absorption and spatial variations of the guiding potential. For matterwave guides based on electromagnetic potentials, absorption plays no role. In most cases the shapes of the guiding potentials are defined either by a physical structure such as wires in the case of magnetic potentials or by light-fields in the case of dipole traps. Examples include, imperfections in the shapes of the wire⁷⁵, the

grain size of the copper⁶³³ and for the dipole finite amplitude control²⁴, diffraction and speckles. There are a number of solutions to reduce the impact of the imperfections of magnetic waveguides, such as improved manufacturing techniques and periodic current reversal⁷⁵. Optical techniques employ feedback to image the potential using cold atoms and then correct the imperfections in a feedback loop²⁴. Nevertheless, since some level of imperfection in the magnetic wire structure or in the dipole imaging system is unavoidable, waveguides created by artificial structures will always have a certain degree of roughness.

The effect of these imperfections is characterized by the spatial wavelength λ and amplitude $a(k)$ of the modulation of the waveguide potential: A tighter bend will have a stronger effect than a very smooth one. For optical traps this strength can be calculated directly by estimating the level of control one has over the optical potential, e.g. by imaging the speckles or by estimating the noise level in the feedback to the shape of the waveguide. In the case of magnetic waveguides, the variation of the potential can be imaging the break-up of a Bose-Einstein condensate, which is brought close to the wires. An absolute scale can be established from the resulting images via chemical potential of the BEC.

Increasing the distance between the atoms and the current-carrying conductor decreasing the transverse trapping frequency and reduces the roughness of the waveguide. For distances (d) from the waveguide much larger than the characteristic wavelength (λ), this reduction (K) in roughness can be estimated as a function of the spatial frequency ($k = 2\pi/\lambda$) as⁶³³:

$$K(d, \lambda) = (kd)^{-1/2} e^{-kd} \quad (99)$$

By increasing d it was possible to observe interference fringes between two condensates after propagating them on a magnetic atomchip waveguide for up to $120 \mu\text{m}$, albeit reducing the transverse trapping frequency from the kHz level down to $\omega_{\perp} = 2\pi \cdot 120 \text{ Hz}$ ⁶³⁴. If no propagation is required, even spatially modulated waveguides can exhibit robust coherence¹⁴⁶.

Very smooth optical dipole matterwave guides can be achieved by weakly focussing a laser beam and taking care to avoid laser speckles. If the imaging system is Fourier limited then it cannot produce any structure smaller than the focus, resulting in a perfectly smooth waveguide. By the same token, however, no structure other than a simple linear waveguide can be produced by this method.

A different approach has been recently demonstrated, where the shape of a ring-shaped waveguide is defined by modifying a simple DC quadrupole field using only homogeneous audio-frequency and radio-frequency fields⁸⁶. In the so-called Time-Averaged Adiabatic Potentials, the radial and vertical confinement is limited to a ring and the maximum spatial azimuthal frequency that can be addressed is $\phi = 4\pi$. Since the field generating magnets only have to produce homogeneous and quadrupole fields, they can be far away. Eq.(99) predicts a reduction of the field modulations down to a factor 10^{-138} of their strength at the magnets, thus practically eliminating them. This has made it possible to propagate Bose-

Einstein Condensates over distances of more than 10 cm without causing any additional heating.

A very interesting perspective is to combine the TAAP rings with optical potentials. The standard way to load atoms into the TAAP ring is currently to transfer them from an optical dipole trap^{86,87}. Using radio-frequency or microwaves it would be possible to create a beam splitter between the ring and the optical potential. This couples the magnetically or rotational sensitive state in the ring to a magnetically and rotational non-sensitive one in the optical guide. Possible configurations would include, for example, a (a-)symmetric ring-lead system (Fig. 60a and 60b), a dipole guide coupled tangentially to the ring (Fig. 60c). Since the diameter of TAAP rings and therefore their resonant angular momentum is easily tuned they could act as a velocity-selective resonator. The waveguide could be used to read-out the rotational state of the ring⁶³⁵. Finally, as shown in Fig. 60d one could use a TAAP ring to couple two dipole waveguides to each other in a velocity selective fashion, much like wavelength selective multiplexing using tuneable whispering gallery resonators^{636,637}.

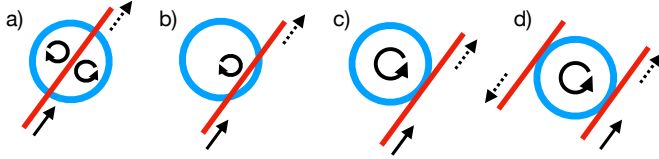


FIG. 60. Possible configurations for coupling of a TAAP ring (blue) to an optical guide potential (red). In all cases the atoms are in a magnetically or rotational sensitive state in the TAAP potential, which is then coupled to a magnetically or rotational non-selective state by tunnel coupling or a spatially selective microwave transition. a) a symmetric ring-lead system, b) asymmetric ring-lead system. c) tangential configuration, where dipole is coupled to only one direction of rotation in the ring. d) TAAP ring coupler between two dipole waveguides. Note that in a) and b) the coupling on the two sides of the ring can be individually tuned.

B. Ring-leads system

Model– The Bose-Hubbard model describes the dynamics of bosonic atoms in a lattice system⁹⁴. A ring with an even number of lattice sites L and two leads (see Fig. 59b) is given by the Hamiltonian $\mathcal{H} = \mathcal{H}_r + \mathcal{H}_l$. The ring part of the Hamiltonian is given by

$$\mathcal{H}_r = - \sum_{j=0}^{L-1} \left(J e^{i2\pi\Phi/L} \hat{a}_j^\dagger \hat{a}_{j+1} + \text{H.C.} \right) + \frac{U}{2} \sum_{j=0}^{L-1} \hat{n}_j (\hat{n}_j - 1), \quad (100)$$

where \hat{a}_j and \hat{a}_j^\dagger are the annihilation and creation operator at site j , $\hat{n}_j = \hat{a}_j^\dagger \hat{a}_j$ is the particle number operator, J is the intra-ring hopping, U is the on-site interaction between particles and Φ is the total flux through the ring. Periodic boundary conditions are applied: $\hat{a}_L^\dagger = \hat{a}_0^\dagger$. The two leads dubbed source (S) and drain (D) consist of a single site each, which are coupled symmetrically at opposite sites to the ring with

coupling strength K . In both of them, local potential energy and on-site interaction are set to zero as the leads are considered to be large with low atom density. The lead Hamiltonian is $\mathcal{H}_l = -K(\hat{a}_S^\dagger \hat{a}_0 + \hat{a}_D^\dagger \hat{a}_{L/2} + \text{H.C.})$, where \hat{a}_S^\dagger and \hat{a}_D^\dagger are the creation operators of source and drain respectively.

Results– The non-equilibrium dynamics can be studied by initially preparing all atoms in the source, and ring and drain being empty. Then, the atoms flow out of the source reservoir, and propagate via the ring to the drain. In the weak-coupling regime $K/J \ll 1$, the lead-ring tunneling is slow compared to the dynamics inside the ring (see Fig. 61a,b,c). In this regime, the condensate mostly populates the drain and source, leaving the ring nearly empty. As a result, the scattering due to on-site interaction U has a negligible influence on the dynamics. With

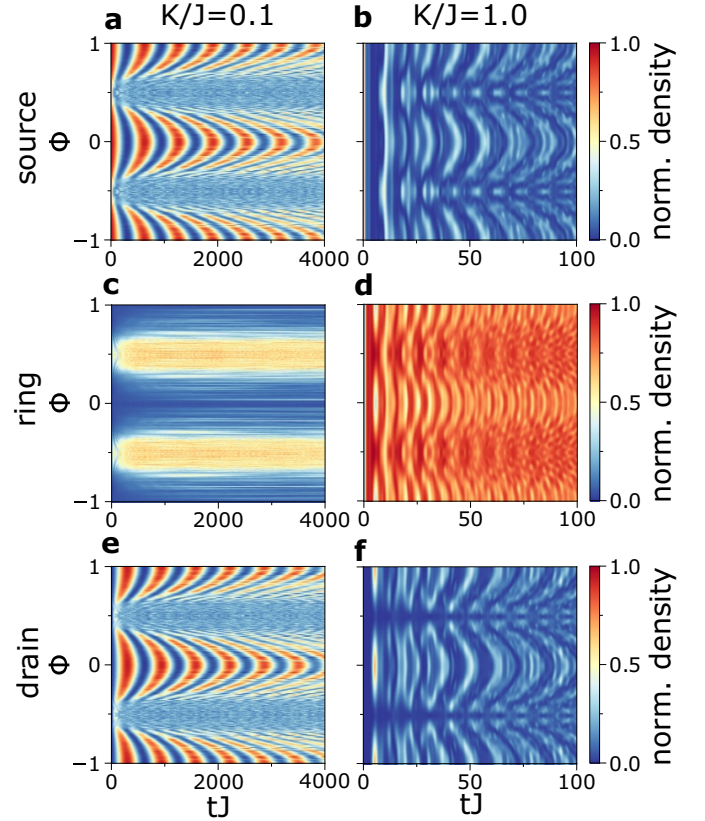


FIG. 61. **Time evolution of density** in source **a,b**), ring **c,d**) and drain **e,f**) plotted against flux Φ . **a,c,e**) weak ring-lead coupling $K/J = 0.1$ (on-site interaction $U/J = 5$). **b,d,f**) strong ring-lead coupling $K/J = 1$ ($U/J = 0.2$). Time is indicated tJ in units of inter-ring tunneling parameter J . The number of ring sites is $L = 14$ with $N_p = 4$ particles initially in the source. The density in the ring is $n_{\text{ring}} = 1 - n_{\text{source}} - n_{\text{drain}}$.

increasing Φ the oscillation becomes faster and the ring populates, resulting in increased scattering and washed-out density oscillations. In the strong-coupling regime $K/J \approx 1$, the lead-ring and the intra-ring dynamics are characterized by the same frequency and cannot be treated separately. Here, a superposition of many oscillation frequencies appears, and after a short time the condensate is evenly spread both in leads and ring (Fig. 61d,e,f). The density in the ring is large and scattering

affects the dynamics by washing out the oscillations. Close to $\Phi = 0.5$, the oscillations slow down, especially for weak interaction, due to destructive interference⁶³⁸.

We now highlight the dynamics for a different initial condition, where the system is initially filled with atoms. In Fig.62 we couple particle reservoirs with the leads to drive a current through the now open system. We model it using the Lindblad master equation

$$\frac{\partial \rho}{\partial t} = -\frac{i}{\hbar} [H, \rho] - \frac{1}{2} \sum_m \{ \hat{L}_m^\dagger \hat{L}_m, \rho \} + \sum_m \hat{L}_m \rho \hat{L}_m^\dagger$$

for the reduced density matrix (tracing out the baths)⁶³⁹. The bath-lead coupling is assumed to be weak and within the Born-Markov approximation. We consider two types of reservoirs: The first type allows multiple particles per reservoir state $L_1 = \sqrt{\Gamma n_S} \hat{a}_S^\dagger$, $L_2 = \sqrt{\Gamma(n_S + 1)} \hat{a}_S$, $L_3 = \sqrt{\Gamma n_D} \hat{a}_D^\dagger$ and $L_4 = \sqrt{\Gamma(n_D + 1)} \hat{a}_D$ (n_S (n_D) is the density of the source (drain) site if uncoupled to the ring). The other type is restricted to a single particle per state (Pauli-principle) $L_1 = \sqrt{\Gamma} \hat{a}_S^\dagger$, $L_2 = \sqrt{\Gamma} \hat{a}_S$, and $L_3 = \sqrt{\Gamma} \hat{a}_D$ (r characterizes the back-tunneling into the source reservoir). We solve the equations for the steady state of the density matrix $\frac{\partial \rho_{SS}}{\partial t} = 0$ numerically⁶⁴⁰. The current operator is $j = -iK(\hat{a}_S^\dagger \hat{a}_0 - \hat{a}_0^\dagger \hat{a}_S)$ and its expectation value is $\langle j \rangle = \text{Tr}(j \rho_{SS})$. We generalize the particle statistics with the parameter η ($\eta = \{0, 2\}$ fermions, $\eta = 1$ bosons, else anyons) using the transformation $\hat{a}_n^\dagger \rightarrow \hat{a}_n^\dagger \prod_{j=n+1}^L e^{i\pi(1-\eta)\hat{n}_j}$ ⁶⁴¹. In Fig.4 a) -c), we compare the open system Lindblad approach with a full simulation of both ring and reservoirs using DMRG^{642,643}. Both methods yield similar results, with the Lindblad approach smoothing out the oscillation found in DMRG. This shows that leads modeled as Markovian bath without memory is sufficient to describe the dynamics. Using both methods, we calculate the evolution towards the steady-state. Remarkably, for the current the *initial dynamics depends on the flux*, showing the Aharonov-Bohm effect of the dynamics. However we find surprisingly, that *the steady-state reached after long times is nearly independent of flux*.

For vanishing atom-atom interactions, the equilibrium scattering-based results of Büttiker et al.⁶⁴⁴ and the non-equilibrium steady state current yield similar result – Fig.62d). Next, we enforce the Pauli-principle ($U = \infty$) in both leads and ring and vary the particle statistics and the average number of particles in the system (filling factor). Fermions are then non-interacting, while anyons and bosons interact more strongly with increasing filling. Now, we use the open system method to characterize the steady-state current. We find that the type of particle and inter-particle interaction has a profound influence on the Aharonov-Bohm effect–Fig.62 e) - h). While non-interacting fermions or bosons react strongly to an applied flux, interacting bosons have only weak dependence on the flux. Fermions have zero current at the degeneracy point, while anyons have a specific point with minimal current, which depends on the reservoir properties. When the filling of atoms in the ring is increased, fermions show no change in the current. However, for anyons a shift of the Aharonov-

Bohm minimum in flux is observed. The minimum weakens the closer the statistical factor is to the bosonic exchange factor. For hard-core bosons, we find that the current becomes minimal at half-flux for low filling, however *vanishes with increasing filling*. The scattering between atoms increases with the filling factor, washing out the Aharonov-Bohm effect.

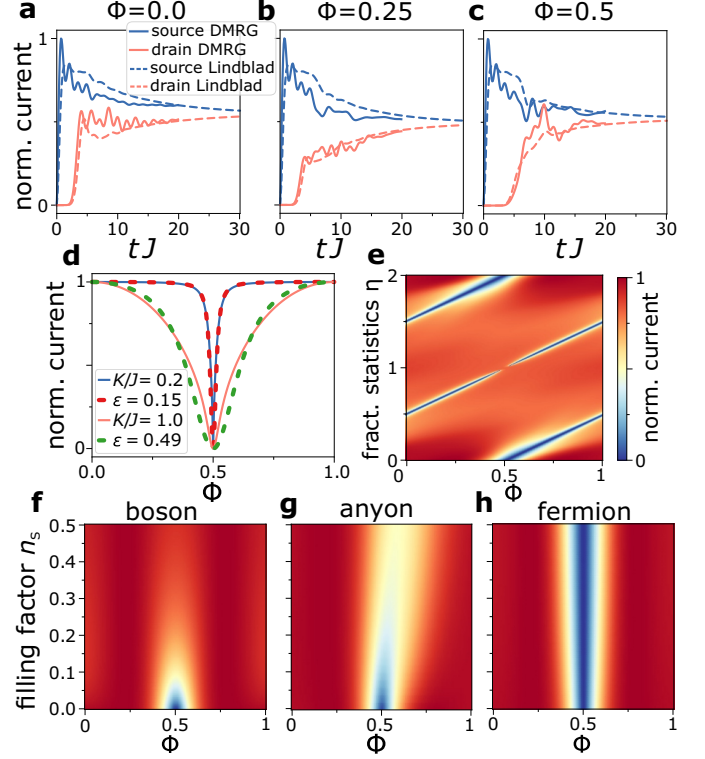


FIG. 62. Current through the Aharonov-Bohm ring a-c) Evolution of source and drain current towards the steady state (when both currents are the same) with DMRG (solid line) and Lindblad formalism (dashed) for hard-core bosons, $K = 1$ and $L_R = 10$. For DMRG, both reservoirs and ring are solved with Schrödinger equation as a closed system. Source and drain are modeled as chains of hard-core bosons with equal length $L_S = L_D = 30$. Initially, the source is prepared at half-filling ($N_p = 15$) in its ground state (ring and drain are empty) decoupled from the ring ($K(t=0) = 0$). For $t > 0$ the coupling is suddenly switched on ($K(t > 0) = J$). Due to numerical limitations, we analyse the short-time dynamics. For the open system, the reservoirs obey Pauli-principle with $r = 0.65$ and $\Gamma = 1.5$. **d)** Solid lines: steady-state current (j_{SS}) we obtained applying the method presented in^{645,646} for non-interacting particles with $L = 100$. Dashed lines: a fit ($\epsilon = \{0.15, 0.49\}$) with the transmission equations derived by Büttiker et al.⁶⁴⁴. **e)** j_{SS} for infinite on-site interaction in both leads and ring plotted against flux Φ and fractional statistics η ($\eta = \{0, 2\}$ non-interacting fermions, $\eta = 1$ hard-core bosons, else anyons) for strong source-drain imbalance. The reservoirs obey the Pauli principle with $r = 0$, $\Gamma = 1/2$. The number of ring sites is $L/2 = 3$ and the ring-lead coupling is $K/J = 1$. At the transition to bosons, there is a discontinuity in the current. **f-h)** j_{SS} for hard-core bosons, anyons ($\eta = 0.25$) and fermions plotted against flux and the filling factor n_S . The reservoirs can have multiple particles per state and have a small particle number imbalance between source and drain with $n_S - n_D = 0.01$. The current is normalized to one for each value of filling independently.

C. Y-junctions

Model– The Y-junction is a system consisting of three one-dimensional chains, which are coupled together at a single point (see Fig.59c). Such systems have been proposed and realized experimentally^{19,119,122,647–649}. The Hamiltonian for the Y-junction is $\mathcal{H}_S + \mathcal{H}_D + \mathcal{H}_I$, with the source lead Hamiltonian (analogue for the two drain leads)

$$\mathcal{H}_S = - \sum_{j=1}^{L_S-1} \left(J \hat{s}_j^\dagger \hat{s}_{j+1} + \text{H.C.} \right) + \sum_{j=1}^{L_S} \frac{U}{2} \hat{n}_j^s (\hat{n}_j^s - 1), \quad (101)$$

where \hat{s}_j and \hat{s}_j^\dagger are the annihilation and creation operator at site j in the source lead, $\hat{n}_j^s = \hat{s}_j^\dagger \hat{s}_j$ is the particle number operator of the source, J is the intra-lead hopping, L_S the number of source lead sites and U is the on-site interaction between particles. All units are rescaled in terms of the hopping term J . The Hamiltonian \mathcal{H}_D for the two drain leads have similar Hamiltonians, where we replace the index s with respective d (for first drain) and f (second drain), and define the drain length L_D . We chose interaction U globally the same everywhere in the system in source, system and drain. We define N_p as the number of atoms in the total system, which is a conserved quantity.

The coupling Hamiltonian between the source lead and the two drain leads is

$$\mathcal{H}_I = -K \hat{s}_1^\dagger (\hat{d}_1 + \hat{f}_1) + \text{H.C.}, \quad (102)$$

where K is the coupling strength between source and drain leads. The current through the Y-junction is defined as

$$j_Y = -iK \hat{s}_0^\dagger \hat{d}_0 + \text{H.C.}, \quad (103)$$

To study the propagation of a density excitation through our setups, we prepare the system in the ground state of the full Hamiltonian with initially a small local potential offset in the lead Hamiltonian. This will create a localized density bump in the source lead. We add the following Hamiltonian for the offset potential to the source Hamiltonian

$$\mathcal{H}_P = -\varepsilon_D \sum_{j=1}^{L_S} \exp\left(-\frac{(j-d)^2}{2\sigma^2}\right) \hat{n}_j^s, \quad (104)$$

where d is the distance of the initial excitation to the junction, and σ is the width of the potential offset, which we set to $\sigma = 2$ unless specified otherwise. At the start of the time evolution the offset potential is instantaneously switched off. The density bump will propagate as an excitation in both positive and negative direction. In this paper, we are only interested in the forward direction, and disregard the excitation in backward direction.

To evaluate the dynamics, we calculate the total density of the incoming wave by taking the first a sites of the source lead at a specific time t_{in} when the density waves has entered this region, and subtracting from it the density at time $t = 0$ before

the wave has entered the region

$$N_{\text{inc}} = \sum_{i \in a \text{ sites of source}} [n_i(t_{\text{in}}) - n_i(0)]. \quad (105)$$

Here, $n_i(t)$ is the expectation value of the density at the i -th site of the system at time t . We find the transmission coefficient by dividing the change in atom number in the drain density by the total density of the incoming wave

$$T = \frac{\sum_{i \in \text{drain}} [n_i(t) - n_i(0)]}{N_{\text{inc}}} \quad (106)$$

and the reflection coefficient as

$$R = 1 - T. \quad (107)$$

Results– The limiting cases of infinitely strong on-site interaction with hard-core bosons is presented in Fig.63. In Fig.63a-c, we study the propagation for different values of lead coupling K . In the source lead an initial excitation bump is prepared. At $t = 0$, the potential offset is quenched, and the excitation starts moving in forward and backward direction. We ignore the backward propagating part of the wave. The forward moving part of the wave propagates from the source through the junction to the two drain leads. We find that the wave at the junction (site 160) is both transmitted and reflected. For the reflection amplitude, we find three characteristic reflection regimes, which are controlled by the junction coupling K . First, we look at the reflection peak as seen in Fig.63e) at time $tJ = 27$. In the strong coupling regime $K = 1J$, we see a negative (Andreev-like) reflection amplitude peak. For the intermediate coupling regime $K \approx 0.5$ the back reflection amplitude is very small, and the reflected wave consists of a small, first positive and then negative part, of nearly equal weight. Finally, for the weak coupling regime with K small, we find a large positive back-reflection and small transmission. In the table below Fig.63, we plot the total transmitted and reflected density at time $t = 31/J$ (calculated using Eq.105-107). This gives us the transmission coefficient and reflection coefficient of the density wave packet. For strong coupling $K = 1J$, we find a transmission coefficient of nearly $T = 4/3$, which corresponds to the theoretical value predicted for a Y-junction in the Gross-Pitaevskii limit⁶²².

How does the reflection and transmission change for finite interaction, instead of the hard-core limit of infinite interaction? For the Bose-Hubbard model with finite U more than one particle is allowed per site. In Fig.64, we plot the current and density in time for different junction couplings K for the Y-junction with the Bose-Hubbard model. Again, we observe a regime with negative reflection (strong coupling) and a regime with mostly positive reflection (weak coupling). However, in the intermediate regime the reflection amplitude is not flat as in the hard-core limit, but has first a positive and then a negative part. Note that for finite U , the effective coupling of the leads is renormalized^{364,650} with interaction. The coupling regime is a function of both interaction and coupling K (e.g. for half-filling and for finite U , we find that $K = 0.5J$ is the strong-coupling regime, while for hard-core bosons $U = \infty$, it

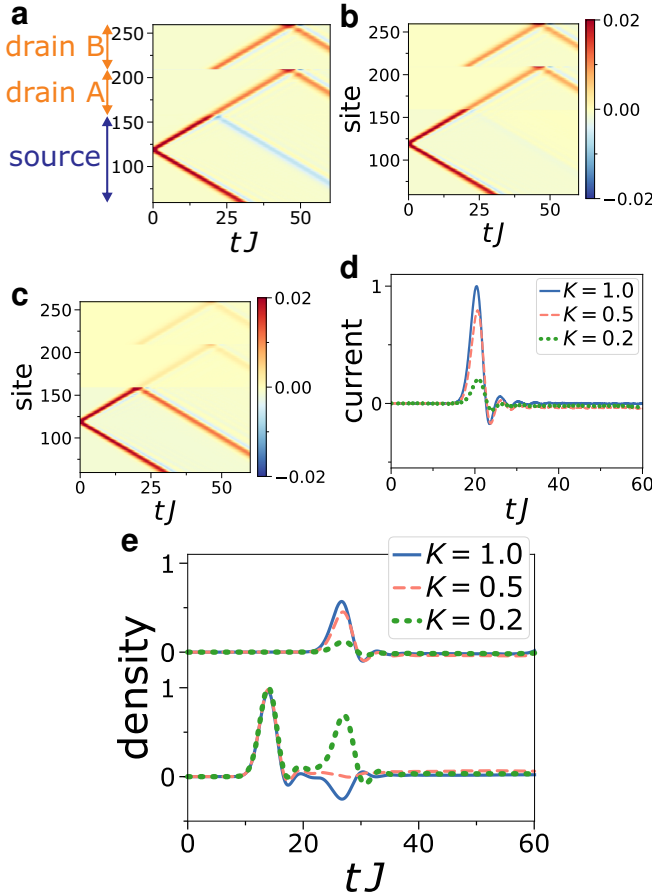


FIG. 63. Propagation of small excitation in a Y-junction for the hard-core boson model. The source lead has length $L_S = 160$, the drain lead each $L_D = 50$, the particle number $N = 130$, initial distance of the excitation to the junction $d = 40$ and $\varepsilon_D = 0.3J$. The source lead is from site 1 to 160, the first drain lead from 160 to 210, and the second one from site 210 to 260. The coupling at the junction (site 160) is **a)** $K = 1J$, **b)** $K = 0.5J$, **c)** $K = 0.2J$. **d)** Current through the junction (Eq.103) in time. **e)** The propagation of the density excitation in time. The upper curves show the transmitted density wave into the drain lead (integrated between site 170 and 175), and the lower curves the incoming and reflected wave in the source lead (145 and 150). The background density is subtracted. For $K = 1J$ (solid) we observe a negative reflection (Andreev-like), $K = 0.5J$ (dashed) nearly no reflection, $K = 0.2J$ (dots) a large positive reflection amplitude. The table below shows the transmission and reflection coefficients, calculated at $t = 31/J$ with Eq.105-107 ($t_{in} = 15$, $a = 30$).

	$K = 1$	$K = 0.5$	$K = 0.2$
transmission	1.332	0.947	0.207
reflection	-0.332	0.053	0.793

is in the intermediate coupling regime).

D. Differences between fermions and hard-core boson

Bosons and fermions differ fundamentally in their particle exchange relations: The bosonic many-body wavefunction is symmetric, while fermions are anti-symmetric under ex-

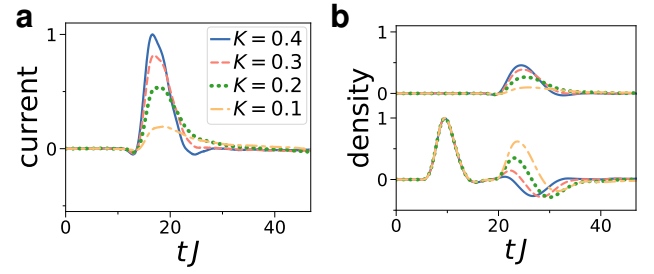


FIG. 64. Propagation of small excitation in a Y-junction for the Bose-Hubbard model for $U = 5J$. The source lead has length $L_S = 80$, the drain lead each $L_D = 40$, the particle number $N = 80$ and $d = 30$. The source lead is from site 1 to 80, the first drain lead from 80 to 120, and the second one from site 120 to 160. **a)** Current at the junction in time. **b)** The propagation of the density excitation in time. The upper curves show the transmitted density wave into the drain lead (integrated between site 80 and 85), and the lower curves the incoming and reflected wave in the source lead (65 and 70). The background density is subtracted. For $K = 0.4J$ we observe a negative reflection (Andreev-like), $K = 0.1J$ (dots) a mostly positive reflection amplitude. In between for $K = 0.3J$ and $K = 0.2J$, the reflection changes in time from positive to negative. The maximum number of atoms per site is restricted to 4.

change of two particles. As a result of these properties, the Pauli principle is enforced for fermions: at a single site only zero or one fermion can exist, while non-interacting bosons do not have this restriction. However, for strongly interacting bosons in the hard-core limit, only one hard-core bosons can be at a single site. While in one dimensions, a mapping between fermions and hard-core bosons exists, this is not the case beyond one-dimensional systems. In a Y-junction, fermions and hard-core bosons show fundamentally different types of reflection behavior. Fig.65, shows the density wave for transmission and reflection. Hard-core bosons show a clear Andreev-reflection, while spinless fermions do not.

Similar differences arise in a ring-lead system, that is composed of two one-dimensional chains, dubbed source and drain, attached at opposite ends to a ring lattice. In a half-filled system, a density wave is excited similar to procedure detailed earlier introduced in Sec.XII C. We show the reflected and transmitted density wave for zero and half-flux in Fig.66. For zero flux, the reflected density wave is different for fermions and bosons. For hard-core bosons, we find the same characteristic Andreev-like negative reflection peak as seen in the strongly coupled Y-junction. The transmission and reflection for hard-core bosons are flux independent. For spinless fermions, the density waves are transmitted for zero flux, while at half-flux we observe zero transmission due to Aharonov-Bohm interference. In short, density excitations for fermions show Aharonov-Bohm oscillations, while for interacting bosons the Aharonov-Bohm effect is absent.

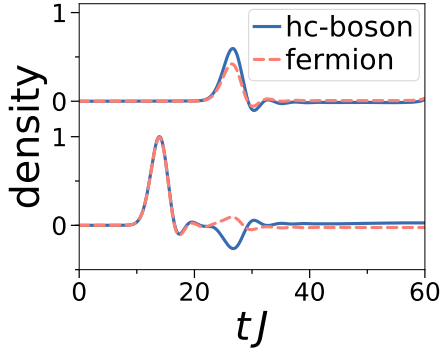


FIG. 65. Comparison between hard-core bosons and spinless fermions for the transmission and reflection of a small density excitation in a Y-junction. Bosons show clear negative Andreev-reflection, in contrast to fermions. The source lead has length $L_S = 160$, the drain lead each $L_D = 50$, the particle number $N = 130$, $d = 40$, $K = J$, initial half-filling and $\varepsilon_D = 0.3J$. The propagation of the density excitation in time. The upper curves show the transmitted density wave into the drain lead (integrated between site 170 and 175), and the lower curves the incoming and reflected wave in the source lead (145 and 150). The background density is subtracted. The transmission coefficients for hard-core bosons is $T = 1.332$, while for fermions $T = 1.061$ (calculated at $t = 31/J$ with Eq.105-107, $t_{in} = 15$, $a = 30$).

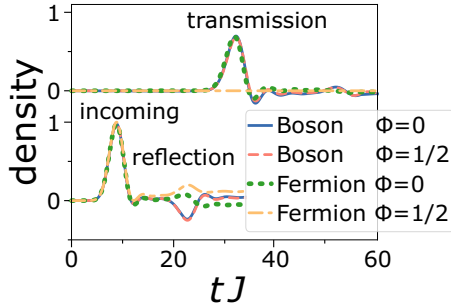


FIG. 66. Propagation of a small density excitation in a ring-lead system for hard-core bosons and spinless fermions for zero and half-flux. Fermion transmission is flux-dependent, while hard-core bosons are flux independent. The source and drain lead has length $L_S = L_D = 80$ and the ring $L_R = 40$, the particle number $N = 100$, strong coupling with $K = J$ and $\varepsilon_D = 0.3J$. The propagation of the density excitation in time. The upper curves show the transmitted density wave into the drain lead (integrated between site 130 and 135), and the lower curves the incoming and reflected wave in the source lead (65 and 70). The background density is subtracted.

E. Entangled state generation with topological pumping in ring circuits

Topological pumping, pioneered by Thouless^{651,652}, can transport excitations, with the added feature that the excitation is protected against noise and imperfections by topological properties of the system. This is realized by driving the system periodically in time while protecting the band gaps. This idea can be extended to interacting many-body systems^{631,632}. It can be used to transport atoms through ring-lead circuits⁶²³,

with a similar setup as introduced the ring-lead circuit (see Sec.XII B). To enable pumping, a time-dependent and spatially varying chemical potential is added to the system. This will pump atoms from the source, through the ring, into the drain. Due to the effect of artificial magnetic field piercing the ring, the topological transport becomes flux dependent, as well as the reflection coefficients are a function of the system parameters. Here, we highlight an interesting feature of this setup: It can create highly entangled states. Due to the Bose-Hubbard interaction, when atoms are pumped through the ring-lead interface acts effectively as a non-linear beam-splitter. As a result, N initial atoms in the source become an entangled NOON-like superposition between two sides of the ring ($|\Psi_{\text{NOON}}\rangle = \frac{1}{\sqrt{2}}(|0\rangle \otimes (|N0\rangle + |0N\rangle))$). We plot the fidelity $F = |\langle \Psi_{\text{NOON}} | \Psi \rangle|^2$ of the creation of the NOON like entangled state by adiabatically changing the potential in the ring-lead junction in Fig.67. We observe that for our parameters a NOON state of up to 6 particles with nearly unit fidelity can be created. For more particles or higher interaction the fidelity decreases due to the exponential suppression of the energy gap.

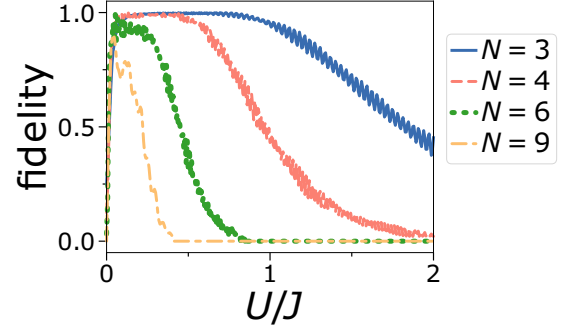


FIG. 67. Fidelity of creating a NOON-like entangled state after pumping through a simplified ring-lead junction. It consists of three lattice sites, with one site connected to the other two sites. All particles are initialized on the first site, the NOON state is measured between the other two sites. Fidelity is plotted against interaction U in units of inter-site hopping J . Pumping with driving frequency $\Omega = 0.01J$ and potential strength $P_0 = 40J$.

F. Outlook

Transport in quantum many-body systems is a fundamental problem important for quantum information and condensed matter physics. With the recent advances in quantum technologies, cold atoms can be used to simulate these problems in a novel way. Transport with nearly no heating can be achieved by extremely smooth atom waveguides. New regimes of transport can be studied by attaching reservoirs of atoms to the system that induce a current through the system. Studying the current can reveal properties of the system that are hard to extract otherwise. Here, we reviewed the properties of two atomic circuits: ring-lead systems and Y-junctions. The current through these circuits holds some surprises: Bosonic Y-junctions show Andreev-reflections, known from fermionic

superconductor-metal interfaces. By tuning the coupling of the Y-junction, the type of reflection can be tuned, between regular (positive) and negative Andreev reflections. Intermediate levels show a positive-negative oscillating behavior. For transport through a ring, we find that interacting bosons are independent of flux. This is in stark contrast to fermionic systems, which are highly flux dependent. By utilizing topological pumping, highly entangled states of NOON-type can be generated in these kind of setups. Experimental implementations require precise control over the confining potential. Atomtronics can create arbitrary potential shapes for cold atoms and thus is an ideal platform to realize these systems⁴. Techniques from machine learning could enhance the engineering of circuits to generate desired quantum state⁶⁵³. In future quantum technology, there is a need for large-scale quantum networks. Using the knowledge on transport through elemental circuits like rings and Y-junctions, larger circuits composed of many different kind of these elements can be constructed. These circuits can be efficiently interconnected via smooth matter waveguides. These systems could be interesting platforms for quantum information processing and to realize new types of quantum-enhanced sensors for quantum technologies.

XIII. ARTIFICIAL QUANTUM MATTER IN LADDER GEOMETRIES

V. Ahufingher, R. Citro, S. De Palo, A. Minguzzi, J. Mompert, E. Orignac, N. Victorin

The Fractional Quantum Hall Effect^{654,655} is a striking example of the interplay of interaction and topology in condensed matter physics. It is characterized by many fascinating properties such as a precise quantization of the Hall resistance depending only on fundamental constants, excitations carrying fractional charges with anyonic statistics, and dissipationless chiral edge modes. While the effect has been initially observed with fermions, bosonic analogues have been proposed by Regnault and Jolicoeur in rotating clouds of ultracold atoms⁶⁵⁶. Recently, the realization in experiments of artificial gauge fields^{527,657–659} has opened another route for observing Quantum Hall phases with ultracold atoms. As a first step towards the realization of Quantum Hall phases with ultracold atoms it is interesting to consider the so called ladder systems^{660–684}, *i.e.* two dimensional systems that are of finite size along one of the dimensions. Such deceptively simple system is already sensitive to the effect of the applied flux and can exhibit analogues of the Quantum Hall phase^{668,669,678}. Moreover, it shows a wealth of phases, emerging from interplay of rung and leg tunnel, interactions, artificial gauge field, filling^{663,664,668,682,683}. For bosonic atoms, in low flux, an analogue of the Meissner phase is obtained^{660,661}. At high flux, a quasi-long range ordered vortex phase is formed^{660,661}. Interleg interactions can stabilize an atomic density wave at intermediate flux^{683,684}. For a flux commensurate with the density the analogue of QHE is found^{668,669,678}. At a different commensuration between flux and density, an incommensu-

ration driven by interchain hopping is obtained⁶⁸¹. Furthermore, a variant of the ladder in form of a diamond chain has topological properties³⁷⁷ and allows to simulate quantum magnetism^{685,686}.

A. The boson ladder at strong interaction

We consider a model of bosons on a two-leg ladder in the presence of an artificial U(1) gauge field^{676,678}:

$$H = -t \sum_{j,\sigma} (b_{j,\sigma}^\dagger e^{i\lambda\sigma} b_{j+1,\sigma} + b_{j+1,\sigma}^\dagger e^{-i\lambda\sigma} b_{j,\sigma}) + \frac{\Omega}{2} \sum_{j,\alpha,\beta} b_{j,\alpha}^\dagger (\sigma^x)_{\alpha\beta} b_{j,\beta} + \sum_{j,\alpha,\beta} U_{\alpha\beta} n_{j\alpha} n_{j\beta}, \quad (108)$$

where $\sigma = \uparrow, \downarrow$ represents the leg index or the internal mode of the atom^{609,687,688}, $b_{j,\sigma}$ annihilates a boson on leg σ on the j -th site, $n_{j\alpha} = b_{j\alpha}^\dagger b_{j\alpha}$, t is the hopping amplitude along the chain, Ω is the tunneling between the legs or laser induced tunneling between internal modes, λ is the Peierls phase of the effective magnetic field associated to the gauge field, $U_{\uparrow\uparrow} = U_{\downarrow\downarrow}$ is the repulsion between bosons on the same leg, $U_{\uparrow\downarrow} = U_{\downarrow\uparrow}$ the interaction between bosons on opposite legs. This model can be mapped to a spin-1/2 bosons with spin-orbit interaction model⁶⁸², where Ω is the transverse magnetic field, λ measures the spin-orbit coupling, $U_{\uparrow\uparrow} = U_{\downarrow\downarrow}$ is the repulsion between bosons of identical spins, $U_{\uparrow\downarrow} = U_{\downarrow\uparrow}$ the interaction between bosons of opposite spins. The low-energy effective theory for the Hamiltonian (108), treating Ω and U_{\perp} as perturbations, can be obtained by using Haldane's bosonization of interacting bosons.⁶⁸⁹ Introducing⁶⁸⁹ the fields $\phi_\alpha(x)$ and $\Pi_\alpha(x)$ satisfying canonical commutation relations $[\phi_\alpha(x), \Pi_\beta(y)] = i\delta(x-y)$ as well as the dual $\theta_\alpha(x) = \pi \int^x dy \Pi_\alpha(y)$ of $\phi_\alpha(x)$, and after introducing the respective combinations of operators $\phi_{c,s} = \phi_{\rightarrow} \pm \phi_{\downarrow}$ we can represent the low-energy Hamiltonian as $H = H_c + H_s$, where

$$H_c = \int \frac{dx}{2\pi} \left[u_c K_c (\pi \Pi_c)^2 + \frac{u_c}{K_c} (\partial_x \phi_c)^2 \right] \quad (109)$$

describes the total density fluctuations for incommensurate filling when umklapp terms are irrelevant, and

$$H_s = \int \frac{dx}{2\pi} \left[u_s K_s \left(\pi \Pi_s + \frac{\lambda}{a\sqrt{2}} \right)^2 + \frac{u_s}{K_s} (\partial_x \phi_s)^2 \right] - 2\Omega A_0^2 \int dx \cos \sqrt{2}\theta_s + \frac{U_{\perp} a B_1^2}{2} \int dx \cos \sqrt{8}\phi_s \quad (110)$$

describes the antisymmetric density fluctuations. In Eq. (110) and (109), u_s and u_c are respectively the velocity of antisymmetric and total density excitations, A_0 and B_1 are non universal coefficients⁶⁹⁰ while K_s and K_c are the corresponding Tomonaga-Luttinger (TL) exponents⁶⁸⁴. They can be expressed as a function of the velocity of excitations u , and Tomonaga-Luttinger liquid exponent K of the isolated chain⁶⁸⁴.

For an isolated chain of hard core bosons, we have $u =$

$2t \sin(\pi\rho_\sigma^0)$ and $K = 1$. The phase diagram of the Hamiltonian can be determined by looking at the physical observables as the rung and leg current, momentum distribution and correlation functions. Physical observables can be all represented in bosonization. The rung current, or the flow of bosons from the upper leg to the lower leg, is:

$$\begin{aligned} J_\perp(j) &= -i\Omega(b_{j,\uparrow}^\dagger b_{j,\downarrow} - b_{j,\downarrow}^\dagger b_{j,\uparrow}) \\ &= 2\Omega A_0^2 \sin \sqrt{2}\theta_s + \dots \end{aligned} \quad (111)$$

The chiral current, *i.e.* the difference between the currents of upper and lower leg, is defined as

$$\begin{aligned} J_\parallel(j, \lambda) &= -it \sum_\sigma \sigma (b_{j,\sigma}^\dagger e^{i\lambda\sigma} b_{j+1,\sigma} - b_{j+1,\sigma}^\dagger e^{-i\lambda\sigma} b_{j,\sigma}) \\ &= \frac{u_s K_s}{\pi\sqrt{2}} \left(\partial_x \theta_s + \frac{\lambda}{a\sqrt{2}} \right). \end{aligned} \quad (113)$$

The density difference between the chains $S_j^z = n_{j\uparrow} - n_{j\downarrow}$, is written in bosonization as:

$$S_j^z = -\frac{\sqrt{2}}{\pi} \partial_x \phi_s - 2B_1 \sin(\sqrt{2}\phi_c - \pi\rho x) \sin \sqrt{2}\phi_s, \quad (114)$$

while the density of particles per rung is:

$$n_j = -\frac{\sqrt{2}}{\pi} \partial_x \phi_c - 2B_1 \cos(\sqrt{2}\phi_c - \pi\rho x) \cos \sqrt{2}\phi_s. \quad (115)$$

When $\Omega \neq 0$, $U_\perp = 0$, and $\lambda \rightarrow 0$, the antisymmetric modes Hamiltonian Eq. (110) reduces to a quantum sine-Gordon Hamiltonian. For $K_s > 1/4$, the spectrum of H_s is gapped and the system is in the so-called Meissner state^{660,661} characterized by $\langle \theta_s \rangle = 0$. In such state, the chiral current increases linearly with the applied flux at small λ , while the average rung current $\langle J_\perp \rangle = 0$ and its correlations $\langle J_\perp(j)J_\perp(0) \rangle$ decay exponentially with distance. The transition from the Meissner to the Vortex phase is signaled by the splitting of the momentum distribution $n(k)$ from $k = 0$ to a finite $Q = \sqrt{\lambda^2 - \lambda_c^2}$ that depends on the spin-orbit interaction λ . For this reason the transition falls into the universality class of the commensurate-incommensurate transitions (C-IC). The rung current correlation function develops two symmetric peaks and the spin static structure is linear at low momentum. The phase diagram for a hard-core bosonic ladder at $n = 1$, obtained using density renormalization group (DMRG) technique^{691,692}, is shown in Fig. 68 together with the momentum distribution $n(k)$ as a function of lambda across the C-IC transition. Compared to the non-interacting case, the phase diagram as a function of Ω/J and λ shows an enlargement of the Meissner phase and its persistence above a certain value of Ω/J . Above a certain value of λ a second incommensuration appears in the rung current correlation functions and the static structure factor. Such incommensuration is associated to the appearance of an extra peak in the rung current correlation function at wavevectors $P = \sqrt{\lambda^2 + p(\Omega^2)}$ and $\pi \pm P$, with $p(\Omega)$ a function of the interchain tunneling. For $\lambda = \pi$ the correlation functions show a tendency to a localized regime.

With $\Omega \neq 0$, $U_\perp \neq 0$ the C-IC transition is replaced by a Meissner-to-incommensurate charge density wave (ICDW)

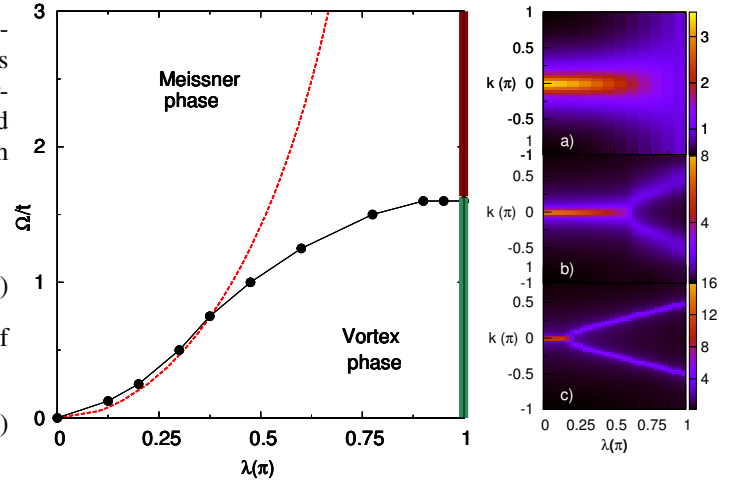


FIG. 68. Phase diagram for hard-core bosons on the two-leg ladder as a function of flux per plaquette λ and the interchain hopping Ω . The boundaries between the Meissner and the Vortex phase are shown by the red and black solid lines respectively for the non-interacting and the interacting case. At $\lambda = \pi$ the thick solid green-line shows the occurrence of the second incommensuration. The three insets in the right panel show intensity plots of $n(k, \lambda)$ for the three different values of $\Omega/t = 0.25, 1.25$ and 2 . In panels b) and c) the system enters the Vortex phase for $\lambda > \lambda_c$: the single peak at $k = 0$ splits into two maxima symmetric around $k = 0$ at $\pm q(\lambda)$. At large $\Omega/t = 2$, panel a), the system stays always in Meissner phase and in the vicinity of $\lambda = \pi$, $n(k)$ becomes independent of k indicating the formation of a fully localized state (thick solid dark-red line).

which falls into the Ising universality class, followed by a melting of the Vortex phase at large enough λ , going towards a BKT transition when entering the Vortex phase⁶⁸⁴. The melting of the Vortex phase is signaled by the Lorentzian shape peaks of the rung current correlation function preceded by a Lifshitz point⁶⁹³. In the phase diagram, see Fig. 69 for the case of a hard-core bosonic ladder in the presence of an attractive interaction U_\perp , obtained using DMRG simulations, it is possible to trace these features.

B. A ring ladder at weak interactions

Model: We consider N bosons occupying two coupled one-dimensional concentric lattice rings subjected to two artificial gauge fields ad organized on a planar geometry. The stacked geometry has also been thoroughly studied^{515,624}. This system could be experimentally realized *e. g.* using dressed potentials⁸⁰, or Laguerre-Gauss beams¹⁰⁹. The

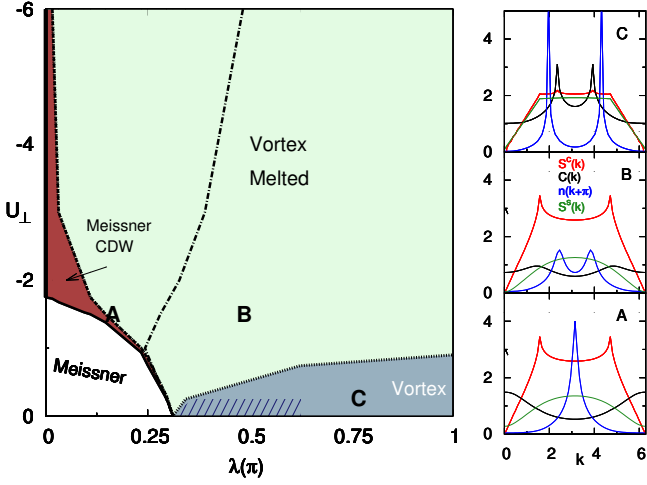


FIG. 69. (Color online) Phase diagram at $n = 0.5$ for a fixed value of interchain hopping $\Omega/t = 0.5$ as a function of the applied flux λ and as function of the strength of the interchain interaction U_{\perp} . The dashed black line is the boundary between the Meissner phase and the Meissner-CDW phase (dark-red region). In the Melted vortex phase (light-green region) the dot-dashed line indicates the Lifshitz point. At large λ the Vortex phase is re-established (light-blue region under the dotted black line). In the shaded blue area second-incommensuration occurs. The three insets in the right panel show the behavior of $n(k)$ (blue solid lines), the spin static structure factor $S^s(k)$ (solid dark-green line), the charge static structure factor $S^c(k)$ (solid red line) and the current-current correlation function $C(k)$ (solid black lines), for the three points A, B and C shown in the phase diagram, respectively for the CDW-Meissner, Melted Vortex and Vortex phase.

Hamiltonian reads

$$\begin{aligned} \hat{H} &= \hat{H}_0 + \hat{H}_{int} = \\ &-J \sum_{l=1, p=1,2}^{N_s} \left(a_{l,p}^{\dagger} a_{l+1,p} e^{i\Phi_p} + a_{l+1,p}^{\dagger} a_{l,p} e^{-i\Phi_p} \right) \\ &-K \sum_{l=1}^{N_s} \left(a_{l,1}^{\dagger} a_{l,2} + a_{l,2}^{\dagger} a_{l,1} \right) + \frac{U}{2} \sum_{l=1, p=1,2}^{N_s} a_{l,p}^{\dagger} a_{l,p}^{\dagger} a_{l,p} a_{l,p} \end{aligned} \quad (116)$$

where $a_{l,p}$ are the bosonic field operators for the p -th ring, l indicates the site position on each ring made of N_s sites, J is the tunneling amplitude along each ring, threaded by the fluxes $\Phi_{1,2}$ respectively and K is the inter-ring tunneling amplitude. In the non-interacting regime $U = 0$, this model is readily diagonalized, yielding a two-band excitation spectrum

$$E_{\pm}(k) = -2J \cos(\phi/2) \cos(k - \Phi) \pm \sqrt{K^2 + (2J)^2 \sin(\phi/2)^2 \sin(k - \Phi)^2}. \quad (117)$$

where we have set $\phi = \Phi_1 - \Phi_2$ and average flux $\Phi = (\Phi_1 + \Phi_2)/2$. Depending on the ratio K/J and on ϕ , the lowest band of the excitation spectrum has either one or two minima centered at $k = \Phi$. The ground state of the Bose gas is a Bose-Einstein condensate occupying the minima of such excitation

spectrum. In the case of a single minimum the ground state corresponds to the Meissner phase and in the case of a coherent superposition of the occupancy of the two minima, the ground state is in the vortex phase. The Meissner phase is characterized by vanishing transverse current and homogeneous density profile. The vortex phase has non-zero transverse current and density modulations along the ring. The vortex to Meissner phase transition has been experimentally observed in⁶⁹⁴. The chiral current on the ring, *i. e.* the difference of longitudinal currents among the two rings, is characterized by subsequent jumps each time a vortex enters into the system.

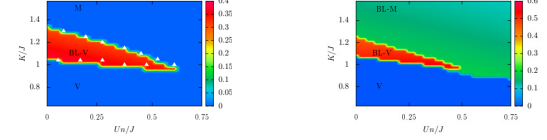


FIG. 70. (Color online) Color map of the imbalance among particle numbers in each ring, in the $(K/J, UN/JN_s)$ plane, for (upper panel) $\phi = \pi/2$, $\Phi = 6\pi/N_s$ and $N_s = 20$, (lower panel) $\phi = \pi/2$, $\Phi = \pi/N_s$ and $N_s = 20$. The letters indicate the parameter regimes where we find a biased-ladder phase (BL-V) where the single-particle spectrum has a double minimum, a Meissner phase (M), a vortex phase (V) and a biased-ladder phase (BL-M) where the single-particle spectrum has a single minimum. White triangles represent the frontiers between biased-ladder phase and the two other phase, namely vortex phase and Meissner phase as calculated with the variational Ansatz including finite size effect.

Ground state of weakly interacting ring We assume large occupancy of the lattice sites and weak interactions $U/J \ll 1$. In this regime, we describe the system by the mean-field approximation. Setting $\Psi_{l,p}(t) = \langle a_{l,p}(t) \rangle$ the condensate wave-function, we solve the coupled discrete non-linear Schroedinger equations (DNLSE)

$$i\partial_t \Psi_{l,1}(t) = -J\Psi_{l+1,1}(t)e^{i(\Phi+\phi/2)} - J\Psi_{l-1,1}(t)e^{-i(\Phi+\phi/2)} - K\Psi_{l,2}(t) + U|\Psi_{l,1}(t)|^2\Psi_{l,1}(t) \quad (118)$$

$$i\partial_t \Psi_{l,2}(t) = -J\Psi_{l+1,2}(t)e^{i(\Phi-\phi/2)} - J\Psi_{l-1,2}(t)e^{-i(\Phi-\phi/2)} - K\Psi_{l,1}(t) + U|\Psi_{l,2}(t)|^2\Psi_{l,2}(t) \quad (119)$$

At varying UN/JN_s and K/J , the ground state displays three phases⁶⁹⁵: the vortex (V) and Meissner (M) phases found in the non-interacting regime, as well as the biased-ladder phase, characterized by imbalanced density populations among the two rings and uniform density profile. We denote the latter (BL-V) or (BL-M) depending whether for the same values of ϕ and K/J the corresponding non-interacting spectrum has one or two minima.

Excitation spectrum of weakly interacting ring We next present our results for the excitation spectrum of the weakly interacting Bose gas on a ring lattice⁶⁹⁶. Withing the Bogoliubov approximation, we set $\hat{a}_{l,p} = \Psi_{l,p}^{(0)} + \delta\hat{a}_{l,p}$, where $\Psi_{l,p}^{(0)}$ is the ground state solution with chemical potential μ . we find the excitation spectrum using the expansion of the fluctuation

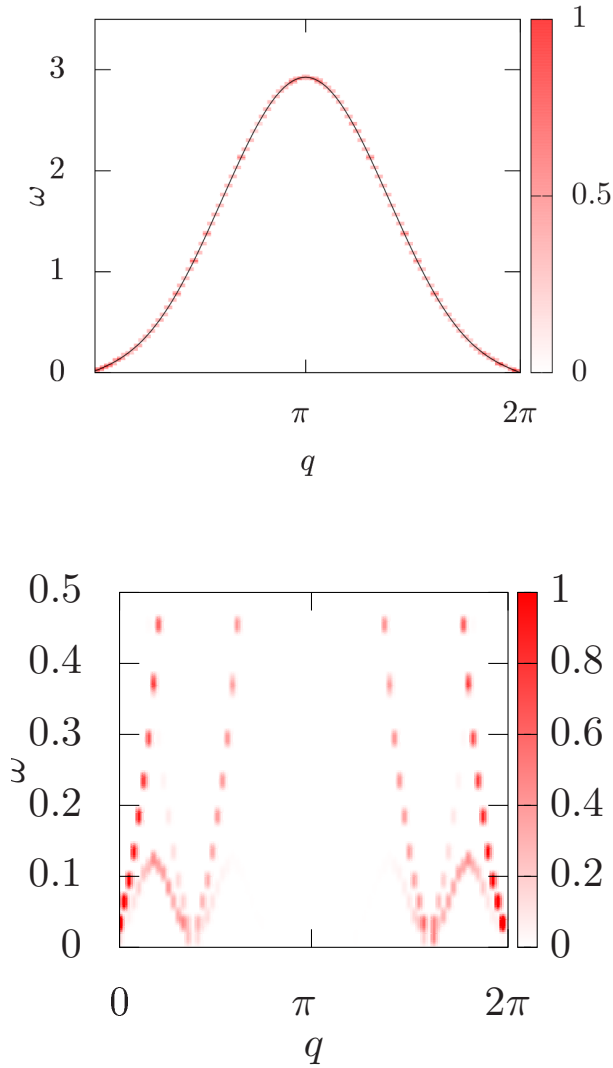


FIG. 71. (Color online) Dynamic structure factor in the frequency-wavevector plane in the frequency-wavevector plane (color map, q in units of $1/a$ with a lattice spacing and ω in units of J) Upper panel: in the Meissner phase, for $Un/J = 0.2$, $\phi = \pi/2$, $K/J = 3$. Lower panel: in the vortex phase for $K/J = 0.8$, $\phi = \pi/2$, $Un/J = 0.2$. For both panels $N_s = 80$.

operator $\delta\hat{a}_{l,p}$ in normal modes with energy ω_v , according to

$$\delta\hat{a}_{l,p} = \sum_v h_{v,l}^{(p)} \hat{\gamma}_v - Q_{v,l}^{*(p)} \hat{\gamma}_v^\dagger, \quad (120)$$

The solution Bogoliubov-de Gennes eigenvalue equations for the mode amplitudes $h_{v,l}^{(p)}$ and $Q_{v,l}^{(p)}$ yields the excitation spectrum. We use both eigenvalues and eigenvectors of the Bogoliubov equations to compute the dynamic structure factor

$$S_{p,p'}(q, \omega) = \sum_{s \neq 0} |\langle s | \hat{\rho}_q^{(p,p')} | 0 \rangle|^2 \delta(\omega - \omega_s) \quad (121)$$

As an example, we show the results for the excitation spectrum in the Meissner and in the vortex phase. The excitation spectrum is strongly dependent on the phase of the underlying ground state. In the Meissner phase a single Goldstone mode is found, and corresponds to the $U(1)$ symmetry breaking associated to the formation of a Bose-Einstein condensate. In the vortex phase, two Goldstone modes are observed. Indeed in the vortex phase, a second symmetry is broken, *i. e.* the discrete translational symmetry. We have shown that this is associated to the emergence of supersolidity of the gas, and is corroborated by the calculation of the static structure factor, displaying a well-defined peak, and the first-order correlation function, demonstrating phase coherence.

C. Ultracold atoms carrying orbital angular momentum in a diamond chain

Topological edge states and Aharonov-Bohm caging We consider a ladder with a diamond-chain shape with a unit cell formed by three cylindrically symmetric potentials of radial frequency ω , and forming a triangle with central angle Θ and nearest-neighbor separation d . Non-interacting ultracold atoms of mass m that may occupy the two degenerate OAM $l = 1$ states with positive or negative circulation localized at each site are loaded into the ladder. Three independent tunneling amplitudes⁶⁹⁷ exist in the system: J_1 , which corresponds to the self-coupling at each site between the two OAM states with different circulations, and J_2 and J_3 , which correspond to the cross-coupling tunneling amplitudes between OAM states in different sites with equal or different circulations, respectively. For $\Theta = \pi/2$, J_1 and J_3 acquire a relative phase of π along one of the diagonals of the chain and, due to destructive interference between neighboring sites, the self-coupling vanishes everywhere except for the sites at the left edge. The model possesses inversion and chiral symmetry but, due to the two-fold degeneracy, Zak's phases⁶⁹⁸ are ill-defined. Thus, a series of exact mappings are required to fully characterize topologically the system. In addition, the model here obtained corresponds to a square-root topological insulator^{699,700}, *i. e.*, the quantized values of the Zak's phases are recovered after taking the square of the bulk Hamiltonian.

Under periodic boundary conditions, the diagonalization of the bulk Hamiltonian yields six energy bands in three degenerate pairs and a gap appears in the spectrum. In the $J_2 = J_3$ limit, all bands become flat. Exact diagonalization, in the case of open boundary conditions, shows the presence of four in-gap states localized at the right edge of the chain, which persist as long as the energy gap is open (see Fig. 72).

We perform first a rotation into a basis of symmetric and antisymmetric states, which decouples the diamond chain with six states per unit cell into two independent and identical diamond subchains with three states per unit cell. This explains the two-fold degeneracy of the spectrum and the presence of gaps in the band structure. A second basis rotation maps each of the diamond subchains into a modified Su-Schrieffer-Heeger (SSH) model⁷⁰¹ with an extra dangling state per unit cell, which allows to understand the existence of in-gap edge

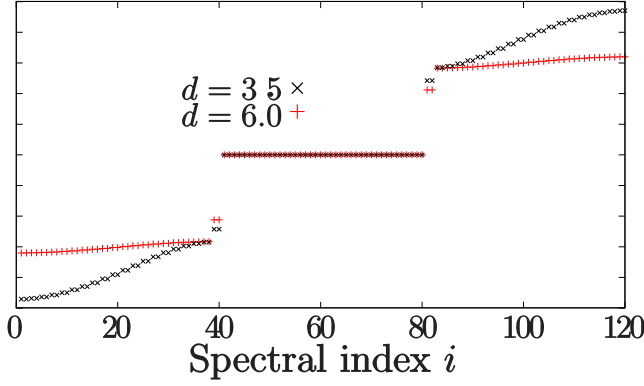


FIG. 72. Exact diagonalization spectra of a diamond chain of $N_c = 20$ unit cells for $d = 3.5\sigma$, corresponding to $J_3/J_2 = 1.67$ (black solid line) and $d = 6\sigma$ corresponding to $J_3/J_2 = 1.13$ (red dotted line), where $\sigma = \sqrt{\hbar/(m\omega)}$

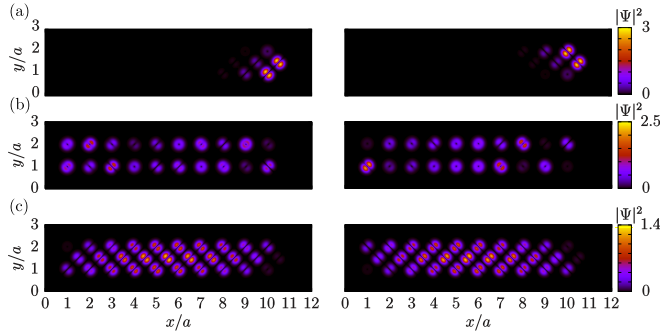


FIG. 73. Density profiles of numerically obtained eigenstates for a diamond chain of $N_c = 10$ units cells and inter-site separation $d = 6\sigma$, corresponding to $J_3/J_2 = 1.13$. (a) Two degenerate edge states. (b) Two states of the flat band. (c) The two degenerate ground states of the system.

states localized at the right edge of the chain (Fig. 73(a)), the zero-energy flat band states without population in the central sites (Fig. 73(b)) and the flattening of the bands in the $J_2 = J_3$ limit. Fig. 73(c) shows the two degenerate ground states of the system. The decoupled subchains do not have inversion symmetry, so that the Zak's phase can yield non-quantized values. Thus, a third mapping to recover inversion symmetry has been introduced⁷⁰² obtaining a diamond chain with alternating tunneling amplitudes topologically characterized in^{703,704}. A striking feature of the topology of this model, directly carried over to the original OAM $l = 1$ model, is that there is no topological transition across the gap closing point, as can be seen by fixing either J_2 or J_3 and varying the other across zero.

Finally, we have also demonstrated that the system can exhibit Aharonov-Bohm caging in the $J_2 = J_3$ limit since, in this limit, the states involving the central site of a unit cell can be expressed in terms of flat-band states that occupy solely the four sites surrounding it. Thus, an initial state prepared in an arbitrary superposition of the central sites states will oscillate coherently to its four neighboring sites with a frequency

given by the absolute value of the energies of the top/bottom flat-band states without leaving the cage formed by two consecutive unit cells.

Simulating quantum magnetism with strongly interacting ultracold bosons Up to here, we have neglected interactions among the ultracold atoms. However, as discussed in^{685,686}, strongly interacting ultracold bosons loaded into OAM states of lattices of side-coupled cylindrically symmetric traps, e.g., a quasi-one-dimensional ladder of ring potentials or a diamond chain, can realize a variety of spin 1/2 models, including the XYZ Heisenberg model with or without external fields. In⁶⁸⁶, we have focused on the Mott insulator regime at unit filling, where each trap is occupied by a single boson and a direct mapping between the degree of freedom corresponding to the two opposite circulations $\pm l$ of the OAM states to a spin 1/2 can be performed. Thus, by tuning the relative phases in the tunneling amplitudes, which depend on the relative orientation between the traps, the system can be used to simulate different spin 1/2 models of quantum magnetism. To this aim, we have computed first, by means of second-order perturbation theory, the explicit dependence of the effective tunneling couplings on the relative angle between the traps. Then, we have discussed for which particular geometries the XYZ Heisenberg model with uniform or staggered external fields could be obtained. As an example, for a quasi-one dimensional ladder of ring potentials with central angle tuned to $\Theta^l = (2s + 1)\pi/(2l)$ with $s \in \mathbb{N}$, single spin flips mediated by interactions do not take place and only isotropic two-spin flips occur. In this situation, the effective Hamiltonian of the system becomes a XYZ Heisenberg Hamiltonian without external field⁶⁸⁶:

$$H_{\text{eff}}^l = \sum_{j=1}^N J_{xx}^l \sigma_j^x \sigma_{j+1}^x + J_{yy}^l \sigma_j^y \sigma_{j+1}^y + J_{zz}^l \sigma_j^z \sigma_{j+1}^z \quad (122)$$

where $J_{xx}^l = -((J_2^l)^2 + (J_3^l)^2)/(2U)$, $J_{yy}^l = -((J_2^l)^2 - (J_3^l)^2)/(2U)$, and $J_{zz}^l = -3((J_2^l)^2 - (J_3^l)^2)/(2U)$, being J_2^l and J_3^l the cross-coupling tunneling amplitudes between states of OAM l possessing equal and different circulations, respectively, while U is the non-linear interaction parameter.

Worth to highlight, besides engineering different spin 1/2 models by tuning the geometry of the lattice, the system also allows to adjust the relative strength between the effective couplings by changing the radius of the ring traps and their separation. In fact, we have shown that this additional parameter of control can be exploited in realistic experimental set-ups to explore distinct phases of the XYZ model without external field. Moreover, we have analyzed the effect of experimental imperfections, such as the influence on the tunneling phases of the presence of small fluctuations in the relative angle between the traps. Regarding the physical implementation of the proposal, we have discussed several possibilities to realize a lattice of ring potentials with a tunable geometry and have analyzed single-site addressing techniques that could allow to retrieve the state of each individual spin. Finally, we have also investigated the collisional stability of the system and concluded that the anharmonic energy spacing between OAM states introduced by the ring geometry allows extend-

ing the lifetime of the Mott state.

D. Conclusions and outlook

The examples detailed in this chapter show that the ring geometry allows both to study the phase diagram and the main features of the excitation spectrum of the infinite ladder to large accuracy as well as to highlight interesting parity and commensurability effects typical of finite rings. Furthermore, the ring geometry allows for new probes of the various phases *e. g.* by the measurement of persistent currents or via spiral interferometry. It also displays Josephson modes.

In outlook, one should develop suitable theoretical methods to describe the crossover from the weak-interaction and large occupancy regime down to the strongly correlated regime reached at large interactions and small filling⁷⁰⁵. To make contact with a real experimental situation it is necessary to investigate how much the signatures of these phases are robust against the finite temperature effects together with the possibility of having long-ranged interactions between the atoms. Also, the experimental realization of ring ladders seems close to reach and would provide a benchmark of atomtronic devices.

XIV. QUANTUM-ENHANCED ATOMTRONICS WITH SOLITONS

P. Naldesi, J. Polo, S. A. Gardiner, M. Olshanii, A. Minguzzi, L. Amico

Quantum coherent states of macroscopic degrees of freedom are hard to achieve, due to decoherence. Cold bosonic systems tend to remain in a Bose-condensed state that can be perfectly described by a mean-field theory. However, for attractive condensates, there are points in the space of parameters where the mean-field theory predicts sudden jumps. The relevant example corresponds to a single one-dimensional bosonic soliton^{706–708} or any other quantum droplet that is scattered off a barrier^{709,710}. For the incident kinetic energies (per particle) below 1/4 of the magnitude of the soliton chemical potential, a “forbidden window” on the axis of the transmission coefficients must emerge⁷¹¹ (see also^{486,712}); it appears because in this regime the amount of the incident kinetic energy is insufficient to compensate for the loss of the interaction energy in a 50%–50% splitting.

As we scan the barrier height from a lower value up, the transmission coefficient increases and at some barrier height, abruptly jumps up⁷¹¹. At the mean-field level, the jump is infinitely sharp. Indeed, a dissociation of the soliton onto the transmitted and reflected parts costs interaction energy, and the incident kinetic energy may not be sufficient to pay for it.

Such a discontinuity is unphysical. As has been shown in^{713,714}, the key to ensure the continuity of the transmission coefficient curve is to recognize that at the apparent discontinuity point the condensate becomes fragmented and the transmission events acquire a quantum randomness. This regime

will soon be within experimental reach⁷¹⁰. The good news is that a highly desirable Schrödinger cat is itself a fragmented state; the bad news is that if the number of occupied one-body orbitals becomes large, the macroscopic coherence becomes unusable. The paper⁷¹³ suggests a secure way of suppressing the undesirable fragments: the soliton kinetic energy must be decreased even further, to a point where the *total* kinetic energy becomes less than the chemical potential, thus ensuring no relative motion of the constituent atoms, with only “cold soliton transmitted” and “cold soliton reflected” allowed orbitals as the result. While conceptually elegant, this method of generating a macroscopic coherence requires center-of-mass kinetic energies N times lower than those currently used (N being the number of atoms in the soliton) and scattering regimes where the barrier becomes completely classical from the soliton center-of-mass point of view. (Accordingly⁷¹³ suggests using extended center-of-mass coherent wavepackets with a non-zero velocity width, where the barrier is used as a classical velocity filter — see also⁴⁸⁴) However, a private communication⁷¹⁵ indicates — based on numerical evidence — that even at moderate kinetic energies, there remain only two populated orbitals. If this is indeed the case, then it is clear what these orbitals are: they are nothing else but the state of the condensate just before and just after the mean-field jump in the transmission coefficient.

Note that even in the favorable two-orbital case, the macroscopic coherence may still remain unusable due to the entanglement between the center-of-mass motion and possible excitations created during the scattering event. Even if these excitations are small at the level of the BEC wavefunction, the difference between the internal states of the transmitted and reflected condensates may still be large due to the orthogonality catastrophe. Nonetheless, the macroscopic coherence may be potentially preserved if a limited number of atoms is used. The upper bound for this number is yet an open question, which will require an intensive numerical study.

While in the proposal^{713,714}, the center-of-mass of the incident soliton is assumed to be in a coherent state prior to the splitting, the cooling of a macroscopic variable to that state is difficult *per se*. However in^{716,717} it is shown that in a factor of four quench of the coupling constant, one can create, while at a finite temperature, an exponentially cold quantum state of a relative distance between the centers-of-mass of two solitons^{718–721}, itself a macroscopic variable. The theoretical estimates⁷¹⁷ show that under realistic experimental conditions, quantum fluctuations of the inter-soliton velocity will lead to an observable inter-soliton separation after a time

$$\tau \approx 4.7 \text{ s}.$$

Further beam-splitting of the inter-soliton distance degree of freedom requires additional study, while its initial coherence is already guaranteed. Classically, the above states would correspond to Gross–Pitaevskii breathers^{722,723} with fluctuating parameters. These have recently been experimentally realized, albeit in the classical regime, as describe in⁷²⁴.

A. Creation and manipulation of Quantum Solitons

1. Quantum solitons in the Bose-Hubbard model

Attractive bosons confined in a one dimensional lattice system can be described by the Bose-Hubbard model, which Hamiltonian reads

$$\mathcal{H} = -J \sum_{j=1}^L (a_j^\dagger a_{j+1} + \text{h.c.}) - \frac{|U|}{2} \sum_{j=1}^L \hat{n}_j (\hat{n}_j - 1) \quad (123)$$

where the operators a_i^\dagger obey the canonical commutation relations $[a_i, a_j^\dagger] = \delta_{ij}$, $n_i = a_i^\dagger a_i$ is the number operator at the site i ; the operators a_i and L is the number of sites in the chain. The parameters J , U in (123) are the hopping amplitude and the strength of the on-site interaction, respectively. Periodic boundary conditions are implemented requiring that $a_L^\dagger a_L = a_1^\dagger a_1$. The lattice is loaded with N bosons. While some exact results are available for $N=2^{638,725,726}$ and an effective model can be built to explain the spectrum for $N=3^{727,728}$, for larger number of particles the system is not solvable and numerical simulations are necessary^{729,730}.

2-particle sector The problem of two attracting bosons on a lattice is exactly solvable *à la* coordinate Bethe Ansatz by transforming the wave function in the center of mass and relative coordinates. This solution is also valid in the presence of an synthetic gauge field⁷²⁶. The eigenstates of the system form two bands depending on the nature of relative momentum. For imaginary solutions we have the lowest energy branch composed by L bound-state (solitons), while the real solutions correspond to scattering states which form the second band at higher energy. The energy gap separating the two increases with interactions and it is found that for $U/J \geq 4$ the two bands completely detach for each momenta⁷²⁶.

N -particle sector For larger number of particles, the BHM (123) is not solvable by the coordinate Bethe ansatz. The failure results because of finite probabilities that a given site is occupied by *more than two* particles, whose interaction cannot be factorized in 2-body scattering^{731–733}.

Information on the available excitations in the system as a function of their momentum k and energy ω is provided by the dynamical structure factor $S(k, \omega)$:

$$S(k, \omega) = \sum_{\alpha \neq 0} \sum_r |\langle \alpha | e^{-ikr} \hat{n}_r | 0 \rangle|^2 \delta(\omega - \omega_\alpha). \quad (124)$$

where \hat{n}_r is the number operator acting on the site r , $|0\rangle$ is the ground state and α labels the states with increasing energy (ie $\alpha=1$ is the first excited state). The peaks of $S(k, \omega)$ reconstruct the energy bands of the system^{727,728} and are shown in Fig. 74. Numerical results show a scenario similar to the two-particle case with a low-energy band that is separated from the rest of the spectrum. The nature of such a band can be analyzed by the study of correlation functions: $C(r) = \langle n_{L/2} n_{L/2+r} \rangle$. The numerical analysis shows that the lowest energy band is composed of bound states. In fact all these states are characterized by an exponential decaying of

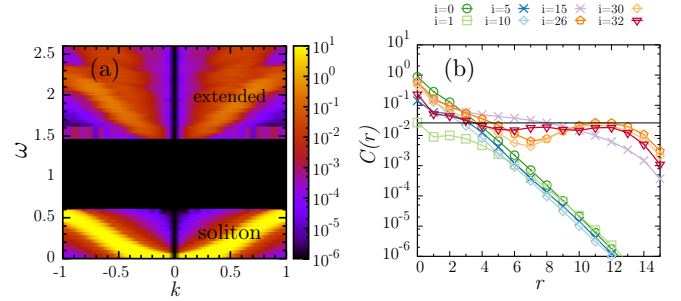


FIG. 74. Panel (a): dynamical structure factor $S(k, \omega)$ for a chain of $L=30$ sites. Numerical results for $N=5$ particles and interactions $U=1.2$. Panel (b): Density-Density correlation function $C(r)$ for $N=5$ particles in a chain of $L=30$ sites and interactions $U=0.6 < U_c$. Correlations are computed over several excited states labelled by i (i -th excited state, $i=0$ correspond to the ground state).

correlations $C(r) \sim \exp(-r/\xi)$. The correlation length ξ is fixed only by the interactions and decreases with increasing U . For states belonging to the second branch $C(r)$ approaches, at intermediate distances, a plateau $\sim n_{as} = (N/L)^2$, before dropping down when approaching the walls of the box. We thus can conclude that the higher branch contains extended states. Also in this case the bands gap increases with interactions and the critical interaction to have a complete detachment of the bands scales like $U_c \sim 1/N$.

2. Soliton stability

Finally, we devise a specific dynamical protocol to study the solitons stability and evidence the features of the band structure.

By initially breaking the lattice translational symmetry with an attractive potential $\mathcal{H}_i(\mu, U) = \mathcal{H}(U) + \mu(U)n_{i_0}$, a soliton is pinned in a given site i_0 of the lattice, and then let it expand by removing the pinning. In this way, while for small U we populate both scattering and bound states, for $U > U_c$ when the gap separates the two bands, mostly bound states are populated.

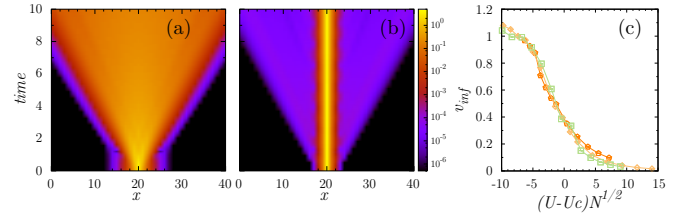


FIG. 75. Panels (a-b): expansion of a soliton composed by $N=5$ particles, pinned to the center of a chain with $L=41$ sites for interactions $U=0.4$ and $U=1.8$. Panel (c): asymptotic expansion velocity v_∞ as a function of $U-U_c(N)$ and of $(U-U_c(N))\sqrt{N}$.

In Fig. 75 (a-b) we show the expansion dynamics of the density for two cases: $U < U_c$, and $U > U_c$. Increasing the interaction strength, the density profile remains closer and closer

to the one of the initial state. Only a small fraction is spreading into the chain leading to a higher stability of the soliton. This phenomenon can be studied more quantitatively by analyzing the expansion velocity: $v(t) = (d/dt)\sqrt{R^2(t) - R^2(0)}$, with $R^2(t) = (1/N)\sum_{i=1}^L n_i(t)(i - i_0)^2$ and its asymptotic value at large times v_∞ . The inspection of v_∞ in Fig. 75 (c) further shows the difference between the two regimes. While there is no criticality in the system close to U_c , v_∞ displays a peculiar scaling behaviour and acts like an order parameters for the system.

3. Solitons in rotation

An atomtronic-interferometer can be made of attracting neutral bosonic atoms flowing in a ring-shaped lattice potential of mesoscopic size which sustains a neutral persistent current flow. The effect of an induced rotation, or more generally of a (synthetic) gauge field, on such a system as been extensively studied⁵²⁷. It's in fact well known that quantum system in a ring geometry displays a staircase response to an applied gauge field of intensity Ω . The induced angular momentum increases in quantized steps as a function of Ω ^{110,387} and the amplitude of persistent currents displays periodic oscillations with Ω ^{734,735}. The periodicity of such oscillation is completely fixed by the effective flux quantum present in the system, and does not depend on the intensity of particle-particle interactions⁷³⁶. In the following, without loss of generality, we will refer only to the case of an artificial gauge field induced by a global rotation at angular frequency Ω . Our discussions can be applied to any type of artificial gauge fields.

For strongly correlated one-dimensional bosons with attractive interactions, as we discuss in the following, the nature of flux quantum is non trivial, due to the formation of many-body bound states. This feature has dramatic effects on the persistent current that oscillates with a periodicity N times smaller than in the standard case corresponding to repulsive interactions. Remarkably, the periodicity depends on interaction, which leads to an extension of the Leggett theorem.

Continuous ring For a continuous ring, the system can be described through the Bose-gas integrable theory, i.e. the Lieb-Liniger model⁷³⁷. This is the case when the density N/L of bosons, where N is the particle number and $L = 2\pi R$ is the perimeter of the ring of radius R , is small. For such systems, exact results are well known²¹³. The Lieb-Liniger Hamiltonian in the rotating frame reads:

$$\mathcal{H}_{LL} = \sum_{j=1}^N \frac{1}{2m} \left(p_j - m\Omega R \right)^2 + g \sum_{j<l} \delta(x_j - x_l) - E_\Omega, \quad (125)$$

where m and the p_i 's are respectively the mass and the momentum of each particle, $L_z = \sum_{j=1}^N L_{z,j}$ is the total angular momentum of the N particles, g is the interaction strength and $E_\Omega = Nm\Omega^2 R^2/2$.

The solution of the model dramatically change according to the sign of the interactions. For repulsive interactions, independently on their strength, the ground state energy E_{GS} is

periodic in Ω with period $\Omega_0 = \hbar/mR^2$. The persistent current in the rotating frame defined as $I_p = -(\Omega_0/\hbar)\partial E_{GS}/\partial\Omega$ displays a sawtooth behaviour versus Ω ⁷³⁶, corresponding to a staircase behaviour of angular momentum L_z .

For attractive interactions the scenario changes completely; the ground state is a many-body bound state, i.e. a 'molecule' made of N bosons, corresponding to the quantum analog of a bright soliton^{729,738,739}. The ground state energy for arbitrary Ω then reads

$$E_{GS} = \frac{\hbar^2}{2MR^2} \left(\ell - N \frac{\Omega}{\Omega_0} \right)^2 - \frac{N(N^2 - 1)g^2}{12}, \quad (126)$$

where the second term accounts for the interaction energy E_{int} and is independent on the rotation frequency. This result clearly shows how, under the effect of the artificial gauge field, attracting bosons effectively behave as a single massive object of mass $M = Nm$. The energy displays a $1/N$ -periodicity as a function of the artificial gauge field, Ω , in units of Ω_0 corresponding to *fractionalisation* of angular momentum per particle.

Lattice ring When the density of particles is not small, the lattice effects, that break the integrability of the model, start to be relevant. In this situation the system is well described by the Bose-Hubbard Model (BHM):

$$\mathcal{H}_{BH} = \sum_{j=1}^{N_s} \frac{U}{2} n_j(n_j - 1) - J \left(e^{-i\tilde{\Omega}} a_j^\dagger a_{j+1} + \text{h.c.} \right), \quad (127)$$

where a_j and a_j^\dagger are site j annihilation and creation Bose operators and $n_j = a_j^\dagger a_j$ is number operator. The parameters $J, U < 0$ in (127) are respectively the hopping amplitude and the strength of the on-site interaction, N_s being the number of sites in the lattice and $\tilde{\Omega} \doteq 2\pi\Omega/(\Omega_0 N_s)$ for brevity.

In the lattice model (127), the center-of-mass and relative coordinates, at any finite interaction, cannot be decouple. This feature has a profound implication on the behaviour of persistent current. As we will discuss below, in contrast with the continuous theory, here the persistent current periodicity does depend on interaction strength.

In Fig. 76 we show the numerical results angular momentum: also in this case the $1/N$ periodicity in Ω/Ω_0 of the persistent currents emerges, as well as fractionalization of angular momentum. While fractionalization always occurs, the $1/N$ periodicity, is affected by the interplay between system size and interaction strength.

When interactions are sufficiently large the 'size of the many-body bound state', i.e. the decay length of the density-density correlations⁷²⁹, is much smaller than the size of the system. Upon decreasing the interactions, the size of the many-body bound state increases more and more over the chain and the solitonic nature of the state gets less and less pronounced. All the observed features are purely quantum many-body effects tracing back to specific quantum correlations since they completely disappear in a mean-field Gross-Pitaevskii description of the system.

Angular momentum fractionalization and the related per-

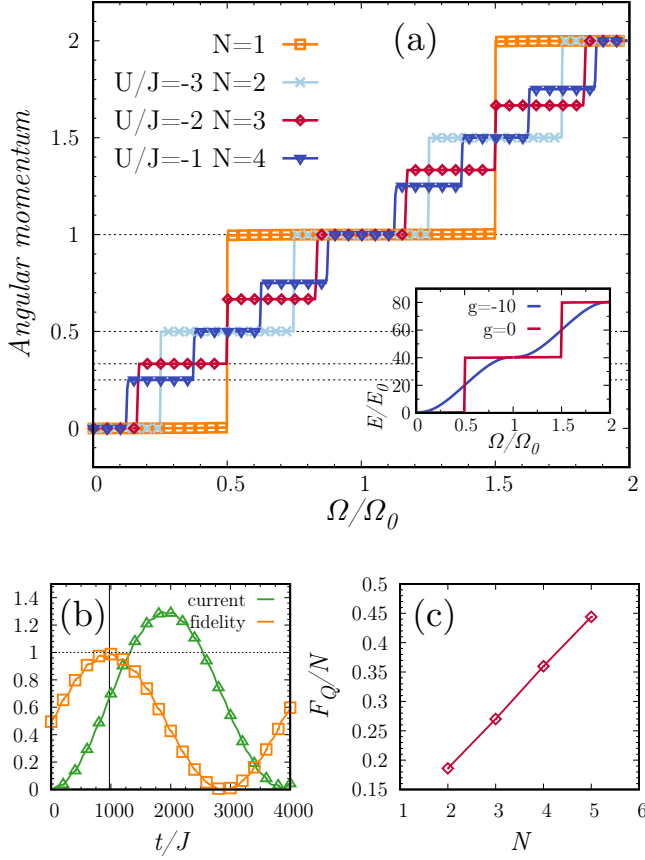


FIG. 76. Panel (a): average angular momentum per particle (inset: GP analysis) as a function of the artificial gauge field for different particle number and for particular values of interaction strength. Panel (b): time dependent current (in units of the hopping constant J) following a quench from $\Omega/\Omega_0=0$ to $\Omega/\Omega_0=1/2$. Here we set $L=28$, $N=3$, $U/J=-0.51$ and $\Delta_0/J=0.015$. Panel (c): Quantum Fisher information as a function of the particle number showing the Heisenberg-limited behaviour $F_Q \propto N^2$.

sistent current periodicity can be observed with standard time-of-flight (TOF) techniques. Measuring the distributions of the atoms after releasing the trap confinement and turning off interactions we have access to the momentum distribution, defined as $n(\mathbf{k}) = |w(\mathbf{k})|^2 \sum_{j,l} e^{i\mathbf{k} \cdot (\mathbf{x}_j - \mathbf{x}_l)} \langle a_j^\dagger a_l \rangle$. In fact we find that the mean-square radius of the distribution increases in fractional steps of for $\Omega/\Omega_0 = \ell/N^{95}$.

4. Entangling solitons with different L_z

We finally demonstrate how the scenario above can be harnessed to create specific entangled states of persistent currents. Such entangled states are characterised by an increased sensitivity to the effective magnetic field that reaches the Heisenberg limit. In the following, we propose a specific dynamical protocol that allows us to create such type of state.

Since the Hamiltonians in Eqs.(125), (127) commute with the total angular momentum, dynamically mix entangled states

with different angular momentum, the rotational invariance of the system needs to be broken. The ring is then interrupted with a potential barrier of strength Δ_0 localized in a single lattice site. Then the artificial gauge field is quenched from $\Omega=0$ to $\Omega=\Omega_0/2$. This procedure is capable to dynamically entangle the angular momentum state at $\Omega=0$, ie $L_z=0$, with the one at $\Omega=\Omega_0$, ie $L_z=N$ (see Fig. 76), yielding $|\psi\rangle_{NOON} = \frac{1}{\sqrt{2}} (|L_z=0\rangle + |L_z=N\rangle)$ when the current reaches the half of its maximum value.

The response of such a state to an external rotation is $|\psi(\phi)\rangle = e^{i\phi \hat{L}_z/\hbar} |\psi\rangle_{NOON}$, and the quantum Fisher information^{740,741} $F_Q = 4(\langle \psi'(\phi) | \psi'(\phi) \rangle - |\langle \psi'(\phi) | \psi(\phi) \rangle|^2)$, being $|\psi'(\phi)\rangle = \partial |\psi(\phi)\rangle / \partial \phi$. For our state we find $F_Q \sim N^2$, ie it reaches the Heisenberg limit - see Fig. 76. The corresponding sensitivity $\delta\phi$, therefore, is

$$\delta\phi \geq \frac{1}{(F_Q)^{1/2}} = \frac{1}{N}, \quad (128)$$

This shows that entangled states of quantum solitons with different angular momenta lead to a quantum advantage of the sensitivity.

B. Conclusions and outlook

We have extensively studied attractive bosons in the quantum regime. Its ground state is an N -body bound state, which on a lattice is protected by a gap with respect to the first branch of excitations, corresponding to scattering states. We have shown that this implies the stability of a soliton initially prepped in a pinning site. We have also shown that quantum solitons on a ring display an enhanced response to artificial gauge field Ω , with a $1/N$ periodicity as a function of Ω/Ω_0 . This corresponds to fractionalization of angular momentum per particle, intrinsically due to the presence of many-body bound states. Finally, we have identified a protocol to create a non-classical superposition of angular momentum states by a suitable quench of the artificial gauge field, based on angular momentum fractionalization. The use of quantum coherent macroscopic superposition states in atom interferometry devices can increase considerably the phase sensitivity. The states studied in this chapter can yield an N -fold enhancement in sensitivity to rotation in a ring-based gyroscope. From a theoretical point of view, the next challenge is the study of the effects of decoherence and losses, and the identification of the optimal working parameters for such an interferometer.

XV. MANIPULATING RYDBERG ATOMS

W. Li and O. Morsch

Atoms excited to high-lying energy states (with principal quantum number n larger than ≈ 15) are known as Rydberg atoms⁷⁴². They have considerably longer lifetimes than atoms in low-lying excited states, and much larger (by several orders

of magnitude, with strong scaling with n) electric polarizability as well as dipole and van der Waals interactions. Rydberg atoms have been studied for several decades, with renewed interest sparked by the invention of laser cooling, which made more accurate studies possible, and also due to the advent of quantum computation and quantum simulation, for which Rydberg atoms are a promising building block⁵⁰⁷. Generally, the combination of controllability, strong interactions and long coherence times make Rydberg atoms promising candidates for the realization of future quantum information technologies.

For the purposes of atomtronics, Rydberg atoms are an interesting system to study in regard to the propagation of excitations in disordered or ordered arrays. In fact, many transport properties, both in the quantum and semiclassical regimes, can be studied using Rydberg excitations. In this chapter we give a brief review of some experiments from our groups, including studies of percolation phenomena, microwave control of Rydberg atoms, and manipulation of Rydberg atoms in ordered arrays. Techniques developed and insights obtained in these experiments could be relevant in further exploring Rydberg systems for atomtronics enable technologies.

A. Driven-dissipative Rydberg systems

An important aspect of transport phenomena is the interplay between an external drive and the natural dissipation of the system. In samples of ultra-cold Rydberg atoms (with temperatures around $T \approx 120 \mu\text{K}$, so on the timescales of typical experiments atomic motion can be neglected) we can study this interplay by driving a transition between the ground state of the atom (87-rubidium in our case) and a high-lying Rydberg state with $n \approx 70 - 80$. In our experiments in Pisa we use S states (zero angular momentum), for which the van der Waals interaction is repulsive. This interaction leads to two distinct many-body effects. For resonant driving, it prevents the excitation of more than one Rydberg atom inside the "blockade sphere"; this is known as the dipole blockade^{743,744}. On the other hand, for off-resonant driving the van der Waals interaction can lead to the compensation of the detuning if a ground state atom is at a certain "facilitation distance" from a Rydberg atom^{745,746}. At that distance, the off-resonant driving is shifted into resonance and thus the excitation of the ground state atom is "facilitated".

It turns out that by adding the natural decay of a Rydberg state due to spontaneous emission (with timescales of a few hundred μs) it is possible to realize a paradigmatic model from statistical physics called directed percolation⁷⁴⁷. This model can be characterized by two processes in a spin-1/2 example: offspring production, in which a "spin up" causes a nearby "spin down" to flip its state at a certain rate; and sudden death, in which a "spin up" spontaneously flips down. For our Rydberg system, these two processes can be directly translated into facilitation with rate Γ_{fac} and spontaneous decay with rate Γ_{spon} . We note here that both processes are incoherent (in particular, we choose a Rabi frequency for Rydberg excitation that is smaller than the decoherence rate).

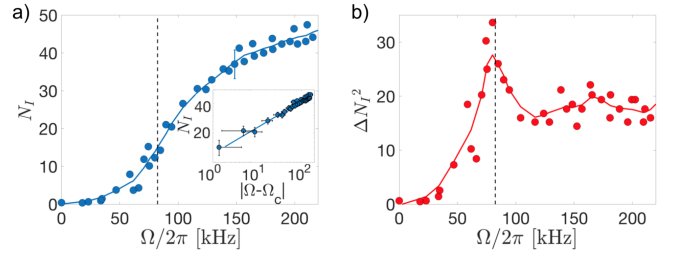


FIG. 77. Evidence for an absorbing state phase transition in a Rydberg gas. a) Number of excitations in the stationary state as a function of Ω (the solid line is a sliding average to guide the eye). The inset shows a power-law fit around the critical value Ω_c , indicated by the dashed line in the main figure. In b) the peak in the variance plotted as a function of Ω indicates the critical point. Adapted from ref. ⁷⁴⁸.

From statistical physics we know that this directed percolation model exhibits a phase transition between its absorbing state (all spins "down", or all atoms in the ground state) and an active state in which, on average, a macroscopic number of spins are "up" (i.e., atoms are in Rydberg states).

We realized this model using Rb Rydberg atoms in a magneto-optical trap⁷⁴⁸. By varying the Rabi frequency of the off-resonant laser driving (a two-photon excitation via an intermediate $6P$ state was used) we were able to scan the ratio $\Gamma_{\text{fac}}/\Gamma_{\text{spon}}$ across the critical value for the absorbing-state phase transition (Γ_{fac} is related to Ω via $\Gamma_{\text{fac}} = (\Omega^2/2\gamma)$, where γ is the decoherence rate). Fig. 77 shows the results of those experiments. In order to prepare the system away from the absorbing state with all atoms in the ground state (from which, by definition, the system cannot escape), we initially excited around 30 Rydberg atoms in the cloud and then allowed the system to evolve under constant driving for 1.5 ms before measuring the number of Rydberg excitations by field ionization. The directed percolation phase transition is visible both in the plot of the number of excitations as a function of Ω (Fig. 77 a)) and as a peak in the variance of the number of excitations (Fig. 77 b)).

This is one example of a transport/percolation problem implemented using cold Rydberg atoms. In future experiments, this concept can be extended to (partially) coherent driving^{749,750} and/or ordered arrays^{751,752}, as well to tailored and controllable dissipation.

B. Microwave-optical conversion using Rydberg atoms

Rydberg atoms feature transitions of very large dipole moments in the microwave frequency range⁷⁴², which has been utilized for sensitive detection of microwave electric field^{753,754} and for efficient conversion from microwave to optical photons⁷⁵⁵. In quantum simulation using Rydberg atoms, nearby Rydberg states are commonly encoded as spin states, and their populations and dynamics can be conveniently manipulated with microwave radiation^{18,756}.

Here we present a demonstration of coherent microwave-to-optical conversion of classical fields via six-wave mixing

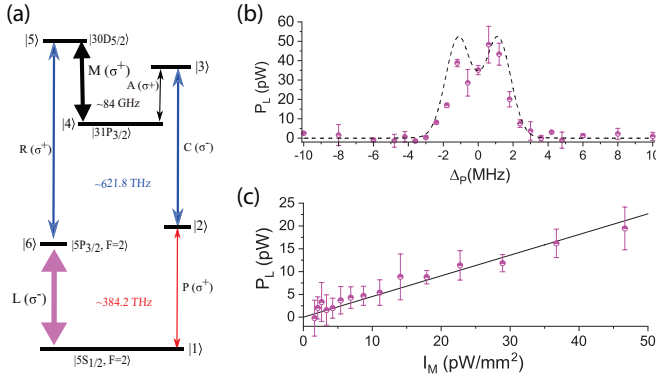


FIG. 78. Efficient microwave-to-optical conversion using Rydberg atoms. (a) Energy level diagram and coupled transitions. The polarization of the fields are indicated inside parentheses. (b) Spectrum of the generated light power P_L . The dashed line is a simulated result obtained using Maxwell-Bloch equations. (c) The power of the generated light is plotted versus I_M in the range of 0 to 50 pW/mm². The solid line is the result of a linear fit. This figure is adapted from Ref. 759.

in Rydberg atoms. In quantum regime, such coherent conversion is essential for coupling superconducting qubits operating at microwave frequencies to photonic qubits used in quantum communication over long distances⁷⁵⁷, and therefore has been intensively pursued in quite a few different physical systems⁷⁵⁸.

The principle of our conversion experiment using Rydberg atoms is as follows. A cloud of cold polarized ^{87}Rb atoms is illuminated by four auxiliary electromagnetic fields P, C, A, R as well as the microwave field M to be converted. By non-linear frequency mixing of the six waves in the atomic medium, the field M is converted into the optical field L. The chosen configuration of energy levels is displayed in Fig. 78(a), where the six waves are near-resonant with the atomic transitions shown in the figure with $|1\rangle \equiv |5S_{1/2}, F=2, m_F=2\rangle$, $|2\rangle \equiv |5P_{3/2}, F=3, m_F=3\rangle$, $|3\rangle \equiv |30D_{3/2}, m_J=1/2\rangle$, $|4\rangle \equiv |31P_{3/2}, m_J=-1/2\rangle$, $|5\rangle \equiv |30D_{5/2}, m_J=1/2\rangle$, and $|6\rangle \equiv |5P_{3/2}, F=2, m_F=1\rangle$. In the absence of the microwave field M, the system is in the configuration of microwave dressed electromagnetically induced transparency involving Rydberg states (Rydberg EIT), formed by the two optical waves P and C, and the auxiliary microwave field A. Once the M and R fields are added, the coherence induced between the ground state $|1\rangle$ and the intermediate state $|6\rangle$ triggers the generation of the converted optical field L.

A typical spectrum of the measured power P_L of the generated L field vs. the input P field detuning Δ_P is shown in Fig. 78(b). The conversion is most efficient around $\Delta_P = 0$, which is consistent with the non-linearity responsible for the frequency mixing being maximum close to resonance. The behavior P_L for $\Delta_P = 0$ is approximately linear as a function of the input intensity I_M of field M, as shown in Fig. 78(c). Given $P_L \approx \alpha I_M$, a linear fit to the data yields the photon conversion efficiency of the process to be $\eta = 0.051$. This conversion efficiency is seventeen times larger than the one reported in Ref.⁷⁵⁵, and this enhancement is due to an improved ex-

perimental configuration, which makes the conversion occur over a longer distance. Our theoretical study shows that by using a carefully selected energy level scheme to minimize the absorption of the input P field when propagating through the conversion medium, a conversion efficiency above 50% can be reached even with all-resonance six-wave mixing similar to that in Fig. 78(a)⁷⁵⁹.

This conversion method is an application example from the strong coupling between microwave and Rydberg atoms. To reach near-unit conversion efficiency for quantum state transfer at the single photon level, one may consider implementing stimulated Raman adiabatic passage⁷⁶⁰, or tuning two of the fields (for example fields C and A) off-resonance to realize an effective two-photon transition in our system^{761,762}. Besides its potential for quantum state transfer, this method is also promising for the sensitive detection of microwave or THz photons since these photons could be very efficiently converted into optical photons before photo-detection.

Acknowledgments O.M. acknowledges financial support through the H2020-FETPROACT-2014 grant No. 640378 (RYSQ). W.L. acknowledges the support by the National Research Foundation, Prime Minister's Office, Singapore and the Ministry of Education, Singapore under the Research Centres of Excellence programme.

- ¹J. P. Dowling and G. J. Milburn, "Quantum technology: the second quantum revolution," *Philosophical Transactions of the Royal Society of London A: Mathematical, Physical and Engineering Sciences* **361**, 1655–1674 (2003).
- ²A. Acín, I. Bloch, H. Buhrman, T. Calarco, C. Eichler, J. Eisert, D. Esteve, N. Gisin, S. J. Glaser, F. Jelezko, *et al.*, "The quantum technologies roadmap: a european community view," *New Journal of Physics* **20**, 080201 (2018).
- ³H. Rubinsztein-Dunlop, A. Forbes, M. V. Berry, M. R. Dennis, D. L. Andrews, M. Mansuripur, C. Denz, C. Alpmann, P. Banzer, T. Bauer, *et al.*, "Roadmap on structured light," *Journal of Optics* **19**, 013001 (2016).
- ⁴R. Dumke, Z. Lu, J. Close, N. Robins, A. Weis, M. Mukherjee, G. Birkel, C. Hufnagel, L. Amico, M. G. Boshier, *et al.*, "Roadmap on quantum optical systems," *J. Opt.* **18**, 093001 (2016).
- ⁵L. Amico, G. Birkel, M. Boshier, and L.-C. Kwek, "Focus on atomtronics-enabled quantum technologies," *New Journal of Physics* **19**, 020201 (2017).
- ⁶M. Tinkham, *Introduction to superconductivity* (Courier Corporation, 2004).
- ⁷S. Eckel, J. G. Lee, F. Jendrzejewski, N. Murray, C. W. Clark, C. J. Lobb, W. D. Phillips, M. Edwards, and G. K. Campbell, "Hysteresis in a quantized superfluid/atomtronic circuit," *Nature* **506**, 200–203 (2014).
- ⁸G. Birkel and J. Fortágh, "Micro traps for quantum information processing and precision force sensing," *Laser & Photonics Reviews* **1**, 12–23 (2007).
- ⁹J.-F. Schaff, T. Langen, and J. Schmiedmayer, "Interferometry with atoms," *La Rivista del Nuovo Cimento* **37**, 509–589 (2014).
- ¹⁰I. O. Kulik and R. Ellialtıogamallu, *Quantum Mesoscopic Phenomena and Mesoscopic Devices in Microelectronics*, Vol. 559 (Springer Science & Business Media, 2012).
- ¹¹R. Fazio, V. Gantmakher, and Y. Imry, *New Directions in Mesoscopic Physics (Towards Nanoscience)*, Vol. 125 (Springer Science & Business Media, 2003).
- ¹²Y. V. Nazarov, *Quantum noise in mesoscopic physics*, Vol. 97 (Springer Science & Business Media, 2012).
- ¹³D. Barredo, S. de Léséleuc, V. Lienhard, T. Lahaye, and A. Browaeys, "An atom-by-atom assembler of defect-free arbitrary two-dimensional atomic arrays," *Science* **354**, 1021–1023 (2016).
- ¹⁴D. Barredo, V. Lienhard, S. de Léséleuc, T. Lahaye, and A. Browaeys, "Synthetic three-dimensional atomic structures assembled atom by atom," *Nature* **561**, 79–82 (2018).

- D. Ohl, D. de Mello, D. Schäffner, T. Werkmann, T. Preuschoff, L. Kohfahl, M. Schlosser, and G. Birkel, "Defect-free assembly of 2d clusters of more than 100 single-atom quantum systems," *Phys. Rev. Lett.* **122**, 203601 (2019).
- ¹⁶H. Kim, W. Lee, H. Lee, H. Jo, Y. Song, and J. Ahn, "In situ single-atom array synthesis using dynamic holographic optical tweezers," *Nature Communications* **7**, 13317 (2016).
- ¹⁷D. Barredo, V. Lienhard, P. Scholl, S. de Léséleuc, T. Boulier, A. Browaeys, and T. Lahaye, "Three-dimensional trapping of individual rydberg atoms in ponderomotive bottle beam traps," *Phys. Rev. Lett.* **124**, 023201 (2020).
- ¹⁸S. de Léséleuc, V. Lienhard, P. Scholl, D. Barredo, S. Weber, N. Lang, H. P. Büchler, T. Lahaye, and A. Browaeys, "Observation of a symmetry-protected topological phase of interacting bosons with rydberg atoms," *Science* **365**, 775–780 (2019).
- ¹⁹C. Ryu and M. G. Boshier, "Integrated coherent matter wave circuits," *New Journal of Physics* **17**, 092002 (2015).
- ²⁰G. Gauthier, S. S. Szigeti, M. T. Reeves, M. Baker, T. A. Bell, H. Rubinsztein-Dunlop, M. J. Davis, and T. W. Neely, "Quantitative acoustic models for superfluid circuits," *Phys. Rev. Lett.* **123**, 260402 (2019).
- ²¹S. C. Caliga, C. J. E. Straatsma, and D. Z. Anderson, "Transport dynamics of ultracold atoms in a triple-well transistor-like potential," *New Journal of Physics* **18**, 025010 (2016).
- ²²C. Ryu, P. W. Blackburn, A. A. Blinova, and M. G. Boshier, "Experimental realization of josephson junctions for an atom squid," *Phys. Rev. Lett.* **111**, 205301 (2013).
- ²³S. Eckel, A. Kumar, T. Jacobson, I. B. Spielman, and G. K. Campbell, "A rapidly expanding bose-einstein condensate: An expanding universe in the lab," *Phys. Rev. X* **8**, 021021 (2018).
- ²⁴T. A. Bell, J. A. P. Glidden, L. Humbert, M. W. J. Bromley, S. A. Haine, M. J. Davis, T. W. Neely, M. A. Baker, and H. Rubinsztein-Dunlop, "Bose-einstein condensation in large time-averaged optical ring potentials," *New Journal of Physics* **18**, 035003 (2016).
- ²⁵W. J. Kwon, G. Del Pace, R. Panza, M. Inguscio, W. Zwerger, M. Zaccanti, F. Scazza, and G. Roati, "Strongly correlated superfluid order parameters from dc josephson supercurrents," *Science* **369**, 84–88 (2020).
- ²⁶A. L. Gaunt, T. F. Schmidutz, I. Gotlibovych, R. P. Smith, and Z. Hadzibabic, "Bose-einstein condensation of atoms in a uniform potential," *Phys. Rev. Lett.* **110**, 200406 (2013).
- ²⁷R. Saint-Jalm, P. C. M. Castilho, E. Le Cerf, B. Bakkali-Hassani, J.-L. Ville, S. Nascimbene, J. Beugnon, and J. Dalibard, "Dynamical symmetry and breathers in a two-dimensional bose gas," *Phys. Rev. X* **9**, 021035 (2019).
- ²⁸S. K. Schnelle, E. D. van Ooijen, M. J. Davis, N. R. Heckenberg, and H. Rubinsztein-Dunlop, "Versatile two-dimensional potentials for ultracold atoms," *Opt. Express* **16**, 1405–1412 (2008).
- ²⁹K. Henderson, C. Ryu, C. MacCormick, and M. G. Boshier, "Experimental demonstration of painting arbitrary and dynamic potentials for bose-einstein condensates," *New Journal of Physics* **11**, 043030 (2009).
- ³⁰T. A. Bell, G. Gauthier, T. W. Neely, H. Rubinsztein-Dunlop, M. J. Davis, and M. A. Baker, "Phase and micromotion of bose-einstein condensates in a time-averaged ring trap," *Phys. Rev. A* **98**, 013604 (2018).
- ³¹A. Lenef, T. D. Hammond, E. T. Smith, M. S. Chapman, R. A. Rubenstein, and D. E. Pritchard, "Rotation sensing with an atom interferometer," *Phys. Rev. Lett.* **78**, 760–763 (1997).
- ³²L. M. Ayccock, H. M. Hurst, D. K. Efimkin, D. Genkina, H.-I. Lu, V. M. Galitski, and I. B. Spielman, "Brownian motion of solitons in a bose-einstein condensate," *Proceedings of the National Academy of Sciences* **114**, 2503–2508 (2017).
- ³³C. S. Chisholm, R. Thomas, A. B. Deb, and N. Kjærgaard, "A three-dimensional steerable optical tweezer system for ultracold atoms," *Review of Scientific Instruments* **89**, 103105 (2018).
- ³⁴M. Tajik, B. Rauer, T. Schweigler, F. Cataldini, J. Sabino, F. S. M. Åller, S.-C. Ji, I. E. Mazets, and J. Schmiedmayer, "Designing arbitrary one-dimensional potentials on an atom chip," **27**, 33474–33487.
- ³⁵G. Gauthier, "Transport and turbulence in quasi-uniform and versatile bose-einstein condensates," (2019).
- ³⁶P. Zupancic, P. M. Preiss, R. Ma, A. Lukin, M. E. Tai, M. Rispoli, R. Islam, and M. Greiner, "Ultra-precise holographic beam shaping for microscopic quantum control," *Optics express* **24**, 13881–13893 (2016).
- ³⁷G. Gauthier, I. Lenton, N. M. Parry, M. Baker, M. J. Davis, H. Rubinsztein-Dunlop, and T. W. Neely, "Direct imaging of a digital-micromirror device for configurable microscopic optical potentials," *Optica* **3**, 1136–1143 (2016).
- ³⁸J. Ville, T. Bienaimé, R. Saint-Jalm, L. Corman, M. Aidelsburger, L. Chomaz, K. Kleinlein, D. Perconte, S. Nascimbène, J. Dalibard, *et al.*, "Loading and compression of a single two-dimensional Bose gas in an optical accordion," *Physical Review A* **95**, 013632 (2017).
- ³⁹J. Liang, R. N. Kohn Jr, M. F. Becker, and D. J. Heinzen, "1.5% root-mean-square flat-intensity laser beam formed using a binary-amplitude spatial light modulator," *Applied optics* **48**, 1955–1962 (2009).
- ⁴⁰G. Gauthier, M. T. Reeves, X. Yu, A. S. Bradley, M. A. Baker, T. A. Bell, H. Rubinsztein-Dunlop, M. J. Davis, and T. W. Neely, "Giant vortex clusters in a two-dimensional quantum fluid," *Science* **364**, 1264–1267 (2019).
- ⁴¹S. P. Johnstone, A. J. Groszek, P. T. Starkey, C. J. Billington, T. P. Simula, and K. Helmerson, "Evolution of large-scale flow from turbulence in a two-dimensional superfluid," *Science* **364**, 1267–1271 (2019).
- ⁴²A. R. Fritsch, M. Lu, G. H. Reid, A. M. Piñeiro, and I. B. Spielman, "Creating solitons with controllable and near zero velocity in bose-einstein condensates," (2020), arXiv:2004.04200.
- ⁴³O. R. Stockdale, M. T. Reeves, X. Yu, G. Gauthier, K. Goddard-Lee, W. P. Bowen, T. W. Neely, and M. J. Davis, "Universal expansion of vortex clusters in a dissipative two-dimensional superfluid," (2019), arXiv:1912.09535.
- ⁴⁴E. Samson, K. Wilson, Z. Newman, and B. P. Anderson, "Deterministic creation, pinning, and manipulation of quantized vortices in a Bose-Einstein condensate," *Physical Review A* **93**, 023603 (2016).
- ⁴⁵B.-S. K. Skagerstam, U. Hohenester, A. Eiguren, and P. K. Rekdal, "Spin decoherence in superconducting atom chips," *Physical review letters* **97**, 070401 (2006).
- ⁴⁶U. Hohenester, A. Eiguren, S. Scheel, and E. Hinds, "Spin-flip lifetimes in superconducting atom chips: Bardeen-cooper-schrieffer versus eliasberg theory," *Physical Review A* **76**, 033618 (2007).
- ⁴⁷R. Fermani, T. Mueller, B. Zhang, M. J. Lim, and R. Dumke, "Heating rate and spin flip lifetime due to near-field noise in layered superconducting atom chips," *Journal of Physics B: Atomic, Molecular and Optical Physics* **43**, 095002 (2010).
- ⁴⁸S. Scheel, P.-K. Rekdal, P. L. Knight, and E. A. Hinds, "Atomic spin decoherence near conducting and superconducting films," *Physical Review A* **72**, 042901 (2005).
- ⁴⁹V. Dikovskiy, V. Sokolovskiy, B. Zhang, C. Henkel, and R. Folman, "Superconducting atom chips: advantages and challenges," *The European Physical Journal D* **51**, 247–259 (2009).
- ⁵⁰A. Emmert, A. Lupaşcu, G. Nogues, M. Brune, J.-M. Raimond, and S. Haroche, "Measurement of the trapping lifetime close to a cold metallic surface on a cryogenic atom-chip," *The European Physical Journal D* **51**, 173–177 (2009).
- ⁵¹G. Bensky, R. Amsüss, J. Majer, D. Petrosyan, J. Schmiedmayer, and G. Kurizki, "Controlling quantum information processing in hybrid systems on chips," *Quantum Information Processing* **10**, 1037 (2011).
- ⁵²T. Thiele, S. Filipp, J. A. Agner, H. Schmutz, J. Deiglmayr, M. Stammeier, P. Allmendinger, F. Merkt, and A. Wallraff, "Manipulating rydberg atoms close to surfaces at cryogenic temperatures," *Physical Review A* **90**, 013414 (2014).
- ⁵³C. Hermann-Avigliano, R. C. Teixeira, T. Nguyen, T. Cantat-Moltrecht, G. Nogues, I. Dotsenko, S. Gleyzes, J. Raimond, S. Haroche, and M. Brune, "Long coherence times for rydberg qubits on a superconducting atom chip," *Physical Review A* **90**, 040502 (2014).
- ⁵⁴L. Sárkány, J. Fortágh, and D. Petrosyan, "Long-range quantum gate via rydberg states of atoms in a thermal microwave cavity," *Physical Review A* **92**, 030303 (2015).
- ⁵⁵D. Yu, A. Landra, M. M. Valado, C. Hufnagel, L. C. Kwek, L. Amico, and R. Dumke, "Superconducting resonator and rydberg atom hybrid system in the strong coupling regime," *Physical Review A* **94**, 062301 (2016).
- ⁵⁶D. Yu, A. Landra, L. C. Kwek, L. Amico, and R. Dumke, "Stabilizing rabi oscillation of a charge qubit via the atomic clock technique," *New Journal of Physics* **20**, 023031 (2018).
- ⁵⁷D. Petrosyan, K. Mølmer, J. Fortágh, and M. Saffman, "Microwave to optical conversion with atoms on a superconducting chip," *New Journal of*

- Physics **21**, 073033 (2019).
- ⁵⁸S. Bergamini, B. Darquie, M. Jones, L. Jacubowicz, A. Browaeys, and P. Grangier, "Holographic generation of microtrap arrays for single atoms by use of a programmable phase modulator," *J. Opt. Soc. Am. B* **21**, 1889–1894 (2004).
 - ⁵⁹V. Boyer, R. M. Godun, G. Smirne, D. Cassettari, C. M. Chandrashekar, A. B. Deb, Z. J. Laczik, and C. J. Foot, "Dynamic manipulation of Bose-Einstein condensates with a spatial light modulator," *Phys. Rev. A* **73**, 031402 (2006).
 - ⁶⁰S. Tao and W. Yu, "Beam shaping of complex amplitude with separate constraints on the output beam," *Opt. Express* **23**, 1052–1062 (2015).
 - ⁶¹L. Wu, S. Cheng, and S. Tao, "Simultaneous shaping of amplitude and phase of light in the entire output plane with a phase-only hologram," *Scientific Reports* **5**, 15426 (2015).
 - ⁶²T. Harte, G. D. Bruce, J. Keeling, and D. Cassettari, "Conjugate gradient minimisation approach to generating holographic traps for ultracold atoms," *Opt. Express* **22**, 26548 (2014).
 - ⁶³D. Bowman, T. L. Harte, V. Chardonnet, C. D. Groot, S. J. Denny, G. L. Goc, M. Anderson, P. Ireland, D. Cassettari, and G. D. Bruce, "High-fidelity phase and amplitude control of phase-only computer generated holograms using conjugate gradient minimisation," *Opt. Express* **25**, 11692–11700 (2017).
 - ⁶⁴F. Buccheri, G. D. Bruce, A. Trombettoni, D. Cassettari, H. Babujian, V. E. Korepin, and P. Sodano, "Holographic optical traps for atom-based topological kondo devices," *New Journal of Physics* **18**, 075012 (2016).
 - ⁶⁵P. Ireland, *Portable and Versatile Cold Atom Experiments*, Ph.D. thesis, University of St Andrews (2019).
 - ⁶⁶D. Bowman, *Ultracold atoms in flexible holographic traps*, Ph.D. thesis, University of St Andrews (2018).
 - ⁶⁷A. Ramanathan, K. C. Wright, S. R. Muniz, M. Zelan, W. T. Hill, C. J. Lobb, K. Helmerson, W. D. Phillips, and G. K. Campbell, "Superflow in a toroidal Bose-Einstein condensate: An atom circuit with a tunable weak link," *Phys. Rev. Lett.* **106**, 130401 (2011).
 - ⁶⁸M. Huo, W. Nie, D. Hutchinson, and L. C. Kwek, "A solenoidal synthetic field and the non-abelian Aharonov-Bohm effects in neutral atoms," *Sci Rep* **4**, 5992 (2015).
 - ⁶⁹V. E. Lembessis, J. Courtial, N. Radwell, A. Selyem, S. Franke-Arnold, O. M. Aldossary, and M. Babiker, "Graphene-like optical light field and its interaction with two-level atoms," *Phys. Rev. A* **92**, 063833 (2015).
 - ⁷⁰J. A. Sauer, M. D. Barrett, and M. S. Chapman, "Storage ring for neutral atoms," *Phys. Rev. Lett.* **87**, 270401 (2001).
 - ⁷¹S. Wu, W. Rooijakkers, P. Striehl, and M. Prentiss, "Bidirectional propagation of cold atoms in a "stadium"-shaped magnetic guide," *Phys. Rev. A* **70**, 013409 (2004).
 - ⁷²A. S. Arnold, C. S. Garvie, and E. Riis, "Large magnetic storage ring for Bose-Einstein condensates," *Phys. Rev. A* **73**, 041606 (2006).
 - ⁷³J. Fortágh and C. Zimmermann, "Magnetic microtraps for ultracold atoms," *Reviews of Modern Physics* **79**, 235–289 (2007).
 - ⁷⁴M. Keil, O. Amit, S. Zhou, D. Groszasser, Y. Japha, and R. Folman, "Fifteen years of cold matter on the atom chip: promise, realizations, and prospects," *Journal of Modern Optics* **63**, 1840–1885 (2016), <https://doi.org/10.1080/09500340.2016.1178820>.
 - ⁷⁵J.-B. Trebbia, C. L. Garrido Alzar, R. Cornelussen, C. I. Westbrook, and I. Bouchoule, "Roughness suppression via rapid current modulation on an atom chip," *Physical Review Letters* **98**, 263201 (2007).
 - ⁷⁶P. M. Baker, J. A. Stickney, M. B. Squires, J. A. Scoville, E. J. Carlson, W. R. Buchwald, and S. M. Miller, "Adjustable microchip ring trap for cold atoms and molecules," *Phys. Rev. A* **80**, 063615 (2009).
 - ⁷⁷C. Garrido Alzar, "Compact chip-scale guided cold atom gyrometers for inertial navigation: Enabling technologies and design study," *AVS Quantum Science* **1**, 014702 (2019), <https://doi.org/10.1116/1.5120348>.
 - ⁷⁸C. Cohen-Tannoudji and S. Reynaud, "Dressed-atom description of resonance fluorescence and absorption spectra of a multi-level atom in an intense laser beam," *J. Phys. B: At. Mol. Opt. Phys.* **10**, 345–363 (1977).
 - ⁷⁹B. M. Garraway and H. Perrin, "Recent developments in trapping and manipulation of atoms with adiabatic potentials," *Journal of Physics B: Atomic, Molecular and Optical Physics* **49**, 172001 (2016).
 - ⁸⁰H. Perrin and B. M. Garraway, "Trapping atoms with radio-frequency adiabatic potentials," in *Advances in Atomic, Molecular, and Optical Physics*, Vol. 66, edited by E. Arimondo, C. C. Lin, and S. F. Yelin (Academic Press, 2017) Chap. 4, pp. 181–262.
 - ⁸¹O. Zobay and B. M. Garraway, "Atom trapping and two-dimensional Bose-Einstein condensates in field-induced adiabatic potentials," *Phys. Rev. A* **69**, 023605 (2004).
 - ⁸²O. Zobay and B. M. Garraway, "Two-dimensional atom trapping in field-induced adiabatic potentials," *Phys. Rev. Lett.* **86**, 1195–1198 (2001).
 - ⁸³N. Lundblad, R. A. Carollo, C. Lannert, M. J. Gold, X. Jiang, D. Paseltiner, N. Sergay, and D. C. Aveline, "Shell potentials for microgravity Bose-Einstein condensates," *npj Microgravity* **5**, 30 (2019).
 - ⁸⁴G. A. Sinuco-León, N. Lundblad, and B. M. Garraway, "Optimised shell potential for microgravity Bose-Einstein condensates," unpublished (2020).
 - ⁸⁵E. R. Elliott, M. C. Krutzik, J. R. Williams, R. J. Thompson, and D. C. Aveline, "NASA's cold atom lab (CAL): system development and ground test status," *npj Microgravity* **4**, 16 (2018).
 - ⁸⁶S. Pandey, H. Mas, G. Drougakis, P. Thekkeppatt, V. Bolpasi, G. Vasilakis, K. Poullos, and W. von Klitzing, "Hypersonic Bose-Einstein condensates in accelerator rings," *Nature* **570**, 205–209 (2019).
 - ⁸⁷P. Navez, S. Pandey, H. Mas, K. Poullos, T. Fernholz, and W. von Klitzing, "Matter-wave interferometers using TAP rings," *New Journal of Physics* **18**, 075014 (2016).
 - ⁸⁸I. Lesanovsky and W. von Klitzing, "Time-averaged adiabatic potentials: Versatile matter-wave guides and atom traps," *Physical Review Letters* **99**, 083001 (2007).
 - ⁸⁹A small micro-motion of the atom cloud remains present but can be safely ignored in most circumstances since it is very small for large modulation frequencies^{763,764}.
 - ⁹⁰N. Cooper, "Rapidly rotating atomic gases," *Advances in Physics* **57**, 539–616 (2008).
 - ⁹¹I. Bloch, J. Dalibard, and S. Nascimbène, "Quantum simulations with ultracold quantum gases," *Nature Physics* **8**, 267–276 (2012).
 - ⁹²T.-L. Ho, "Bose-Einstein condensates with large number of vortices," *Phys. Rev. Lett.* **87**, 060403 (2001).
 - ⁹³A. Aftalion, X. Blanc, and J. Dalibard, "Vortex patterns in a fast rotating Bose-Einstein condensate," *Phys. Rev. A* **71**, 023611 (2005).
 - ⁹⁴I. Bloch, J. Dalibard, and W. Zwerger, "Many-body physics with ultracold gases," *Rev. Mod. Phys.* **80**, 885–964 (2008).
 - ⁹⁵V. Bretin, S. Stock, Y. Seurin, and J. Dalibard, "Fast rotation of a Bose-Einstein condensate," *Phys. Rev. Lett.* **92**, 050403 (2004).
 - ⁹⁶K. Merloti, R. Dubessy, L. Longchambon, A. Perrin, P.-E. Pottie, V. Lorent, and H. Perrin, "A two-dimensional quantum gas in a magnetic trap," *New Journal of Physics* **15**, 033007 (2013).
 - ⁹⁷Y. Guo, R. Dubessy, M. d. G. de Herve, A. Kumar, T. Badr, A. Perrin, L. Longchambon, and H. Perrin, "Supersonic rotation of a superfluid: A long-lived dynamical ring," *Phys. Rev. Lett.* **124**, 025301 (2020).
 - ⁹⁸C. L. Garrido Alzar, H. Perrin, B. M. Garraway, and V. Lorent, "Evaporative cooling in a radio-frequency trap," *Phys. Rev. A* **74**, 053413 (2006).
 - ⁹⁹R. Kollengode Easwaran, L. Longchambon, P.-E. Pottie, V. Lorent, H. Perrin, and B. M. Garraway, "RF spectroscopy in a resonant RF-dressed trap," *J. Phys. B: At., Mol. Opt. Phys.* **43**, 065302 (2010).
 - ¹⁰⁰M. Cozzini, A. L. Fetter, B. Jackson, and S. Stringari, "Oscillations of a Bose-Einstein condensate rotating in a harmonic plus quartic trap," *Phys. Rev. Lett.* **94**, 100402 (2005).
 - ¹⁰¹K. Kasamatsu, M. Tsubota, and M. Ueda, "Giant hole and circular superflow in a fast rotating Bose-Einstein condensate," *Physical Review A* **66**, 053606 (2002).
 - ¹⁰²A. L. Fetter, B. Jackson, and S. Stringari, "Rapid rotation of a Bose-Einstein condensate in a harmonic plus quartic trap," *Phys. Rev. A* **71**, 013605 (2005).
 - ¹⁰³C. K. Law, C. M. Chan, P. T. Leung, and M.-C. Chu, "Motional Dressed States in a Bose-Einstein Condensate: Superfluidity at Supersonic Speed," *Physical Review Letters* **85**, 1598–1601 (2000).
 - ¹⁰⁴N. Pavloff, "Breakdown of superfluidity of an atom laser past an obstacle," *Physical Review A* **66**, 013610 (2002).
 - ¹⁰⁵A. Paris-Mandoki, J. Shearring, F. Mancarella, T. M. Fromhold, A. Trombettoni, and P. Krüger, "Superfluid flow above the critical velocity," *Scientific Reports* **7**, 9070 (2017).
 - ¹⁰⁶D. I. Bradley, S. N. Fisher, A. M. Guénault, R. P. Haley, C. R. Lawson, G. R. Pickett, R. Schanen, M. Skyba, V. Tsepelin, and D. E.

- Zmeev, "Breaking the superfluid speed limit in a fermionic condensate," *Nature Physics* **12**, 1017–1021 (2016).
- ¹⁰⁷D. Dries, S. E. Pollack, J. M. Hitchcock, and R. G. Hulet, "Dissipative transport of a Bose-Einstein condensate," *Physical Review A* **82**, 033603 (2010).
- ¹⁰⁸R. Grimm, M. Weidemüller, and Y. B. Ovchinnikov, "Optical dipole traps for neutral atoms," in *Advances in atomic, molecular, and optical physics*, Vol. 42 (Elsevier, 2000) pp. 95–170.
- ¹⁰⁹E. M. Wright, J. Arlt, and K. Dholakia, "Toroidal optical dipole traps for atomic Bose-Einstein condensates using Laguerre-Gaussian beams," *Phys. Rev. A* **63**, 013608 (2000).
- ¹¹⁰S. Moulder, S. Beattie, R. P. Smith, N. Tammuz, and Z. Hadzibabic, "Quantized supercurrent decay in an annular Bose-Einstein condensate," *Phys. Rev. A* **86**, 013629 (2012).
- ¹¹¹S. Beattie, S. Moulder, R. J. Fletcher, and Z. Hadzibabic, "Persistent currents in spinor condensates," *Physical Review Letters* **110** (2013), 10.1103/physrevlett.110.025301.
- ¹¹²C. Ryu, K. C. Henderson, and M. G. Boshier, "Creation of matter wave Bessel beams and observation of quantized circulation in a Bose-Einstein condensate," *New Journal of Physics* **16**, 013046 (2014).
- ¹¹³C. Ryu, E. C. Samson, and M. G. Boshier, "Quantum interference of currents in an atomtronic SQUID," *Nature Communications* **11**, 3338 (2020).
- ¹¹⁴A. Turpin, J. Polo, Y. V. Loiko, J. Küber, F. Schmaltz, T. K. Kalkanidjev, V. Ahufinger, G. Birkel, and J. Mompert, "Blue-detuned optical ring trap for Bose-Einstein condensates based on conical refraction," *Opt. Express* **23**, 1638–1650 (2015).
- ¹¹⁵A. Kumar, N. Anderson, W. Phillips, S. Eckel, G. Campbell, and S. Stringari, "Minimally destructive, Doppler measurement of a quantized flow in a ring-shaped Bose-Einstein condensate," *New Journal of Physics* **18**, 025001 (2016).
- ¹¹⁶R. Mathew, A. Kumar, S. Eckel, F. Jendrzejewski, G. K. Campbell, M. Edwards, and E. Tiesinga, "Self-heterodyne detection of the in situ phase of an atomic superconducting quantum interference device," *Physical Review A* **92**, 033602 (2015).
- ¹¹⁷A. Kumar, R. Dubessy, T. Badr, C. De Rossi, M. de Goër de Herve, L. Longchambon, and H. Perrin, "Producing superfluid circulation states using phase imprinting," *Phys. Rev. A* **97**, 043615 (2018).
- ¹¹⁸T. Bell, *Engineering Time-Averaged Optical Potentials for Bose-Einstein Condensates*, Ph.D. thesis, University of Queensland (2020).
- ¹¹⁹G. Birkel, F. Buchkremer, R. Dumke, and W. Ertmer, "Atom optics with microfabricated optical elements," *Optics Communications* **191**, 67–81 (2001).
- ¹²⁰R. Dumke, M. Volk, T. Mütter, F. B. J. Buchkremer, G. Birkel, and W. Ertmer, "Micro-optical realization of arrays of selectively addressable dipole traps: A scalable configuration for quantum computation with atomic qubits," *Phys. Rev. Lett.* **89**, 097903 (2002).
- ¹²¹D. Schäffner, T. Preuschoff, S. Ristok, L. Brozio, M. Schlosser, H. Giessen, and G. Birkel, "Arrays of individually controllable optical tweezers based on 3d-printed microlens arrays," *Opt. Express* **28**, 8640–8645 (2020).
- ¹²²R. Dumke, T. Mütter, M. Volk, W. Ertmer, and G. Birkel, "Interferometer-type structures for guided atoms," *Phys. Rev. Lett.* **89**, 220402 (2002).
- ¹²³M. Schlosser, S. Tichelmann, J. Kruse, and G. Birkel, "Scalable architecture for quantum information processing with atoms in optical microstructures," *Quantum Information Processing* **10**, 907–924 (2011).
- ¹²⁴A. Benseny, S. Fernández-Vidal, J. Bagudà, R. Corbalán, A. Picón, L. Roso, G. Birkel, and J. Mompert, "Atomtronics with holes: Coherent transport of an empty site in a triple-well potential," *Phys. Rev. A* **82**, 013604 (2010).
- ¹²⁵O. Morizot, Y. Colombe, V. Lorent, H. Perrin, and B. M. Garraway, "Ring trap for ultracold atoms," *Phys. Rev. A* **74**, 023617 (2006).
- ¹²⁶W. H. Heathcote, E. Nugent, B. T. Sheard, and C. J. Foot, "A ring trap for ultracold atoms in an RF-dressed state," *New Journal of Physics* **10**, 043012 (2008).
- ¹²⁷M. de Goër de Herve, Y. Guo, C. De Rossi, A. Kumar, T. Badr, R. Dubessy, L. Longchambon, and H. Perrin, (2020), in preparation.
- ¹²⁸K. C. Wright, R. Blakestad, C. Lobb, W. Phillips, and G. Campbell, "Driving phase slips in a superfluid atom circuit with a rotating weak link," *Phys. Rev. Lett.* **110**, 025302 (2013).
- ¹²⁹R. Folman, P. Krüger, J. Schmiedmayer, J. Denschlag, and C. Henkel, "Microscopic atom optics: from wires to an atom chip," *Adv. At. Mol. Opt. Phys.* **48**, 263 (2002).
- ¹³⁰K. R. Patton and U. R. Fischer, "Hybrid of superconducting quantum interference device and atomic bose-einstein condensate: An architecture for quantum information processing," *Phys. Rev. A* **87**, 052303 (2013).
- ¹³¹D. Yu, M. M. Valado, C. Hufnagel, L. C. Kwek, L. Amico, and R. Dumke, "Charge-qubit-atom hybrid," *Phys. Rev. A* **93**, 042329 (2016).
- ¹³²G. Kurizki, P. Bertet, Y. Kubo, K. Mølmer, D. Petrosyan, P. Rabl, and J. Schmiedmayer, "Quantum technologies with hybrid systems," *Proc. Natl. Acad. Sci. U.S.A* **112**, 3866 (2015).
- ¹³³Y. Japha, S. Zhou, M. Keil, R. Folman, C. Henkel, and A. Vardi, "Suppression and enhancement of decoherence in an atomic Josephson junction," *New J. Phys.* **18**, 055008 (2016).
- ¹³⁴E. Charron, M. A. Cirone, A. Negretti, J. Schmiedmayer, and T. Calarco, "Theoretical analysis of a realistic atom-chip quantum gate," *Phys. Rev. A* **74**, 012308 (2006).
- ¹³⁵J. A. Stickney, D. Z. Anderson, and A. A. Zozulya, "Transistorlike behavior of a bose-einstein condensate in a triple-well potential," *Phys. Rev. A* **75**, 013608 (2007).
- ¹³⁶G. A. Sinuco-León, K. A. Burrows, A. S. Arnold, and B. M. Garraway, "Inductively guided circuits for ultracold dressed atoms," *Nature Communications* **5** (2014), 10.1038/ncomms6289.
- ¹³⁷Y. Japha, O. Arzouan, Y. Avishai, and R. Folman, "Using Time-Reversal Symmetry for Sensitive Incoherent Matter-Wave Sagnac Interferometry," *Phys. Rev. Lett.* **99**, 060402 (2007).
- ¹³⁸R. Salem, Y. Japha, J. Chabé, B. Hadad, M. Keil, K. A. Milton, and R. Folman, "Nanowire atomchip traps for sub-micron atom-surface distances," *New J. Phys.* **12**, 023039 (2010).
- ¹³⁹J.-B. Béguin, A. P. Burgers, X. Luan, Z. Qin, S. P. Yu, and H. J. Kimble, "An advanced apparatus for the integration of nanophotonics and cold atoms," (2019), arXiv:1912.02198 [physics.atom-ph].
- ¹⁴⁰V. Dikovsky, Y. Japha, C. Henkel, and R. Folman, "Reduction of magnetic noise in atom chips by material optimization," *Eur. Phys. J. D* **35**, 87 (2005).
- ¹⁴¹T. David, Y. Japha, V. Dikovsky, R. Salem, C. Henkel, and R. Folman, "Magnetic interactions of cold atoms with anisotropic conductors," *Eur. Phys. J. D* **48**, 321 (2008).
- ¹⁴²P. G. Petrov, S. Machluf, S. Younis, R. Macaluso, T. David, B. Hadad, Y. Japha, M. Keil, E. Joselevich, and R. Folman, "Trapping cold atoms using surface-grown carbon nanotubes," *Phys. Rev. A* **79**, 043403 (2009).
- ¹⁴³Y. Japha, O. Entin-Wohlman, T. David, R. Salem, S. Aigner, J. Schmiedmayer, and R. Folman, "Model for organized current patterns in disordered conductors," *Phys. Rev. B* **77**, 201407(R) (2008).
- ¹⁴⁴S. Aigner, L. D. Pietra, Y. Japha, O. Entin-Wohlman, T. David, R. Salem, R. Folman, and J. Schmiedmayer, "Long-Range Order in Electronic Transport Through Disordered Metal Films," *Science* **319**, 1226 (2008).
- ¹⁴⁵S. Zhou, J. Chabé, R. Salem, T. David, D. Groswasser, M. Keil, Y. Japha, and R. Folman, "Phase space tomography of cold-atom dynamics in a weakly corrugated potential," *Phys. Rev. A* **90**, 033620 (2014).
- ¹⁴⁶S. Zhou, D. Groswasser, M. Keil, Y. Japha, and R. Folman, "Robust spatial coherence 5 μm from a room-temperature atom chip," *Phys. Rev. A* **93**, 063615 (2016).
- ¹⁴⁷M. Rosenblit, P. Horak, S. Hellsby, and R. Folman, "Single-atom detection using whispering-gallery modes of microdisk resonators," *Phys. Rev. A* **70**, 053808 (2004).
- ¹⁴⁸M. Rosenblit, Y. Japha, P. Horak, and R. Folman, "Simultaneous optical trapping and detection of atoms by microdisk resonators," *Phys. Rev. A* **73**, 063805 (2006).
- ¹⁴⁹M. Rosenblit, P. Horak, E. Fleminger, Y. Japha, and R. Folman, "Design of microcavity resonators for single-atom detection," *J. Nanophoton.* **1**, 011670 (2007).
- ¹⁵⁰S. Machluf, Y. Japha, and R. Folman, "Coherent Stern-Gerlach momentum splitting on an atom chip," *Nature Communications* **4**, 2424 (2013).
- ¹⁵¹Y. Margalit, Z. Zhou, S. Machluf, Y. Japha, S. Moukouri, and R. Folman, "Analysis of a high-stability Stern-Gerlach spatial fringe interferometer," *New J. Phys.* **21**, 073040 (2019).
- ¹⁵²Y. Margalit, Z. Zhou, O. Dobkowski, Y. Japha, D. Rohrlach, S. Moukouri, and R. Folman, "Realization of a complete Stern-Gerlach interferometer," (2018), arXiv:1801.02708 [quant-ph].
- ¹⁵³O. Amit, Y. Margalit, O. Dobkowski, Z. Zhou, Y. Japha, M. Zimmermann, M. A. Efremov, F. A. Narducci, E. M. Rasel, W. P. Schleich, and

- R. Folman, “ T^3 Stern-Gerlach Matter-Wave Interferometer,” *Phys. Rev. Lett.* **123**, 083601 (2019).
- ¹⁵⁴Y. Margalit, Z. Zhou, S. Machluf, D. Rohrlach, Y. Japha, and R. Folman, “A self-interfering clock as a “which path” witness,” *Science* **349**, 1205 (2015).
- ¹⁵⁵Z. Zhou, Y. Margalit, D. Rohrlach, Y. Japha, and R. Folman, “Quantum complementarity of clocks in the context of general relativity,” *Class. Quantum Gravity* **35**, 185003 (2018).
- ¹⁵⁶Z. Zhou, Y. Margalit, S. Moukouri, Y. Meir, and R. Folman, “An experimental test of the geodesic rule proposition for the non-cyclic geometric phase,” *Science Advances* **6**, eaay8345 (2020).
- ¹⁵⁷C. L. Degen, F. Reinhard, and P. Cappellaro, “Quantum sensing,” *Rev. Mod. Phys.* **89**, 035002 (2017).
- ¹⁵⁸A. Günther, M. Kemmler, S. Kraft, C. J. Vale, C. Zimmermann, and J. Fortágh, “Combined chips for atom-optics,” *Phys. Rev. A* **71**, 063619 (2005).
- ¹⁵⁹S. Kraft, A. Günther, P. Wicke, B. Kasch, C. Zimmermann, and J. Fortágh, “Atom-optical elements on micro chips,” *Eur. Phys. J. D* **35**, 119 (2005).
- ¹⁶⁰S. Bernon, H. Hattermann, D. Bothner, M. Knufinke, P. Weiss, F. Jessen, D. Cano, M. Kemmler, R. Kleiner, D. Koelle, and J. Fortágh, “Manipulation and coherence of ultra-cold atoms on a superconducting atom chip,” *Nat. Commun.* **4**, 2380 (2013).
- ¹⁶¹M. Gierling, P. Schneeweiss, G. Visanescu, P. Federsel, D. K. M. Häffner, T. E. Judd, A. Günther, and J. Fortágh, “Cold-atom scanning probe microscopy,” *Nat. Nanotechnol.* **6**, 446 (2011).
- ¹⁶²A. Günther, H. Hölscher, and J. Fortágh, “Cold Atom Scanning Probe Microscopy: An Overview, Book chapter in Fundamentals of Picoscience,” (Taylor & Francis, 2013) Chap. 16, p. 287.
- ¹⁶³P. Schneeweiss, M. Gierling, G. Visanescu, D. P. Kern, T. E. Judd, A. Günther, and J. Fortágh, “Dispersion forces between ultracold atoms and a carbon nanotube,” *Nat. Nanotechnol.* **7**, 515 (2012).
- ¹⁶⁴B. Jetter, J. Märkle, P. Schneeweiss, M. Gierling, S. Scheel, A. Günther, J. Fortágh, and T. E. Judd, “Scattering and absorption of ultracold atoms by nanotubes,” *New J. Phys.* **15**, 73009 (2013).
- ¹⁶⁵A. Günther, H. Bender, A. Stibor, J. Fortágh, and C. Zimmermann, “Observing quantum gases in real time: Single-atom detection on a chip,” *Phys. Rev. A* **80**, 011604(R) (2009).
- ¹⁶⁶A. Stibor, S. Kühnhold, J. Fortágh, C. Zimmermann, and A. Günther, “Single-atom detection on a chip: from realization to application,” *New J. Phys.* **12**, 065034 (2010).
- ¹⁶⁷T. Menold, P. Federsel, C. Rogulj, H. Hölscher, J. Fortágh, and A. Günther, “Dynamic of cold-atoms tips in anharmonic potentials,” *Beilstein J. Nanotechnol.* **7**, 1543 (2016).
- ¹⁶⁸O. Kálmán, T. Kiss, and J. F. and P. Domokos, “Quantum galvanometer by interfacing a vibrating nanowire and cold atoms,” *Nano Lett.* **12**, 435 (2012).
- ¹⁶⁹Z. Darázs, Z. Kurucz, O. Kálmán, T. Kiss, J. Fortágh, and P. Domokos, “Parametric Amplification of the Mechanical Vibrations of a Suspended Nanowire by Magnetic Coupling to a Bose-Einstein Condensate,” *Phys. Rev. Lett.* **112**, 133603 (2014).
- ¹⁷⁰P. Federsel, C. Rogulj, T. Menold, J. Fortágh, and A. Günther, “Spectral response of magnetically trapped Bose gases to weak microwave fields,” *Phys. Rev. A* **92**, 033603 (2015).
- ¹⁷¹P. Federsel, C. Rogulj, T. Menold, Z. Darázs, P. Domokos, A. Günther, and J. Fortágh, “Noise spectroscopy with a quantum gas,” *Phys. Rev. A* **95**, 043603 (2017).
- ¹⁷²P. Weiss, M. Knufinke, S. Bernon, D. Bothner, L. Sárkány, C. Zimmermann, R. Kleiner, D. Koelle, J. Fortágh, and H. Hattermann, “Sensitivity of Ultracold Atoms to Quantized Flux in a Superconducting Ring,” *Phys. Rev. Lett.* **114**, 113003 (2015).
- ¹⁷³D. Cano, H. Hattermann, B. Kasch, C. Zimmermann, R. Kleiner, D. Koelle, and J. Fortágh, “Experimental system for research on ultracold atomic gases near superconducting microstructures,” *Eur. Phys. J. D* **63**, 17 (2011).
- ¹⁷⁴D. Bothner, M. Knufinke, H. Hattermann, R. Wölbing, B. Ferdinand, P. Weiss, S. Bernon, J. Fortágh, D. Koelle, and R. Kleiner, “Inductively coupled superconducting half wavelength resonators as persistent current traps for ultracold atoms,” *New J. Phys.* **15**, 093024 (2013).
- ¹⁷⁵L. Sárkány, P. Weiss, H. Hattermann, and J. Fortágh, “Controlling the magnetic-field sensitivity of atomic-clock states by microwave dressing,” *Phys. Rev. A* **90**, 053416 (2014).
- ¹⁷⁶H. Hattermann, D. Bothner, L. Ley, B. Ferdinand, D. Wiedmaier, L. Sárkány, R. Kleiner, D. Koelle, and J. Fortágh, “Coupling ultracold atoms to a superconducting coplanar waveguide resonator,” *Nat. Comm.* **8**, 2254 (2017).
- ¹⁷⁷M. Mack, J. Grimm, F. Karlewski, L. Sárkány, H. Hattermann, and J. Fortágh, “All-optical measurement of Rydberg-state lifetimes,” *Phys. Rev. A* **92**, 012517 (2015).
- ¹⁷⁸F. Karlewski, M. Mack, J. Grimm, N. Sándor, and J. Fortágh, “State-selective all-optical detection of Rydberg atoms,” *Phys. Rev. A* **91**, 043422 (2015).
- ¹⁷⁹M. Mack, F. Karlewski, H. Hattermann, S. Höckh, F. Jessen, D. Cano, and J. Fortágh, “Measurement of absolute transition frequencies of rb 87 to nS and nD Rydberg states by means of electromagnetically induced transparency,” *Phys. Rev. A* **83**, 052515 (2011).
- ¹⁸⁰J. Grimm, M. Mack, F. Karlewski, F. Jessen, M. Reinschmidt, N. Sándor, and J. Fortágh, “Measurement and numerical calculation of Rubidium Rydberg Stark spectra,” *New J. Phys.* **17**, 053005 (2015).
- ¹⁸¹H. Hattermann, M. Mack, F. Karlewski, F. Jessen, D. Cano, and J. Fortágh, “Detrimental adsorbate fields in experiments with cold Rydberg gases near surfaces,” *Phys. Rev. A* **86**, 022511 (2012).
- ¹⁸²A. Tauschinsky, R. M. T. Thijssen, S. Whitlock, H. B. van Linden van den Heuvel, and R. J. C. Spreeuw, “Spatially resolved excitation of Rydberg atoms and surface effects on an atom chip,” *Phys. Rev. A* **81**, 063411 (2010).
- ¹⁸³A. Sanayei, N. Schopohl, J. Grimm, M. Mack, F. Karlewski, and J. Fortágh, “Quasiclassical theory of quantum defect and spectrum of highly excited rubidium atoms,” *Phys. Rev. A* **91**, 032509 (2015).
- ¹⁸⁴L. A. Jones, J. D. Carter, and J. D. D. Martin, “Rydberg atoms with a reduced sensitivity to dc and low-frequency electric fields,” *Phys. Rev. A* **87**, 023423 (2013).
- ¹⁸⁵F. Jessen, M. Knufinke, S. C. Bell, P. Vergien, H. Hattermann, P. Weiss, M. Rudolph, M. Reinschmidt, K. Meyer, T. Gaber, D. Cano, A. Günther, S. Bernon, D. Koelle, R. Kleiner, and J. Fortágh, “Trapping of ultracold atoms in a $3He/4He$ dilution refrigerator,” *Appl. Phys. B* **116**, 665 (2013).
- ¹⁸⁶A. Landra, C. Hufnagel, C. C. Lim, T. Weigner, Y. S. Yap, L. H. Nguyen, and R. Dumke, “Design of an experimental platform for hybridization of atomic and superconducting quantum systems,” *Phys. Rev. A* **99**, 053421 (2019).
- ¹⁸⁷T. Müller, B. Zhang, R. Fermini, K. S. Chan, M. J. Lim, and R. Dumke, “Programmable trap geometries with superconducting atom chips,” *Phys. Rev. A* **81**, 053624 (2010).
- ¹⁸⁸B. Zhang, R. Fermini, T. Müller, M. J. Lim, and R. Dumke, “Design of magnetic traps for neutral atoms with vortices in type-II superconducting microstructures,” *Phys. Rev. A* **81**, 063408 (2010).
- ¹⁸⁹T. Müller, B. Zhang, R. Fermini, K. S. Chan, Z. W. Wang, C. B. Zhang, M. J. Lim, and R. Dumke, “Trapping of ultra-cold atoms with the magnetic field of vortices in a thin-film superconducting micro-structure,” *New J. Phys.* **12**, 043016 (2010).
- ¹⁹⁰F. Tosto, P. Baw Swe, N. T. Nguyen, C. Hufnagel, M. Martínez Valado, L. Prigozhin, V. Sokolovsky, and R. Dumke, “Optically tailored trapping geometries for ultracold atoms on a type-II superconducting chip,” *Appl. Phys. Lett.* **114**, 222601 (2019).
- ¹⁹¹J. Verdú, H. Zoubi, C. Koller, J. Majer, H. Ritsch, and J. Schmiedmayer, “Strong Magnetic Coupling of an Ultracold Gas to a Superconducting Waveguide Cavity,” *Phys. Rev. Lett.* **103**, 043603 (2009).
- ¹⁹²D. Yu, L. C. Kwek, L. Amico, and R. Dumke, “Superconducting qubit-resonator-atom hybrid system,” *Quantum Sci. Technol.* **2**, 035005 (2017).
- ¹⁹³D. Yu, M. M. Valado, C. Hufnagel, L. C. Kwek, L. Amico, and R. Dumke, “Quantum State Transmission in a Superconducting Charge Qubit-Atom Hybrid,” *Scientific Reports* **6**, 1 (2016).
- ¹⁹⁴K. R. Patton and U. R. Fischer, “Ultrafast quantum random access memory utilizing single rydberg atoms in a bose-einstein condensate,” *Phys. Rev. Lett.* **111**, 240504 (2013).
- ¹⁹⁵M. H. T. Extavour, L. J. LeBlanc, J. McKeever, A. B. Bardon, S. Aubin, S. Myrskog, T. Schumm, and J. H. Thywissen, “Atom Chips,” (Wiley, 2011) Chap. 12, pp. 365–394.
- ¹⁹⁶S. A. Meek, H. Conrad, and G. Meijer, “Trapping molecules on a chip,” *Science* **324**, 1699–1702 (2009).
- ¹⁹⁷G. Santambrogio, “Trapping molecules on chips,” *EPI Techniques and In-*

- strumentation **2**, 14 (2015).
- ¹⁹⁸C. D. Bruzewicz, J. Chiaverini, R. McConnell, and J. M. Sage, “Trapped-ion quantum computing: Progress and challenges,” *Applied Physics Reviews* **6**, 021314 (2019).
 - ¹⁹⁹F. Yang, A. J. Kollár, S. F. Taylor, R. W. Turner, and B. L. Lev, “Scanning quantum cryogenic atom microscope,” *Phys. Rev. Applied* **7**, 034026 (2017).
 - ²⁰⁰J. Schmiedmayer, “Thermodynamics in the Quantum Regime,” (Springer, 2018) Chap. 34, pp. 823–851.
 - ²⁰¹T. Schweigler, V. Kasper, S. Erne, I. Mazets, F. Cataldini, T. Langen, T. Gasenzer, J. Berges, and J. Schmiedmayer, “Experimental characterization of a quantum many-body system via higher-order correlations,” *Nature* **545**, 323 (2017).
 - ²⁰²M. DeAngelis and et al., “iSense: A Portable Ultracold-Atom-Based Gravimeter,” *Procedia Computer Science* **7**, 334 (2011).
 - ²⁰³S. Herrmann, H. Dittus, and C. L. and, “Testing the equivalence principle with atomic interferometry,” *Classical and Quantum Gravity* **29**, 184003 (2012).
 - ²⁰⁴N. Leefer, K. Krimmel, W. Bertsche, D. Budker, J. Fajans, R. Folman, H. Häffner, and F. Schmidt-Kaler, “Investigation of two-frequency paul traps for antihydrogen production,” *Hyperfine Interactions* **238**, 12 (2016).
 - ²⁰⁵C. Rylands and N. Andrei, “Non-equilibrium aspects of integrable models,” *Annual Review of Condensed Matter Physics* **11**, 147–168 (2020).
 - ²⁰⁶P. Calabrese and J. Cardy, “Evolution of entanglement entropy in one-dimensional systems,” *Journal of Statistical Mechanics: Theory and Experiment* **2005**, 04010 (2005).
 - ²⁰⁷A. Mitra, “Quantum Quench Dynamics,” *Annual Review of Condensed Matter Physics* **9**, 245–259 (2018), arXiv:1703.09740 [cond-mat.quant-gas].
 - ²⁰⁸N. Andrei, “Quench dynamics in integrable systems,” *Les Houches Summer School 2012*, Oxford University Press (2016), arXiv:1606.08911 [cond-mat.quant-gas].
 - ²⁰⁹M. Heyl, A. Polkovnikov, and S. Kehrein, “Dynamical quantum phase transitions in the transverse-field ising model,” *Phys. Rev. Lett.* **110**, 135704 (2013).
 - ²¹⁰J. Goold, F. Plastina, A. Gambassi, and A. Silva, “The role of quantum work statistics in many-body physics,” *ArXiv e-prints* (2018), arXiv:1804.02805 [quant-ph].
 - ²¹¹M. Rigol, V. Dunjko, and M. Olshanii, “Thermalization and its mechanism for generic isolated quantum systems,” *Nature* **452**, 854–858 (2008).
 - ²¹²D. Iyer, H. Guan, and N. Andrei, “Exact formalism for the quench dynamics of integrable models,” *Phys. Rev. A* **87**, 053628 (2013).
 - ²¹³E. H. Lieb and W. Liniger, “Exact analysis of an interacting bose gas. i. the general solution and the ground state,” *Phys. Rev.* **130**, 1605–1616 (1963).
 - ²¹⁴E. H. Lieb, “Exact analysis of an interacting bose gas. ii. the excitation spectrum,” *Phys. Rev.* **130**, 1616–1624 (1963).
 - ²¹⁵J.-S. Caux and R. M. Konik, “Constructing the generalized gibbs ensemble after a quantum quench,” *Phys. Rev. Lett.* **109**, 175301 (2012).
 - ²¹⁶J.-S. Caux and F. H. Essler, “Time evolution of local observables after quenching to an integrable model,” *Phys. Rev. Lett.* **110**, 257203 (2013).
 - ²¹⁷V. I. Rupasov and V. I. Iudson, “A rigorous theory of Dicke superradiation - Bethe wave functions in a model with discrete atoms,” *Zhurnal Eksperimentalnoi i Teoreticheskoi Fiziki* **86**, 819–825 (1984).
 - ²¹⁸G. Goldstein and N. Andrei, “Equilibration and Generalized GGE in the Lieb Liniger gas,” *arXiv e-prints*, arXiv:1309.3471 (2013), arXiv:1309.3471 [cond-mat.quant-gas].
 - ²¹⁹V. E. Korepin, N. M. Bogoliubov, and A. G. Izergin, *Quantum inverse scattering method and correlation functions*, Vol. 3 (Cambridge university press, 1997).
 - ²²⁰R. Hanbury Brown, “A Test of a New Type of Stellar Interferometer on Sirius,” *Nature* **178**, 1046–1048 (1956).
 - ²²¹T. Jelte, J. M. McNamara, W. Hogervorst, W. Vassen, V. Krachmalnicoff, M. Schellekens, A. Perrin, H. Chang, D. Boiron, A. Aspect, and C. I. Westbrook, “Hanbury Brown Twiss effect for bosons versus fermions,” *arXiv e-prints*, cond-mat/0612278 (2006), arXiv:cond-mat/0612278 [cond-mat.other].
 - ²²²D. Iyer and N. Andrei, “Quench dynamics of the interacting bose gas in one dimension,” *Phys. Rev. Lett.* **109**, 115304 (2012).
 - ²²³D. Jukić and H. Buljan, “Reflection of a Lieb-Liniger wave packet from the hard-wall potential,” *New Journal of Physics* **12**, 055010 (2010), arXiv:0911.0260 [cond-mat.quant-gas].
 - ²²⁴D. Jukić, R. Pezer, T. Gasenzer, and H. Buljan, “Free expansion of a lieb-liniger gas: Asymptotic form of the wave functions,” *Phys. Rev. A* **78**, 053602 (2008).
 - ²²⁵D. Jukić, B. Klajn, and H. Buljan, “Momentum distribution of a freely expanding lieb-liniger gas,” *Phys. Rev. A* **79**, 033612 (2009).
 - ²²⁶J. M. Wilson, N. Malvania, Y. Le, Y. Zhang, M. Rigol, and D. S. Weiss, “Observation of dynamical fermionization,” *Science* **367**, 1461–1464 (2020).
 - ²²⁷R. Vasseur, K. Trinh, S. Haas, and H. Saleur, “Crossover physics in the nonequilibrium dynamics of quenched quantum impurity systems,” *Phys. Rev. Lett.* **110**, 240601 (2013).
 - ²²⁸D. M. Kennes, V. Meden, and R. Vasseur, “Universal quench dynamics of interacting quantum impurity systems,” *Phys. Rev. B* **90**, 115101 (2014).
 - ²²⁹C. Rylands and N. Andrei, “Quantum work of an optical lattice,” *Phys. Rev. B* **100**, 064308 (2019).
 - ²³⁰S. Sotiriadis, A. Gambassi, and A. Silva, “Statistics of the work done by splitting a one-dimensional quasicondensate,” *Phys. Rev. E* **87**, 052129 (2013), arXiv:1303.0782 [cond-mat.stat-mech].
 - ²³¹P. Smacchia and A. Silva, “Work distribution and edge singularities for generic time-dependent protocols in extended systems,” *Phys. Rev. E* **88**, 042109 (2013).
 - ²³²C. Rylands and N. Andrei, “Loschmidt amplitude and work distribution in quenches of the sine-Gordon model,” *Phys. Rev. B* **99**, 085133 (2019), arXiv:1809.05582 [cond-mat.str-el].
 - ²³³J. B. McGuire, “Study of Exactly Soluble One-Dimensional N-Body Problems,” *Journal of Mathematical Physics* **5**, 622–636 (1964).
 - ²³⁴C. Jarzynski, “Nonequilibrium equality for free energy differences,” *Phys. Rev. Lett.* **78**, 2690–2693 (1997).
 - ²³⁵C. Jarzynski, “Equalities and inequalities: Irreversibility and the second law of thermodynamics at the nanoscale,” *Annual Review of Condensed Matter Physics* **2**, 329–351 (2011), https://doi.org/10.1146/annurev-conmatphys-062910-140506.
 - ²³⁶O. Maillet, P. A. Erdman, V. Cavina, B. Bhandari, E. T. Mannila, J. T. Peltonen, A. Mari, F. Taddei, C. Jarzynski, V. Giovannetti, et al., “Optimal probabilistic work extraction beyond the free energy difference with a single-electron device,” *Physical review letters* **122**, 150604 (2019).
 - ²³⁷H. Bethe, “Zur Theorie der Metalle,” *Zeitschrift für Physik* **71**, 205–226 (1931).
 - ²³⁸R. Orbach, “Linear antiferromagnetic chain with anisotropic coupling,” *Phys. Rev.* **112**, 309–316 (1958).
 - ²³⁹W. Liu and N. Andrei, “Quench Dynamics of the Anisotropic Heisenberg Model,” *Phys. Rev. Lett.* **112**, 257204 (2014), arXiv:1311.1118 [cond-mat.quant-gas].
 - ²⁴⁰S. Groha and F. H. L. Essler, “Spinon decay in the spin-1/2 Heisenberg chain with weak next nearest neighbour exchange,” *Journal of Physics A Mathematical General* **50**, 334002 (2017), arXiv:1702.06550 [cond-mat.str-el].
 - ²⁴¹T. Fukuhara, P. Schauß, M. Endres, S. Hild, M. Cheneau, I. Bloch, and C. Gross, “Microscopic observation of magnon bound states and their dynamics,” *Nature* **502**, 76–79 (2013), arXiv:1305.6598 [cond-mat.quant-gas].
 - ²⁴²M. Gaudin and J.-S. Caux, *The Bethe Wavefunction*, by Michel Gaudin, Translated by Jean-Sébastien Caux, Cambridge, UK: Cambridge University Press, 2014 (2014).
 - ²⁴³C. N. Yang, “Some exact results for the many-body problem in one dimension with repulsive delta-function interaction,” *Phys. Rev. Lett.* **19**, 1312–1315 (1967).
 - ²⁴⁴H. Guan and N. Andrei, “Quench Dynamics of the Gaudin-Yang Model,” *arXiv e-prints*, arXiv:1803.04846 (2018), arXiv:1803.04846 [cond-mat.quant-gas].
 - ²⁴⁵P. Fulde and R. A. Ferrell, “Superconductivity in a strong spin-exchange field,” *Phys. Rev.* **135**, A550–A563 (1964).
 - ²⁴⁶A. I. Larkin and Y. N. Ovchinnikov, “Nonuniform state of superconductors,” *Zh. Eksp. Teor. Fiz.* **47**, 1136–1146 (1964), [*Sov. Phys. JETP* **20**, 762 (1965)].
 - ²⁴⁷A. Culver and N. Andrei, in preparation (2019).
 - ²⁴⁸R. Tourani and N. Andrei, in preparation (2019).
 - ²⁴⁹O. A. Castro-Alvaredo, B. Doyon, and T. Yoshimura, “Emergent hydrodynamics in integrable quantum systems out of equilibrium,” *Phys. Rev. X*

- 6, 041065 (2016).
- ²⁵⁰V. B. Bulchandani, R. Vasseur, C. Karrasch, and J. E. Moore, "Solvable hydrodynamics of quantum integrable systems," *Phys. Rev. Lett.* **119**, 220604 (2017).
 - ²⁵¹V. B. Bulchandani, R. Vasseur, C. Karrasch, and J. E. Moore, "Bethe-Boltzmann hydrodynamics and spin transport in the XXZ chain," *Physical Review B* **97**, 045407 (2018), arXiv:1702.06146 [cond-mat.stat-mech].
 - ²⁵²V. A. Yurovsky, M. Olshanii, and D. S. Weiss, "Collisions, correlations, and integrability in atom waveguides," *Advances in Atomic, Molecular, and Optical Physics* **55**, 61–138 (2008).
 - ²⁵³I. Bouchoule, N. Van Druten, and C. I. Westbrook, "Atom chips and one-dimensional bose gases," arXiv preprint arXiv:0901.3303 (2009).
 - ²⁵⁴M. Cazalilla, R. Citro, T. Giamarchi, E. Orignac, and M. Rigol, "One dimensional bosons: From condensed matter systems to ultracold gases," *Rev. Mod. Phys.* **83**, 1405 (2011).
 - ²⁵⁵A. Polkovnikov, K. Sengupta, A. Silva, and M. Vengalattore, "Colloquium: Nonequilibrium dynamics of closed interacting quantum systems," *Rev. Mod. Phys.* **83**, 863 (2011).
 - ²⁵⁶T. Kinoshita, T. Wenger, and D. S. Weiss, "A quantum newton's cradle," *Nature* **440**, 900 (2006).
 - ²⁵⁷M. Olshanii, "Atomic scattering in the presence of an external confinement and a gas of impenetrable bosons," *Phys. Rev. Lett.* **81**, 938 (1998).
 - ²⁵⁸S. Inouye, M. Andrews, J. Stenger, H.-J. Miesner, D. Stamper-Kurn, and W. Ketterle, "Observation of feshbach resonances in a bose-einstein condensate," *Nature* **392**, 151–154 (1998).
 - ²⁵⁹P. Calabrese and J. Cardy, "Time dependence of correlation functions following a quantum quench," *Phys. Rev. Lett.* **96**, 136801 (2006).
 - ²⁶⁰P. Calabrese and J. Cardy, "Quantum quenches in extended systems," *J. Stat. Mech.* **2007**, P06008 (2007).
 - ²⁶¹P. Calabrese, F. H. Essler, and G. Mussardo, "Introduction to 'quantum integrability in out of equilibrium systems'," *J. Stat. Mech.* **2016**, 064001 (2016).
 - ²⁶²M. Cazalilla and M. Rigol, "Focus on dynamics and thermalization in isolated quantum many-body systems," *New J. Phys.* **12**, 055006 (2010).
 - ²⁶³L. D'Alessio, Y. Kafri, A. Polkovnikov, and M. Rigol, "From quantum chaos and eigenstate thermalization to statistical mechanics and thermodynamics," *Adv. Phys.* **65**, 239–362 (2016).
 - ²⁶⁴M. Rigol, V. Dunjko, V. Yurovsky, and M. Olshanii, "Relaxation in a completely integrable many-body quantum system: An ab initio study of the dynamics of the highly excited states of 1d lattice hard-core bosons," *Phys. Rev. Lett.* **98**, 050405 (2007).
 - ²⁶⁵L. Vidmar and M. Rigol, "Generalized gibbs ensemble in integrable lattice models," *J. Stat. Mech.* **2016**, 064007 (2016).
 - ²⁶⁶F. H. Essler and M. Fagotti, "Quench dynamics and relaxation in isolated integrable quantum spin chains," *J. Stat. Mech.* **2016**, 064002 (2016).
 - ²⁶⁷M. Fagotti, "On conservation laws, relaxation and pre-relaxation after a quantum quench," *J. Stat. Mech.* **2014**, P03016 (2014).
 - ²⁶⁸E. Ilievski, J. De Nardis, B. Wouters, J.-S. Caux, F. H. Essler, and T. Prosen, "Complete generalized gibbs ensembles in an interacting theory," *Phys. Rev. Lett.* **115**, 157201 (2015).
 - ²⁶⁹E. Ilievski, E. Quinn, J. De Nardis, and M. Brockmann, "String-charge duality in integrable lattice models," *J. Stat. Mech.* **2016**, 063101 (2016).
 - ²⁷⁰E. Ilievski, M. Medenjak, T. Prosen, and L. Zadnik, "Quasilocal charges in integrable lattice systems," *J. Stat. Mech.* **2016**, 064008 (2016).
 - ²⁷¹E. Ilievski, E. Quinn, and J.-S. Caux, "From interacting particles to equilibrium statistical ensembles," *Phys. Rev. B* **95**, 115128 (2017).
 - ²⁷²B. Pozsgay, E. Vernier, and M. Werner, "On generalized gibbs ensembles with an infinite set of conserved charges," *J. Stat. Mech.* **2017**, 093103 (2017).
 - ²⁷³T. Kinoshita, T. Wenger, and D. S. Weiss, "Local pair correlations in one-dimensional bose gases," *Phys. Rev. Lett.* **95**, 190406 (2005).
 - ²⁷⁴B. Pozsgay, "Local correlations in the 1d bose gas from a scaling limit of the xxz chain," *J. Stat. Mech.* **2011**, P11017 (2011).
 - ²⁷⁵L. Piroli and P. Calabrese, "Exact formulas for the form factors of local operators in the lieb-liniger model," *J. Phys. A: Math. Theor.* **48**, 454002 (2015).
 - ²⁷⁶J. Mossel and J.-S. Caux, "Exact time evolution of space-and time-dependent correlation functions after an interaction quench in the one-dimensional bose gas," *New J. Phys.* **14**, 075006 (2012).
 - ²⁷⁷S. Sotiriadis and P. Calabrese, "Validity of the gge for quantum quenches from interacting to noninteracting models," *J. Stat. Mech.* **2014**, P07024 (2014).
 - ²⁷⁸V. Gritsev, T. Rostunov, and E. Demler, "Exact methods in the analysis of the non-equilibrium dynamics of integrable models: application to the study of correlation functions for non-equilibrium 1d bose gas," *Jo. Stat. Mech.* **2010**, P05012 (2010).
 - ²⁷⁹D. Muth and M. Fleischhauer, "Dynamics of pair correlations in the attractive lieb-liniger gas," *Phys. Rev. Lett.* **105**, 150403 (2010).
 - ²⁸⁰D. Muth, B. Schmidt, and M. Fleischhauer, "Fermionization dynamics of a strongly interacting one-dimensional bose gas after an interaction quench," *New J. Phys.* **12**, 083065 (2010).
 - ²⁸¹M. Kormos, A. Shashi, Y.-Z. Chou, J.-S. Caux, and A. Imambekov, "Interaction quenches in the one-dimensional bose gas," *Phys. Rev. B* **88**, 205131 (2013).
 - ²⁸²M. Collura, S. Sotiriadis, and P. Calabrese, "Quench dynamics of a tonks-girardeau gas released from a harmonic trap," *J. Stat. Mech.* **2013**, P09025 (2013).
 - ²⁸³M. Collura, M. Kormos, and P. Calabrese, "Stationary entanglement entropies following an interaction quench in 1d bose gas," *J. Stat. Mech.* **2014**, P01009 (2014).
 - ²⁸⁴M. Kormos, M. Collura, and P. Calabrese, "Analytic results for a quantum quench from free to hard-core one-dimensional bosons," *Phys. Rev. A* **89**, 013609 (2014).
 - ²⁸⁵J.-S. Caux, "The quench action," *J. Stat. Mech.* **2016**, 064006 (2016).
 - ²⁸⁶K. Kozłowski and B. Pozsgay, "Surface free energy of the open xxz spin-1/2 chain," *J. Stat. Mech.* **2012**, P05021 (2012).
 - ²⁸⁷B. Pozsgay, "Overlaps between eigenstates of the xxz spin-1/2 chain and a class of simple product states," *J. Stat. Mech.* **2014**, P06011 (2014).
 - ²⁸⁸P. Calabrese and P. Le Doussal, "Interaction quench in a lieb-liniger model and the kpz equation with flat initial conditions," *J. Stat. Mech.* **2014**, P05004 (2014).
 - ²⁸⁹L. Piroli and P. Calabrese, "Recursive formulas for the overlaps between bethe states and product states in xxz heisenberg chains," *J. Phys. A: Math. Theor.* **47**, 385003 (2014).
 - ²⁹⁰L. Piroli, B. Pozsgay, and E. Vernier, "What is an integrable quench?" *Nucl. Phys. B* **925**, 362–402 (2017).
 - ²⁹¹M. Brockmann, "Overlaps of q-raised néel states with xxz bethe states and their relation to the lieb-liniger bose gas," *J. Stat. Mech.* **2014**, P05006 (2014).
 - ²⁹²M. Brockmann, J. De Nardis, B. Wouters, and J.-S. Caux, "A gaudin-like determinant for overlaps of néel and xxz bethe states," *J. Phys. A: Math. Theor.* **47**, 145003 (2014).
 - ²⁹³M. Brockmann, J. De Nardis, B. Wouters, and J.-S. Caux, "Néel-xxz state overlaps: odd particle numbers and lieb-liniger scaling limit," *J. Phys. A: Math. Theor.* **47**, 345003 (2014).
 - ²⁹⁴D. Horváth, S. Sotiriadis, and G. Takács, "Initial states in integrable quantum field theory quenches from an integral equation hierarchy," *Nucl. Phys. B* **902**, 508–547 (2016).
 - ²⁹⁵D. Horváth and G. Takács, "Overlaps after quantum quenches in the sine-gordon model," *Phys. Lett. B* **771**, 539–545 (2017).
 - ²⁹⁶D. Horváth, M. Kormos, and G. Takács, "Overlap singularity and time evolution in integrable quantum field theory," *JHEP* **2018**, 170 (2018).
 - ²⁹⁷M. Brockmann and J.-M. Stéphan, "Universal terms in the overlap of the ground state of the spin-1/2 xxz chain with the néel state," *J. Phys. A: Math. Theor.* **50**, 354001 (2017).
 - ²⁹⁸M. de Leeuw, C. Kristjansen, and K. Zarembo, "One-point functions in defect cft and integrability," *JHEP* **2015**, 98 (2015).
 - ²⁹⁹I. Buhl-Mortensen, M. de Leeuw, C. Kristjansen, and K. Zarembo, "One-point functions in ads/dcft from matrix product states," *JHEP* **2016**, 52 (2016).
 - ³⁰⁰O. Foda and K. Zarembo, "Overlaps of partial néel states and bethe states," *J. Stat. Mech.* **2016**, 023107 (2016).
 - ³⁰¹M. de Leeuw, C. Kristjansen, and S. Mori, "Ads/dcft one-point functions of the su(3) sector," *Phys. Lett. B* **763**, 197–202 (2016).
 - ³⁰²M. De Leeuw, C. Kristjansen, and G. Linardopoulos, "Scalar one-point functions and matrix product states of ads/dcft," *Phys. Lett. B* **781**, 238–243 (2018).
 - ³⁰³B. Pozsgay, L. Piroli, and E. Vernier, "Integrable matrix product states from boundary integrability," *SciPost Phys.* **6** (2019).

- ³⁰⁴Y. Jiang and B. Pozsgay, “On exact overlaps in integrable spin chains,” *JHEP* **2020**, 1–35 (2020).
- ³⁰⁵M. Kormos, G. Mussardo, and A. Trombettoni, “Expectation values in the lieb-liniger bose gas,” *Phys. Rev. Lett.* **103**, 210404 (2009).
- ³⁰⁶M. Kormos, G. Mussardo, and A. Trombettoni, “One-dimensional lieb-liniger bose gas as nonrelativistic limit of the sinh-gordon model,” *Phys. Rev. A* **81**, 043606 (2010).
- ³⁰⁷A. Bastianello, L. Piroli, and P. Calabrese, “Exact local correlations and full counting statistics for arbitrary states of the one-dimensional interacting bose gas,” *Phys. Rev. Lett.* **120**, 190601 (2018).
- ³⁰⁸A. Bastianello and L. Piroli, “From the sinh-gordon field theory to the one-dimensional bose gas: exact local correlations and full counting statistics,” *J. Stat. Mech.* **2018**, 113104 (2018).
- ³⁰⁹J. De Nardis, B. Wouters, M. Brockmann, and J.-S. Caux, “Solution for an interaction quench in the lieb-liniger bose gas,” *Phys. Rev. A* **89**, 033601 (2014).
- ³¹⁰J. De Nardis, L. Piroli, and J.-S. Caux, “Relaxation dynamics of local observables in integrable systems,” *J. Phys. A: Math. Theor.* **48**, 43FT01 (2015).
- ³¹¹J. De Nardis and J.-S. Caux, “Analytical expression for a post-quench time evolution of the one-body density matrix of one-dimensional hard-core bosons,” *J. Stat. Mech.* **2014**, P12012 (2014).
- ³¹²R. van den Berg, B. Wouters, S. Eliëns, J. De Nardis, R. M. Konik, and J.-S. Caux, “Separation of time scales in a quantum newton’s cradle,” *Phys. Rev. Lett.* **116**, 225302 (2016).
- ³¹³G. Peretto, L. Piroli, and A. Gambassi, “Quench action and large deviations: Work statistics in the one-dimensional bose gas,” *Physical Review E* **100**, 032114 (2019).
- ³¹⁴A. Silva, “Statistics of the work done on a quantum critical system by quenching a control parameter,” *Phys. Rev. Lett.* **101**, 120603 (2008).
- ³¹⁵A. Gambassi and A. Silva, “Large Deviations and Universality in Quantum Quenches,” *Phys. Rev. Lett.* **109**, 250602 (2012), 1210.3341 [cond-mat.stat-mech].
- ³¹⁶L. Piroli, P. Calabrese, and F. H. L. Essler, “Multiparticle bound-state formation following a quantum quench to the one-dimensional bose gas with attractive interactions,” *Phys. Rev. Lett.* **116**, 070408 (2016).
- ³¹⁷L. Piroli, P. Calabrese, and F. H. L. Essler, “Quantum quenches to the attractive one-dimensional Bose gas: exact results,” *SciPost Phys.* **1**, 001 (2016).
- ³¹⁸G. E. Astrakharchik, J. Boronat, J. Casulleras, and S. Giorgini, “Beyond the tonks-girardeau gas: Strongly correlated regime in quasi-one-dimensional bose gases,” *Phys. Rev. Lett.* **95**, 190407 (2005).
- ³¹⁹M. Batchelor, M. Bortz, X.-W. Guan, and N. Oelkers, “Evidence for the super tonks-girardeau gas,” *J. Stat. Mech.* **2005**, L10001 (2005).
- ³²⁰E. Haller, M. Gustavsson, M. J. Mark, J. G. Danzl, R. Hart, G. Pupillo, and H.-C. Nägerl, “Realization of an excited, strongly correlated quantum gas phase,” *Science* **325**, 1224–1227 (2009).
- ³²¹S. Chen, L. Guan, X. Yin, Y. Hao, and X.-W. Guan, “Transition from a tonks-girardeau gas to a super-tonks-girardeau gas as an exact many-body dynamics problem,” *Phys. Rev. A* **81**, 031609 (2010).
- ³²²M. Kormos, G. Mussardo, and A. Trombettoni, “Local correlations in the super-tonks-girardeau gas,” *Phys. Rev. A* **83**, 013617 (2011).
- ³²³W. Tschischik and M. Haque, “Repulsive-to-attractive interaction quenches of a one-dimensional bose gas in a harmonic trap,” *Phys. Rev. A* **91**, 053607 (2015).
- ³²⁴J. C. Zill, T. M. Wright, K. V. Kheruntsyan, T. Gasenzer, and M. J. Davis, “Quantum quench dynamics of the attractive one-dimensional Bose gas via the coordinate Bethe ansatz,” *SciPost Phys.* **4**, 011 (2018).
- ³²⁵J. C. Zill, T. M. Wright, K. V. Kheruntsyan, T. Gasenzer, and M. J. Davis, “Relaxation dynamics of the lieb-liniger gas following an interaction quench: A coordinate bethe-ansatz analysis,” *Phys. Rev. A* **91**, 023611 (2015).
- ³²⁶J. C. Zill, T. M. Wright, K. V. Kheruntsyan, T. Gasenzer, and M. J. Davis, “A coordinate bethe ansatz approach to the calculation of equilibrium and nonequilibrium correlations of the one-dimensional bose gas,” *New J. Phys.* **18**, 045010 (2016).
- ³²⁷A. Colcelli, G. Mussardo, G. Sierra, and A. Trombettoni, “Integrable floquet hamiltonian for a periodically tilted 1d gas,” *Phys. Rev. Lett.* **123**, 130401 (2019).
- ³²⁸A. Colcelli, G. Mussardo, G. Sierra, and A. Trombettoni, “Dynamics of one-dimensional quantum many-body systems in time-periodic linear potentials,” *arXiv:2006.11299* (2020), *arXiv:2006.11299*.
- ³²⁹B. Bertini, M. Collura, J. De Nardis, and M. Fagotti, “Transport in out-of-equilibrium xxz chains: Exact profiles of charges and currents,” *Phys. Rev. Lett.* **117**, 207201 (2016).
- ³³⁰B. Doyon, J. Dubail, R. Konik, and T. Yoshimura, “Large-scale description of interacting one-dimensional bose gases: Generalized hydrodynamics supersedes conventional hydrodynamics,” *Phys. Rev. Lett.* **119**, 195301 (2017).
- ³³¹B. Doyon and T. Yoshimura, “A note on generalized hydrodynamics: inhomogeneous fields and other concepts,” *SciPost Phys.* **2**, 63 (2017).
- ³³²J.-S. Caux, B. Doyon, J. Dubail, R. Konik, and T. Yoshimura, “Hydrodynamics of the interacting bose gas in the quantum newton cradle setup,” *SciPost Phys.* **6**, 070 (2019).
- ³³³P. Ruggiero, P. Calabrese, B. Doyon, and J. Dubail, “Quantum generalized hydrodynamics,” *Phys. Rev. Lett.* **124**, 140603 (2020).
- ³³⁴A. Bastianello, V. Alba, and J.-S. Caux, “Generalized hydrodynamics with space-time inhomogeneous interactions,” *Phys. Rev. Lett.* **123**, 130602 (2019).
- ³³⁵A. Bastianello, J. De Nardis, and A. De Luca, “Generalised hydrodynamics with dephasing noise,” *arXiv:2003.01702* (2020), *arXiv:2003.01702*.
- ³³⁶M. Schemmer, I. Bouchoule, B. Doyon, and J. Dubail, “Generalized hydrodynamics on an atom chip,” *Phys. Rev. Lett.* **122**, 090601 (2019).
- ³³⁷X.-W. Guan, M. T. Batchelor, and C. Lee, “Fermi gases in one dimension: From bethe ansatz to experiments,” *Rev. Mod. Phys.* **85**, 1633–1691 (2013).
- ³³⁸G. Pagano, M. Mancini, G. Cappellini, P. Lombardi, F. Schäfer, H. Hu, X.-J. Liu, J. Catani, C. Sias, M. Inguscio, and L. Fallani, “A one-dimensional liquid of fermions with tunable spin,” *Nature Phys.* **10**, 198–201 (2014).
- ³³⁹N. Mestyán, B. Bertini, L. Piroli, and P. Calabrese, “Spin-charge separation effects in the low-temperature transport of one-dimensional fermi gases,” *Phys. Rev. B* **99**, 014305 (2019).
- ³⁴⁰L. Peng, Y. Yu, and X.-W. Guan, “Grüneisen parameters for the lieb-liniger and yang-gaudin models,” *Phys. Rev. B* **100**, 245435 (2019).
- ³⁴¹N. Murray, M. Krygier, M. Edwards, K. C. Wright, G. K. Campbell, and C. W. Clark, “Probing the circulation of ring-shaped bose-einstein condensates,” *Phys. Rev. A* **88**, 053615 (2013).
- ³⁴²A. I. Yakimenko, Y. M. Bidasyuk, M. Weyrauch, Y. I. Kuriatnikov, and S. I. Vilchinskii, “Vortices in a toroidal bose-einstein condensate with a rotating weak link,” *Phys. Rev. A* **91**, 033607 (2015).
- ³⁴³A. I. Yakimenko, K. O. Isaieva, S. I. Vilchinskii, and E. A. Ostrovskaya, “Vortex excitation in a stirred toroidal bose-einstein condensate,” *Phys. Rev. A* **91**, 023607 (2015).
- ³⁴⁴A. I. Yakimenko, S. I. Vilchinskii, Y. M. Bidasyuk, Y. I. Kuriatnikov, K. O. Isaieva, and M. Weyrauch, “Generation and decay of persistent current in a toroidal bose-einstein condensate,” *Rom. Rep. Phys.* **67**, 249–272 (2015).
- ³⁴⁵S. Beattie, S. Moulder, R. J. Fletcher, and Z. Hadzibabic, “Persistent currents in spinor condensates,” *Phys. Rev. Lett.* **110**, 025301 (2013).
- ³⁴⁶A. Yakimenko, K. Isaieva, S. Vilchinskii, and M. Weyrauch, “Stability of persistent currents in spinor bose-einstein condensates,” *Physical Review A* **88**, 051602 (2013).
- ³⁴⁷G.-S. Paraoanu, “Persistent currents in a circular array of bose-einstein condensates,” *Phys. Rev. A* **67**, 023607 (2003).
- ³⁴⁸S. Rooney, T. Neely, B. Anderson, and A. Bradley, “Persistent-current formation in a high-temperature bose-einstein condensate: An experimental test for classical-field theory,” *Phys. Rev. A* **88**, 063620 (2013).
- ³⁴⁹A. C. Mathey, C. W. Clark, and L. Mathey, “Decay of a superfluid current of ultracold atoms in a toroidal trap,” *Phys. Rev. A* **90**, 023604 (2014).
- ³⁵⁰K. Wright, L. Leslie, and N. Bigelow, “Optical control of the internal and external angular momentum of a bose-einstein condensate,” *Phys. Rev. A* **77**, 041601 (2008).
- ³⁵¹C. Ryu, M. F. Andersen, P. Cladé, V. Natarajan, K. Helmerson, and W. D. Phillips, “Observation of persistent flow of a bose-einstein condensate in a toroidal trap,” *Phys. Rev. Lett.* **99**, 260401 (2007).
- ³⁵²F. Jendrzejewski, S. Eckel, N. Murray, C. Lanier, M. Edwards, C. J. Lobb, and G. K. Campbell, “Resistive flow in a weakly interacting bose-einstein condensate,” *Physical review letters* **113**, 045305 (2014).
- ³⁵³S. Eckel, J. G. Lee, F. Jendrzejewski, C. J. Lobb, G. K. Campbell, and W. T. Hill, “Contact resistance and phase slips in mesoscopic superfluid-atom transport,” *Phys. Rev. A* **93**, 063619 (2016).

- ³⁵⁴L. Corman, L. Chomaz, T. Bienaimé, R. Desbuquois, C. Weitenberg, S. Nascimbene, J. Dalibard, and J. Beugnon, “Quench-induced supercurrents in an annular bose gas,” *Phys. Rev. Lett.* **113**, 135302 (2014).
- ³⁵⁵M. Aidelburger, J. L. Ville, R. Saint-Jalm, S. Nascimbene, J. Dalibard, and J. Beugnon, “Relaxation dynamics in the merging of n independent condensates,” *Phys. Rev. Lett.* **119**, 190403 (2017).
- ³⁵⁶A. Das, J. Sabbatini, and W. H. Zurek, “Winding up superfluid in a torus via bose einstein condensation,” *Sci. Rep.* **2**, 352 (2012).
- ³⁵⁷T. Bland, Q. Marolleau, P. Comaron, B. Malomed, and N. P. Proukakis, “Persistent current formation in double-ring geometries,” *J. Phys. B*, **53**, 115301 (2020).
- ³⁵⁸J. Brand, T. J. Haigh, and U. Zülicke, “Rotational fluxons of Bose-Einstein condensates in coplanar double-ring traps,” *Phys. Rev. A* **80**, 011602 (2009).
- ³⁵⁹C. Baals, H. Ott, J. Brand, and A. Mateo, “Nonlinear standing waves in an array of coherently coupled bose-einstein condensates,” *Phys. Rev. A* **98**, 053603 (2018).
- ³⁶⁰D. Aghamalyan, L. Amico, and L. C. Kwek, “Effective dynamics of cold atoms flowing in two ring-shaped optical potentials with tunable tunneling,” *Physical Review A* **88**, 063627 (2013).
- ³⁶¹A. Oliinyk, A. Yakimenko, and B. Malomed, “Tunneling of persistent currents in coupled ring-shaped bose-einstein condensates,” *J. Phys. B: At. Mol. Opt. Phys.* **52**, 225301 (2019).
- ³⁶²A. Oliinyk, B. Malomed, and A. Yakimenko, “Symmetry breaking in interacting ring-shaped superflows of bose-einstein condensates,” *Symmetry* **11**, 1312 (2019).
- ³⁶³A. Oliinyk, B. Malomed, and A. Yakimenko, “Nonlinear dynamics of Josephson vortices in merging superfluid rings,” *Commun. Nonlinear Sci. Numer. Simul.* **83**, 105113 (2020).
- ³⁶⁴M. Cominotti, D. Rossini, M. Rizzi, F. Hekking, and A. Minguzzi, “Optimal persistent currents for interacting bosons on a ring with a gauge field,” *Phys. Rev. Lett.* **113**, 025301 (2014).
- ³⁶⁵T. W. Kibble, “Topology of cosmic domains and strings,” *J. Phys. A: Math. Gen.* **9**, 1387 (1976).
- ³⁶⁶W. H. Zurek, “Cosmological experiments in superfluid helium?” *Nature* **317**, 505 (1985).
- ³⁶⁷D. Gallucci and N. Proukakis, “Engineering dark solitary waves in ring-trap bose-einstein condensates,” *New J. Phys.* **18**, 025004 (2016).
- ³⁶⁸H. T. C. Stoof and M. J. Bijlsma, “Dynamics of fluctuating Bose-Einstein condensates,” *J. Low Temp. Phys.* **124**, 431–442 (2001).
- ³⁶⁹C. W. Gardiner and M. J. Davis, “The stochastic gross-pitaevskii equation: II,” *J. Phys. B: At. Mol. Opt. Phys.* **36**, 4731–4753 (2003).
- ³⁷⁰A. S. Bradley, C. W. Gardiner, and M. J. Davis, “Bose-einstein condensation from a rotating thermal cloud: Vortex nucleation and lattice formation,” *Phys. Rev. A* **77**, 033616 (2008).
- ³⁷¹N. P. Proukakis and B. Jackson, “Finite-temperature models of bose-einstein condensation,” *J. Phys. B: At. Mol. Opt. Phys.* **41**, 203002 (2008).
- ³⁷²P. Blakie, A. Bradley, M. Davis, R. Ballagh, and C. Gardiner, “Dynamics and statistical mechanics of ultra-cold bose gases using c-field techniques,” *Adv. Phys.* **57**, 363–455 (2008).
- ³⁷³S. Rooney, P. Blakie, and A. Bradley, “Stochastic projected gross-pitaevskii equation,” *Phys. Rev. A* **86**, 053634 (2012).
- ³⁷⁴N. P. Proukakis, S. Gardiner, M. Davis, and M. Szymańska, eds., *Quantum Gases: Finite Temperature and Non-Equilibrium Dynamics: I (Cold Atoms)* (ICP, 2013).
- ³⁷⁵N. G. Berloff, M. Brachet, and N. P. Proukakis, “Modeling quantum fluid dynamics at nonzero temperatures,” *Proceedings of the National Academy of Sciences* **111**, 4675–4682 (2014).
- ³⁷⁶G. Pelegrí, J. Polo, A. Turpin, M. Lewenstein, J. Mompart, and V. Ahufinger, “Single-atom edgelike states via quantum interference,” *Phys. Rev. A* **95**, 013614 (2017).
- ³⁷⁷G. Pelegrí, A. Marques, R. Dias, A. Daley, V. Ahufinger, and J. Mompart, “Topological edge states with ultracold atoms carrying orbital angular momentum in a diamond chain,” *Phys. Rev. A* **99**, 023612 (2019).
- ³⁷⁸G. Pelegrí, A. Marques, R. Dias, A. Daley, J. Mompart, and V. Ahufinger, “Topological edge states and aharonov-bohm caging with ultracold atoms carrying orbital angular momentum,” *Phys. Rev. A* **99**, 023613 (2019).
- ³⁷⁹A. Gallemí, A. M. Mateo, R. Mayol, and M. Guilleumas, “Coherent quantum phase slip in two-component bosonic atomtronic circuits,” *New J. Phys.* **18**, 015003 (2015).
- ³⁸⁰R. Driben, Y. Kartashov, B. A. Malomed, T. Meier, and L. Torner, “Three-dimensional hybrid vortex solitons,” *New J. Phys.* **16**, 063035 (2014).
- ³⁸¹D. Yan, R. Carretero-González, D. J. Frantzeskakis, P. G. Kevrekidis, N. P. Proukakis, and D. Sporn, “Exploring vortex dynamics in the presence of dissipation: Analytical and numerical results,” *Phys. Rev. A* **89**, 043613 (2014).
- ³⁸²E. Varoquaux, “Anderson’s considerations on the flow of superfluid helium: Some offshoots,” *Rev. Mod. Phys.* **87**, 803–854 (2015).
- ³⁸³P. W. Anderson, “Considerations on the flow of superfluid helium,” *Rev. Mod. Phys.* **38**, 298–310 (1966).
- ³⁸⁴S. Levy, E. Lahoud, I. Shomroni, and J. Steinhauer, “The a.c. and d.c. josephson effects in a bose-einstein condensate,” *Nature* **449**, 579 (2007).
- ³⁸⁵D. McKay, M. White, M. Pasienski, and B. DeMarco, “Phase-slip-induced dissipation in an atomic bose-hubbard system,” *Nature* **453**, 76 (2008).
- ³⁸⁶G. Valtolina, A. Burchianti, A. Amico, E. Neri, K. Khani, J. A. Seman, A. Trombettoni, A. Smerzi, M. Zaccanti, M. Inguscio, and G. Roati, “Josephson effect in fermionic superfluids across the bec-bcs crossover,” *Science* **350**, 1505–1508 (2015).
- ³⁸⁷K. C. Wright, R. B. Blakestad, C. J. Lobb, W. D. Phillips, and G. K. Campbell, “Threshold for creating excitations in a stirred superfluid ring,” *Phys. Rev. A* **88**, 063633 (2013).
- ³⁸⁸A. Muñoz Mateo, A. Gallemí, M. Guilleumas, and R. Mayol, “Persistent currents supported by solitary waves in toroidal bose-einstein condensates,” *Phys. Rev. A* **91**, 063625 (2015).
- ³⁸⁹A. Kumar, S. Eckel, F. Jendrzejewski, and G. K. Campbell, “Temperature-induced decay of persistent currents in a superfluid ultracold gas,” *Phys. Rev. A* **95**, 021602(R) (2017).
- ³⁹⁰F. Piazza, L. A. Collins, and A. Smerzi, “Vortex-induced phase-slip dissipation in a toroidal Bose-Einstein condensate flowing through a barrier,” *Phys. Rev. A* **80**, 021601(R) (2009).
- ³⁹¹M. Kunimi and I. Danshita, “Thermally activated phase slips of one-dimensional bose gases in shallow optical lattices,” *Phys. Rev. A* **95**, 033637 (2017).
- ³⁹²A. Burchianti, F. Scazza, A. Amico, G. Valtolina, J. A. Seman, C. Fort, M. Zaccanti, M. Inguscio, and G. Roati, “Connecting dissipation and phase slips in a josephson junction between fermionic superfluids,” *Phys. Rev. Lett.* **120**, 025302 (2018).
- ³⁹³K. Khani, E. Neri, L. Galantucci, F. Scazza, A. Burchianti, K.-L. Lee, C. F. Barenghi, A. Trombettoni, M. Inguscio, M. Zaccanti, G. Roati, and N. P. Proukakis, “Critical transport and vortex dynamics in a thin atomic josephson junction,” *Phys. Rev. Lett.* **124**, 045301 (2020).
- ³⁹⁴J. Polo, R. Dubessy, P. Pedri, H. Perrin, and A. Minguzzi, “Oscillations and decay of superfluid currents in a one-dimensional bose gas on a ring,” *Phys. Rev. Lett.* **123**, 195301 (2019).
- ³⁹⁵G. Gauthier, S. S. Szigeti, M. T. Reeves, M. Baker, T. A. Bell, H. Rubinsztein-Dunlop, M. J. Davis, and T. W. Neely, “An atomtronic oscillator circuit for quantum gases,” *arXiv preprint arXiv:1903.04086* (2019).
- ³⁹⁶J. Polo, V. Ahufinger, F. W. Hekking, and A. Minguzzi, “Damping of josephson oscillations in strongly correlated one-dimensional atomic gases,” *Phys. Rev. Lett.* **121**, 090404 (2018).
- ³⁹⁷M. Pigneur, T. Berrada, M. Bonneau, T. Schumm, E. Demler, and J. Schmiedmayer, “Relaxation to a phase-locked equilibrium state in a one-dimensional bosonic josephson junction,” *Phys. Rev. Lett.* **120**, 173601 (2018).
- ³⁹⁸A. Smerzi, S. Fantoni, S. Giovanazzi, and S. R. Shenoy, “Quantum Coherent Atomic Tunneling between Two Trapped Bose-Einstein Condensates,” *Phys. Rev. Lett.* **79**, 4950–4953 (1997).
- ³⁹⁹S. Raghavan, A. Smerzi, S. Fantoni, and S. R. Shenoy, “Coherent oscillations between two weakly coupled bose-einstein condensates: Josephson effects, π oscillations, and macroscopic quantum self-trapping,” *Phys. Rev. A* **59**, 620–633 (1999).
- ⁴⁰⁰M. Albiez, R. Gati, J. Fölling, S. Hunsmann, M. Cristiani, and M. K. Oberthaler, “Direct observation of tunneling and nonlinear self-trapping in a single bosonic josephson junction,” *Phys. Rev. Lett.* **95**, 010402 (2005).
- ⁴⁰¹G. Spagnolli, G. Semeghini, L. Masi, G. Ferioli, A. Trenkwalder, S. Coop, M. Landini, L. Pezzè, G. Modugno, M. Inguscio, A. Smerzi, and M. Fattori, “Crossing over from attractive to repulsive interactions in a tunneling bosonic josephson junction,” *Phys. Rev. Lett.* **118**, 230403 (2017).
- ⁴⁰²F. Piazza, L. A. Collins, and A. Smerzi, “Instability and vortex ring

- dynamics in a three-dimensional superfluid flow through a constriction,” *New Journal of Physics* **13**, 043008 (2011).
- ⁴⁰³M. Abad, M. Guilleumas, R. Mayol, F. Piazza, D. M. Jezek, and A. Smerzi, “Phase slips and vortex dynamics in josephson oscillations between bose-einstein condensates,” *EPL (Europhysics Letters)* **109**, 40005 (2015).
- ⁴⁰⁴K. Khani, L. Galantucci, C. Barengi, G. Roati, A. Trombettoni, and N. Proukakis, “Dynamical phase diagram of ultracold josephson junctions,” (2020), arXiv:2007.13102.
- ⁴⁰⁵A. Griffin, T. Nikuni, and E. Zaremba, *Bose-Condensed Gases at Finite Temperatures* (Cambridge University Press, 2009).
- ⁴⁰⁶B. Jackson, N. P. Proukakis, C. F. Barengi, and E. Zaremba, “Finite-temperature vortex dynamics in bose-einstein condensates,” *Phys. Rev. A* **79**, 053615 (2009).
- ⁴⁰⁷A. J. Allen, E. Zaremba, C. F. Barengi, and N. P. Proukakis, “Observable vortex properties in finite-temperature bose gases,” *Phys. Rev. A* **87**, 013630 (2013).
- ⁴⁰⁸B. Paredes, A. Widera, V. Murg, O. Mandel, S. Fölling, I. Cirac, G. V. Shlyapnikov, T. W. Hänsch, and I. Bloch, “Tonks–girardeau gas of ultracold atoms in an optical lattice,” *Nature* **429**, 277 (2004).
- ⁴⁰⁹T. Kinoshita, T. Wenger, and D. S. Weiss, “Observation of a one-dimensional tonks–girardeau gas,” *Science* **305**, 1125 (2004).
- ⁴¹⁰S. Hofferberth, I. Lesanovsky, B. Fischer, T. Schumm, and J. Schmiedmayer, “Non-equilibrium coherence dynamics in one-dimensional bose gases,” *Nature* **449**, 324–327 (2007), 0706.2259.
- ⁴¹¹S. Hofferberth, I. Lesanovsky, T. Schumm, A. Imambekov, V. Gritsev, E. Demler, and J. Schmiedmayer, “Probing quantum and thermal noise in an interacting many-body system,” *Nat. Phys.* **4**, 489–495 (2008), 0710.1575.
- ⁴¹²B. Yang, Y.-Y. Chen, Y.-G. Zheng, H. Sun, H.-N. Dai, X.-W. Guan, Z.-S. Yuan, and J.-W. Pan, “Quantum criticality and the tomonaga–luttinger liquid in one-dimensional bose gases,” *Phys. Rev. Lett.* **119**, 165701 (2017).
- ⁴¹³M. A. Cazalilla, “Bosonizing one-dimensional cold atomic gases,” *J. Phys. B: At. Mol. Opt. Phys.* **37**, S1 (2004).
- ⁴¹⁴A. O. Caldeira and A. J. Leggett, “Influence of dissipation on quantum tunneling in macroscopic systems,” *Phys. Rev. Lett.* **46**, 211–214 (1981).
- ⁴¹⁵A. Caldeira and A. Leggett, “Quantum tunnelling in a dissipative system,” *Ann. Phys.* **149**, 374–456 (1983).
- ⁴¹⁶G. Schön and A. Zaikin, “Quantum coherent effects, phase transitions, and the dissipative dynamics of ultra small tunnel junctions,” *Phys. Rep.* **198**, 237–412 (1990).
- ⁴¹⁷M. Girardeau, “Relationship between systems of impenetrable bosons and fermions in one dimension,” *J. Math. Phys.* **1**, 516–523 (1960).
- ⁴¹⁸M. D. Girardeau and E. M. Wright, “Dark solitons in a one-dimensional condensate of hard core bosons,” *Phys. Rev. Lett.* **84**, 5691–5694 (2000).
- ⁴¹⁹V. I. Yukalov and M. D. Girardeau, “Fermi-bose mapping for one-dimensional bose gases,” *Laser Physics Letters* **2**, 375 (2005).
- ⁴²⁰A. Pérez Obiol and T. Cheon, “Bose-einstein condensate confined in a one-dimensional ring stirred with a rotating delta link,” *Phys. Rev. E* **101**, 022212 (2020).
- ⁴²¹A. Pérez-Obiol, J. Polo, and T. Cheon, “Current production in ring condensates with a weak link,” (2020), arXiv:2007.11243 [cond-mat.quant-gas].
- ⁴²²O. Fialko, M.-C. Delattre, J. Brand, and A. R. Kolovsky, “Nucleation in finite topological systems during continuous metastable quantum phase transitions,” *Phys. Rev. Lett.* **108**, 250402 (2012).
- ⁴²³Y. Li, W. Pang, and B. A. Malomed, “Nonlinear modes and symmetry breaking in rotating double-well potentials,” *Phys. Rev. A* **86**, 023832 (2012).
- ⁴²⁴A. Muñoz Mateo, V. Delgado, M. Guilleumas, R. Mayol, and J. Brand, “Nonlinear waves of bose-einstein condensates in rotating ring-lattice potentials,” *Phys. Rev. A* **99**, 023630 (2019).
- ⁴²⁵B. T. Seaman, L. D. Carr, and M. J. Holland, “Effect of a potential step or impurity on the bose-einstein condensate mean field,” *Phys. Rev. A* **71**, 033609 (2005).
- ⁴²⁶A. Pérez-Obiol and T. Cheon, “Stationary real solutions of the nonlinear schrödinger equation on a ring with a defect,” *J. Phys. Soc. Jpn* **88**, 034005 (2019).
- ⁴²⁷L. D. Carr, C. W. Clark, and W. P. Reinhardt, “Stationary solutions of the one-dimensional nonlinear schrödinger equation. i. case of repulsive nonlinearity,” *Phys. Rev. A* **62**, 063610 (2000).
- ⁴²⁸L. Dobrek, M. Gajda, M. Lewenstein, K. Sengstock, G. Birkl, and W. Ertmer, “Optical generation of vortices in trapped bose-einstein condensates,” *Phys. Rev. A* **60**, R3381–R3384 (1999).
- ⁴²⁹Y. Zheng and J. Javanainen, “Classical and quantum models for phase imprinting,” *Phys. Rev. A* **67**, 035602 (2003).
- ⁴³⁰M. J. Davis, S. A. Morgan, and K. Burnett, “Simulations of bose fields at finite temperature,” *Phys. Rev. Lett.* **87**, 160402 (2001).
- ⁴³¹K. V. Kheruntsyan, D. M. Gangardt, P. D. Drummond, and G. V. Shlyapnikov, “Pair Correlations in a Finite-Temperature 1D Bose Gas,” *Phys. Rev. Lett.* **91**, 040403 (2003).
- ⁴³²T. Karpiuk, P. Deuar, P. Bienias, E. Witkowska, K. Pawłowski, M. Gajda, K. Rządowski, and M. Brewczyk, “Spontaneous Solitons in the Thermal Equilibrium of a Quasi-1D Bose Gas,” *Phys. Rev. Lett.* **109**, 205302 (2012).
- ⁴³³N. Bilas and N. Pavloff, “Dark soliton past a finite-size obstacle,” *Phys. Rev. A* **72**, 033618 (2005).
- ⁴³⁴J. E. Mooij and Y. V. Nazarov, “Superconducting nanowires as quantum phase-slip junctions,” *Nature Phys.* **2**, 169 (2006).
- ⁴³⁵J. W. Park, B. Ko, and Y. Shin, “Critical vortex shedding in a strongly interacting fermionic superfluid,” *Phys. Rev. Lett.* **121**, 225301 (2018).
- ⁴³⁶M. Z. Hasan and C. L. Kane, “Colloquium: Topological insulators,” *Rev. Mod. Phys.* **82**, 3045–3067 (2010).
- ⁴³⁷N. R. Cooper, J. Dalibard, and I. B. Spielman, “Topological bands for ultracold atoms,” *Rev. Mod. Phys.* **91**, 015005 (2019).
- ⁴³⁸S. Krinner, T. Esslinger, and J.-P. Brantut, “Two-terminal transport measurements with cold atoms,” *Journal of Physics: Condensed Matter* **29**, 343003 (2017).
- ⁴³⁹S. C. Caliga, C. J. E. Straatsma, and D. Z. Anderson, “Experimental demonstration of an atomtronic battery,” *New Journal of Physics* **19**, 013036 (2017).
- ⁴⁴⁰A. A. Zozulya and D. Z. Anderson, “Principles of an atomtronic battery,” *Phys. Rev. A* **88**, 043641 (2013).
- ⁴⁴¹J. G. Lee, B. J. McIlvain, and C. J. a. Lobb, “Analogues of basic electronic circuit elements in a free-space atom chip,” *Scientific Reports* **3**, 1034 (2013).
- ⁴⁴²F. Damon, G. Condon, P. Cheiney, A. Fortun, B. Georgeot, J. Billy, and D. Guéry-Odelin, “Band-gap structures for matter waves,” *Phys. Rev. A* **92**, 033614 (2015).
- ⁴⁴³B. Seaman, M. Krämer, D. Anderson, and M. Holland, “Atomtronics: Ultracold-atom analogs of electronic devices,” *Phys. Rev. A* **75**, 023615 (2007).
- ⁴⁴⁴R. A. Pepino, J. Cooper, D. Meiser, D. Z. Anderson, and M. J. Holland, “Open quantum systems approach to atomtronics,” *Phys. Rev. A* **82**, 013640 (2010).
- ⁴⁴⁵S. C. Caliga, C. J. E. Straatsma, A. A. Zozulya, and D. Z. Anderson, “Principles of an atomtronic transistor,” *New Journal of Physics* **18**, 015012 (2016).
- ⁴⁴⁶R. Gati, M. Albiez, J. Fölling, B. Hemmerling, and M. Oberthaler, “Realization of a single Josephson junction for Bose–Einstein condensates,” *Applied Physics B* **82**, 207–210 (2006).
- ⁴⁴⁷R. Gati and M. K. Oberthaler, “A bosonic Josephson junction,” *Journal of Physics B: Atomic, Molecular and Optical Physics* **40**, R61–R89 (2007).
- ⁴⁴⁸R. L. Fagaly, “Superconducting quantum interference device instruments and applications,” *Review of Scientific Instruments* **77**, 101101 (2006), <https://doi.org/10.1063/1.2354545>.
- ⁴⁴⁹K. U. Schreiber and J.-P. R. Wells, “Invited review article: Large ring lasers for rotation sensing,” *Review of Scientific Instruments* **84**, 041101 (2013).
- ⁴⁵⁰V. M. N. Passaro, A. Cuccovillo, L. Vaiani, M. D. Carlo, and C. E. Campanella, “Gyroscope technology and applications: A review in the industrial perspective,” *Sensors* **17**, 2284 (2017).
- ⁴⁵¹T. W. Kornack, R. K. Ghosh, and M. V. Romalis, “Nuclear spin gyroscope based on an atomic comagnetometer,” *Physical Review Letters* **95** (2005), 10.1103/physrevlett.95.230801.
- ⁴⁵²F. Riehle, T. Kisters, A. Witte, J. Helmcke, and C. J. Bordé, “Optical ramsey spectroscopy in a rotating frame: Sagnac effect in a matter-wave interferometer,” *Phys. Rev. Lett.* **67**, 177–180 (1991).
- ⁴⁵³T. L. Gustavson, P. Bouyer, and M. A. Kasevich, “Precision rotation measurements with an atom interferometer gyroscope,” *Phys. Rev. Lett.* **78**, 2046–2049 (1997).

- ⁴⁵⁴B. Barrett, R. Geiger, I. Dutta, M. Meunier, B. Canuel, A. Gauguier, P. Bouyer, and A. Landragin, "The sagnac effect: 20 years of development in matter-wave interferometry," *Comptes Rendus Physique* **15**, 875–883 (2014).
- ⁴⁵⁵F. M. Crompton, H. L. Bethlem, R. T. Jongma, and G. Meijer, "A prototype storage ring for neutral molecules," *Nature* **411**, 174–176 (2001).
- ⁴⁵⁶S. Gupta, K. W. Murch, K. L. Moore, T. P. Purdy, and D. M. Stamper-Kurn, "Bose-einstein condensation in a circular waveguide," *Physical Review Letters* **95** (2005), 10.1103/physrevlett.95.143201.
- ⁴⁵⁷A. S. Arnold, "Adaptable-radius, time-orbiting magnetic ring trap for bose-einstein condensates," *Journal of Physics B: Atomic, Molecular and Optical Physics* **37**, L29–L33 (2004).
- ⁴⁵⁸M. Andersen, C. Ryu, P. Cladé, V. Natarajan, A. Vaziri, K. Helmerson, and W. Phillips, "Quantized rotation of atoms from photons with orbital angular momentum," *Physical Review Letters* **97** (2006), 10.1103/physrevlett.97.170406.
- ⁴⁵⁹I. Lesanovsky, T. Schumm, S. Hofferberth, L. M. Andersson, P. Krüger, and J. Schmiedmayer, "Adiabatic radio-frequency potentials for the coherent manipulation of matter waves," *Physical Review A* **73** (2006), 10.1103/physreva.73.033619.
- ⁴⁶⁰E. Courtade, O. Houde, J.-F. Clément, P. Verkerk, and D. Hennequin, "Dark optical lattice of ring traps for cold atoms," *Physical Review A* **74** (2006), 10.1103/physreva.74.031403.
- ⁴⁶¹P. Jain, A. S. Bradley, and C. W. Gardiner, "Quantum de laval nozzle: Stability and quantum dynamics of sonic horizons in a toroidally trapped bose gas containing a superflow," *Physical Review A* **76** (2007), 10.1103/physreva.76.023617.
- ⁴⁶²M. Bhattacharya, "Lattice with a twist: Helical waveguides for ultracold matter," *Optics Communications* **279**, 219–222 (2007).
- ⁴⁶³S. Wu, E. Su, and M. Prentiss, "Demonstration of an area-enclosing guided-atom interferometer for rotation sensing," *Physical Review Letters* **99** (2007), 10.1103/physrevlett.99.173201.
- ⁴⁶⁴S. E. Olson, M. L. Terraciano, M. Bashkansky, and F. K. Fatemi, "Cold-atom confinement in an all-optical dark ring trap," *Physical Review A* **76** (2007), 10.1103/physreva.76.061404.
- ⁴⁶⁵T. Fernholz, R. Gerritsma, P. Krüger, and R. J. C. Spreeuw, "Dynamically controlled toroidal and ring-shaped magnetic traps," *Physical Review A* **75** (2007), 10.1103/physreva.75.063406.
- ⁴⁶⁶S. Franke-Arnold, J. Leach, M. J. Padgett, V. E. Lembessis, D. Ellinas, A. J. Wright, J. M. Girkin, P. Öhberg, and A. S. Arnold, "Optical ferris wheel for ultracold atoms," *Optics Express* **15**, 8619 (2007).
- ⁴⁶⁷S. K. Schnelle, E. D. van Ooijen, M. J. Davis, N. R. Heckenberg, and H. Rubinsztein-Dunlop, "Versatile two-dimensional potentials for ultracold atoms," *Optics Express* **16**, 1405 (2008).
- ⁴⁶⁸P. F. Griffin, E. Riis, and A. S. Arnold, "Smooth inductively coupled ring trap for atoms," *Physical Review A* **77** (2008), 10.1103/physreva.77.051402.
- ⁴⁶⁹N. Houston, E. Riis, and A. S. Arnold, "Reproducible dynamic dark ring lattices for ultracold atoms," *Journal of Physics B: Atomic, Molecular and Optical Physics* **41**, 211001 (2008).
- ⁴⁷⁰B. E. Sherlock, M. Gildemeister, E. Owen, E. Nugent, and C. J. Foot, "Time-averaged adiabatic ring potential for ultracold atoms," *Physical Review A* **83** (2011), 10.1103/physreva.83.043408.
- ⁴⁷¹G. D. Bruce, J. Mayoh, G. Smirne, L. Torralbo-Campo, and D. Cassettari, "A smooth, holographically generated ring trap for the investigation of superfluidity in ultracold atoms," *Physica Scripta* **T143**, 014008 (2011).
- ⁴⁷²J. D. Pritchard, A. N. Dinkelaker, A. S. Arnold, P. F. Griffin, and E. Riis, "Demonstration of an inductively coupled ring trap for cold atoms," *New Journal of Physics* **14**, 103047 (2012).
- ⁴⁷³A. S. Arnold, "Extending dark optical trapping geometries," *Optics Letters* **37**, 2505 (2012).
- ⁴⁷⁴G. E. Marti, R. Olf, and D. M. Stamper-Kurn, "Collective excitation interferometry with a toroidal bose-einstein condensate," *Physical Review A* **91** (2015), 10.1103/physreva.91.013602.
- ⁴⁷⁵I. Dutta, D. Savoie, B. Fang, B. Venon, C. G. Alzar, R. Geiger, and A. Landragin, "Continuous cold-atom inertial sensor with 1 nrad/sec rotation stability," *Physical Review Letters* **116** (2016), 10.1103/physrevlett.116.183003.
- ⁴⁷⁶E. Moan, R. Horne, T. Arpornthip, Z. Luo, A. Fallon, S. Berl, and C. Sackett, "Quantum rotation sensing with dual sagnac interferometers in an atom-optical waveguide," *Physical Review Letters* **124**, 120403 (2020).
- ⁴⁷⁷M. G. Boshier, talk at Atomtronics 2019 (2019).
- ⁴⁷⁸P. L. Halkyard, M. P. A. Jones, and S. A. Gardiner, "Rotational response of two-component bose-einstein condensates in ring traps," *Phys. Rev. A* **81**, 061602 (2010).
- ⁴⁷⁹J. L. Helm, T. P. Billam, A. Rakonjac, S. L. Cornish, and S. A. Gardiner, "Spin-orbit-coupled interferometry with ring-trapped bose-einstein condensates," *Phys. Rev. Lett.* **120**, 063201 (2018).
- ⁴⁸⁰S. A. Haine, "Mean-field dynamics and fisher information in matter wave interferometry," *Phys. Rev. Lett.* **116**, 230404 (2016).
- ⁴⁸¹J. L. Helm, S. L. Cornish, and S. A. Gardiner, "Sagnac interferometry (2004) using bright matter-wave solitons," *Phys. Rev. Lett.* **114**, 134101 (2015).
- ⁴⁸²J. L. Helm, T. P. Billam, and S. A. Gardiner, "Bright matter-wave soliton collisions at narrow barriers," *Phys. Rev. A* **85**, 053621 (2012).
- ⁴⁸³J. Polo and V. Ahufinger, "Soliton-based matter-wave interferometer," *Physical Review A* **88**, 053628 (2013).
- ⁴⁸⁴O. J. Wales, A. Rakonjac, T. P. Billam, J. L. Helm, S. A. Gardiner, and S. L. Cornish, "Splitting and recombination of bright-solitary-matter waves," *Comm. Phys.* **3**, 51 (2020).
- ⁴⁸⁵G. D. McDonald, C. C. N. Kuhn, K. S. Hardman, S. Bennetts, P. J. Everitt, P. A. Altin, J. E. Debs, J. D. Close, and N. P. Robins, "Bright solitonic matter-wave interferometer," *Phys. Rev. Lett.* **113**, 013002 (2014).
- ⁴⁸⁶J. L. Helm, S. J. Rooney, C. Weiss, and S. A. Gardiner, "Splitting bright matter-wave solitons on narrow potential barriers: Quantum to classical transition and applications to interferometry," *Phys. Rev. A* **89**, 033610 (2014).
- ⁴⁸⁷S. A. Haine, "Quantum noise in bright soliton matterwave interferometry," *New Journal of Physics* **20**, 033009 (2018).
- ⁴⁸⁸S. P. Nolan, J. Sabbatini, M. W. J. Bromley, M. J. Davis, and S. A. Haine, "Quantum enhanced measurement of rotations with a spin-1 bose-einstein condensate in a ring trap," *Phys. Rev. A* **93**, 023616 (2016).
- ⁴⁸⁹Y. Che, F. Yao, H. Liang, G. Li, and X. Wang, "Phase-space geometric sagnac interferometer for rotation sensing," *Phys. Rev. A* **98**, 053609 (2018).
- ⁴⁹⁰D. Robbes, "Highly sensitive magnetometers—a review," *Sensors and Actuators A: Physical* **129**, 86 (2006).
- ⁴⁹¹S. J. Ingleby, C. O'Dwyer, P. F. Griffin, A. S. Arnold, and E. Riis, "Vector magnetometry exploiting phase-geometry effects in a double-resonance alignment magnetometer," *Phys. Rev. Applied* **10**, 034035 (2018).
- ⁴⁹²M. L. Terraciano, M. Bashkansky, and F. K. Fatemi, "A single-shot imaging magnetometer using cold atoms," *Opt. Express* **16**, 13062 (2008).
- ⁴⁹³K. Hardman, P. Everitt, G. McDonald, P. Manju, P. Wigley, M. Sooriyabandara, C. Kuhn, J. Debs, J. Close, and N. Robins, "Simultaneous precision gravimetry and magnetic gradiometry with a bose-einstein condensate: A high precision, quantum sensor," *Phys. Rev. Lett.* **117**, 138501 (2016).
- ⁴⁹⁴T. Isayama, Y. Takahashi, N. Tanaka, K. Toyoda, K. Ishikawa, and T. Yabuzaki, "Observation of larmor spin precession of laser-cooled rb atoms via paramagnetic faraday rotation," *Phys. Rev. A* **59**, 4836 (1999).
- ⁴⁹⁵M. Vengallatore, J. M. Higbie, S. R. Leslie, J. Guzman, L. E. Sadler, and D. M. Stamper-Kurn, "High-resolution magnetometry with a spinor bose-einstein condensate," *Phys. Rev. Lett.* **98**, 200801 (2007).
- ⁴⁹⁶F. K. Fatemi and M. Bashkansky, "Spatially resolved magnetometry using cold atoms in dark optical tweezers," *Opt. Express* **18**, 2190 (2010).
- ⁴⁹⁷Y. Eto, H. Ikeda, H. Suzuki, S. Hasegawa, Y. Tomiyama, M. S. S. Sekine, and T. Hirano, "Spin-echo-based magnetometry with spinor bose-einstein condensates," *Phys. Rev. A* **88**, 031602(R) (2013).
- ⁴⁹⁸Y. Eto, S. Sekine, S. Hasegawa, M. Sadgrove, H. Saito, and T. Hirano, "Control and detection of the larmor precession of $f = 2^{87}$ rb bose-einstein condensates by ramsey interferometry and spin-echo," *Appl. Phys. Express* **6**, 05280 (2013).
- ⁴⁹⁹W. Muessel, H. Strobel, D. Linnemann, D. Hume, and M. Oberthaler, "Scalable spin squeezing for quantum-enhanced magnetometry with bose-einstein condensates," *Phys. Rev. Lett.* **113**, 103004 (2014).
- ⁵⁰⁰S. Tojo, Y. Taguchi, Y. Masuyama, T. Hayashi, H. Saito, and T. Hirano, "Controlling phase separation of binary bose-einstein condensates via mixed-spin-channel feshbach resonance," *Phys. Rev. A* **82**, 033609 (2010).
- ⁵⁰¹S. Wildermuth, S. Hofferberth, I. Lesanovsky, E. Haller, L. M. Andersson, S. Groth, I. Bar-Joseph, P. Krüger, and J. Schmiedmayer, "Microscopic magnetic-field imaging," *Nature* **435**, 440 (2005).

- ⁵⁰²S. Wildermuth, S. Hofferberth, I. Lesanovsky, S. Groth, P. Krüger, and J. Schmiedmayer, “Sensing electric and magnetic fields with bose-einstein condensates,” *Appl. Phys. Lett.* **88**, 264103 (2006).
- ⁵⁰³G. Pelegrí, V. Ahufinger, and J. Mompert, “Quantum sensing using imbalanced counter-propagating bose-einstein condensate modes,” *New Journal of Physics* **20**, 103001 (2018).
- ⁵⁰⁴Y. Wang, A. Kumar, F. Jendrzejewski, R. M. Wilson, M. Edwards, S. Eckel, G. K. Campbell, and C. W. Clark, “Resonant wavepackets and shock waves in an atomtronic squid,” *New J. Phys.* **17**, 125012 (2015).
- ⁵⁰⁵J. Clarke and F. K. Wilhelm, “Superconducting quantum bits,” *Nature* **453**, 1031–1042 (2008).
- ⁵⁰⁶I. Bloch, “Quantum coherence and entanglement with ultracold atoms in optical lattices,” *Nature* **453**, 1016–1022 (2008).
- ⁵⁰⁷M. Saffman, T. Walker, and K. Mölmer, “Quantum information with rydberg atoms,” *Reviews of Modern Physics* **82**, 2313 (2010).
- ⁵⁰⁸R. Blatt and D. Wineland, “Entangled states of trapped atomic ions,” *Nature* **453**, 1008–1015 (2008).
- ⁵⁰⁹L. M. Vandersypen, M. Steffen, G. Breyta, C. S. Yannoni, M. H. Sherwood, and I. L. Chuang, “Experimental realization of shor’s quantum factoring algorithm using nuclear magnetic resonance,” *Nature* **414**, 883–887 (2001).
- ⁵¹⁰J. Petta, A. C. Johnson, J. Taylor, E. Laird, A. Yacoby, M. D. Lukin, C. Marcus, M. Hanson, and A. Gossard, “Coherent manipulation of coupled electron spins in semiconductor quantum dots,” *Science* **309**, 2180–2184 (2005).
- ⁵¹¹W. S. Bakr, A. Peng, M. E. Tai, R. Ma, J. Simon, J. I. Gillen, S. Foelling, L. Pollet, and M. Greiner, “Probing the superfluid-to-mott insulator transition at the single-atom level,” *Science* **329**, 547–550 (2010).
- ⁵¹²J. F. Sherson, C. Weitenberg, M. Endres, M. Cheneau, I. Bloch, and S. Kuhr, “Single-atom-resolved fluorescence imaging of an atomic mott insulator,” *Nature* **467**, 68–72 (2010).
- ⁵¹³E. Lucero, R. Barends, Y. Chen, J. Kelly, M. Mariantoni, A. Megrant, P. O’Malley, D. Sank, A. Vainsencher, J. Wenner, *et al.*, “Computing prime factors with a josephson phase qubit quantum processor,” *Nature Physics* **8**, 719–723 (2012).
- ⁵¹⁴L. Amico, A. Osterloh, and F. Cataliotti, “Quantum many particle systems in ring-shaped optical lattices,” *Phys. Rev. Lett.* **95**, 063201 (2005).
- ⁵¹⁵L. Amico, D. Aghamalyan, F. Aukstolz, H. Crepaz, R. Dumke, and L. C. Kwek, “Superfluid qubit systems with ring shaped optical lattices,” *Sci. Rep.* **4**, 4298 (2014).
- ⁵¹⁶D. Aghamalyan, M. Cominotti, M. Rizzi, D. Rossini, F. Hekking, A. Minguzzi, L.-C. Kwek, and L. Amico, “Coherent superposition of current flows in an atomtronic quantum interference device,” *New journal of Physics* **17**, 045023 (2015).
- ⁵¹⁷D. Aghamalyan, N. Nguyen, F. Aukstolz, K. Gan, M. M. Valado, P. Condylis, L.-C. Kwek, R. Dumke, and L. Amico, “An atomtronic flux qubit: a ring lattice of bose-einstein condensates interrupted by three weak links,” *New Journal of Physics* **18**, 075013 (2016).
- ⁵¹⁸M. Cominotti, M. Rizzi, D. Rossini, D. Aghamalyan, L. Amico, L. C. Kwek, F. Hekking, and A. Minguzzi, “Optimal scaling of persistent currents for interacting bosons on a ring,” *The European Physical Journal Special Topics* **224**, 519–524 (2015).
- ⁵¹⁹D. W. Hallwood, K. Burnett, and J. Dunningham, “Macroscopic superpositions of superfluid flows,” *New Journal of Physics* **8**, 180 (2006).
- ⁵²⁰A. Nunnenkamp, A. M. Rey, and K. Burnett, “Generation of macroscopic superposition states in ring superlattices,” *Physical Review A* **77**, 023622 (2008).
- ⁵²¹K. Madison, F. Chevy, W. Wohlleben, and J. Dalibard, “Vortex formation in a stirred bose-einstein condensate,” *Physical Review Letters* **84**, 806 (2000).
- ⁵²²J. Abo-Shaeer, C. Raman, J. Vogels, and W. Ketterle, “Observation of vortex lattices in bose-einstein condensates,” *Science* **292**, 476–479 (2001).
- ⁵²³Y.-J. Lin, R. L. Compton, K. Jiménez-García, W. D. Phillips, J. V. Porto, and I. B. Spielman, “A synthetic electric force acting on neutral atoms,” *Nature Physics* **7**, 531–534 (2011).
- ⁵²⁴J. Mooij, T. Orlando, L. Levitov, L. Tian, C. H. Van der Wal, and S. Lloyd, “Josephson persistent-current qubit,” *Science* **285**, 1036–1039 (1999).
- ⁵²⁵D. Solenov and D. Mozyrsky, “Macroscopic two-state systems in trapped atomic condensates,” *Physical Review A* **82**, 061601 (2010).
- ⁵²⁶T. Haug, J. Tan, M. Theng, R. Dumke, L.-C. Kwek, and L. Amico, “Readout of the atomtronic quantum interference device,” *Phys. Rev. A* **97**, 013633 (2018).
- ⁵²⁷J. Dalibard, F. Gerbier, G. Juzeliūnas, and P. Öhberg, “Colloquium: Artificial gauge potentials for neutral atoms,” *Rev. Mod. Phys.* **83**, 1523 (2011).
- ⁵²⁸D. Loss, “Parity effects in a luttinger liquid: Diamagnetic and paramagnetic ground states,” *Phys. Rev. Lett.* **69**, 343 (1992).
- ⁵²⁹L. Amico and V. Penna, “Time-dependent mean-field theory of the superfluid-insulator phase transition,” *Physical Review B* **62**, 1224 (2000).
- ⁵³⁰R. Fazio and H. van der Zant, “Quantum phase transitions and vortex dynamics in superconducting networks,” *Phys. Rep.* **355**, 235–334 (2001).
- ⁵³¹D. Aghamalyan, “Atomtronics: Quantum technology with cold atoms in ring shaped optical lattices,” *PhDT* (2015).
- ⁵³²G. Rastelli, I. M. Pop, and F. W. Hekking, “Quantum phase slips in josephson junction rings,” *Phys. Rev. B* **87**, 174513 (2013).
- ⁵³³A. L. Fetter, “Rotating trapped bose-einstein condensates,” *Reviews of Modern Physics* **81**, 647 (2009).
- ⁵³⁴A. Leanhardt, A. Görlitz, A. Chikkatur, D. Kielpinski, Y. Shin, D. Pritchard, and W. Ketterle, “Imprinting vortices in a bose-einstein condensate using topological phases,” *Phys. Rev. Lett.* **89**, 190403 (2002).
- ⁵³⁵Y.-J. Lin, R. L. Compton, K. Jimenez-Garcia, J. V. Porto, and I. B. Spielman, “Synthetic magnetic fields for ultracold neutral atoms,” *Nature* **462**, 628–632 (2009).
- ⁵³⁶F. Chiodi, M. Ferrier, K. Tikhonov, P. Virtanen, T. Heikkilä, M. Feigelman, S. Guéron, and H. Bouchiat, “Microwave response of an ns ring coupled to a superconducting resonator,” *arXiv preprint arXiv:1005.0406* (2010).
- ⁵³⁷D. Solenov and D. Mozyrsky, “Cold atom qubits,” *J. Comput. Theor. Nanosci.* **8**, 481 (2011).
- ⁵³⁸H. Fan, V. Roychowdhury, and T. Szkopek, “Optimal two-qubit quantum circuits using exchange interactions,” *Physical Review A* **72**, 052323 (2005).
- ⁵³⁹D. Loss and D. P. DiVincenzo, “Quantum computation with quantum dots,” *Physical Review A* **57**, 120 (1998).
- ⁵⁴⁰S. Eckel, F. Jendrzejewski, A. Kumar, C. Lobb, and G. Campbell, “Interferometric measurement of the current-phase relationship of a superfluid weak link,” *Phys. Rev. X* **4**, 031052 (2014).
- ⁵⁴¹T. Roscilde, M. F. Faulkner, S. T. Bramwell, and P. C. Holdsworth, “From quantum to thermal topological-sector fluctuations of strongly interacting bosons in a ring lattice,” *New J. Phys.* **18**, 075003 (2016).
- ⁵⁴²E. Altman, E. Demler, and M. D. Lukin, “Probing many-body states of ultracold atoms via noise correlations,” *Phys. Rev. A* **70**, 013603 (2004).
- ⁵⁴³F. Gerbier, S. Trotzky, S. Fölling, U. Schnorrberger, J. Thompson, A. Widera, I. Bloch, L. Pollet, M. Troyer, B. Capogrosso-Sansone, *et al.*, “Expansion of a quantum gas released from an optical lattice,” *Phys. Rev. Lett.* **101**, 155303 (2008).
- ⁵⁴⁴J. Slater, “A soluble problem in energy bands,” *Phys. Rev.* **87**, 807 (1952).
- ⁵⁴⁵M. Chiofalo, M. Polini, and M. Tosi, “Collective excitations of a periodic bose condensate in the wannier representation,” *Eur. Phys. J. D* **11**, 371–378 (2000).
- ⁵⁴⁶Y. Castin and J. Dalibard, “Relative phase of two bose-einstein condensates,” *Phys. Rev. A* **55**, 4330 (1997).
- ⁵⁴⁷W. Mullin, R. Krotkov, and F. Laloë, “The origin of the phase in the interference of bose-einstein condensates,” *Am. J. Phys.* **74**, 880–887 (2006).
- ⁵⁴⁸S. Fölling, F. Gerbier, A. Widera, O. Mandel, T. Gericke, and I. Bloch, “Spatial quantum noise interferometry in expanding ultracold atom clouds,” *Nature* **434**, 481–484 (2005).
- ⁵⁴⁹M.-K. Kang and U. R. Fischer, “Revealing single-trap condensate fragmentation by measuring density-density correlations after time of flight,” *Phys. Rev. Lett.* **113**, 140404 (2014).
- ⁵⁵⁰A. Nunnenkamp, A. M. Rey, and K. Burnett, “Superposition states of ultracold bosons in rotating rings with a realistic potential barrier,” *Physical Review A* **84**, 053604 (2011).
- ⁵⁵¹M. Pasiński and B. DeMarco, “A high-accuracy algorithm for designing arbitrary holographic atom traps,” *Optics express* **16**, 2176–2190 (2008).
- ⁵⁵²A. L. Gaunt and Z. Hadzibabic, “Robust digital holography for ultracold atom trapping,” *Scientific reports* **2** (2012).
- ⁵⁵³G. D. Bruce, M. Y. Johnson, E. Cormack, D. A. Richards, J. Mayoh, and D. Cassettari, “Feedback-enhanced algorithm for aberration correction of holographic atom traps,” *Journal of Physics B: Atomic, Molecular and Optical Physics* **48**, 115303 (2015).
- ⁵⁵⁴T. Li, H. Kelkar, D. Medellin, and M. Raizen, “Real-time control of the

- periodicity of a standing wave: an optical accordion," *Optics express* **16**, 5465–5470 (2008).
- ⁵⁵⁵B. Anderson, K. Dholakia, and E. Wright, "Atomic-phase interference devices based on ring-shaped bose-einstein condensates: Two-ring case," *Physical Review A* **67**, 033601 (2003).
- ⁵⁵⁶J. Clarke and A. I. Braginski, *The SQUID handbook: Applications of SQUIDs and SQUID systems* (John Wiley & Sons, 2006).
- ⁵⁵⁷J. I. Cirac and P. Zoller, "Goals and opportunities in quantum simulation," *Nat Phys* **8**, 264–266 (2012).
- ⁵⁵⁸W. Ketterle and M. W. Zwierlein, "Making, probing and understanding ultracold fermi gases," in *Ultra-cold Fermi gases*, Proceedings of the International School of Physics "Enrico Fermi", Vol. 164, edited by M. Inguscio, W. Ketterle, and C. Salomon (IOS press, Amsterdam, 2008) pp. 95–287.
- ⁵⁵⁹S. Giorgini, L. P. Pitaevskii, and S. Stringari, "Theory of ultracold atomic fermi gases," *Rev. Mod. Phys.* **80**, 1215–1274 (2008).
- ⁵⁶⁰W. Zwerger, *The BCS-BEC crossover and the unitary Fermi gas*, Vol. 836 (Springer Science & Business Media, 2011).
- ⁵⁶¹M. Zwierlein, *Proceedings of the International School of Physics' Enrico Fermi*, Vol. 191 (2016) pp. 143–220.
- ⁵⁶²I. Ferrier-Barbut, M. Delehaye, S. Laurent, A. Grier, M. Pierce, B. Rem, F. Chevy, and C. Salomon, "A mixture of Bose and Fermi superfluids," *Science* **345**, 1035–1038 (2014).
- ⁵⁶³M. Abad, A. Recati, S. Stringari, and F. Chevy, "Counter-flow instability of a quantum mixture of two superfluids," *Eur. Phys. J. D* **69**, 126 (2015).
- ⁵⁶⁴M. Delehaye, S. Laurent, I. Ferrier-Barbut, S. Jin, F. Chevy, and C. Salomon, "Critical velocity and dissipation of an ultracold bose-fermi counterflow," *Phys. Rev. Lett.* **115**, 265303 (2015).
- ⁵⁶⁵J.-P. Brantut, J. Meineke, D. Stadler, S. Krinner, and T. Esslinger, "Conduction of ultracold fermions through a mesoscopic channel," *Science* **337**, 1069–1071 (2012).
- ⁵⁶⁶S. Krinner, M. Lebrat, D. Husmann, C. Grenier, J.-P. Brantut, and T. Esslinger, "Mapping out spin and particle conductances in a quantum point contact," *Proc. Nat. Acad. Sci.* **113**, 8144–8149 (2016).
- ⁵⁶⁷J.-P. Brantut, C. Grenier, J. Meineke, D. Stadler, S. Krinner, C. Kollath, T. Esslinger, and A. Georges, "A thermoelectric heat engine with ultracold atoms," *Science* **342**, 713–715 (2013).
- ⁵⁶⁸L. Landau, "Theory of the superfluidity of helium ii," *Phys. Rev.* **60**, 356–358 (1941).
- ⁵⁶⁹R. Combescot, M. Kagan, and S. Stringari, "Collective mode of homogeneous superfluid Fermi gases in the BEC-BCS crossover," *Phys. Rev. A* **74**, 042717 (2006).
- ⁵⁷⁰D. E. Miller, J. K. Chin, C. A. Stan, Y. Liu, W. Setiawan, C. Sanner, and W. Ketterle, "Critical velocity for superfluid flow across the bec-bcs crossover," *Phys. Rev. Lett.* **99**, 070402 (2007).
- ⁵⁷¹W. Weimer, K. Morgener, V. P. Singh, J. Siegl, K. Hueck, N. Luick, L. Mathey, and H. Moritz, "Critical velocity in the BEC-BCS crossover," *Phys. Rev. Lett.* **114**, 095301 (2015).
- ⁵⁷²X.-C. Yao, H.-Z. Chen, Y.-P. Wu, X.-P. Liu, X.-Q. Wang, X. Jiang, Y. Deng, Y.-A. Chen, and J.-W. Pan, "Observation of coupled vortex lattices in a mass-imbalance bose and fermi superfluid mixture," *Phys. Rev. Lett.* **117**, 145301 (2016).
- ⁵⁷³Y. Castin, I. Ferrier-Barbut, and C. Salomon, "The landau critical velocity for a particle in a fermi superfluid," *Comptes Rendus Physique* **16**, 241–253 (2015).
- ⁵⁷⁴W. Zheng and H. Zhai, "Quasiparticle lifetime in a mixture of Bose and fermi superfluids," *Phys. Rev. Lett.* **113**, 265304 (2014).
- ⁵⁷⁵V. Yukalov and E. Yukalova, "Stratification of moving multicomponent Bose-Einstein condensates," *Laser Physics Letters* **1**, 50 (2004).
- ⁵⁷⁶H. Kurkjian, Y. Castin, and A. Sinatra, "Concavity of the collective excitation branch of a fermi gas in the bec-bcs crossover," *Physical Review A* **93**, 013623 (2016).
- ⁵⁷⁷P. Fedichev and G. Shlyapnikov, "Critical velocity in cylindrical Bose-Einstein condensates," *Phys. Rev. A* **63**, 045601 (2001).
- ⁵⁷⁸C. Tozzo and F. Dalfovo, "Bogoliubov spectrum and bragg spectroscopy of elongated Bose-Einstein condensates," *New Journal of Physics* **5**, 54 (2003).
- ⁵⁷⁹P.-P. Crépín, X. Leyronas, and F. Chevy, "Hydrodynamic spectrum of a superfluid in an elongated trap," *EPL (Europhysics Letters)* **114**, 60005 (2016).
- ⁵⁸⁰S. Jin, S. Laurent, and F. Chevy, "Hydrodynamic response of a trapped superfluid to a periodic perturbation," *EPJ Special Topics* **227**, 2263–2273 (2019).
- ⁵⁸¹L. Onsager, "Statistical hydrodynamics," *Il Nuovo Cimento* (1943-1954) **6**, 279–287 (1949).
- ⁵⁸²R. Feynman, *Chapter II: Application of Quantum Mechanics to Liquid Helium*, edited by C. Gorter, *Progr. Low Temp. Phys.*, Vol. 1 (Elsevier, 1955) pp. 17–53.
- ⁵⁸³M. Lebrat, P. Grišins, D. Husmann, S. Häusler, L. Corman, T. Giamarchi, J.-P. Brantut, and T. Esslinger, "Band and correlated insulators of cold fermions in a mesoscopic lattice," *Phys. Rev. X* **8**, 011053 (2018).
- ⁵⁸⁴M. Lebrat, S. Häusler, P. Fabritius, D. Husmann, L. Corman, and T. Esslinger, "Quantized Conductance through a Spin-Selective Atomic Point Contact," *Phys. Rev. Lett.* **123**, 193605 (2019).
- ⁵⁸⁵L. J. LeBlanc, A. B. Bardon, J. McKeever, M. H. T. Extavour, D. Jervis, J. H. Thywissen, F. Piazza, and A. Smerzi, "Dynamics of a tunable superfluid junction," *Phys. Rev. Lett.* **106**, 025302 (2011).
- ⁵⁸⁶D. Stadler, S. Krinner, J. Meineke, J.-P. Brantut, and T. Esslinger, "Observing the drop of resistance in the flow of a superfluid fermi gas," *Nature* **491**, 736 (2012).
- ⁵⁸⁷D. Husmann, S. Uchino, S. Krinner, M. Lebrat, T. Giamarchi, T. Esslinger, and J.-P. Brantut, "Connecting strongly correlated superfluids by a quantum point contact," *Science* **350**, 1498–1501 (2015).
- ⁵⁸⁸B. J. van Wees, H. van Houten, C. W. J. Beenakker, J. G. Williamson, L. P. Kouwenhoven, D. van der Marel, and C. T. Foxon, "Quantized conductance of point contacts in a two-dimensional electron gas," *Physical Review Letters* **60**, 848–850 (1988).
- ⁵⁸⁹R. Labouvie, B. Santra, S. Heun, S. Wimberger, and H. Ott, "Negative Differential Conductivity in an Interacting Quantum Gas," *Phys. Rev. Lett.* **115**, 050601 (2015).
- ⁵⁹⁰S. Krinner, D. Stadler, D. Husmann, J.-P. Brantut, and T. Esslinger, "Observation of quantized conductance in neutral matter," *Nature* **517**, 64–67 (2015).
- ⁵⁹¹S. Häusler, S. Nakajima, M. Lebrat, D. Husmann, S. Krinner, T. Esslinger, and J.-P. Brantut, "Scanning Gate Microscope for Cold Atomic Gases," *Phys. Rev. Lett.* **119**, 030403 (2017).
- ⁵⁹²A. Luther and V. J. Emery, "Backward Scattering in the One-Dimensional Electron Gas," *Phys. Rev. Lett.* **33**, 589–592 (1974).
- ⁵⁹³L. Corman, P. Fabritius, S. Häusler, J. Mohan, L. H. Dogra, D. Husmann, M. Lebrat, and T. Esslinger, "Quantized conductance through a dissipative atomic point contact," *Phys. Rev. A* **100**, 053605 (2019).
- ⁵⁹⁴G. E. W. Bauer, A. H. MacDonald, and S. Maekawa, "Spin Caloritronics," *Solid State Commun.* **150**, 459–460 (2010).
- ⁵⁹⁵F. S. Bergeret, M. Silaev, P. Virtanen, and T. T. Heikkilä, "Colloquium: Nonequilibrium effects in superconductors with a spin-splitting field," *Rev. Mod. Phys.* **90**, 041001 (2018).
- ⁵⁹⁶C. Beenakker, "Search for Majorana Fermions in Superconductors," *Annu. Rev. Condens. Matter Phys.* **4**, 113–136 (2013).
- ⁵⁹⁷R. A. Duine and H. T. C. Stoof, "Spin drag in noncondensed bose gases," *Phys. Rev. Lett.* **103**, 170401 (2009).
- ⁵⁹⁸A. Sommer, M. Ku, G. Roati, and M. W. Zwierlein, "Universal spin transport in a strongly interacting fermi gas," *Nature* **472**, 201–204 (2011).
- ⁵⁹⁹O. Goulko, F. Chevy, and C. Lobo, "Spin drag of a fermi gas in a harmonic trap," *Phys. Rev. Lett.* **111**, 190402 (2013).
- ⁶⁰⁰E. Fava, T. Bienaimé, C. Mordini, G. Colzi, C. Qu, S. Stringari, G. Lamporesi, and G. Ferrari, "Observation of spin superfluidity in a bose gas mixture," *Phys. Rev. Lett.* **120**, 170401 (2018).
- ⁶⁰¹M. A. Nichols, L. W. Cheuk, M. Okan, T. R. Hartke, E. Mendez, T. Senthil, E. Khatami, H. Zhang, and M. W. Zwierlein, "Spin transport in a mott insulator of ultracold fermions," *Science* **363**, 383–387 (2019).
- ⁶⁰²D. V. Fil and S. I. Shevchenko, "Nondissipative drag of superflow in a two-component bose gas," *Phys. Rev. A* **72**, 013616 (2005).
- ⁶⁰³J. Nespolo, G. E. Astrakharchik, and A. Recati, "Andreev-bashkin effect in superfluid cold gases mixtures," *New J. Phys.* **19**, 125005 (2017).
- ⁶⁰⁴L. Parisi, G. E. Astrakharchik, and S. Giorgini, "Spin dynamics and andreev-bashkin effect in mixtures of one-dimensional bose gases," *Phys. Rev. Lett.* **121**, 025302 (2018).
- ⁶⁰⁵D. Pines and P. Nozières, *Theory of Quantum Liquids: Normal Fermi Liquids* (Benjamin, New York, 1966).
- ⁶⁰⁶E. M. Lifshitz and L. P. Pitaevskii, *Statistical Physics, Part 2* (Pergamon

- Press, Oxford, 1980).
- ⁶⁰⁷A. Recati and S. Stringari, “Spin fluctuations, susceptibility, and the dipole oscillation of a nearly ferromagnetic fermi gas,” *Phys. Rev. Lett.* **106**, 080402 (2011).
 - ⁶⁰⁸J. R. Engelbrecht, M. Randeria, and L. Zhang, “Landau f function for the dilute fermi gas in two dimensions,” *Phys. Rev. B* **45**, 10135–10138 (1992).
 - ⁶⁰⁹A. Celi, P. Massignan, J. Ruseckas, N. Goldman, I. B. Spielman, G. Juzeliūnas, and M. Lewenstein, “Synthetic gauge fields in synthetic dimensions,” *Phys. Rev. Lett.* **112**, 043001 (2014).
 - ⁶¹⁰G. Salerno, H. M. Price, M. Lebrat, S. Häusler, T. Esslinger, L. Corman, J.-P. Brantut, and N. Goldman, “Quantized hall conductance of a single atomic wire: A proposal based on synthetic dimensions,” *Phys. Rev. X* **9**, 041001 (2019).
 - ⁶¹¹P. T. Brown, D. Mitra, E. Guardado-Sanchez, R. Nourafkan, A. Reymbaut, C.-D. Hébert, S. Bergeron, A.-M. S. Tremblay, J. Kokalj, D. A. Huse, P. Schauf, and W. S. Bakr, “Bad metallic transport in a cold atom fermi-hubbard system,” *Science* **363**, 379–382 (2019).
 - ⁶¹²R. Anderson, F. Wang, P. Xu, V. Venu, S. Trotzky, F. Chevy, and J. H. Thywissen, “Conductivity spectrum of ultracold atoms in an optical lattice,” *Phys. Rev. Lett.* **122**, 153602 (2019).
 - ⁶¹³W. Neuhauser, M. Hohenstatt, P. E. Toschek, and H. Dehmelt, “Localized visible Ba^+ mono-ion oscillator,” *Phys. Rev. A* **22**, 1137–1140 (1980).
 - ⁶¹⁴R. Bücker, A. Perrin, S. Manz, T. Betz, C. Koller, T. Plisson, J. Rottmann, T. Schumm, and J. Schmiedmayer, “Single-particle-sensitive imaging of freely propagating ultracold atoms,” *New J. Phys.* **11**, 103039 (2009).
 - ⁶¹⁵D. B. Hume, I. Stroescu, M. Joos, W. Muessel, H. Strobel, and M. K. Oberthaler, “Accurate atom counting in mesoscopic ensembles,” *Phys. Rev. Lett.* **111**, 253001 (2013).
 - ⁶¹⁶C. Gross and I. Bloch, “Microscopy of many-body states in optical lattices,” in *Annual Review of Cold Atoms and Molecules*, Vol. Volume 3 (World Scientific, 2015) pp. 181–199.
 - ⁶¹⁷S. Uchino, M. Ueda, and J.-P. Brantut, “Universal noise in continuous transport measurements of interacting fermions,” *Phys. Rev. A* **98**, 063619 (2018).
 - ⁶¹⁸B. A. Bernevig and T. L. X. Hughes, *Topological insulators and topological superconductors* (Princeton university press, 2013).
 - ⁶¹⁹A. Y. Kitaev, “Unpaired majorana fermions in quantum wires,” *Physics-Uspekhi* **44**, 131 (2001).
 - ⁶²⁰Y. Loiko, V. Ahufinger, R. Menchon-Enrich, G. Birkel, and J. Mompert, “Coherent injecting, extracting, and velocity filtering of neutral atoms in a ring trap via spatial adiabatic passage,” *The European Physical Journal D* **68**, 147 (2014).
 - ⁶²¹T. Haug, H. Heimonen, R. Dumke, L.-C. Kwek, and L. Amico, “The aharonov-bohm effect in mesoscopic bose-einstein condensates,” *Phys. Rev. A* (2019).
 - ⁶²²T. Haug, R. Dumke, L.-C. Kwek, and L. Amico, “Andreev-reflection and aharonov-bohm dynamics in atomtronic circuits,” *Quantum Sci. Technol.* **4**, 045001 (2019).
 - ⁶²³T. Haug, L. Amico, L.-C. Kwek, W. Munro, and V. Bastidas, “Topological pumping of quantum correlations,” *Phys. Rev. Res.* **2**, 013135 (2020).
 - ⁶²⁴T. Haug, L. Amico, R. Dumke, and L.-C. Kwek, “Mesoscopic vortex-meissner currents in ring ladders,” *Quantum Sci. Technol.* **3**, 035006 (2018).
 - ⁶²⁵A. Tokuno, M. Oshikawa, and E. Demler, “Dynamics of one-dimensional bose liquids: Andreev-like reflection at y junctions and the absence of the aharonov-bohm effect,” *Phys. Rev. Lett.* **100**, 140402 (2008).
 - ⁶²⁶A. Daley, P. Zoller, and B. Trauzettel, “Andreev-like reflections with cold atoms,” *Phys. Rev. Lett.* **100**, 110404 (2008).
 - ⁶²⁷I. Zapata and F. Sols, “Andreev reflection in bosonic condensates,” *Phys. Rev. Lett.* **102**, 180405 (2009).
 - ⁶²⁸S. Watabe and Y. Kato, “Reflection and refraction of bose-einstein condensate excitations,” *Phys. Rev. A* **78**, 063611 (2008).
 - ⁶²⁹R. A. Webb, S. Washburn, C. Umbach, and R. Laibowitz, “Observation of h/e aharonov-bohm oscillations in normal-metal rings,” *Phys. Rev. Lett.* **54**, 2696 (1985).
 - ⁶³⁰M. Lohse, C. Schweizer, O. Zilberberg, M. Aidelsburger, and I. Bloch, “A Thouless quantum pump with ultracold bosonic atoms in an optical superlattice,” *Nat. Phys.* **12**, 350–354 (2016).
 - ⁶³¹T. Haug, L. Amico, L.-C. Kwek, W. Munro, and V. Bastidas, “Duality and topological pumping on entanglement and disorder,” *arXiv:1905.03807* (2019).
 - ⁶³²J. Tangpanitanon, V. M. Bastidas, S. Al-Assam, P. Roushan, D. Jaksch, and D. G. Angelakis, “Topological pumping of photons in nonlinear resonator arrays,” *Phys. Rev. Lett.* **117**, 213603 (2016).
 - ⁶³³M. Jones, C. Vale, D. Sahagun, B. Hall, C. Eberlein, B. Sauer, K. Furusawa, D. Richardson, and E. Hinds, “Cold atoms probe the magnetic field near a wire,” *Journal of Physics B: Atomic, Molecular and Optical Physics* **37**, L15 (2003).
 - ⁶³⁴Y. J. Wang, D. Z. Anderson, V. M. Bright, E. A. Cornell, Q. Diot, T. Kishimoto, M. Prentiss, R. A. Saravanan, S. R. Segal, and S. J. Wu, “Atom michelson interferometer on a chip using a bose-einstein condensate,” *Physical Review Letters* **94**, 090405 (2005).
 - ⁶³⁵S. Safaei, L.-C. Kwek, R. Dumke, and L. Amico, “Monitoring currents in cold-atom circuits,” *Phys. Rev. A* **100**, 013621 (2019).
 - ⁶³⁶S. Boriskina, T. Benson, P. Sewell, and A. Nosich, “Tuning of elliptic whispering-gallery-mode microdisk waveguide filters,” *Journal of Light-wave Technology* **21**, 1987–1995 (2003).
 - ⁶³⁷W. von Klitzing, R. Long, V. S. Ilchenko, J. Hare, and V. Lefevre-Seguin, “Tunable whispering gallery modes for spectroscopy and cqed experiments,” *New Journal of Physics* , 141–1414 (2001).
 - ⁶³⁸M. Valiente and D. Petrosyan, “Two-particle states in the hubbard model,” *J. Phys. B* **41**, 161002 (2008).
 - ⁶³⁹H.-P. Breuer and F. Petruccione, *The theory of open quantum systems* (Oxford University Press on Demand, 2002).
 - ⁶⁴⁰C. Guo and D. Poletti, “Dissipatively driven hardcore bosons steered by a gauge field,” *Phys. Rev. B* **96**, 165409 (2017).
 - ⁶⁴¹L. Amico, A. Osterloh, and U. Eckern, “One-dimensional xxz model for particles obeying fractional statistics,” *Phys. Rev. B* **58**, R1703 (1998).
 - ⁶⁴²S. R. White and A. E. Feiguin, “Real-time evolution using the density matrix renormalization group,” *Phys. Rev. Lett.* **93**, 076401 (2004).
 - ⁶⁴³E. M. Stoudenmire and S. R. White, *ITensor Library (version 2.1.1)*.
 - ⁶⁴⁴M. Büttiker, Y. Imry, and M. Y. Azbel, “Quantum oscillations in one-dimensional normal-metal rings,” *Phys. Rev. A* **30**, 1982 (1984).
 - ⁶⁴⁵T. Prosen, “Third quantization: a general method to solve master equations for quadratic open fermi systems,” *New J. Phys.* **10**, 043026 (2008).
 - ⁶⁴⁶C. Guo and D. Poletti, “Solutions for bosonic and fermionic dissipative quadratic open systems,” *Phys. Rev. A* **95**, 052107 (2017).
 - ⁶⁴⁷P. Kevrekidis, D. Frantzeskakis, G. Theoharis, and I. Kevrekidis, “Guidance of matter waves through y -junctions,” *Phys. Lett. A* **317**, 513–522 (2003).
 - ⁶⁴⁸M. E. S. Andersen and N. T. Zinner, “Physical approach to quantum networks with massive particles,” *Phys. Rev. B* **97**, 155407 (2018).
 - ⁶⁴⁹H. Kreutzmann, U. V. Poulsen, M. Lewenstein, R. Dumke, W. Ertmer, G. Birkel, and A. Sanpera, “Coherence properties of guided-atom interferometers,” *Phys. Rev. Lett.* **92**, 163201 (2004).
 - ⁶⁵⁰C. Kane and M. P. Fisher, “Transport in a one-channel luttinger liquid,” *Phys. Rev. Lett.* **68**, 1220 (1992).
 - ⁶⁵¹D. J. Thouless, M. Kohmoto, M. P. Nightingale, and M. den Nijs, “Quantized hall conductance in a two-dimensional periodic potential,” *Phys. Rev. Lett.* **49**, 405 (1982).
 - ⁶⁵²D. Thouless, “Quantization of particle transport,” *Phys. Rev. B* **27**, 6083 (1983).
 - ⁶⁵³T. Haug, R. Dumke, L.-C. Kwek, C. Miniatura, and L. Amico, “Engineering quantum current states with machine learning,” *arXiv:1911.09578* (2019).
 - ⁶⁵⁴H. L. Stormer, “Nobel lecture: the fractional quantum hall effect,” *Rev. Mod. Phys.* **71**, 875 (1999).
 - ⁶⁵⁵C. Glattli, in *High Magnetic Fields: Applications in Condensed Matter Physics and Spectroscopy*, edited by C. Berthier *et al.* (Springer-Verlag, Berlin, 2002) p. 1.
 - ⁶⁵⁶N. Regnault and T. Jolicoeur, “Quantum Hall Fractions in Rotating Bose-Einstein Condensates,” *Phys. Rev. Lett.* **91**, 030402 (2003), *arXiv:cond-mat/0212477*.
 - ⁶⁵⁷J. Ruseckas, G. Juzeliūnas, P. Öhberg, and M. Fleischhauer, “Non-abelian gauge potentials for ultracold atoms with degenerate dark states,” *Phys. Rev. Lett.* **95**, 010404 (2005).
 - ⁶⁵⁸Y. Lin, K. Jimenez-Garcia, and I. B. Spielman, “Spin-orbit-coupled bose-einstein condensates,” *Nature (London)* **471**, 83 (2011).
 - ⁶⁵⁹V. Galitski and I. B. Spielman, “Spin-orbit coupling in quantum gases,”

- Nature (London) **494**, 49–54 (2013).
- ⁶⁶⁰M. Kardar, “Josephson-junction ladders and quantum fluctuations,” Phys. Rev. B **33**, 3125 (1986).
- ⁶⁶¹E. Orignac and T. Giamarchi, “Meissner effect in a bosonic ladder,” Phys. Rev. B **64**, 144515 (2001).
- ⁶⁶²M.-C. Cha and J.-G. Shin, “Two peaks in the momentum distribution of bosons in a weakly frustrated two-leg optical ladder,” Phys. Rev. A **83**, 055602 (2011).
- ⁶⁶³A. Dhar, M. Maji, T. Mishra, R. V. Pai, S. Mukerjee, and A. Paramekanti, “Bose-Hubbard model in a strong effective magnetic field: Emergence of a chiral Mott insulator ground state,” Phys. Rev. A **85**, 041602 (2012).
- ⁶⁶⁴A. Dhar, T. Mishra, M. Maji, R. V. Pai, S. Mukerjee, and A. Paramekanti, “Chiral Mott insulator with staggered loop currents in the fully frustrated Bose-Hubbard model,” Phys. Rev. B **87**, 174501 (2013).
- ⁶⁶⁵A. Tokuno and A. Georges, “Ground states of a bose-hubbard ladder in an artificial magnetic field: field-theoretical approach,” New J. Phys. **16**, 073005 (2014).
- ⁶⁶⁶S. Uchino and A. Tokuno, “Population-imbalance instability in a bose-hubbard ladder in the presence of a magnetic flux,” Phys. Rev. A **92**, 013625 (2015).
- ⁶⁶⁷A. Petrescu and K. Le Hur, “Bosonic Mott Insulator with Meissner Currents,” Phys. Rev. Lett. **111**, 150601 (2013).
- ⁶⁶⁸A. Petrescu and K. Le Hur, “Chiral mott insulators, meissner effect, and Laughlin states in quantum ladders,” Phys. Rev. B **91**, 054520 (2015).
- ⁶⁶⁹A. Petrescu, M. Piraud, G. Roux, I. McCulloch, and K. L. Hur, “Precursor of Laughlin state of hard core bosons on a two leg ladder,” Phys. Rev. B **96**, 014524 (2017), arXiv:1612.05134.
- ⁶⁷⁰M. Piraud, Z. Cai, I. P. McCulloch, and U. Schollwöck, “Quantum magnetism of bosons with synthetic gauge fields in one-dimensional optical lattices: a density matrix renormalization group study,” Phys. Rev. A **89**, 063618 (2014).
- ⁶⁷¹M. Piraud, F. Heidrich-Meisner, I. P. McCulloch, S. Greschner, T. Vekua, and U. Schollwöck, “Vortex and meissner phases of strongly interacting bosons on a two-leg ladder,” Phys. Rev. B **91**, 140406 (2015).
- ⁶⁷²F. Kolley, M. Piraud, I. McCulloch, U. Schollwöck, and F. Heidrich-Meisner, “Strongly interacting bosons on a three-leg ladder in the presence of a homogeneous flux,” New J. Phys. **17**, 092001 (2015).
- ⁶⁷³S. Greschner, M. Piraud, F. Heidrich-Meisner, I. McCulloch, U. Schollwöck, and T. Vekua, “Spontaneous increase of magnetic flux and chiral-current reversal in bosonic ladders: Swimming against the tide,” Phys. Rev. Lett. **115**, 190402 (2015).
- ⁶⁷⁴S. Greschner, M. Piraud, F. Heidrich-Meisner, I. P. McCulloch, U. Schollwöck, and T. Vekua, “Symmetry-broken states in a system of interacting bosons on a two-leg ladder with a uniform abelian gauge field,” Phys. Rev. A **94**, 063628 (2016).
- ⁶⁷⁵A. Richaud and V. Penna, “Quantum dynamics of bosons in a two-ring ladder: dynamical algebra, vortex-like excitations and currents,” Phys. Rev. A **96**, 013620 (2017).
- ⁶⁷⁶S. Barbarino, L. Taddia, D. Rossini, L. Mazza, and R. Fazio, “Synthetic gauge fields in synthetic dimensions: interactions and chiral edge modes,” New J. Phys. **18**, 035010 (2016).
- ⁶⁷⁷L. Taddia, E. Cornfeld, D. Rossini, L. Mazza, E. Sela, and R. Fazio, “Topological fractional pumping with alkaline-earth-like atoms in synthetic lattices,” Phys. Rev. Lett. **118**, 230402 (2017).
- ⁶⁷⁸M. C. Strinati, E. Cornfeld, D. Rossini, S. Barbarino, M. Dalmonte, R. Fazio, E. Sela, and L. Mazza, “Laughlin-like states in bosonic and fermionic atomic synthetic ladders,” Phys. Rev. X **7**, 021033 (2017).
- ⁶⁷⁹M. C. Strinati, F. Gerbier, and L. Mazza, “Spin-gap spectroscopy in a bosonic flux ladder,” New J. Phys. **20**, 015004 (2018).
- ⁶⁸⁰M. C. Strinati, S. Sahoo, K. Shtengel, and E. Sela, “Pretopological fractional excitations in the two-leg flux ladder,” Phys. Rev. B **99**, 245101 (2019).
- ⁶⁸¹M. Di Dio, S. De Palo, E. Orignac, R. Citro, and M.-L. Chiofalo, “Persisting meissner state and incommensurate phases of hard-core boson ladders in a flux,” Phys. Rev. B **92**, 060506 (2015).
- ⁶⁸²E. Orignac, R. Citro, M. Di Dio, S. De Palo, and M.-L. Chiofalo, “Incommensurate phases of a bosonic two-leg ladder under a flux,” New J. Phys. **18**, 055017 (2016).
- ⁶⁸³E. Orignac, R. Citro, M. Di Dio, and S. De Palo, “Vortex lattice melting in a boson-ladder in artificial gauge field,” Phys. Rev. B **96**, 014518 (2017), arXiv:1703.07742.
- ⁶⁸⁴R. Citro, S. D. Palo, M. D. Dio, and E. Orignac, “Quantum phase transitions of a two-leg bosonic ladder in an artificial gauge field,” Phys. Rev. B **97**, 174523 (2018), arXiv:1802.04997.
- ⁶⁸⁵F. Pinheiro, G. M. Bruun, J.-P. Martikainen, and J. Larson, “XYZ Quantum heisenberg models with p-orbital bosons,” Physical Review Letters **111**, 205302 (2013).
- ⁶⁸⁶G. Pelegrí, J. Mompert, V. Ahufinger, and A. J. Daley, “Quantum magnetism with ultracold bosons carrying orbital angular momentum,” Phys. Rev. A **100**, 023615 (2019).
- ⁶⁸⁷T. Y. Saito and S. Furukawa, “Devil’s staircases in synthetic dimensions and gauge fields,” Phys. Rev. A **95**, 043613 (2017).
- ⁶⁸⁸L. Livi, G. Cappellini, M. Diem, L. Franchi, C. Clivati, M. Frittelli, F. Levi, D. Calonico, J. Catani, M. Inguscio, *et al.*, “Synthetic dimensions and spin-orbit coupling with an optical clock transition,” arXiv:1609.04800.
- ⁶⁸⁹F. Haldane, “Effective harmonic-fluid approach to low-energy properties of one-dimensional quantum fluids,” Phys. Rev. Lett. **47**, 1840 (1981).
- ⁶⁹⁰T. Giamarchi, *Quantum Physics in One Dimension* (Oxford University Press, Oxford, 2004).
- ⁶⁹¹S. R. White, Phys. Rev. B **48**, 10345 (1993).
- ⁶⁹²U. Schollwöck, “The density-matrix renormalization group,” Rev. Mod. Phys. **77**, 259 (2005).
- ⁶⁹³R. M. Hornreich, M. Luban, and S. Shtrikman, “Critical behavior at the onset of \vec{k} -space instability on the λ line,” Phys. Rev. Lett. **35**, 1678–1681 (1975).
- ⁶⁹⁴M. Atala, M. Aidelsburger, M. Lohse, J. T. Barreiro, B. Paredes, and I. Bloch, “Observation of chiral currents with ultracold atoms in bosonic ladders,” Nat. Phys. **10**, 588–593 (2014).
- ⁶⁹⁵N. Victorin, F. Hekking, and A. Minguzzi, “Bosonic double ring lattice under artificial gauge fields,” Phys. Rev. A **98**, 053626 (2018).
- ⁶⁹⁶N. Victorin, P. Pedri, and A. Minguzzi, “Excitation spectrum and super-solidity of a two-leg bosonic ring ladder,” Physical Review A **101**, 033618 (2020).
- ⁶⁹⁷J. Polo, J. Mompert, and V. Ahufinger, “Geometrically induced complex tunnelings for ultracold atoms carrying orbital angular momentum,” Phys. Rev. A **93**, 033613 (2016).
- ⁶⁹⁸J. Zak, “Berry’s phase for energy bands in solids,” Physical Review Letters **62**, 2747–2750 (1989).
- ⁶⁹⁹J. Arkininstall, M. H. Teimourpour, L. Feng, R. El-Ganainy, and H. Schomeus, “Topological tight-binding models from nontrivial square roots,” Physical Review B **95** (2017), 10.1103/physrevb.95.165109.
- ⁷⁰⁰M. Kremer, I. Petrides, E. Meyer, M. Heinrich, O. Zilberberg, and A. Szameit, (2018), arXiv:1805.05209.
- ⁷⁰¹W. P. Su, J. R. Schrieffer, and A. J. Heeger, “Solitons in polyacetylene,” Physical Review Letters **42**, 1698–1701 (1979).
- ⁷⁰²G. Pelegrí, A. M. Marques, R. G. Dias, A. J. Daley, V. Ahufinger, and J. Mompert, “Topological edge states with ultracold atoms carrying orbital angular momentum in a diamond chain,” Physical Review A **99**, 023612 (2019).
- ⁷⁰³A. M. Marques and R. G. Dias, “Topological bound states in interacting su-schrieffer-heeger rings,” Journal of Physics: Condensed Matter **30**, 305601 (2018).
- ⁷⁰⁴A. Marques and R. Dias, “Generalization of zak’s phase for lattice models with non-centered inversion symmetry axis,” arXiv:1707.06162 (2017).
- ⁷⁰⁵N. Victorin, T. Haug, L.-C. Kwek, L. Amico, and A. Minguzzi, “Nonclassical states in strongly correlated bosonic ring ladders,” Physical Review A **99**, 033616 (2019).
- ⁷⁰⁶K. E. Strecker, G. B. Partridge, A. G. Truscott, and R. G. Hulet, “Formation and propagation of matter wave soliton trains,” Nature **417**, 150 (2002).
- ⁷⁰⁷L. Khaykovich, F. Schreck, G. Ferrari, T. Bourdel, J. Cubizolles, L. D. Carr, Y. Castin, and C. Salomon, “Formation of a matter-wave bright soliton,” Science **296**, 1290 (2002).
- ⁷⁰⁸A. L. Marchant, T. P. Billam, T. P. Wiles, M. M. H. Yu, S. A. Gardiner, and S. L. Cornish, “Controlled formation and reflection of a bright solitary matter-wave,” Nat. Commun. **4**, 1865 (2013).
- ⁷⁰⁹S. Pollack, D. Dries, E. Olson, and R. Hulet, “Quantum tunneling of a macroscopic matter-wave soliton,” (2010), Bull. Am. Phys. Soc., 55, DAMOP 2010.
- ⁷¹⁰A. Boissé, G. Berthet, L. Fouché, G. Salomon, A. Aspect, S. Lepoutre, and

- T. Bourdel, “Nonlinear scattering of atomic bright solitons in disorder,” *Eur. Phys. Lett.* **117**, 10007 (2017).
- ⁷¹¹S. D. Hansen, N. Nygaard, and K. Mølmer, “Scattering of matter wave solitons on localized potentials,” Preprint at arXiv:1210.1681 (2012).
- ⁷¹²V. Dunjko and M. Olshanii, “Superheated integrability and multisoliton survival through scattering off barriers,” Preprint at arXiv:1501.00075 (2015).
- ⁷¹³C. Weiss and Y. Castin, “Creation and detection of a mesoscopic gas in a nonlocal quantum superposition,” *Phys. Rev. Lett.* **102**, 010403 (2009).
- ⁷¹⁴A. I. Streltsov, O. E. Alon, and L. S. Cederbaum, “Scattering of an attractive Bose-Einstein condensate from a barrier: Formation of quantum superposition states,” *Phys. Rev. A* **80**, 043616 (2009).
- ⁷¹⁵O. E. Alon, private communication.
- ⁷¹⁶V. A. Yurovsky, B. A. Malomed, R. G. Hulet, and M. Olshanii, “Dissociation of one-dimensional matter-wave breathers due to quantum many-body effects,” *Phys. Rev. Lett.* **119**, 220401 (2017).
- ⁷¹⁷O. V. Marchukov, B. A. Malomed, M. Olshanii, V. Dunjko, R. G. Hulet, and V. A. Yurovsky, “Quantum fluctuations of the center-of-mass and relative parameters of nls breathers,” Preprint at arXiv:1911.01369 (2019).
- ⁷¹⁸Y. Lai and H. A. Haus, “Quantum theory of solitons in optical fibers. i. time-dependent Hartree approximation,” *Phys. Rev. A* **40**, 844 (1989).
- ⁷¹⁹Y. Lai and H. A. Haus, “Quantum theory of solitons in optical fibers. ii. exact solution,” *Phys. Rev. A* **40**, 854 (1989).
- ⁷²⁰C.-P. Yeang, “Quantum theory of a second-order soliton based on a linearization approximation,” *J. Opt. Soc. Am. B* **16**, 1269–1279 (1999).
- ⁷²¹B. Opanchuk and P. D. Drummond, “One-dimensional bose gas dynamics: breather relaxation,” *Phys. Rev. A* **96**, 053628 (2017).
- ⁷²²V. E. Zakharov and A. B. Shabat, “Exact theory of two-dimensional self-focusing and one-dimensional self-modulation of waves in nonlinear media,” *Soviet Physics JETP* **34**, 62 (1972).
- ⁷²³J. Satsuma and N. Yajima, “Initial value problems of one-dimensional self-modulation of nonlinear waves in dispersive media,” *Supp. Progr. Theor. Phys.* **55**, 284 (1974).
- ⁷²⁴A. Di Carli, C. D. Colquhoun, G. Henderson, S. Flannigan, G.-L. Oppo, A. J. Daley, S. Kuhr, and E. Haller, “Excitation modes of bright matter-wave solitons,” *Phys. Rev. Lett.* **123**, 123602 (2019).
- ⁷²⁵C. D. E. Boschi, E. Ercolessi, L. Ferrari, P. Naldesi, F. Ortolani, and L. Taddia, “Bound states and expansion dynamics of interacting bosons on a one-dimensional lattice,” *Phys. Rev. A* **90**, 043606 (2014).
- ⁷²⁶J. Polo, P. Naldesi, A. Minguzzi, and L. Amico, “Exact results for persistent currents of two bosons in a ring lattice,” *Phys. Rev. A* **101**, 043418 (2020).
- ⁷²⁷D. C. Mattis, “The few-body problem on a lattice,” *Rev. Mod. Phys.* **58**, 361–379 (1986).
- ⁷²⁸M. Valiente, D. Petrosyan, and A. Saenz, “Three-body bound states in a lattice,” *Phys. Rev. A* **81**, 011601 (2010).
- ⁷²⁹P. Naldesi, J. P. Gomez, B. Malomed, M. Olshanii, A. Minguzzi, and L. Amico, “Rise and fall of a bright soliton in an optical lattice,” *Phys. Rev. Lett.* **122**, 053001 (2019).
- ⁷³⁰P. Naldesi, J. Polo Gomez, V. Dunjko, H. Perrin, M. Olshanii, L. Amico, and A. Minguzzi, “Angular momentum fractionalization: the quantum advantage of entangled bosons,” arXiv e-prints, arXiv:1901.09398 (2019), arXiv:1901.09398 [cond-mat.quant-gas].
- ⁷³¹F. Haldane, “Solidification in a soluble model of bosons on a one-dimensional lattice: The boson-hubbard chain,” *Physics Letters A* **80**, 281–283 (1980).
- ⁷³²T. Choy, “Some exact results for a degenerate hubbard model in one dimension,” *Physics Letters A* **80**, 49–52 (1980).
- ⁷³³T. Choy and F. Haldane, “Failure of bethe-ansatz solutions of generalizations of the hubbard chain to arbitrary permutation symmetry,” *Physics Letters A* **90**, 83–84 (1982).
- ⁷³⁴N. Byers and C. Yang, “Theoretical considerations concerning quantized magnetic flux in superconducting cylinders,” *Phys. Rev. Lett.* **7**, 46 (1961).
- ⁷³⁵L. Onsager, “Magnetic flux through a superconducting ring,” *Physical Review Letters* **7**, 50 (1961).
- ⁷³⁶A. Leggett, in *C.W.J. Beenakker, et al, Granular Nanoelectronics* (Plenum Press, New York, 1991) p. 359.
- ⁷³⁷L. Amico and V. Korepin, “Universality of the one-dimensional bose gas with delta interaction,” *Annals of Physics* **314**, 496–507 (2004).
- ⁷³⁸R. Kanamoto, H. Saito, and M. Ueda, “Symmetry breaking and enhanced condensate fraction in a matter-wave bright soliton,” *Physical review letters* **94**, 090404 (2005).
- ⁷³⁹P. Calabrese and J.-S. Caux, “Correlation functions of the one-dimensional attractive bose gas,” *Physical review letters* **98**, 150403 (2007).
- ⁷⁴⁰S. L. Braunstein and C. M. Caves, “Statistical distance and the geometry of quantum states,” *Phys. Rev. Lett.* **72**, 3439–3443 (1994).
- ⁷⁴¹L. Pezzé and A. Smerzi, “Entanglement, nonlinear dynamics, and the heisenberg limit,” *Phys. Rev. Lett.* **102**, 100401 (2009).
- ⁷⁴²T. F. Gallagher, *Rydberg Atoms* (Cambridge University Press, Cambridge, 1994).
- ⁷⁴³E. Urban, T. A. Johnson, T. Henage, L. Isenhower, D. D. Yavuz, T. G. Walker, and M. Saffman, “Observation of Rydberg blockade between two atoms,” *Nat. Phys.* **5**, 110–114 (2009).
- ⁷⁴⁴A. Gaëtan, Y. Miroshnychenko, T. Wilk, A. Chotia, M. Viteau, D. Comparat, P. Pillet, A. Browaeys, and P. Grangier, “Observation of collective excitation of two individual atoms in the Rydberg blockade regime,” *Nat. Phys.* **5**, 115–118 (2009).
- ⁷⁴⁵C. Simonelli, M. M. Valado, G. Masella, L. Asteria, E. Arimondo, D. Ciampini, and O. Morsch, “Seeded excitation avalanches in off-resonantly driven Rydberg gases,” *J. Phys. B* **49**, 154002 (2016).
- ⁷⁴⁶M. M. Valado, C. Simonelli, M. D. Hoogerland, I. Lesanovsky, J. P. Garrahan, E. Arimondo, D. Ciampini, and O. Morsch, “Experimental observation of controllable kinetic constraints in a cold atomic gas,” *Phys. Rev. A* **93**, 040701(R) (2016).
- ⁷⁴⁷M. Marcuzzi, E. Levi, W. Li, J. P. Garrahan, B. Olmos, and I. Lesanovsky, “Non-equilibrium universality in the dynamics of dissipative cold atomic gases,” *New J. Phys.* **17**, 072003 (2015).
- ⁷⁴⁸R. Gutiérrez, C. Simonelli, M. Archimi, F. Castellucci, E. Arimondo, D. Ciampini, M. Marcuzzi, I. Lesanovsky, and O. Morsch, “Experimental signatures of an absorbing-state phase transition in an open driven many-body quantum system,” *Phys. Rev. A* **96**, 041602(R) (2017).
- ⁷⁴⁹M. Marcuzzi, M. Buchhold, S. Diehl, and I. Lesanovsky, “Absorbing state phase transition with competing quantum and classical fluctuations,” *Phys. Rev. Lett.* **116**, 245701 (2016).
- ⁷⁵⁰M. Buchhold, B. Everest, M. Marcuzzi, I. Lesanovsky, and S. Diehl, “Nonequilibrium effective field theory for absorbing state phase transitions in driven open quantum spin systems,” *Phys. Rev. B* **95**, 014308 (2017).
- ⁷⁵¹C. J. Turner, A. A. Michailidis, D. A. Abanin, M. Serbyn, and Z. Papic, “Quantum many-body scars,” (2017), arXiv:1711.03528 [quant-ph].
- ⁷⁵²M. Schlosser, D. Ohl de Mello, D. Schäffner, T. Preuschoff, L. Kohfahl, and G. Birkl, “Assembled arrays of rydberg-interacting atoms,” *J. Phys. B: At. Mol. Opt. Phys.* **53**, 144001 (2020).
- ⁷⁵³J. A. Sedlacek, A. Schwettmann, H. Kübler, R. Löw, T. Pfau, and J. P. Shaffer, “Microwave electrometry with rydberg atoms in a vapour cell using bright atomic resonances,” *Nucl. Phys.* **8**, 819–824 (2012).
- ⁷⁵⁴M. T. Simons, J. A. Gordon, C. L. Holloway, D. A. Anderson, S. A. Miller, and G. Raithel, “Using frequency detuning to improve the sensitivity of electric field measurements via electromagnetically induced transparency and autler-townes splitting in rydberg atoms,” *Appl. Phys. Lett.* **108**, 174101 (2016).
- ⁷⁵⁵J. Han, T. Vogt, C. Gross, D. Jaksch, M. Kiffner, and W. Li, “Coherent microwave-to-optical conversion via six-wave mixing in rydberg atoms,” *Physical review letters* **120**, 093201 (2018).
- ⁷⁵⁶A. P. Orioli, A. Signoles, H. Wildhagen, G. Günter, J. Berges, S. Whitlock, and M. Weidemüller, “Relaxation of an isolated dipolar-interacting rydberg quantum spin system,” *Phys. Rev. Lett.* **120**, 063601 (2018).
- ⁷⁵⁷H. J. Kimble, “The quantum internet,” *Nature* **453**, 1023–1030 (2008).
- ⁷⁵⁸N. J. Lambert, A. Rueda, F. Sedlmeir, and H. G. Schwefel, “Coherent conversion between microwave and optical photons – an overview of physical implementations,” *Advanced Quantum Technologies* **3**, 1900077 (2020).
- ⁷⁵⁹T. Vogt, C. Gross, J. Han, S. B. Pal, M. Lam, M. Kiffner, and W. Li, “Efficient microwave-to-optical conversion using rydberg atoms,” *Physical Review A* **99**, 023832 (2019).
- ⁷⁶⁰B. T. Gard, K. Jacobs, R. McDermott, and M. Saffman, “Microwave-to-optical frequency conversion using a cesium atom coupled to a superconducting resonator,” *Physical Review A* **96**, 013833 (2017).
- ⁷⁶¹M. Kiffner, A. Feizpour, K. T. Kaczmarek, D. Jaksch, and J. Nunn, “Two-way interconversion of millimeter-wave and optical fields in rydberg gases,” *NJP* **18**, 093030 (2016).
- ⁷⁶²T. Vogt, C. Gross, T. F. Gallagher, and W. Li, “Microwave-assisted rydberg

- electromagnetically induced transparency,” *Optics letters* **43**, 1822–1825 (2018).
- ⁷⁶³V. G. Minogin, M. V. Subbotin, and P. N. Melent’ev, “Dynamics of cold atoms in a quadrupole magnetic trap with an orbiting potential,” *Journal of Experimental and Theoretical Physics* **87**, 12–19 (1998).
- ⁷⁶⁴P. W. Cleary, T. W. Hijmans, and J. T. M. Walraven, “Manipulation of a Bose-Einstein condensate by a time-averaged orbiting potential using phase jumps of the rotating field,” *Physical Review A* **82**, 063635 (2010).